UNIVERSITY OF SOUTHAMPTON

INSTITUTE OF SOUND AND VIBRATION RESEARCH

SIGNAL PROCESSING AND CONTROL GROUP

STRAIN TRANSDUCERS FOR ACTIVE CONTROL

by

Y. Aoki

A thesis submitted for the award of Doctor of Philosophy

September 2008

UNIVERSITY OF SOUTHAMPTON

ABSTRACT

FACULTY OF ENGINEERING, SCIENCE AND MATHEMATICS
Institute of Sound and Vibration Research

Doctor of Philosophy

STRAIN TRANSDUCERS FOR ACTIVE CONTROL

by Yohko Aoki

This thesis presents the results of a theoretical and experimental study of active vibration control using velocity feedback with piezoceramic actuator(s) and closely located velocity sensor(s). The first part of the thesis presents modeling and design studies for a square piezoceramic actuator used to implement a single channel velocity feedback control with a velocity sensor at its center. A fully coupled mobility model of the panel with a square piezoceramic patch actuator is introduced and experimentally validated in order to predict the sensor-actuator open loop response over much wider frequency range than is commonly used, so that the stability of the feedback control loop can be properly assessed using the Nyquist criterion. These simulations suggest that increasing the width and reducing the thickness of the square actuator improves the control performance of a single channel velocity feedback control loop in the case considered. The second part of this thesis investigates a new configuration of the velocity feedback control system, which is composed of a piezoceramic actuator shaped as isosceles triangle with a velocity sensor at its tip. A fully coupled mobility model has been developed, which predicts the response of the sensor-actuator pair more accurately than the conventional modeling method. The implementation of a 16 channel decentralized control system using triangular actuator has been experimentally demonstrated. Significant levels of attenuation, up to 20 dB, are achieved at the first few resonant peaks in term of both structural vibration and sound radiation. Closed loop measurements have highlighted that the control performance are significantly improved by increasing the base length and/or the height of the triangle actuators, with the limitation that the increase of the height reduces the usable frequency range of the control system. [279 words]

Contents

List of Tables

List of Figures

List of Symbols

General Notations

$\mathbf{0}$	Zero Matrix	[-]
$\mathbf{d}$, $\mathbf{D}$	Vector or matrix with 0 and 1	[-]
$\mathbf{I}$	Identity matrix	[-]
ϕ_n	nth mode shape function	[-]
ψ_n	First derivative of nth mode shape function	[-]
ω	Circular frequency	[rad/sec]
ω_n	nth natural frequency	[rad/sec]
π	Circular constant	[-]
λ	Wave length	[m]
σ	Stress	[N/m^2]
j	Imaginary number	[-]
n	Number of element	[-]
t	Time	[sec]
V	Voltage	[V]

Parameters

η	Loss factor	[-]
ν	Poisson's ratio	[-]
ρ	Density	[kg/m^3]
a_{pzt}	Width of a square patch	[m]
b_{pzt}	Base length of a triangular patch	[m]
d_{31}, d_{32}, d_{36}	Piezoelectric strain-charge constant	[m/V]
D	Flexural rigidity	[Nm]
e_{31}, e_{32}, e_{36}	Piezoelectric stress-charge constant	[N/(Vm)]
E	Young's modulus of elasticity	[N/m^2]
h	Thickness	[m]
l_x, l_y	Length of the panel	[m]
m	Mass	[kg]
t_{pzt}	Height of a triangular patch	[m]
$()_{pzt}$	Subscript: piezoceramic actuator	[-]
$()_s$	Subscript: structure	[-]

Phasor and mobilities

f, $\mathbf{f}$	Point force	[N]
m, $\mathbf{m}$	Point moment per unit length	[N]
w, $\mathbf{w}$	Out-of-plane displacement	[m]
u, $\mathbf{u}$	Inplane displacement	[m]
θ, $\boldsymbol{\theta}$	Rotational angle	[m]
Y, $\mathbf{Y}$	Mobility function	[m/(sec N)]
Z, $\mathbf{Z}$	Impedance function	[(sec N)/m]
$()_b$	Subscript: boundary effects	[-]
$()_c$	Subscript: control excitation	[-]
$()_e$	Subscript: inertia effects	[-]
$()_k$	Subscript: stiffness effects	[-]
$()_p$	Subscript: primary excitation	[-]
$()_s$	Subscript: square piezoceramic actuator	[-]
$()_t$	Subscript: triangular piezoceramic actuator	[-]

Control theory

δ_k	Control ratio at kth resonant frequency	[-]
d, $\mathbf{d}$	Sensor signal without control	[-]
G, $\mathbf{G}$	Frequency response function	[-]
H, $\mathbf{H}$	Frequency-constant feedback Control gain	[-]
y, $\mathbf{y}$	Sensor signal with control	[-]
L	Sound pressure level	[N/m^2]
p	Pressure	[N/m^2]
R_k	Maximum reduction index at kth resonant frequency	[dB]

Abbreviations

AR	Aspect Ratio
ASAC	Active Structural Acoustic Control
AVC	Active Vibration Control
FRF	Frequency Response Function
ISVR	Institute of Sound and Vibration Research
MIMO	Multi-Input Multi-Output
PZT	Lead(Pb)-Zirconate(Zr)-Titanate(Ti)
SISO	Single-Input Single-Output

Acknowledgement

This thesis is the result of my research activities between 2005 and 2008 at the Institute of Sound and Vibration Research, University of Southampton, in the UK. At this point, I would like to sincerely thank all institutions, organizations and individuals, who contributed with their advices, practical experience and/or encouragement to the completion of this study.

First I would like to express my deepest gratitude to my supervisor Prof. Paolo Gardonio for his valuable guidance and continuous support throughout this work. The assistance and excellent advices from my second supervisor, Prof. Stephen J. Elliott is acknowledged with sincere thanks and deep appreciation. Special thanks are also due to Dr. Ken Frampton, who shared his precious practical experience with me and greatly supported my research progress.

The technical support received from Dr. Carmen Galassi and Mr. Claudio Capiani (ISTEC in Italy) as well as their efforts to provide us with high quality piezoceramic patches is greatly appreciated for. The help provided by Dr. Marco Gavagni to obtain high quality measurement is deeply acknowledged for.

I am particularly grateful to the entire staff, fellow PhD students and scientists at ISVR (Cristobal, Hong, Ioannis, Jens, Neven, Oil, Paulo and many others) for their suggestions, advices, practical help and useful ideas, which significantly contributed to the successful completion of this thesis.

The significant financial support from the InMAR project during my complete research term, and Nakajima Foundation in Japan is deeply appreciated and acknowledged for.

Last but not least I would like to thank very much my family and my best friends Lumi, Miz and Radu for their useful advices and moral support to complete this thesis. And thank all, who offered me their kind support, but whose names are not mentioned here. It has been a great honor for me to work together with you all, thank you very much for your support.

Chapter 1

Introduction

1.1 The vibration and noise problems

Reducing interior noise is nowadays an important issue for both land and air transportation vehicles, such as aircrafts, helicopters, cars, and trains. The vibro-acoustic problems represent a crucial aspect in the design of modern vehicles, especially airplanes and helicopters. Roughly speaking, there are two main interior noise sources in any vehicle: those arising from aerodynamics and noise sources (e.g. engines), and those generated by the vibration. They are referred to as air-borne and structure-borne noise [1]. Transportation vehicle structures, such as car body and fuselage panels, are mainly constructed by lightweight thin panels, which efficiently radiate the sound to the interior due to their low-damping properties and out-of-plane flexibility. Low audio frequency structure-borne broadband noise is often considered one of the most irritating component of noise, due to interference with speech communication.

Conventionally, passive treatments are often used to suppress vibration and hence sound radiation by thin lightweight panel and shell structures [2–4]. However, classic passive solutions such as insulating and damping materials involve significant weight and space penalties and are most effective only at high frequencies. At low audio frequencies, passive approaches tend to have limited performance and require relatively bulky and heavy treatments.

Alternatively, active control techniques were suggested to reduce the vibration and/or

sound radiation at low audio frequencies. Suppression of interior noise can be achieved by modifying the dynamic behavior of the structure through structural inputs rather than by exciting the acoustic medium [5, 6]. This control approach is referred to as active structural acoustic control (ASAC) and has been tackled in many different projects and publications over the last two decades [6–14]. The appeal of ASAC systems is that sensor and actuator transducers are embedded to the radiating structure, so that a lightweight and compact smart structure is achieved.

Velocity feedback control is one of the most popular control strategies used in ASAC systems, and has been successfully applied for many years, due to its simplicity and efficiency [6, 15]. If an ideal force actuator is used, collocated velocity feedback is equivalent to a sky-hook damper on the structure, as shown in Fig. 1.1. As mentioned earlier, one of the principal structural components of transportation vehicles are lightweight thin panels, whose low frequency structural response is normally controlled by well separated sharp resonances [5, 6, 15]. Since at resonance frequencies the response of a structure is principally controlled by damping, velocity feedback control can add active damping on the structure [5, 15, 16], and thus suppress the response to broadband disturbances.

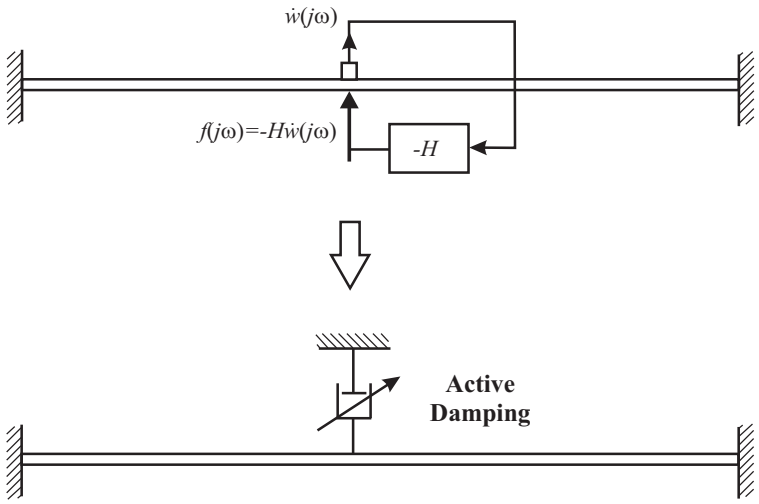

Figure 1.1: Velocity feedback control to generate active damping on a structure.

1.2 Introduction to decentralized control

The application of ASAC on large-scale systems with many structural modes has achieved limited success. This is partly due to the scalability limitations of the centralized control architectures that have been used. Centralized control consists of a system, wherein all sensors signals are fed to a single centralized processor and used to generate all feedback control signals, as shown in left hand side schematics in Fig. 1.2. One of the draw-backs of these architectures is an overwhelming computational burden on the centralized processor when applied to large-scale systems with numerous sensors and actuators, and long cables.

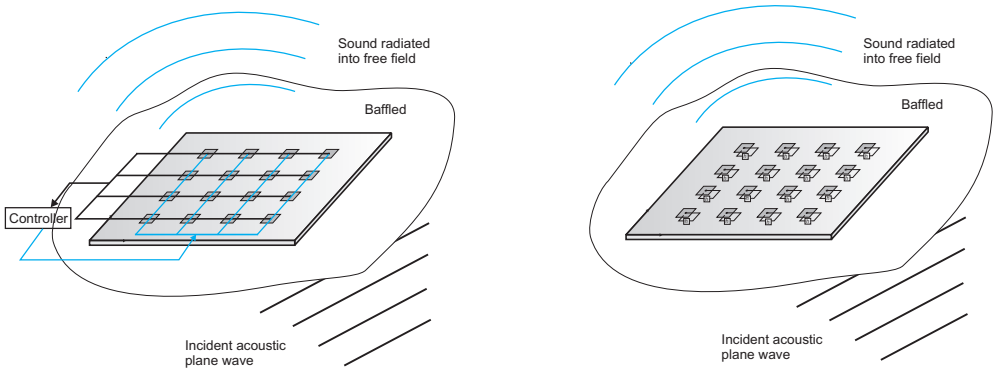

Figure 1.2: A rectangular panel with a large number of centralized (left) and decentralized (right) sensor-actuator pairs.

The difficulty in scaling up centralized control systems has led to the consideration of a simpler control approach, where multiple single channel control units are used in place of a single multiple channel control system [17–22]. Decentralized control, as shown in right hand side in Fig. 1.2, consists of numerous feedback control loops working independently to achieve a global performance objective. Recently, research on distributed control [23, 24] has also started, which consists of more than one controller (or nodes), which receives a subset of the system sensor signals and uses them to produce a subset of the system control signals. This aims to achieve a global performance similar to centralized control, and to retain the scalability advantages of decentralized control.

The number of such feedback loops required to control the vibration depends on the

bandwidth over which control is required, and the size of the structure, which both affect the number of structural modes of the system. In general, a large number of control units leads to greater performance, however, it becomes more difficult to guarantee overall stability of the non-centralized control system [25, 26], since each controller is affected by neighboring units. Balas [27] and Preumont [16] have shown that it is advantageous to consider the use of collocated and dual sensor-actuator pairs [28, 29] to implement decentralized velocity feedback control, because in this case the open loop frequency response function (FRF) is bound to be positive real. Thus, the velocity feedback control loops are unconditionally stable [5, 15, 16]. Therefore, large control gains could be implemented, which produce high levels of damping that reduce the response of the structure at low frequency resonances [5]. Care must be taken, however, to avoid extremely high control gains, since these would pin the structure at the sensor positions and not add global damping [17].

In practice, it is very difficult to implement sensor-actuator pairs, which are truly collocated and dual. Sensors and actuators can be characterized by their physical size and electro-dynamic responses, which introduce non-collocation and non-dual properties. For instance, considerable work has been dedicated to the development of velocity feedback using a proof mass electro-dynamic force actuator and an accelerometer sensor located on the base of the actuator [16, 30–32], in which case the control system is characterized by instability issues due to the fundamental resonance of the actuator at low frequency [33], and the actuator electrodynamic response at higher frequencies [34]. Bingham *et al.* [35] also considered decentralized systems, but without dual collocated transduction, and found that more complex control strategies performed better than constant gain output feedback.

1.2.1 Piezoceramic patch actuator

The use of piezoceramic patch actuators has been suggested in order to overcome the physical limitations of the proof mass electrodynamic actuators, and provide an active compact system that is more integrated with the structure. A significant amount of research effort has been dedicated to the development of active vibration control (AVC) and ASAC systems using piezoceramic patch actuators [5, 6, 36–40]. This thesis concentrates on the case, where a piezoceramic actuator is used with a

conventional accelerometer as a sensor, so that in-plane coupling for piezoceramic actuator and sensor [11] is not accounted for.

Recently Gardonio *et al.* [19–21] have carried out analytical and experimental studies regarding the suppression of structural vibration and sound radiation from a flat panel at low audio frequency using 16 square piezoceramic actuators and closely located accelerometer sensors pairs distributed over the whole panel, as illustrated in left hand side schematics in Fig. 1.3. A number of stability issues have been found with this arrangement, which are caused by the non-perfect duality and collocation between the sensor and actuator transducers.

When a piezoceramic patch actuator is bonded on a plate, it can be simply modeled as generating line moments along its border [6, 41]. These are, however, neither collocated nor dual with respect to the linear velocity measured at the center of the patch [20]. Thus, stability can be guaranteed only for a limited range of feedback control gains even for a single velocity feedback loop. Even though the control system acts at the error sensor positions, provided that moderated feedback control gains are implemented, active damping can be generated on the whole panel, which reduces the response and sound radiation of well separated resonances of low order modes. Bianchi [42] has shown that the response and sound radiation of a rectangular panel can be efficiently reduced at low audio frequencies by a 4 by 4 array of 16 decentralized velocity feedback control loops using piezoceramic patch actuators with accelerometer sensors at their centers.

The stability of these control systems could be improved by changing the shape of the rectangular piezoceramic actuator. A novel configuration has been presented by Gardonio *et al.* [43] to implement velocity feedback control using triangularly shaped piezoceramic actuators arranged along the borders of a panel, and accelerometer sensors at the top vertices of the actuators, as illustrated in right hand side sketch in Fig. 1.3. This arrangement has an advantage in that it is not invasive, and thus could potentially be used in a wider class of applications, including the windows of transportation vehicles, such as aircrafts, helicopters, cars, trucks, coaches, etc. A theoretical study [44] suggests that this sensor-actuator pair enables the implementation of stable feedback control loops with rather high gains.

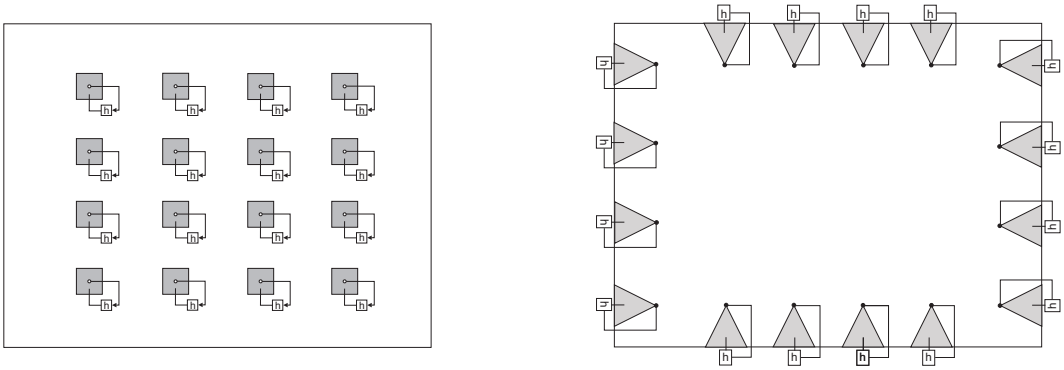

Figure 1.3: A rectangular panel with 16 decentralized sensor-actuator pairs, composed of square piezoceramic actuators and velocity sensors at their centers (left) and triangular piezoceramic actuators and velocity sensors at their tip vertices (right)

1.2.2 Short review on the modeling of piezoceramic actuators

Another way in which to improve the stability properties of a velocity feedback control unit is to add a filter or compensator in the feedback loop [15, 16]. However, the design of these devices relies on the knowledge of the dynamics of the structure, actuators and sensors. They also tend to introduce undesired phase shifts or amplitude variations that could reduce the control effectiveness or even lead to control spillover effects. It is therefore important to design the piezoceramic actuator and velocity sensor pair in such a way that the open loop FRF is as positive real as possible and thus guarantees good stability and control performance properties with a fixed gain feedback loop.

Several approaches to modeling beam, plate, and shell structures with integrated piezoceramic actuators have been introduced, based on analytical formulations [10, 45–52], or approximate finite element formulations [53–55].

Crawley and de Luis [45] presented one of the first comprehensive modeling studies of the flexural response of a structure excited by two symmetric piezoceramic patch actuators. They showed that the actuation field produced by a pair of thin piezoceramic patches bonded on a beam can be modeled in terms of bending moments along the edges of the patches. In their derivation they also considered the local, fully coupled, passive stiffness effect of the piezoceramic patches. The local, fully coupled, passive mass effect, however, of the piezoceramic patches was neglected. Later on, Crawley and Andersson [46] and Lin and Rogers [47] presented improved models

considering a linear strain distribution across the thickness, and a plane stress field for the piezoceramic patch actuators. Dimitriadis *et al.* [10] extended the work by Crawley and de Luis [45] to the case of a flat plate with symmetric piezoceramic patch actuators. Kim and Jones [48] further extended this work to investigate the effects produced by the bonding layer on the actuation strength. Also Gibbs and Fuller [49] derived the response of a beam with a single embedded piezoceramic patch actuator. The works presented in references [10, 48, 49] were focused on the derivation of the actuation bending moment. No explicit formulation was given for the local, passive stiffness and mass effects of the piezoceramic patches.

In parallel to this work on segmented piezoceramic actuators, Lee and Moon [56, 57] and Lee [58] presented models for the response of structures entirely covered by distributed piezoceramic transducers with shaded thin electrodes. In this case the passive stiffness and inertial effects were taken into account in the plate equation of motion by considering the equivalent bending stiffness and mass density of a multilayer plate. Thus the formulation was entirely focused on the derivation of the bending excitation field generated around the edges of the electrodes. Koshigoe and Murdock [59] have developed a similar formulation to that proposed by Lee [58] for a segmented piezoceramic actuator, which explicitly include the local, fully coupled, passive stiffness effect of the piezoceramic patch. The models discussed above are derived for beams and plates with rectangular piezoceramic patches. Sullivan *et al.* [44] have presented a formulation that gives the actuation field produced by distributed piezoceramic actuators with electrodes having an arbitrary spatial distribution. The local, fully coupled, passive mass and stiffness of the piezoceramic patches have been modeled by Hagood *et al.* [50], Charette *et al.* [51] and Wang and Huang [52].

In most of these studies the response of the structure has been analyzed only within the operation frequency range of the controller. However, when a piezoceramic patch actuator is bonded on the surface of a thin structure, actuation strength increases with frequency up to a limit, where the bending wavelength matches the width of the actuator patch [60, 61]. Furthermore the amplitude rise is associated with a rising phase lag effect produced by the time delay it takes for the bending wave generated along the perimeter of the piezoceramic patch to reach the sensor at its

center [20]. These two effects result in stability problems at high frequency, beyond the desirable operation range. Therefore, a better analytical mode is required, which takes into account (1) the physical effects produced by the piezoceramic actuators, and (2) is able to predict the open loop Frequency Response Function (FRF) up to relatively high frequencies, e.g. 80 kHz, in order to properly assess the stability of the feedback control loop using the Nyquist criterion [5, 15, 16].

1.3 Objectives and contributions

The objectives and contributions of the thesis are the following:

1. To develop a fully coupled mobility model of a panel with a square or a triangular piezoceramic patch actuator to predict the sensor-actuator open loop FRF over a frequency range up to 80 kHz (Chapter 2 and 4).

2. To validate the developed mobility models with sensor-actuator open loop FRF measured on test panels (Chapter 2 and 4).

3. To introduce general guidelines regarding the design of square and triangular actuators to implement active velocity feedback control loops with good stability properties (Chapter 3 and 6).

4. To demonstrate the control performance of a decentralized velocity feedback control system, using 16 control loops composed of triangular piezoceramic actuators and accelerometer sensors pairs (Chapter 5 and 6).

1.4 Structure of the thesis

The thesis is organized into seven chapters. This introductory chapter describes the motivation and background of this work. Following the introduction chapter, Chapters 2 and 3 contain theoretical and experimental results regarding modeling and design studies on square piezoceramic actuators to implement velocity feedback control.

Chapter 2 presents fully coupled formulation of the panel with a square piezoceramic patch actuator, which takes into account for both the inertia and stiffness effects of the actuator. The open loop FRF predicted with the fully coupled model is then compared with the FRF predicted with the ideal actuator model in order to present a physical interpretation of the passive inertia and stiffness effects of the piezoceramic patch on the stability of the feedback control loop. The validity and limitations of the fully coupled model is assessed by contrasting the predicted and measured open loop FRFs.

Chapter 3 presents a theoretical and experimental parametric study on the stability and control performance of a single velocity feedback control loop with a square piezoceramic patch actuator. A parametric study is carried out to investigate the effects of the physical dimensions of the actuator on the stability and control performance. The aim of this parametric study is to provide general guidelines for the design of a feasible actuator with good stability properties to achieve high control performance. A simple formula is derived to evaluate the upper bound of the obtainable vibration reduction of a single velocity feedback unit at low frequency resonances.

The second part of this thesis, Chapter 4, 5, and 6, contains theoretical and experimental results obtained with triangular piezoceramic actuators.

Chapter 4 first presents a comparison between a square and a triangular piezoceramic actuator in terms of stability and control performance of velocity feedback loops. Then, this chapter introduces a frequency domain analytical model of a thin panel with a triangular piezoceramic actuators in order to predict the open loop FRF. This model takes into account the boundary conditions of the panel in addition to the mass and stiffness effects of the piezoceramic actuator. Experimental results are presented to validate the fully coupled model.

Chapter 5 presents the implementation of a decentralized velocity feedback control system using 16 triangular piezoceramic actuators and accelerometer sensors. The dynamics of the accelerometer sensor is briefly introduced, and the open loop FRF measured using remote sensor is compared with that measured using an accelerometer sensor attached to the structure to highlight its passive effects. Finally, the

control performance is measured in terms of both vibration and sound radiation reductions. The principal characteristics of the control performance are reviewed to highlight the advantages of the proposed control arrangement.

Chapter 6 presents a theoretical and experimental parametric study on the stability and control performance of (1) single-input single-output (SISO) velocity feedback control loop, and (2) decentralized multi-input multi-output (MIMO) velocity feedback control loops composed of triangular piezoceramic patch actuator(s) and structural sensor(s). The goal of the parametric study is to determine the influence of the physical dimensions of the piezoceramic actuator on the control performance and on the stability properties of the control loop.

The last chapter is a summary of the work, including a list of suggestions for future work.

Chapter 2

Velocity Feedback Control using Square Piezoceramic Actuators

Chapter 2 introduces the mobility model of the panel with a square piezoceramic patch actuator by accounting for the effects of both the stiffness and mass of the actuator on the response of the structure. The discussion begins by considering the idealized actuator with no mass or stiffness, and then accounting for their effects separately. Finally, the fully coupled mathematical model is introduced, which considers both inertial and stiffness effects of the actuator.

The mathematical models suggested in this thesis are derived using the classic Kirchhoff-Love thin plate theory [62], which is valid up to about 80 kHz for the 1 mm thick aluminium plate considered in this study. The model has been used to predict the open loop frequency response function in a wide frequency band, up to 80 kHz, so that the stability of the feedback control loop can be properly assessed using the Nyquist criterion. Full details regarding the panel-actuator coupled models have been discussed, which consider passive inertial and elastic effects of the actuator patch.

2.1 Velocity feedback control

2.1.1 Rectangular panel with a square piezoceramic actuator

The physical arrangement of test structure considered in this study, which is also used in the simulation study, is a thin rectangular aluminium panel with dimensions of 474 mm × 374 mm × 1 mm. As shown in Fig. 2.1, the four edges of the panel are clamped by rigid aluminium frame with 30 mm width by using 12 of M6 screws. The frame restricts the rotation and plane motion of the panel at the boundaries. Thus, the free vibration area of the panel is given by 414 mm × 314 mm. The geometry and physical properties of the panel and the frame are given in Table 2.1.

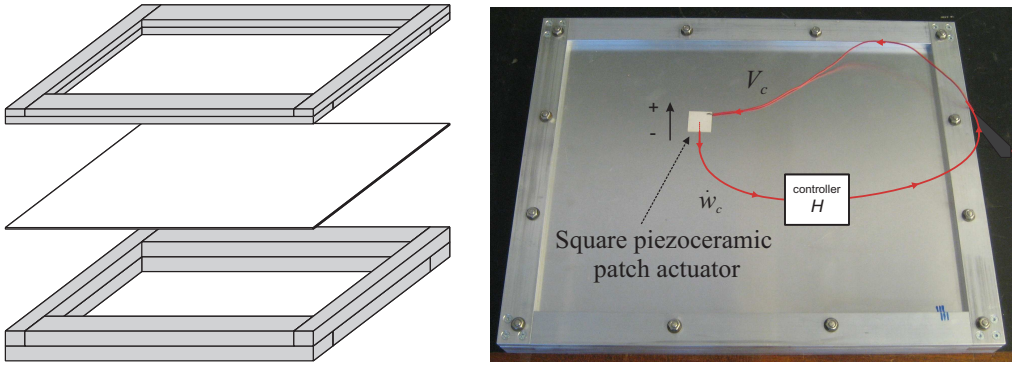

Figure 2.1: Clamped panel with a square piezoceramic patch actuator and an ideal velocity sensor at its center to implement a fixed gain velocity feedback control loop

Table 2.1: Geometric parameter and physical properties of the aluminium panel

parameter	symbol	value
Width [mm]	l_x, l_y	414.0, 314.0
Thickness [mm]	h_s	1.0
Density [kg/m^3]	ρ_s	2700.0
Young's Modulus [GPa]	E_s	72.0
Poisson's Ration	ν_s	0.33
Loss Factor	η_s	0.0093
Top frame width [mm]	–	30.0
Top frame thickness [mm]	–	10.0
Bottom frame width [mm]	–	30.0
Bottom frame thickness [mm]	–	20.0

The panel is equipped with a 20 mm × 20 mm × 1 mm square piezoceramic patch actuator with thin electrodes deposited on the two faces, and poled direction oriented

as shown in Fig. 2.1. The piezoceramic actuators are made of a niobium doped PZT material [63], produced by ISTEC in Italy. The actuator is firmly bonded on the top side of the panel by a thin layer of conductive epoxy glue, with its edges parallel to the borders of the panel. The thickness of the adhesive layer has been measured approximately as 0.05 mm. The center position of the piezoceramic patch is located at (x_c, y_c) = (136.6 mm, 222.9 mm) with reference to the lower left hand side corner of the panel. A wire was soldered directly on left-top corner of the exposed side of the patch to complete the electrical circuit necessary to drive the actuator. The geometry and mechanical properties of the piezoceramic patch are summarized in Table 2.2. More detailed piezoelectric properties of the piezoceramic patch is provided by the manufacturer, and are summarized in Appendix B.

Table 2.2: Geometric parameter and physical properties of the square piezoceramic actuator produced by ISTEC in Italy [63]

parameter	symbol	value
Dimensions [mm]	a_{pzt}	20.0
Thickness [mm]	h_{pzt}	1.0
Center Position [mm]	x_c, y_c	136.6, 222.9
Poisson's Ratio	ν_{pzt}	0.35
Density [kg/m^3]	ρ_{pzt}	7.82×10^3
Piezoelectric charge constant [m/V]	$d_{31} = d_{32}$	-183.5×10^{-3}

The actuation dynamics generated by a square piezoceramic patch is normally modeled in terms of bending moments along the four edges of the patch [45]. The previous studies [10, 45, 48] have shown that, when the piezoceramic actuator is firmly bonded on the base structure, this approximation adequately well models the actuation of the piezoceramic patch. Since piezoceramic transducers are comparatively stiff materials, their actuation strength is normally expressed in terms of the free displacement per unit driving voltage measured on an unconstrained sample of the transducer [16]. Thus, the moment excitations along the four edges of the patch are derived by integrating the product of the bending stress generated by the inverse piezoelectric effect and the offset from the plate middle plane over the lateral

surfaces of the piezoceramic patch [16, 45]:

$$m_{cy} = \int_{y1}^{y2} \int_{\frac{hs}{2}}^{\frac{hs}{2}+hpzt} \sigma_{pzt}^{xx} z dz dy \tag{2.1a}$$

$$m_{cx} = \int_{x1}^{x2} \int_{\frac{hs}{2}}^{\frac{hs}{2}+hpzt} \sigma_{pzt}^{yy} z dz dx, \tag{2.1b}$$

where x_1 and x_2 denote the x-coordinate of edges of the piezoceramic patch parallel to y-axis, and y_1 and y_2 are the y-coordinate of edges of the piezoceramic patch parallel to x-axis, as shown in Fig. 2.2. h_s and h_{pzt} denote the thickness of the plate and piezoceramic patch respectively. σ_{pzt}^{xx} and σ_{pzt}^{yy} are the bending stress components per unit voltage generated in x- and y-directions by the piezoceramic patch:

$$\sigma_{pzt}^{xx} = \frac{E_{pzt}}{1-\nu_{pzt}} \frac{d_{31}}{h_{pzt}} \tag{2.2a}$$

$$\sigma_{pzt}^{yy} = \frac{E_{pzt}}{1-\nu_{pzt}} \frac{d_{32}}{h_{pzt}}, \tag{2.2b}$$

where E_{pzt} and ν_{pzt} are the Young's modulus of elasticity and Poisson's ratio of the piezoceramic material. d_{31} and d_{32} are the piezoelectric charge constants, which give the ratio of mechanical strain to an applied electric field. Therefore, the bending moments generated along the four edges of the patch per unit voltage excitation are given by the following expressions:

$$m_{cy} = \frac{a_{pzt} d_{32} E_{pzt}}{1-\nu_{pzt}} \left(\frac{h_{pzt}+h_s}{2} \right) \tag{2.3a}$$

$$m_{cx} = \frac{a_{pzt} d_{31} E_{pzt}}{1-\nu_{pzt}} \left(\frac{h_{pzt}+h_s}{2} \right), \tag{2.3b}$$

where a_{pzt} denotes the width of the square piezoceramic actuator. As shown in Table 2.2, for the piezoceramic patch considered in this study, the piezoelectric strain constants d_{31} is equal to d_{32}, so that the bending moment in $x-$ and $y-$ directions are the same, i.e. $m_{cx} = m_{cy} = m_c$.

In order to introduce a consistent formulation to those presented in Section 2.2 for the passive inertial and stiffness effects of the piezoceramic patch, the square piezoceramic actuator is modeled n_s by n_s grid of small elements with a square base, as shown in Fig. 2.2. The number of elements has been chosen in such a way

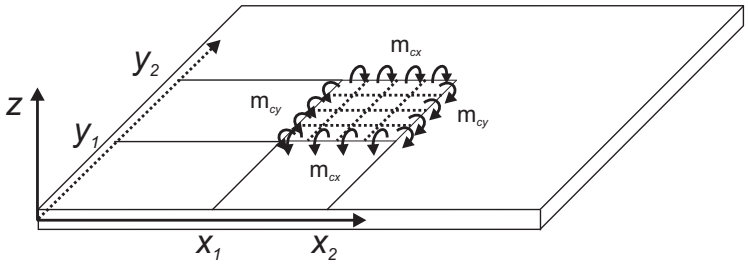

Figure 2.2: Schematic of the model for the piezoceramic patch moment actuation

that the distance between centers of adjacent elements is shorter than a quarter of the flexural wavelength at the maximum frequency considered in this study, i.e. $\lambda_{min} = 6$ mm at 80 kHz. Therefore, the piezoceramic patch have been subdivided into grid of n_s by $n_s = 13$ by 13 elements, such that the distance between the centers of two neighbor elements becomes 1.54 mm.

The actuation moments produced by the square actuator per unit voltage is now modeled by the point moments exerted at four end- surfaces of the n_s^2 elements of the square actuator, as:

$$\mathbf{m_c} = m_c \begin{bmatrix} -\mathbf{d_1} & +\mathbf{d_2} & +\mathbf{d_1} & -\mathbf{d_2} \end{bmatrix}^T, \tag{2.4}$$

where $\mathbf{d_1}$ and $\mathbf{d_2}$ are n_s^2-element column vectors. When the ith element of the square actuator exerts actuation moments, the ith element of $\mathbf{d_1}$ and $\mathbf{d_2}$ is given as 1, otherwise, the value of the vectors is zero. As it is assumed in this study that a piezoceramic actuator generate bending moments only along its border [6, 41], the active moments is generated along the end surface of the n_s elements located along the four edges of the square actuator. Thus, first n_s-elements of $\mathbf{d_1}$ are equal to 1, and the rests are zero, whilst the last n_s-elements of $\mathbf{d_2}$ are equal to 1, and the rests are zero.

2.1.2 Open loop FRF of the idealized actuator

As shown in the right hand side plot in Fig. 2.1, the piezoceramic actuator is used with a velocity sensor at its center to implement velocity feedback control. At this stage, the velocity sensor is considered ideal. It is later implemented using a laser

vibrometer to validate the theory. When the feedback control loop is closed, the output signal of the velocity sensor $\dot{w}_c$ is magnified by a constant negative feedback gain $-H$, and then fed back to the piezoceramic actuator in order to produce an active damping effect on the panel. The stability of the feedback control system is assessed with reference to the open loop FRF between the output signal from the sensor and the input signal to the actuator. For the control system considered in this study, the output signal of the sensor is the out-of-plane velocity of the plate at the control point $\dot{w}_c$, and the input signal is the voltage V_c driving the actuator. Therefore, the open loop FRF G_c is defined as:

$$G_c(j\omega) = \frac{\dot{w}_c(j\omega)}{V_c(j\omega)}, \tag{2.5}$$

where $\dot{w}_c(j\omega)$ and $V_c(j\omega)$ are the complex velocity and voltage assuming harmonic functions with time dependence in the form $\exp(j\omega t)$, and $j = \sqrt{-1}$ and ω is the circular frequency.

The complex velocity of the panel at the ideal point sensor $\dot{w}_c$ has been formulated using the following mobility matrix expression:

$$\dot{w}_c = \mathbf{Y_{cs}}\mathbf{m_c}V_c, \tag{2.6}$$

where $\mathbf{Y_{cs}}$ denotes a $4n_s^2$-element row vector with the mobility functions between the ideal velocity sensor $\dot{w}_c$ and the moment m_c on the four edges of the elements. The kth element of $\mathbf{Y_{cs}}$ is defined as follows:

$$Y_{cs}^k = j\omega \sum_{m=1}^{M}\sum_{n=1}^{N} \frac{F_i F_j}{\Lambda[\omega_{mn}^2(1+j\eta_s)-\omega^2]}, \tag{2.7}$$

where m and n respectively denote the modal index in x- and y-direction, and η_s denotes loss factor of the panel. Λ denotes the modal mass of the panel. ω_{mn} is the (m,n)th mode natural frequency of the plate. The functions F_i and F_j represent the modal contributions respectively for the linear velocity at the sensor position, and the point moment excitations along the edges of the actuator. F_i and F_j have been derived from the natural modes ϕ and their derivatives in $x-$ and $y-$directions, ψ_x and ψ_y, respectively. More detailed analytical expressions for the mobility functions

and mode functions are given in Appendix A.

According to Eqs. (2.5) and (2.6), the open loop FRF between the output from the ideal error velocity sensor and the input to the ideal actuator is derived as:

$$G_c = \mathbf{Y_{cs}} \mathbf{m_c}. \tag{2.8}$$

These mobility models suggested in this study are derived using the classic Kirchhoff-Love thin plate theory [62], which is valid up to 80 kHz for the 1 mm thick panel.

Figure 2.3 shows the Bode and Nyquist plots of G_c predicted with the ideal model with distributed bending moment. The faint line in the Bode plot indicates that the mean amplitude of the FRF tends to rise with frequency. This is a typical feature of strain actuators that generates bending moments along the four edges of the patch and thus better excites the plate as the flexural wavelength approaches or becomes smaller than the width of the actuator, i.e. at higher frequencies [5]. The phase plot indicates that the phase is confined between ±90 degree up to about 25 kHz, and then a constant phase lag takes place. The phase lag of flexural waves Φ is given as the product of the circular frequency ω and the time delay t_b that takes the bending waves generated at the edges of the piezoceramic patch to travel to the center position at the velocity sensor location:

$$\Phi = \omega t_d = \frac{\omega a_{pzt}}{2c_b}, \tag{2.9}$$

where c_b denotes the phase velocity of flexural waves in plates. The phase velocity of the flexural waves in plates is given by the following formula [5]:

$$c_b = \sqrt[4]{\frac{D_s}{\rho_s h_s}} \sqrt{\omega}, \tag{2.10}$$

where D_s is the bending stiffness of the plate:

$$D_s = \frac{E_s}{1-\nu_s^2} \int_{-\frac{h_s}{2}}^{\frac{h_s}{2}} z^2 dz = \frac{E_s h_s^3}{12(1-\nu_s^2)}. \tag{2.11}$$

E_s, ν_s and ρ_s denote the Young's modulus of elasticity, Poisson's ratio, and density of the plate. Thus, substituting Eq. (2.10) into Eq. (2.9), the phase lag of flexural

waves is given by the following formula:

$$\Phi = \frac{a_{pzt}}{2}\sqrt{\omega}\sqrt[4]{\frac{\rho_s h_s}{D_s}}. \tag{2.12}$$

As shown by the dotted line in the Bode plot in Fig. 2.3, the predicted phase lag increases with the square root of the circular frequency and follows the rough outline of the phase lag of the simulated open loop FRF. Therefore, the open loop FRF is bound to be positive real only at low frequencies up to a cut off frequency which is determined by the width of the square actuator and the phase velocity of flexural wave in the plate. The Nyquist plot in Fig. 2.3 is characterized by a series of circles, which are determined by the resonant response of the plate. At low frequencies the circles start close to the origin, and are aligned along the positive real axis. As the frequency rises, the size of the circles tends to increase due to the increased actuation strength of bending moments. At higher frequencies the locus rotates towards the left hand quadrants in a clockwise rotation due to the phase lag generated by the non-perfect collocation between the sensor and the actuator pair. Finally, the locus crosses over the negative real axis, and thus, according to the Nyquist criterion, the feedback control loop is only conditionally stable.

2.1.3 Experimental results

In order to assess the validity of the ideal model with distributed bending moments, the predicted open loop FRF is compared with that measured results using the test rig shown in Fig. 2.1. The out-of-plane velocity of the panel at the error sensor position has been remotely measured with a laser vibrometer. Figure 2.3 shows the Bode and Nyquist plots of the open loop FRF G_c, measured between the velocity at the center of the piezoceramic actuator and the input voltage to the actuator. Both analytical and experimental values of the resonance frequencies for the first 10 flexural bending modes of the panel are listed in Table 2.3. The amplitude plot in Fig. 2.3 highlights large differences between the simulated and measured FRFs. At low frequencies, below 1 kHz, the two FRFs have similar amplitude spectra but shifted by about 15 dB.

Since the modal overlap of plates rises proportionally to frequency [64], at higher

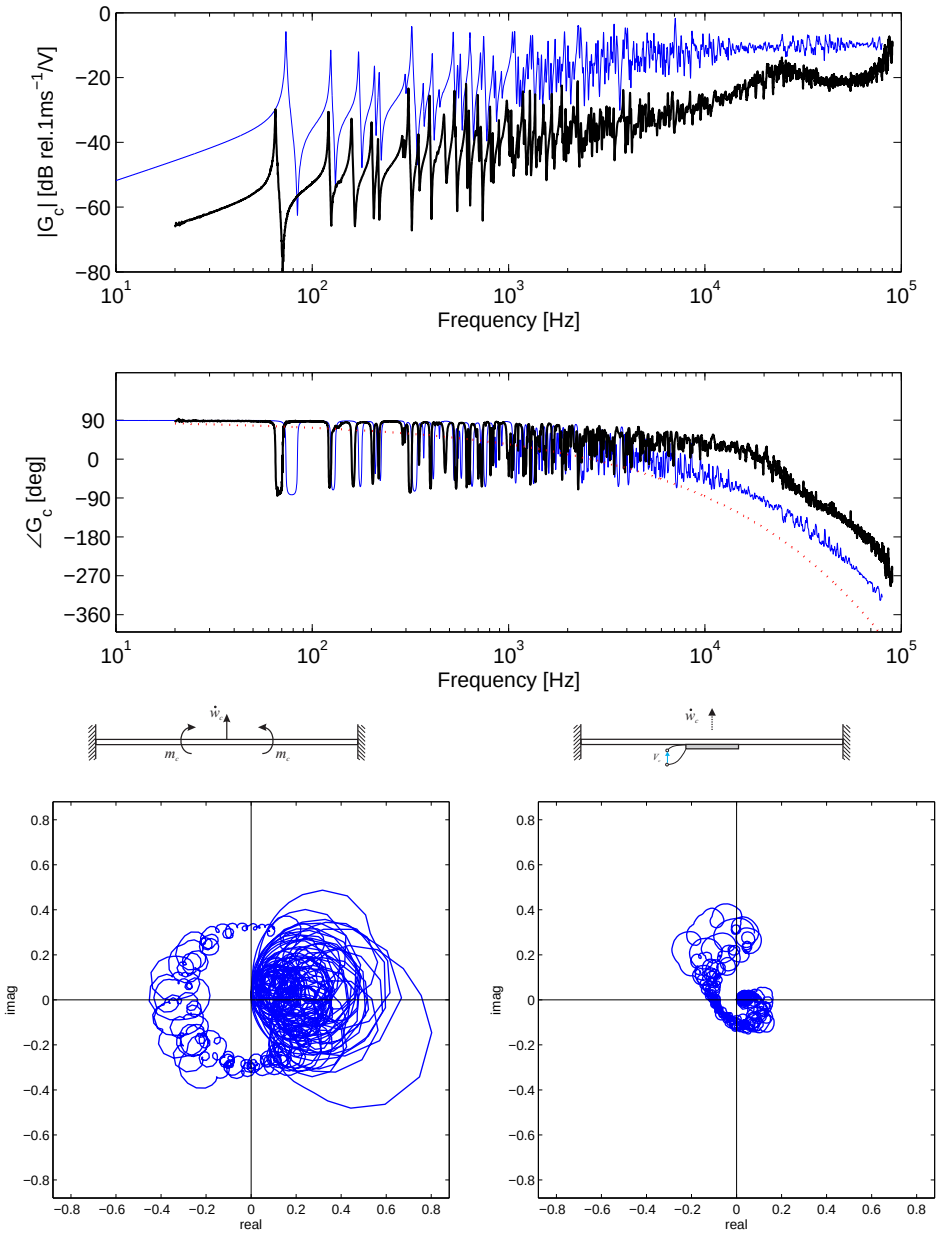

Figure 2.3: Top: Bode plot of the simulated open loop FRF derived with the ideal model with distributed bending moments (blue-faint line) and measured open loop FRF (black-solid line), and predicted phase lag function (red-dashed line). Bottom: Nyquist plots of the simulated open loop FRF derived with the ideal model with distributed bending moments (left) and measured open loop FRF (right)

frequencies, the amplitude spectra of the two FRFs are characterized by clusters of resonant peaks. In this case, the mean spectra are still shifted from each other, although the measured one tends to rise at a smaller rate with frequency so that at about 5 kHz the two spectra are shifted by about 20 dB. Nevertheless the predicted and measured FRF still show very similar phase spectra up to 5 kHz.

Above 5 kHz the amplitude spectrum of the predicted FRF flattens and is much smoother since at each frequency the response is determined by multiple, heavily damped, resonant modes. The amplitude spectrum of the measured FRF is also much smoother although it is characterized by a peculiar modulation effect with a sequence of two wide frequency band peaks with center frequencies at about 20 kHz and 80 kHZ. At these two frequencies the panel flexural wavelength is approximately 19 mm and 10 mm, which are very close to the width and half of the width of the square actuator, respectively. Above 5 kHz the phase spectra of the predicted and measure FRFs also start to diverge although at about 25 kHz they get quite close to each other again.

The discrepancies between the measured and the simulated open loop FRFs highlighted by the Bode plot in Fig. 2.3 suggest that the ideal model is not sufficient to accurately predict the open loop FRF both in the controlled frequency band and also at the high frequencies that are required for a stability analysis. This may be due to the fact that the ideal model neglects all passive physical effects of the piezoceramic actuator. In the following section, more detailed models are introduced for the response of the piezoceramic actuator, which account for the local inertial and stiffness effects of the piezoceramic patch actuator generated on the panel up to high frequencies, where the bending wavelength is shorter than the width of the square actuator. The aim is not only to replicate the measured results, but also to provide a physical interpretation of the principal characteristics of the response function, which can be used to design new configurations of the transducers with open loop FRF that result in better stability properties.

Table 2.3: Resonant frequency of an aluminium panel with 20 mm $\times$ 20 mm $\times$ 1 mm piezoceramic actuator

Mode (m, n)	Measured [Hz]	Predicted [Hz]
(1,1)	64.92	72.64
(2,1)	120.9	123.0
(1,2)	158.5	170.3
(3,1)	200.5	205.6
(2,2)	216.3	216.8
(3,2)	287.5	295.0
(4,1), (1,3)	309.3	318.2
(2,3)	347.5	363.8
(4,2)	396.0	404.6

2.2 Modeling the local dynamics of the actuator

In the previous section, the open loop FRF is simulated with a ideal model that does not take into account the fully coupled passive inertial and the stiffness effects of the actuator on the vibration of the panel. The predicted FRF was compared with the measured FRF, and Fig. 2.3 highlighted the principal modeling problems that need to be improved in order to develop a reliable model for the stability analysis and for the design of the velocity feedback loop. Therefore, in this section, three advanced analytical models are introduced: (1) the first model takes into account the inertial effect of the actuator only, (2) the second model includes only the passive elastic effect of the actuator, and (3) the third model considers both inertial and stiffness effects of the actuator. In this way, it has been possible to separately assess the passive inertial and stiffness effects of the piezoceramic patch.

2.2.1 Modeling distributed mass

As shown in Fig. 2.4, the inertial effect of the actuator mass is modeled by subdividing the piezoceramic patch into n_s by n_s grid of small elements with a square base. The transverse inertial effects of these elements have been modeled in terms of lumped masses located at the centers of these elements. Thus the rotational inertial effects of these elements have been neglected.

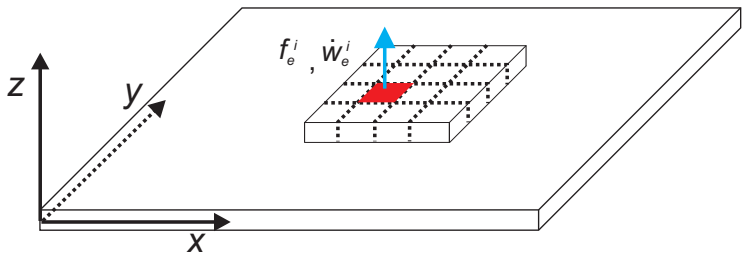

Figure 2.4: Schematic of the model for inertial effect of the actuator mass

When the inertial effect of the piezoceramic patch actuator mass is taken into account, the response can be given as the superposition of the responses due to the moment excitations and the reactive transverse forces produced by the inertia effects of the grid of small elements into which the actuator patch has been subdivided.

Thus the complex transverse velocity at the sensor position $\dot{w}_c$ is given by the following mobility expression:

$$\dot{w}_c = \mathbf{Y_{cs}}\mathbf{m_c}V_c + \mathbf{Y_{ce}}\mathbf{f_e}, \tag{2.13}$$

where $\mathbf{Y_{ce}}$ is a n_s^2-element row vector with the mobility functions between the ideal velocity sensor $\dot{w}_c$ and the forces applied on the centers of lumped mass elements f_e. Expressions for these mobility functions are given in Appendix A. The column vector $\mathbf{f_e}$ contains the forces generated by inertial effects at the center of the mass elements. According to Newton's second and third laws, the force vector is expressed as:

$$\mathbf{f_e} = -m_e\ddot{\mathbf{w}}_\mathbf{e}, \tag{2.14}$$

where m_e denotes the mass of each element that is given by dividing the mass of the actuator m_{pzt} by the number of element n_s^2 as,

$$m_e = \frac{m_{pzt}}{n_s^2}. \tag{2.15}$$

$\ddot{\mathbf{w}}_\mathbf{e}$ is a n_s^2-element column vector with the accelerations at the centers of the mass elements:

$$\ddot{\mathbf{w}}_\mathbf{e} = \left[\begin{array}{cccc} \ddot{w}_e^1 & \ddot{w}_e^2 & \cdots & \ddot{w}_e^{n_s^2} \end{array} \right]^T. \tag{2.16}$$

For the harmonic vibration, $\ddot{\mathbf{w}}_\mathbf{e}$ is expressed in terms of the velocities at the centers of the mass elements, $\ddot{\mathbf{w}}_\mathbf{e} = j\omega\dot{\mathbf{w}}_\mathbf{e}$, so that $\mathbf{f_e}$ is given by:

$$\mathbf{f_e} = -\mathbf{Z_e}\dot{\mathbf{w}}_\mathbf{e}, \tag{2.17}$$

where $\mathbf{Z_e}$ is n_s^2 by n_s^2 impedance matrix due to the inertia of the actuator, given below:

$$\mathbf{Z_e} = j\omega m_e\mathbf{I_d}, \tag{2.18}$$

where $\mathbf{I_d}$ denotes a n_s^2 by n_s^2 identity matrix.

The complex elemental velocity vector $\dot{\mathbf{w}}_\mathbf{e}$ can be derived from the following mobility expressions:

$$\dot{\mathbf{w}}_\mathbf{e} = \mathbf{Y_{es}}\mathbf{m_c}V_c + \mathbf{Y_{ee}}\mathbf{f_e}, \tag{2.19}$$

where $\mathbf{Y_{es}}$ is a n_s^2 by $4n_s^2$ matrix with the mobility functions between the velocities at the centers of the mass elements $\dot{w}_e$ and the moments along the edges of the patch actuator $m_c V_c$. $\mathbf{Y_{ee}}$ is a n_s^2 by n_s^2 matrix with the mobility functions between the velocities at the centers of the mass elements $\dot{w}_e$ and the forces at the centers of the mass elements f_e. Expressions for the mobility functions in these two matrices are given in Appendix A. Substituting Eqs. (2.17) and (2.19) into Eq. (2.13), the velocity at the sensor $\dot{w}_c$ can be expressed with reference to the control voltage only:

$$\dot{w}_c = \left(\mathbf{Y_{cs}} - \mathbf{Y_{ce}}\left[\mathbf{I_d} + \mathbf{Z_e Y_{ee}}\right]^{-1}\mathbf{Z_e Y_{es}}\right)\mathbf{m_c} V_c. \tag{2.20}$$

Thus, according to Eqs. (2.5) and (2.17), the open loop FRF between the output from ideal error velocity sensor and the input to the ideal actuator is derived as

$$G_c = \left(\mathbf{Y_{cs}} - \mathbf{Y_{ce}}\left[\mathbf{I_d} + \mathbf{Z_e Y_{ee}}\right]^{-1}\mathbf{Z_e Y_{es}}\right)\mathbf{m_c}. \tag{2.21}$$

Figure 2.5 shows the Bode and Nyquist plots of the simulated open loop FRF derived with the ideal model and the model with the inertial effect of the piezoceramic patch. Comparing the faint and dashed lines in the Bode plot, it is noted that the mass of the actuator produces no effects up to about 5 kHz. Above this frequency it tends to reduce the amplitude of the FRF and also it enhances the higher frequencies phase lag. Thus, as shown by the Nyquist plots in Fig. 2.5, the inertia effect of the piezoceramic patch slightly squeeze the higher frequency locus of the FRF, which occupies the left hand side quadrants, towards the imaginary axis. In this way the maximum stable gain margin slightly increases. The size of the low frequencies circles in the right hand side quadrants are instead left unaltered so that the maximum reductions of vibration produced by the feedback loop at the low frequency resonances are slightly increased compared to those predicted with the ideal model. In conclusion, the inertial effect of the actuator piezoceramic patch brings a beneficial effect that improves the stability, and thus the low frequency control performance, of the feedback control loop.

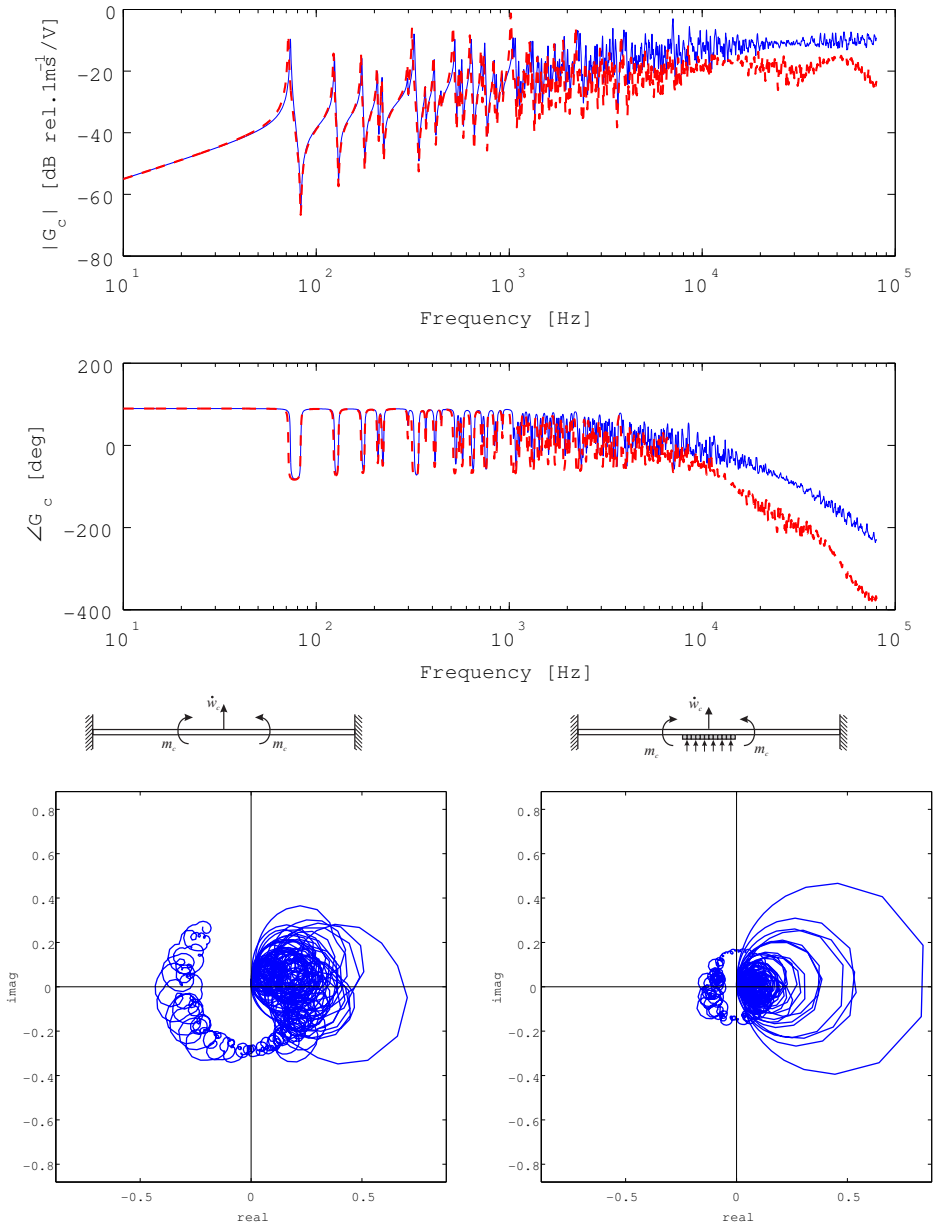

Figure 2.5: Top: Bode plot of the simulated open loop FRF derived with the ideal model with distributed bending moments (blue-faint line) and the model with the inertial effect (red-dashed line). Bottom: Nyquist plots of the open loop FRF derived with the ideal model with distributed bending moments (left) and the model with the inertial effect (right)

2.2.2 Modeling distributed stiffness

The elastic effect of the actuator flexural stiffness is modeled by subdividing the piezoceramic patch into n_s by n_s grid of thin strips over the surface. As shown in Fig. 2.6, these strips are aligned parallel to the edges of the patch. Only the axial stiffness of each strip has been modeled in terms of lumped axial springs. Thus the cross axial stiffness effects between parallel strips have been neglected. Also, the self and mutual shear stiffness effects between parallel springs have been neglected. Finally, the cross stiffness effects due to coupled axial and shear stiffness effects between pairs of strips oriented one orthogonal to the other have been neglected. Thus, the two proposed models for the inertial and stiffness effects are simplified models which however, as will be shown in the next subsections, are sufficient to replicate the main features of the measured open loop FRF both at low and higher frequencies.

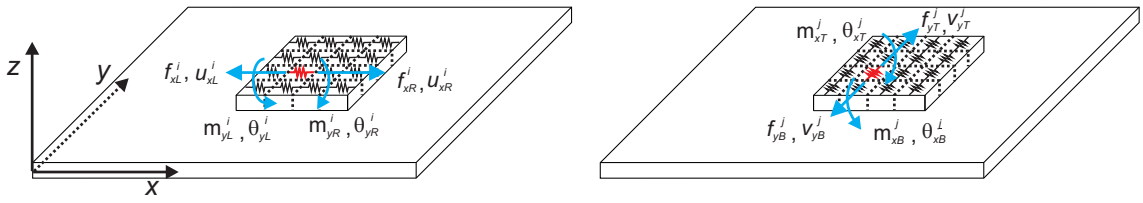

Figure 2.6: Schematic of the models for the elastic effect of the actuator stiffness

When the passive stiffness effect of the piezoceramic patch actuator is taken into account, the response can be given as the superposition of the responses due to the actuation moment excitations shown in Fig. 2.2 and the reactive moment produced by the axial stiffness of the dense grid of strips into which the actuator patch has been subdivided as shown in Fig. 2.6. Thus the complex transverse velocity at the sensor position $\dot{w}_c$ is expressed by the following mobility relation:

$$\dot{w}_c = \mathbf{Y_{cs}}(\mathbf{m_k} + \mathbf{m_c}V_c). \tag{2.22}$$

The passive moment column vector $\mathbf{m_k}$ is composed of four n_s^2-elements vectors, as shown by the schematics in Fig. 2.6, is given by:

$$\mathbf{m_k} = \begin{bmatrix} \mathbf{m_{yL}} & \mathbf{m_{yR}} & \mathbf{m_{xB}} & \mathbf{m_{xT}} \end{bmatrix}^T. \tag{2.23}$$

Each vector denotes the reactive moments generated at the ends of the elastic strips into which the piezoceramic patch actuator has been subdivided:

$$\mathbf{m_{yL}} = \left[\begin{array}{cccc} m_{yL}^1 & m_{yL}^2 & \cdots & m_{yL}^{n_s^2} \end{array} \right]^T \tag{2.24a}$$

$$\mathbf{m_{yR}} = \left[\begin{array}{cccc} m_{yR}^1 & m_{yR}^2 & \cdots & m_{yR}^{n_s^2} \end{array} \right]^T \tag{2.24b}$$

$$\mathbf{m_{xB}} = \left[\begin{array}{cccc} m_{xB}^1 & m_{xB}^2 & \cdots & m_{xB}^{n_s^2} \end{array} \right]^T \tag{2.24c}$$

$$\mathbf{m_{xT}} = \left[\begin{array}{cccc} m_{xT}^1 & m_{xT}^2 & \cdots & m_{xT}^{n_s^2} \end{array} \right]^T. \tag{2.24d}$$

These reactive moments are derived by integrating the products of the distance from the middle plane of the panel, z, and the z-distribution of the reactive axial forces per unit thickness at the end surfaces of the elastic strips over the thickness of the piezoceramic patch actuator. Thus, the reactive moment vector along four edges of the actuator are give by:

$$\mathbf{m_{yL}} = \int_{\frac{hs}{2}}^{\frac{hs}{2}+h_{pzt}} \mathbf{f_{xL}} z dz \tag{2.25a}$$

$$\mathbf{m_{yR}} = \int_{\frac{hs}{2}}^{\frac{hs}{2}+h_{pzt}} \mathbf{f_{xR}} z dz \tag{2.25b}$$

$$\mathbf{m_{xB}} = -\int_{\frac{hs}{2}}^{\frac{hs}{2}+h_{pzt}} \mathbf{f_{yB}} z dz \tag{2.25c}$$

$$\mathbf{m_{xT}} = -\int_{\frac{hs}{2}}^{\frac{hs}{2}+h_{pzt}} \mathbf{f_{yT}} z dz. \tag{2.25d}$$

According to Hooke's law, the tension produced by a pair of reactive forces at the opposite ends of an elastic strip is proportional to the elongation of the strip itself. Thus, the reactive force per length at four edges of the elastic strips are give by:

$$\mathbf{f_{xL}} = -E_{pzt}(\mathbf{u_{xL}} - \mathbf{u_{xR}}) \tag{2.26a}$$

$$\mathbf{f_{xR}} = E_{pzt}(\mathbf{u_{xL}} - \mathbf{u_{xR}}) \tag{2.26b}$$

$$\mathbf{f_{yB}} = -E_{pzt}(\mathbf{u_{yB}} - \mathbf{u_{yT}}) \tag{2.26c}$$

$$\mathbf{f_{yT}} = E_{pzt}(\mathbf{u_{yB}} - \mathbf{u_{yT}}). \tag{2.26d}$$

The above four formulas can be rewritten by using matrix form as:

$$\mathbf{f_k} = \begin{bmatrix} \mathbf{f_{xL}} & \mathbf{f_{xR}} & \mathbf{f_{yB}} & \mathbf{f_{yT}} \end{bmatrix}^T = E_{pzt}\mathbf{D_e}\mathbf{u_k}, \tag{2.27}$$

where $\mathbf{D_e}$ is a $4n_s^2$ by $4n_s^2$ matrix composed of n_s^2 by n_s^2 identity matrix, $\mathbf{I_d}$, and n_s^2 by n_s^2 matrix with zeros, $\mathbf{0}$, as written below:

$$\mathbf{D_e} = \begin{bmatrix} \mathbf{I_d} & -\mathbf{I_d} & \mathbf{0} & \mathbf{0} \\ -\mathbf{I_d} & \mathbf{I_d} & \mathbf{0} & \mathbf{0} \\ \mathbf{0} & \mathbf{0} & \mathbf{I_d} & -\mathbf{I_d} \\ \mathbf{0} & \mathbf{0} & -\mathbf{I_d} & \mathbf{I_d} \end{bmatrix}. \tag{2.28}$$

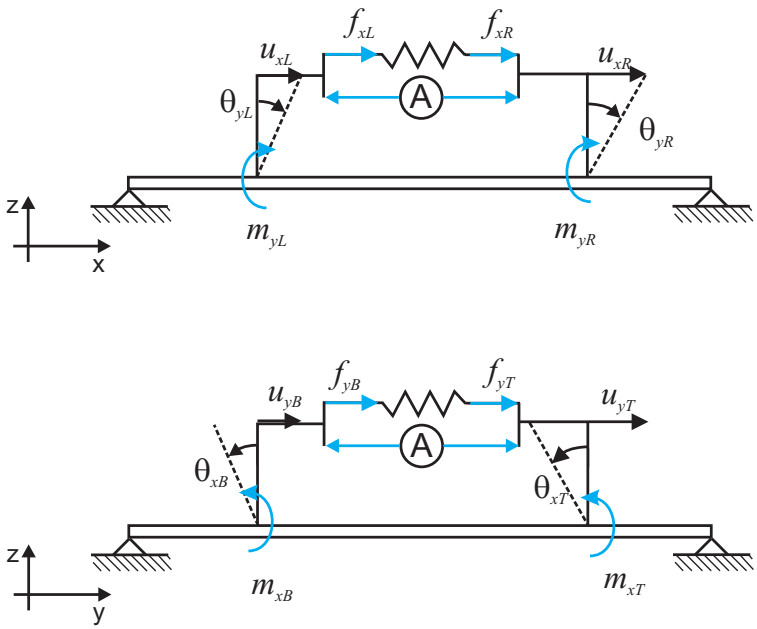

Figure 2.7: Coordinate system for reactive moments

The column vector $\mathbf{u_k}$ is composed by four n_s^2-elements vectors with the z-distribution of the axial displacements at the end surfaces of the strips:

$$\mathbf{u_k} = \begin{bmatrix} \mathbf{u_{xL}} & \mathbf{u_{xR}} & \mathbf{u_{yB}} & \mathbf{u_{yT}} \end{bmatrix}^T. \tag{2.29}$$

As shown in Fig. 2.7, the z-distribution of the axial displacements at the end surfaces of the strips $\mathbf{u_k}$ can be expressed in terms of the distance z from the middle plane of the panel and the rotation angles θ of the end surfaces of the strips with reference

to either x- and y-axis. Assuming that the rotation angles are small, reactive force vectors can be expressed by the following formula:

$$\mathbf{u_{xL}} = z\theta_{yL} \tag{2.30a}$$

$$\mathbf{u_{xR}} = z\theta_{yR} \tag{2.30b}$$

$$\mathbf{u_{yB}} = -z\theta_{xB} \tag{2.30c}$$

$$\mathbf{u_{yT}} = -z\theta_{xT}. \tag{2.30d}$$

The above equation can be rewritten using matrix form as:

$$\mathbf{u_k} = z\mathbf{D_t}\theta_\mathbf{k}, \tag{2.31}$$

where $\mathbf{D_t}$ is a matrix composed of n_s^2 by n_s^2 identity matrix, $\mathbf{I_d}$, and n_s^2 by n_s^2 matrix with zeros, $\mathbf{0}$, as written below:

$$\mathbf{D_t} = \begin{bmatrix} \mathbf{I_d} & \mathbf{0} & \mathbf{0} & \mathbf{0} \\ \mathbf{0} & \mathbf{I_d} & \mathbf{0} & \mathbf{0} \\ \mathbf{0} & \mathbf{0} & -\mathbf{I_d} & \mathbf{0} \\ \mathbf{0} & \mathbf{0} & \mathbf{0} & -\mathbf{I_d} \end{bmatrix}. \tag{2.32}$$

$\theta_\mathbf{k}$ is composed by four n_s^2-elements vectors with the rotations of the end surfaces of the strips either in x- or y-directions:

$$\theta_\mathbf{k} = \begin{bmatrix} \theta_\mathbf{yL} & \theta_\mathbf{yR} & \theta_\mathbf{xB} & \theta_\mathbf{xT} \end{bmatrix}^T. \tag{2.33}$$

Assuming harmonic vibration, the angular displacement vector $\theta_\mathbf{k}$ is given in terms of the angular velocities at the end surfaces of the strips with reference to either x- and y-axis:

$$\theta_\mathbf{k} = \frac{\dot{\theta}_\mathbf{k}}{j\omega}. \tag{2.34}$$

After substituting Eqs. (2.27) and (2.31) into Eq. (2.25), the reactive moment vector $\mathbf{m_k}$ is derived in terms of the vector with the angular velocities of the end surfaces of the strips:

$$\mathbf{m_k} = -\mathbf{Z_k}\dot{\theta}_\mathbf{k}, \tag{2.35}$$

where the impedance matrix $\mathbf{Z_k}$ is given below:

$$\mathbf{Z_k} = \frac{c_k}{j\omega}\mathbf{D_e}. \tag{2.36}$$

c_k is the bending stiffness coefficient:

$$c_k = E_{pzt}h_{pzt}\left(\frac{h_{pzt}+h_s}{2}\right)^2. \tag{2.37}$$

The angular velocity vector $\dot{\theta}_k$ of the end surfaces of the strips can then be derived as the superposition of the responses of the panel generated by the active and reactive moments produced at the end surfaces of the strips into which the piezoceramic patch actuator has been subdivided:

$$\dot{\boldsymbol{\theta}}_\mathbf{k} = \mathbf{Y_{ks}}(\mathbf{m_k} + \mathbf{m_c}V_c), \tag{2.38}$$

where $\mathbf{Y_{ks}}$ denotes $4n_s^2$ by $4n_s^2$ matrix with the mobility functions between angular velocities $\dot{\theta}_k$ and the passive moment m_k along the edge of the stiffness strips. Expressions for these mobility functions are given in Appendix A. Substituting Eqs. (2.35) and (2.38) into Eq. (2.22), the velocity at the sensor $\dot{w}_c$ can be expressed as a function of control moment,

$$\dot{w}_c = \mathbf{Y_{cs}}\left[\mathbf{I_s} + \mathbf{Z_k}\mathbf{Y_{ks}}\right]^{-1}\mathbf{m_c}V_c, \tag{2.39}$$

where $\mathbf{I_s}$ denotes a $4n_s^2$ by $4n_s^2$ identity matrix. Using the equation above and Eq. (2.5), the open loop FRF of the model with distributed stiffness derived as:

$$G_c = \mathbf{Y_{cs}}\left[\mathbf{I_s} + \mathbf{Z_k}\mathbf{Y_{ks}}\right]^{-1}\mathbf{m_c}. \tag{2.40}$$

Figure 2.8 shows the Bode and Nyquist plots of the simulated open loop FRF derived with the ideal model and the model with the stiffness effect of the piezoceramic patch. Comparing the faint and dashed lines in the Bode plot, it is noted that, the passive stiffness effect produced by the piezoceramic patch effectively reduces the amplitude of the FRF at low frequency without affecting the phase. However the stiffness effect falls at a rate of $1/\omega$; thus the difference in amplitudes between the two FRFs

becomes smaller as frequency rises. The passive stiffness effect of the piezoceramic patch also produces an amplitude modulation effect which is characterized by two wide frequency band peaks at about 20 kHz and 80 kHz. Around these frequencies the flexural wave length of the panel is close to the width or half width of the square piezoceramic patch. In this case the flexural vibration of the panel along the borders of the piezoceramic patch is such that the patch does not undergo large axial deformations in both x- and y-directions so that the stiffening effect is largely reduced and thus the amplitude of the FRF tends to raise up to maxima that coincides with the amplitude derived with the ideal model. This phenomenon also tends to reduce the higher frequencies constant phase lag effect noted on the FRF derived with the ideal model. As a result, the FRF remains confined between ± 90 degree up to about 20 kHz.

These amplitude and phase effects have a clear impact on the Nyquist plot of the FRF. In fact, comparing the two Nyquist plots in Fig. 2.8, it is noted that when the stiffness effect of the piezoceramic patch is taken into account, the size of the locus on the right hand side quadrants is halved while its size on the left hand side quadrants remains the same. Therefore the gain margin of the feedback loop remains the same. However, the reduced size of the low frequency resonant circles of the locus in the right hand side quadrants indicates a reduction of the control performance at low frequencies resonances. In summary despite the stiffness effect of the actuator piezoceramic leaves unaltered the maximum control gain, the low frequency control performance of the feedback control loop are lessen.

2.2.3 Fully coupled model and experimental verification

In this section the measured open loop FRF is compared with the simulated open loop FRF derived with the fully coupled model, which takes into account both inertial and stiffness effects of the piezoceramic patch. The formulation of the fully coupled model is derived by combining the two models discussed above. Thus, according to Eqs. (2.13) and (2.22), the complex transverse velocity at the sensor

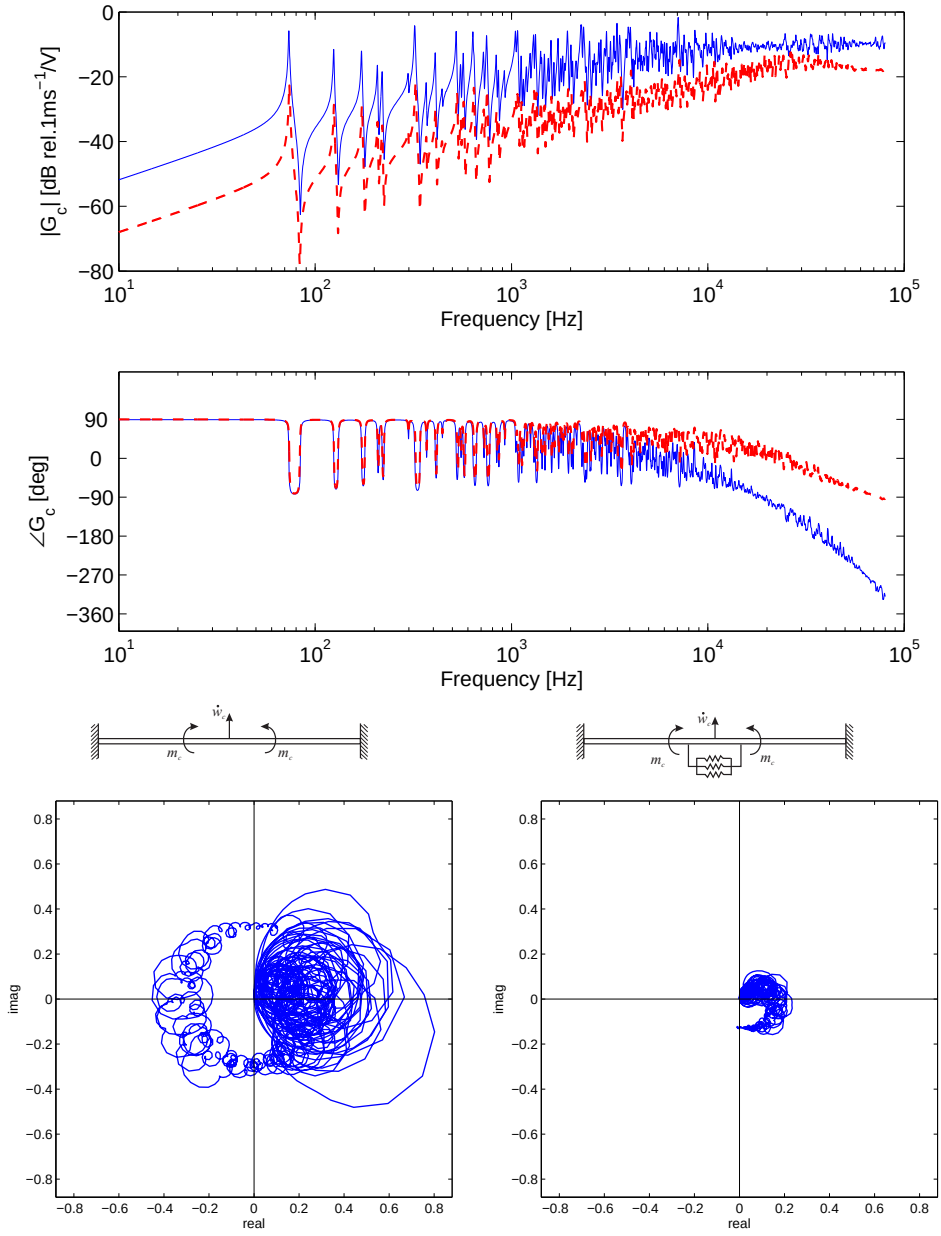

Figure 2.8: Top: Bode plot of the simulated open loop FRF derived with the ideal model (blue-faint line) and the model with the stiffness effects (red-dashed line). Bottom: Nyquist plots of the open loop FRF derived with the ideal model with distributed bending moments (left) and the model with the stiffness effects (right)

position $\dot{w}_c$ can be expressed by the following mobility relation:

$$\dot{w}_c = \left\lfloor \begin{array}{cc} \mathbf{Y_{ce}} & \mathbf{Y_{cs}} \end{array} \right\rfloor \left\{ \begin{array}{c} \mathbf{f_e} \\ \mathbf{m_k} + \mathbf{m_c} V_c \end{array} \right\}, \tag{2.41}$$

where $\mathbf{f_e}$ and $\mathbf{m_k}$ are derived using Eqs. (2.17) and (2.35), which can be cast together in the following matrix expression:

$$\left\{ \begin{array}{c} \mathbf{f_e} \\ \mathbf{m_k} \end{array} \right\} = - \left[\begin{array}{cc} \mathbf{Z_e} & \mathbf{0} \\ \mathbf{0} & \mathbf{Z_k} \end{array} \right] \left\{ \begin{array}{c} \dot{\mathbf{w}}_\mathbf{e} \\ \dot{\theta}_\mathbf{k} \end{array} \right\}. \tag{2.42}$$

According to Eqs. (2.19) and (2.38), the elemental velocity vector $\dot{\mathbf{w}}_\mathbf{e}$ and the angular velocity vector $\dot{\theta}_k$ can be derived from the following mobility expression:

$$\left\{ \begin{array}{c} \dot{\mathbf{w}}_\mathbf{e} \\ \dot{\theta}_\mathbf{k} \end{array} \right\} = \left[\begin{array}{cc} \mathbf{Y_{ee}} & \mathbf{Y_{es}} \\ \mathbf{Y_{ke}} & \mathbf{Y_{ks}} \end{array} \right] \left\{ \begin{array}{c} \mathbf{f_e} \\ \mathbf{m_k} + \mathbf{m_c} V_c \end{array} \right\}, \tag{2.43}$$

where $\mathbf{Y_{ke}}$ denotes a $4n_s^2$ by n_s^2 matrix with the mobility functions between angular velocities along the edges of the actuator $\dot{\theta}_k$ and the forces applied on the centers of lumped mass elements f_e. Expressions for these mobility functions are given in Appendix A. Thus, after substitution of Eq. (2.43) into Eq. (2.42), and then of the resulting equation into Eq. (2.41), after some algebraic manipulations, the following expression is found for the velocity at the control position:

$$\dot{w}_c = \left\lfloor \begin{array}{cc} \mathbf{Y_{ce}} & \mathbf{Y_{cs}} \end{array} \right\rfloor \left[\begin{array}{cc} \mathbf{I_d} + \mathbf{Z_e Y_{ee}} & \mathbf{Z_e Y_{es}} \\ \mathbf{Z_k Y_{ke}} & \mathbf{I_s} + \mathbf{Z_k Y_{ks}} \end{array} \right]^{-1} \left\{ \begin{array}{c} \mathbf{0} \\ \mathbf{m_c} \end{array} \right\} V_c. \tag{2.44}$$

Using the equation above and Eq. (2.5), the open loop FRF of the fully coupled model which includes both inertia and stiffness effects of the piezoceramic patch actuator is derived as:

$$G_c = \left\lfloor \begin{array}{cc} \mathbf{Y_{ce}} & \mathbf{Y_{cs}} \end{array} \right\rfloor \left[\begin{array}{cc} \mathbf{I_d} + \mathbf{Z_e Y_{ee}} & \mathbf{Z_e Y_{es}} \\ \mathbf{Z_k Y_{ke}} & \mathbf{I_s} + \mathbf{Z_k Y_{ks}} \end{array} \right]^{-1} \left\{ \begin{array}{c} \mathbf{0} \\ \mathbf{m_c} \end{array} \right\}. \tag{2.45}$$

Figure 2.9 compares the Bode plots of the open loop FRFs simulated with the fully

coupled model and measured on the test rig shown in Fig. 2.1. Comparing the dashed and thick lines in the Bode plot, it can be noted that the predicted FRF agrees very well with the measured one up to about 6 kHz. At higher frequency, the simulated and measured FRFs show similar spectra, which are characterized by the two wide band peaks due to stiffening effects of the piezoceramic patch, although the predicted peaks are slightly shifted down in frequency, and the amplitude of simulated open loop FRF is lower than that of the measured FRF. Nevertheless, the model proposed in this paper has captured adequately well the principal features that characterize the open loop FRF of the velocity sensor and piezoceramic patch actuator control unit under study. Moreover it has provided a rational interpretation of the physical effects produced by the mechanical and geometrical properties of the piezoceramic patch actuator.

The higher frequencies mismatch between the predicted and measured FRFs could be ascribed to two principal physical effects that have been neglected in the model of the composite plate and piezoceramic patch thick region of the panel: (a) the inertial effects produced by the bending rotations and (b) the effective stiffness that should include both bending and shearing effects. In particular it would be important to properly model the elastic response of the strip without neglecting the cross effects via axial and shear vibration between all strips, including those oriented one orthogonal to the other. Also at very high frequency, it could be important to model the in-plane fully coupled response of the panel and piezoceramic patch actuator. Finally, it is thought that the thin layer of bonding material used to fix the piezoceramic patch should also introduce some viscoelastic effects. Nevertheless, comparing the Bode plots in Fig. 2.9 it is clear that the agreement between the simulation and measured FRFs is significantly improved by using the fully coupled model introduced in this paper. This result confirms the validity of the proposed model for the mass and stiffness loading effects of the piezoceramic patch on the panel.

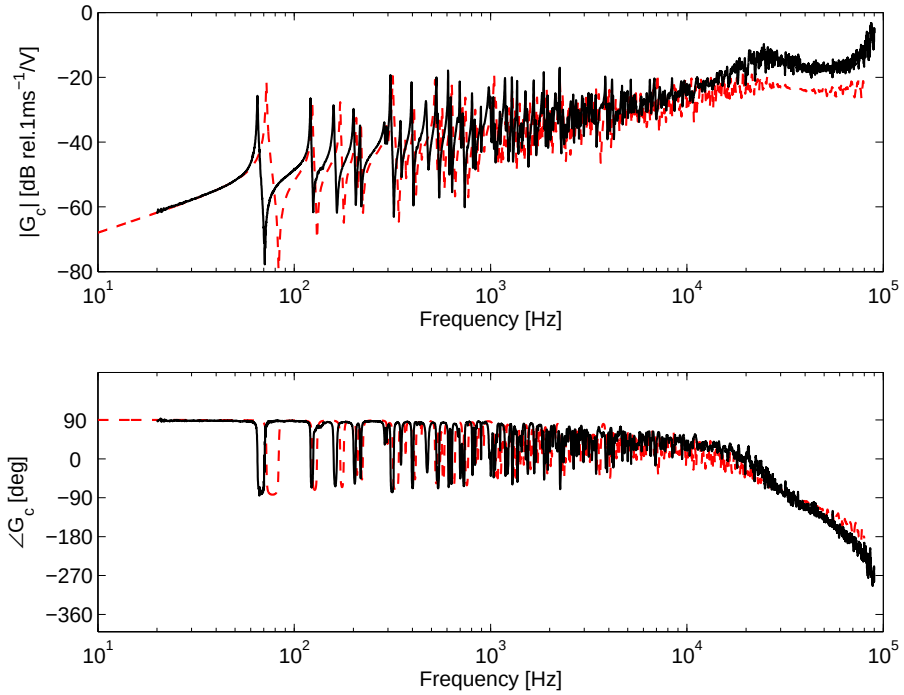

Figure 2.9: Bode plot of the simulated open loop FRF derived with the fully coupled model (red-dashed line) and measured open loop FRF (black-solid line).

2.3 Conclusions

This chapter has introduced a fully coupled mathematical model of a rectangular panel with a square piezoceramic patch actuator. Full details regarding the panel-actuator coupled models have been discussed, which consider passive inertial and elastic effects of the actuator patch.

The piezoceramic patch actuator inertial effect has been modeled by a grid of lumped masses, and the stiffness effect has been modeled by arrays of springs oriented in directions parallel to the lateral edges. With these models it has been possible to identify the principal physical effects produced by the actuator on the open loop FRF of the control system. It has been found that the inertia of the piezoceramic patch generates a constant amplitude roll off and phase lag of the open loop FRF at higher frequencies. Also, the bending stiffness of the piezoceramic patch locally increases the stiffness of the smart panel, and thus lowers the amplitude of the open loop FRF at low frequencies. At higher frequencies, this stiffness effect is modulated by a coincidence phenomenon between the bending wavelength and the width of the square actuators which causes wide frequency band peaks in the open loop FRF.

The FRF predicted by the fully coupled model has been compared with the measurements taken on a panel with the piezoceramic patch actuator. The measured response confirms quite well the validity of the fully coupled model which captures the most important passive effects generated by the patch on the panel.

Chapter 3

Parametric Study of Square Piezoceramic Actuator

This chapter presents a theoretical and experimental parametric study of the control performance of a single velocity feedback control loop with a piezoceramic patch actuator used to suppress the vibration of a thin plate. A stability-performance formula is derived to evaluate the vibration reduction of the plate with reference to the maximum control gain that guarantees stability.

The aim of this parametric study is to provide general guidelines for the design of a feasible actuator with good stability properties allowing high feedback gains in order to obtain good control performance and thus high active damping effects. The fully coupled analytical model derived in the previous chapter is used in this parametric study to investigate the effects of the physical dimensions of the actuator on the control performance. The parametric analysis is performed with reference to a) width, b) thickness, and c) both width and thickness of the square actuator. For the third parametric study, the dimensions are modified in such a way that the volume, and hence the mass of the square actuator, is kept constant.

3.1 Stability and control performance

It is important to quantify the control performance in order to provide a design guide line of the velocity feedback control using a piezoceramic actuator. As the

feedback is primarily effective around the resonance frequencies of the lower modes of the panel [5, 16], the control performance of the velocity feedback loop has been assessed in terms of vibration reduction at resonance frequencies.

Assuming harmonic vibration, the vibration reduction at the error sensor position for the k-th resonance frequency ω_k of the structure can be expressed as the ratio between the error sensor signal without control and the error sensor signal with feedback control, that is:

$$R_k = 20 \log_{10} \left| \frac{d(j\omega_k)}{y(j\omega_k)} \right|, \tag{3.1}$$

where $|d(j\omega_k)|$ and $|y(j\omega_k)|$ respectively represent the frequency dependent complex amplitudes of the time harmonic error sensor signal without control and with feedback control at the k-th resonance frequency ω_k.

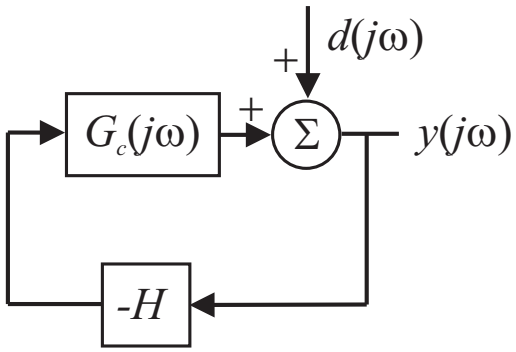

Figure 3.1: Disturbance rejection block diagram of a SISO control system

The block diagram for the velocity feedback loop shown in Fig. 3.1, from which the error sensor signal with control $y(j\omega)$ is given by:

$$y(j\omega) = \frac{d(j\omega)}{1 + G_c(j\omega)H}, \tag{3.2}$$

where H is the constant feedback control gain, and $G_c(j\omega)$ is the open loop FRF as discussed in chapter 2. Substituting Eq. (3.2) into Eq. (3.1), the maximum vibration reduction R_k in decibels is defined as:

$$R_k = 20 \log_{10} |1 + G_c(j\omega_k) H_{max}| \,. \tag{3.3}$$

As discussed in Chapter 2 with reference to the Bode plot, at low frequencies the

open loop FRF is characterized by well separated resonances. Thus, as shown in the top plot in Fig. 3.2, the k-th resonant circle of the locus of $G_c(j\omega)$ starts from the vicinity of the origin, and its center is aligned with the real positive axis so that the resonant point is also located on the real positive axis. Thus, the open loop FRF at the k-th resonance frequency can be approximated by the distance between the origin and the crossover point of the real axis by the locus of the open loop FRF $G_c(j\omega)$:

$$G_c(j\omega_k) = \mathrm{Re}\{G_c(j\omega_k)\}. \tag{3.4}$$

In Eq.(3.3), H_{max} is the maximum control gain that guarantees stability. According to the Nyquist stability criterion, the upper limit of feedback gain H is given by the reciprocal of the distance between the origin and the crossover point of the negative real axis by the locus of the open loop FRF $G_c(j\omega)$. The middle plots in Fig. 3.2 show that as frequency rises, the locus of the open loop FRF drifts away from the positive real axis towards the imaginary negative quadrants. Finally, as shown in the bottom plot, the locus of the open loop FRF crosses the real negative axis, so if the frequency of crossover is ω_0, thus:

$$H_{max} = \frac{1}{|G_c(j\omega_0)|} \tag{3.5a}$$

$$= -\frac{1}{\mathrm{Re}\{G_c(j\omega_0)\}}, \tag{3.5b}$$

This term H_{max} is often expressed in decibels and is equal to the gain margin for a system with unity gain, assuming this is stable.

Substituting Eq. (3.4) and Eq. (3.5) into Eq. (3.3), the maximum reduction index R_k can be approximated as:

$$R_k = 20\log_{10}|1+\delta_k|, \tag{3.6}$$

where δ_k denotes the control ratio at k-th resonant frequency defined as follows:

$$\delta_k = -\frac{\mathrm{Re}\{G_c(j\omega_k)\}}{\mathrm{Re}\{G_c(j\omega_0)\}}. \tag{3.7}$$

Equation (3.6) provides a simple estimate of the control performance of a velocity

feedback control loop at low frequency resonances, using the open loop FRF $G_c(j\omega)$. This formula indicates that the control performance is given as the ratio between the amplitude of $G_c(j\omega)$ at low frequency resonances, where the control action is desired and the amplitude at the frequency when instability would occur. The maximum reduction index R_k has been plotted in Fig. 3.4 for a range of control ratios δ_k between 0 and 5. This graph can be used to directly assess the control performance of a velocity feedback loop at low resonance frequencies. In fact, it is sufficient to estimate the ratio δ_k from the Nyquist plot of the open loop FRF $G_c(j\omega)$ and then convert it into dB reduction using the plot in Fig. 3.4.

For example, the control ratio at the 7th resonant frequency δ_7 is approximated as 1.2 using the Nyquist plot in Fig. 3.3. Therefore, according to Fig. 3.4, this single feedback control unit can generate up to around 7 dB structural attenuations at sensor position. Furthermore, this graph also indicates that, in order to obtain 10 dB vibration reduction at the control position, the size of the low frequency resonant circles in the right hand side quadrants of the Nyquist plot of $G_c(j\omega)$ should be about 2.5 times bigger than the cross over point on the real negative axis of the Nyquist plot of $G_c(j\omega_0)$.

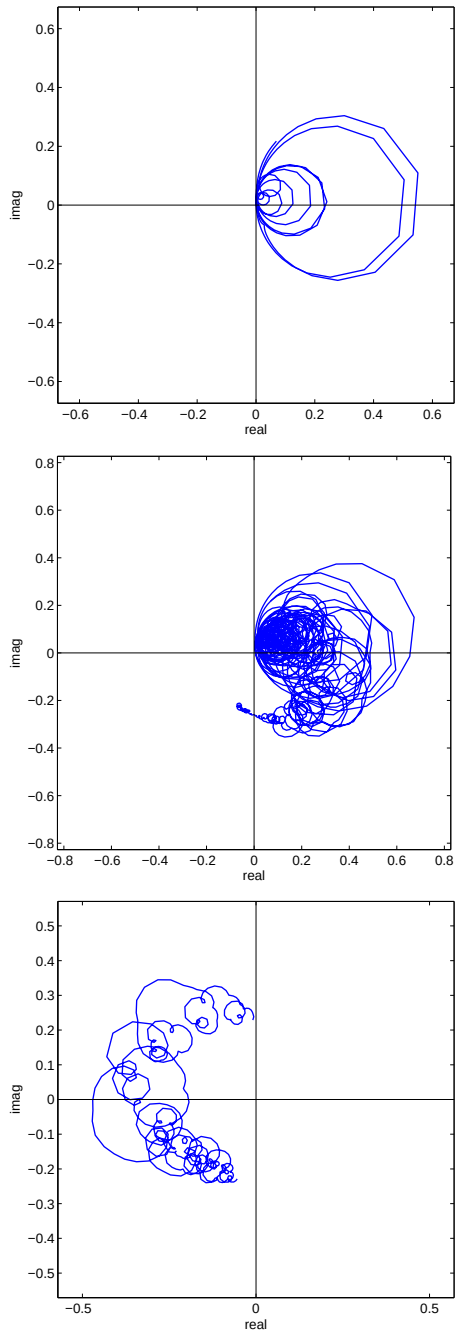

Figure 3.2: Nyquist plots of the simulated open loop FRF on the panel with the square actuator with dimensions of 25 mm × 25 mm × 1.05 mm between 20 and 500 Hz (top), between 500 Hz and 30 kHz (middle), and between 30 and 80 kHz (bottom)

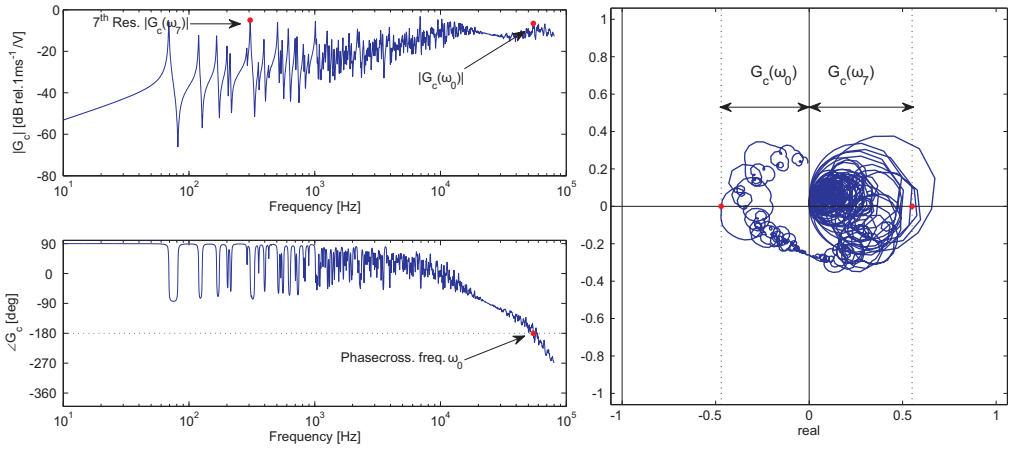

Figure 3.3: Bode (left) and Nyquist (right) plots of the simulated open loop FRF on the panel with the square actuator with dimensions of 25 mm $\times$ 25 mm $\times$ 1.05 mm.

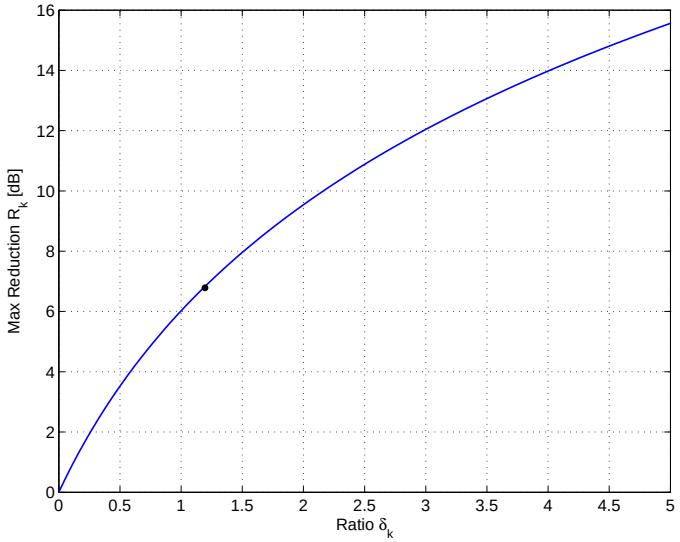

Figure 3.4: Maximum reduction index R_k as a function of the control ratio δ_k. The control ratio at the 7th resonant frequency δ_7 is shown as a solid circle

3.2 Parametric study

A theoretical and experimental parametric analysis has been performed that considers the control performance of the feedback loop with reference to a) width, b) thickness, and c) all dimensions of the square actuator. For the third parametric study, the dimensions are modified in such a way that the volume, and hence the mass of the actuator, is kept constant. As this study is a part of a wider investigation concerning decentralized multiple control system composed of 4 by 4 array of control units [19–21], the width of the square actuator has been limited to 1/6 of the smallest width of the panel. The part of simulation analysis has been validated with three sets of the measured FRFs taken on the panel with the piezoceramic patch actuators.

In order to substantiate the theoretical parametric study, seven identical panels were constructed, and the open loop FRF between the out-of-plane velocity and the input voltage to the piezoceramic actuator is measured. Since the aim of this chapter is to investigate how the dimensions of the piezoceramic patch influence the stability and control performance of the feedback loop, the velocity error signal has been measured remotely with a laser vibrometer pointed to the center of the piezoceramic patch actuator.

Each panel is equipped with a single square piezoceramic actuator, centered at (x, y) = (136.6 mm, 222.9 mm) with reference to the lower left-hand side corner of the panel. The piezoceramic patch has been bonded on the top side of the panel with its edges parallel to the clamping frame. The thickness of the adhesive bonding layer has been measured to be approximately 0.05 mm. All the square piezoceramic actuators used in this study are made of a niobium doped PZT material [63]. The physical properties and geometry of the panel and piezoceramic actuators are summarized in Table 2.1 and Table 2.2, respectively.

The parametric analysis begins with the Bode plot of three examples of the simulated and measured open loop FRFs in order to provide physical insight of the plate-actuator coupled system. The simulation were performed using the fully coupled model, described in Chapter 2, with both distributed mass and stiffness of the actuator accounted for. Then, the maximum achievable reduction using single the

velocity feedback unit R_k is estimated using the predicted open loop FRFs for the 1st, 3rd, and 7th resonances of the panel, which are observed at approximately 70 Hz, 165 Hz and 310 Hz respectively. As shown in Table 2.3, the response of the structure at these frequencies is primarily controlled by the (1,1), (1,2), and (4,1) natural modes of the panel. For further reference, a schematic of the mode shaped for a clamped plate is presented in Figure 3.5.

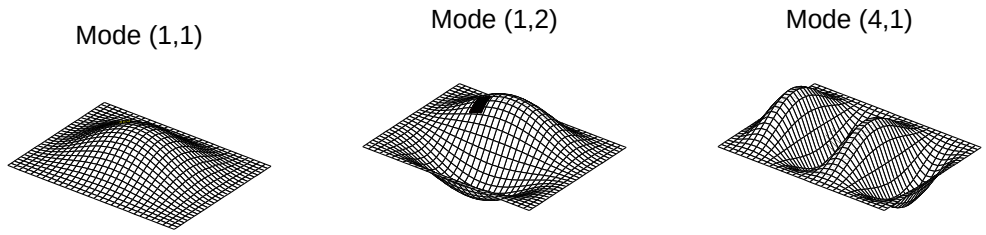

Figure 3.5: Schematics of mode shapes (m, n). The square piezoceramic actuator is shown by black color.

3.2.1 Width with constant thickness

This section investigates the effect of width of the square piezoceramic patch on the stability and control performance. In the simulation study, the width of the square actuator varies between 20 mm and 50 mm, while the thickness is fixed to 1 mm. The part of simulation analysis has been validated by three sets of the measured FRFs taken on the panel with the piezoceramic patch actuators listed in Table 3.1.

Table 3.1: Geometric parameter of the square piezoceramic actuator considered in the parametric study regarding the actuator width.

sample	$a_{pzt} \times a_{pzt} \times h_{pzt}$ [mm]	weight [g]
1	20.0 × 20.0 × 1.00	3.3
2	25.0 × 25.0 × 1.05	5.1
3	30.0 × 30.0 × 1.00	7.0

Figure 3.6 shows the Bode plots of the simulated (top plot) and measured (bottom plot) open loop FRFs $G_c(j\omega)$ between the out-of plane velocity of the panel and the input voltage to the piezoceramic actuators with constant thickness and various widths; i) 20 mm × 20 mm × 1 mm (blue faint line), ii) 25 mm × 25 mm × 1 mm (black solid line), and iii) 30 mm × 30 mm × 1 mm (red dotted line).

The two plots in Fig. 3.6 show that the simulated open loop FRFs agree very well with the measured ones up to around 7 kHz in terms of both amplitude and phase. At higher frequency, although the simulated and measured FRFs show similar spectra that are characterized by a wide amplitude modulation, the mean amplitude of the measured FRFs is in general higher than that of the simulated open loop FRFs, and the measured amplitude modulation is more pronounced. Nevertheless, Fig. 3.6 confirms that the analytical model captures very well the principal features of the response of the panel with the piezoceramic patch actuators in the simulated frequency range.

Both simulated and measured Bode plots show that, at low frequency, the amplitude of the open loop FRF $G_c(j\omega)$ increases with the width of the actuators. This is because the piezoceramic actuator generates bending moment along its edges, and thus better excites the plate, as the width of the actuator approaches the plate bending wavelength. According to classic thin plate theory, the flexural wavelength of a thin plate becomes equivalent to the width of the actuator, i.e. 20 mm, 25 mm, and 30 mm at respectively 23.6 kHz, 15.1 kHz, and 10.5 kHz. Figure 3.6 also highlights that the amplitude modulation is repeated at higher frequency, where the flexural wavelength is comparable to the half width of the square actuator. The phase plots in Fig. 3.6 indicates that, as the width of the actuator rises, the constant phase lag takes effect at lower frequency, and thus a bigger phase lag is generated. Therefore, as shown in the left hand side plot in Fig. 3.7, the phase crossover frequency ω_0 monotonically decreases as the width of the actuator rises.

The right hand plot in Fig. 3.7 shows the maximum stable gain H_{max} with reference to the width of the square actuator. The feedback gain curves has uneven shape, because the locus of the open loop FRF $G_c(j\omega)$ can vary significantly as the width of the actuator is changed. For instance, even little changes of width of the actuator patch produce a change of its local mass and stiffness effects, which a) significantly shift and change the amplitudes of the resonances of the lower order modes and b) significantly shift the modulation effect. As a result the crossover amplitude of the open loop FRF does not follow a smooth curve but can go through abrupt variations. Nevertheless, this plot clearly indicates that the maximum feedback gain H_{max} decreases as the width of the square actuator increases.

In summary, Fig. 3.8 shows that the maximum reduction index R_k, (k = 1, 3, 7) evaluated by using the predicted open loop FRFs for the width of the piezoceramic patch in the range between 20 mm and 50 mm tends to rise as the width increases. It is important to underline that, since the study is related to the implementation of multiple feedback loops over the surface of the panel, the parametric analysis has been limited to piezoceramic patches with width lower than 1/6 of the smallest width of the panel.

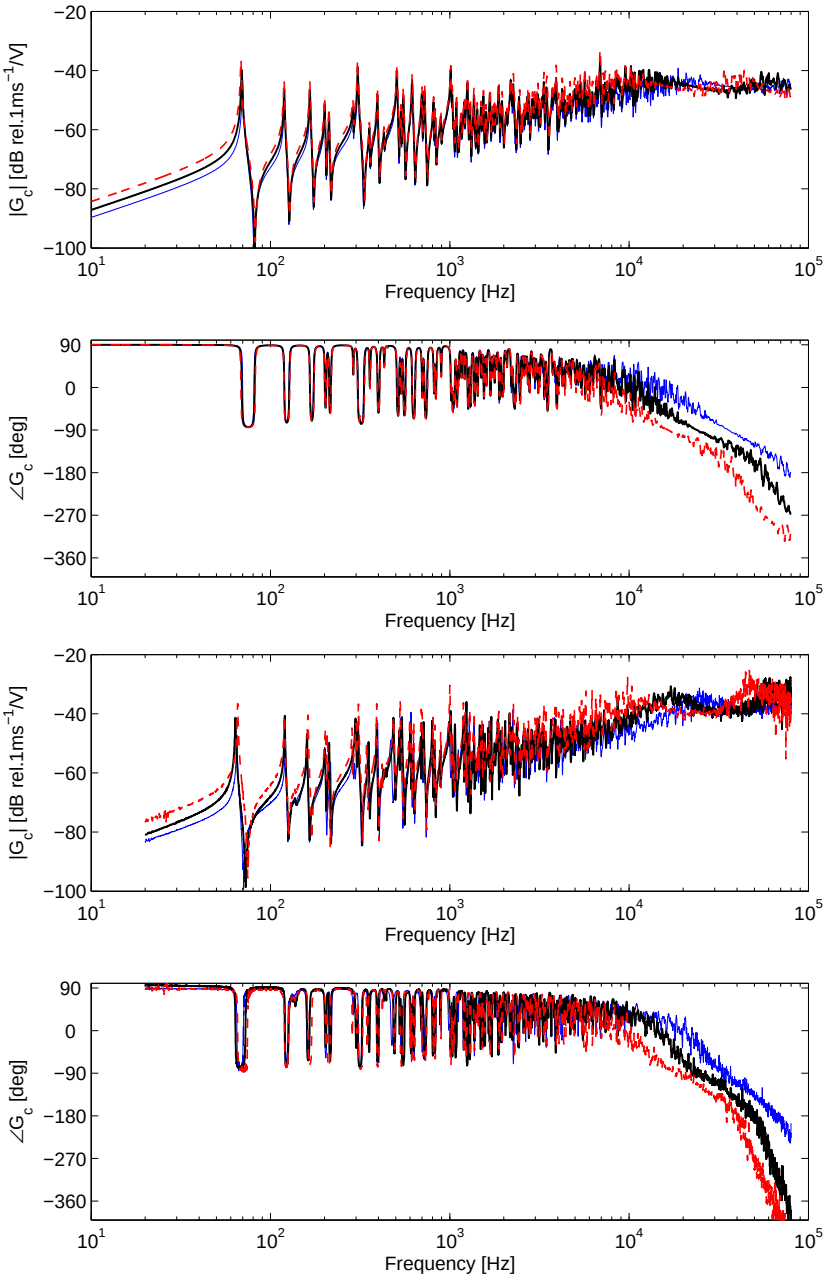

Figure 3.6: Bode plots of the simulated (top) and the measured (bottom) open loop FRFs on the panel with the square piezoceramic actuators with constant thickness 1 mm and various widthes; 20 mm (blue faint line), 25 mm (black solid line), and 30 mm (red dashed line).

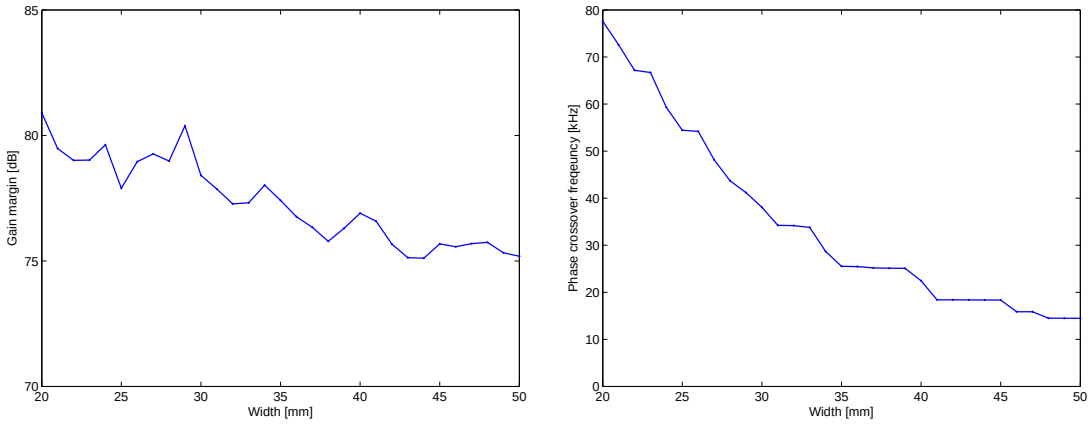

Figure 3.7: Maximum control gain H_{max} (left) and phase crossover frequency ω_0 (right) computed by using simulated open loop FRFs as a function of width for constant thickness.

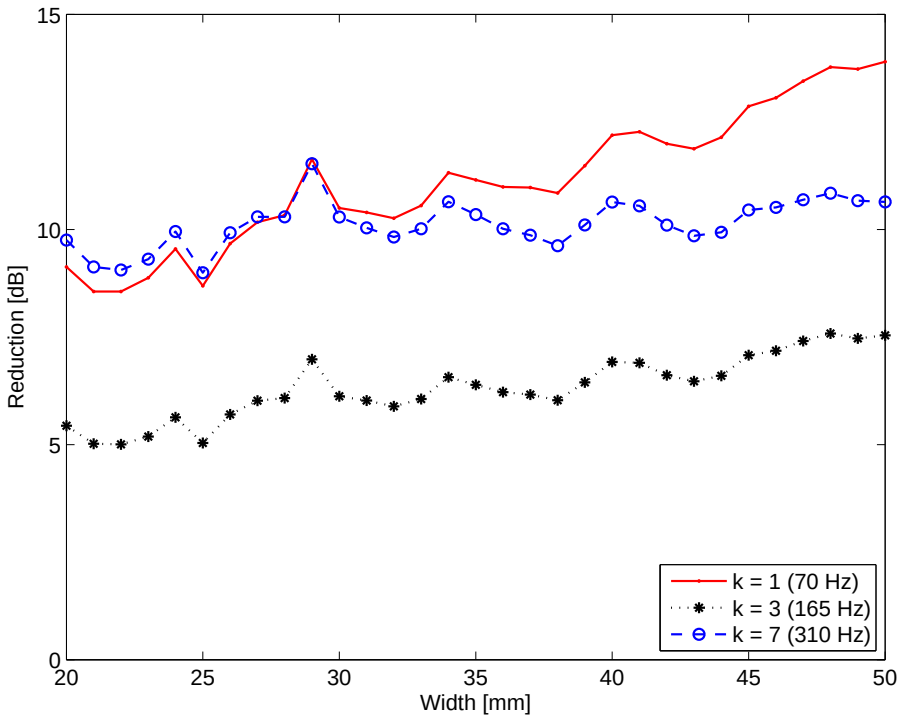

Figure 3.8: Maximum reduction index R_k (k = 1,3,7) computed by using simulated open loop FRFs as a function of width for constant thickness

3.2.2 Thickness with constant width

This section investigates the effect of thickness of the square piezoceramic patch on the stability and control performance. In the simulation study, the thickness of the actuator varies between 0.5 mm and 3.0 mm, while the width is fixed to 20 mm. The part of simulation analysis has been validated with three sets of the measured FRFs taken on the panel with the piezoceramic patch actuators listed in Table 3.2.

Table 3.2: Geometric parameter of the square piezoceramic actuator considered in the parametric study regarding the actuator thickness

sample	$a_{pzt} \times a_{pzt} \times h_{pzt}$ [mm]	weight [g]
1	20.0 × 20.0 × 1.00	3.3
2	20.0 × 20.0 × 1.63	5.1
3	20.0 × 20.0 × 3.00	9.4

Figure 3.9 shows the Bode plots of the simulated (top plot) and measured (bottom plot) open loop FRFs $G_c(j\omega)$ between the out-of-plane velocity of the panel at the error sensor position and the input voltage to the piezoceramic actuator with the same width and various thicknesses i) 20 mm × 20 mm × 1 mm (blue faint line), ii) 20 mm × 20 mm × 1.63 mm (black solid line), and iii) 20 mm × 20 mm × 3.0 mm (red dotted line).

In this case, as well, there is reasonably good agreement between the simulated and measured FRFs up to about 7 kHz. At higher frequencies the spectra are similar although the wide band peaks in the measured FRFs are much sharper than in the simulated open loop FRFs.

Both measured and simulated Bode plots indicate that the thinner the actuator, the larger the amplitude of the FRF at low frequency up to the first peak of the higher frequency modulation. As the thickness of the piezoceramic patch rises, both the bending actuation around the perimeter of the piezoceramic patch and the passive bending stiffness effect of the patch go up. These two phenomena have contrasting effects on the open loop FRF. The first phenomenon tends to increase the amplitude of the FRF while the second one tends to reduce the amplitude of the FRF, especially at low frequencies. Nevertheless the plots in Fig. 3.9 indicate that the increase in stiffening effects is more significant than the increase in actuation strength.

The Bode plots in Fig. 3.9 also indicates that, as the thickness of the actuator increases, the higher frequencies modulation peaks are shifted up in frequency, i.e. towards 24 kHz, 28 kHz, and 40 kHz with the 1.0 mm 1.63 mm, and 3.0 mm thick actuators respectively. The shift of the higher frequencies in modulation peaks is caused by the local stiffening effect produced by the increasing thickness of the patch, which locally stretches the bending wavelength of the panel. Therefore, the local bending wavelength of the panel with an increasingly thicker actuator becomes comparable with the width of the actuator at increasingly higher frequencies.

The phase plot in Fig. 3.9 highlights that, the phase lag effect takes place at higher frequency, as the thickness of the actuator goes up. As shown in the right hand side plot in Fig. 3.10, when the actuator is thicker than 2.5 mm, the phase remains below -180° up to 80 kHz. Therefore, the gain margin, and hence the maximum reduction index R_k, can not be estimated for the third case. For this reason the maximum reduction index R_k shown in Fig. 3.11 has been plotted with reference to piezoceramic patches with 30 mm width and thickness between 0.5 mm and 2.5 mm.

The amplitude plots in Fig. 3.9 highlights that, beyond the wide modulation frequency, the amplitudes of all FRFs become comparable. As the cross over frequency ω_0 is found beyond the wide peak, the maximum stable gain H_{max} remains the same as the width of the actuator rises, as shown in the right hand plot in Fig. 3.10.

In summary, reducing the thickness of the actuator brings a beneficial effect, since at low frequency the amplitude of the open loop FRF is bigger, while the maximum feedback gain remains the same with reference to the thickness. As a result, Fig. 3.11 indicates that the control performance goes down as the thickness of the actuator rises. The thinner the actuator is, the higher the maximum reduction at the control point for the 1st, 3rd, and 7th resonant frequencies is. As an example, the maximum reduction at the first resonant frequency R_1 can be approximately doubled by halving the thickness. This result confirms that the control performance can be significantly improved by modifying the thickness of the actuator. However, it must be noted that reducing the thickness of the piezoceramic actuator results in a lower limit for the maximum voltage that can be feed to the actuator without electrical discharge.

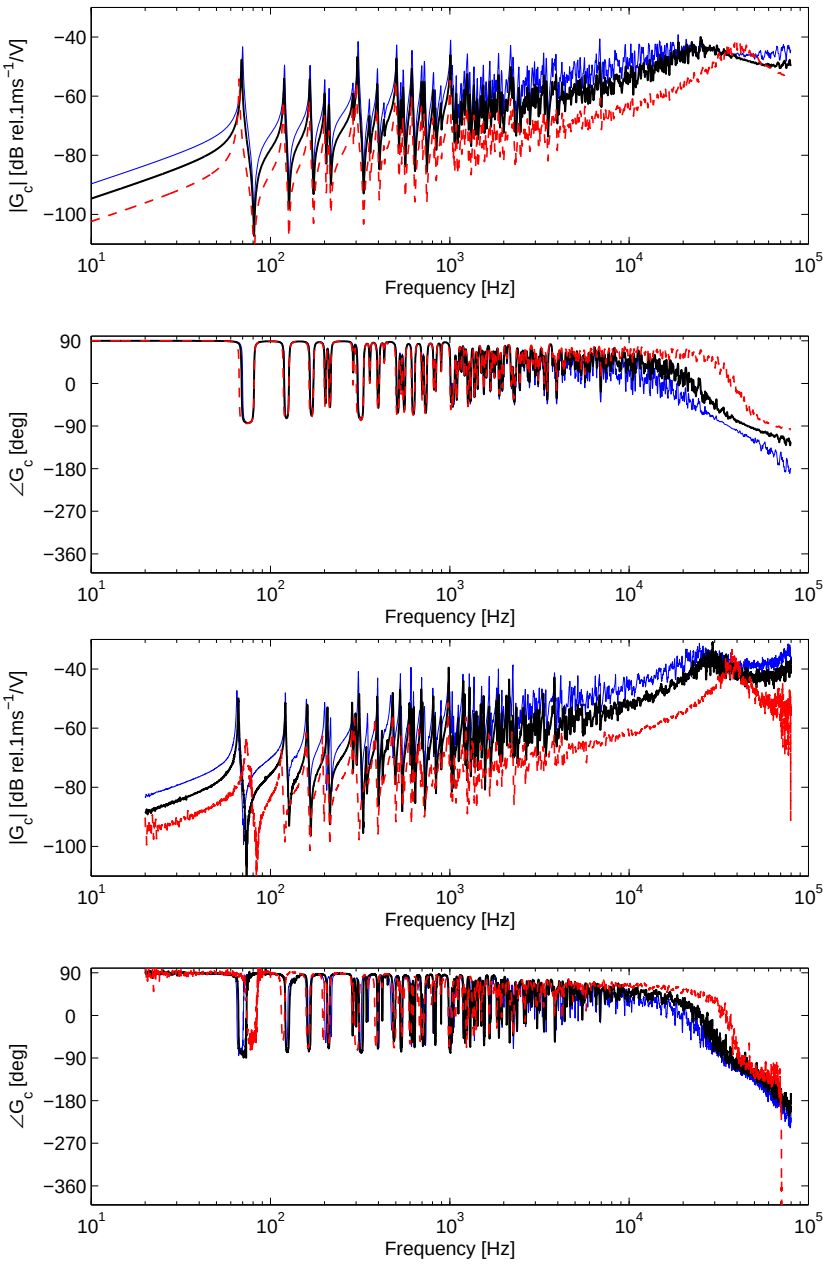

Figure 3.9: Bode plots of the simulated (top) and the measured (bottom) open loop FRFs on the panel with the square piezoceramic actuators with constant width 20 mm and various thicknesses; 1.0 mm (blue faint line), 1.63 mm (black solid line), and 3.0 mm (red dashed line).

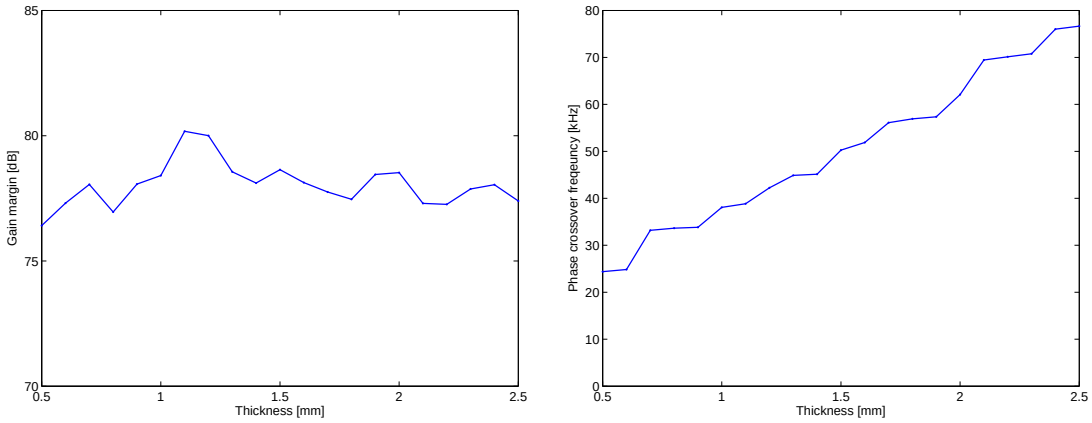

Figure 3.10: Maximum control gain H_{max} (left) and phase crossover frequency ω_0 (right) computed by using simulated open loop FRFs as a function of thickness for constant width

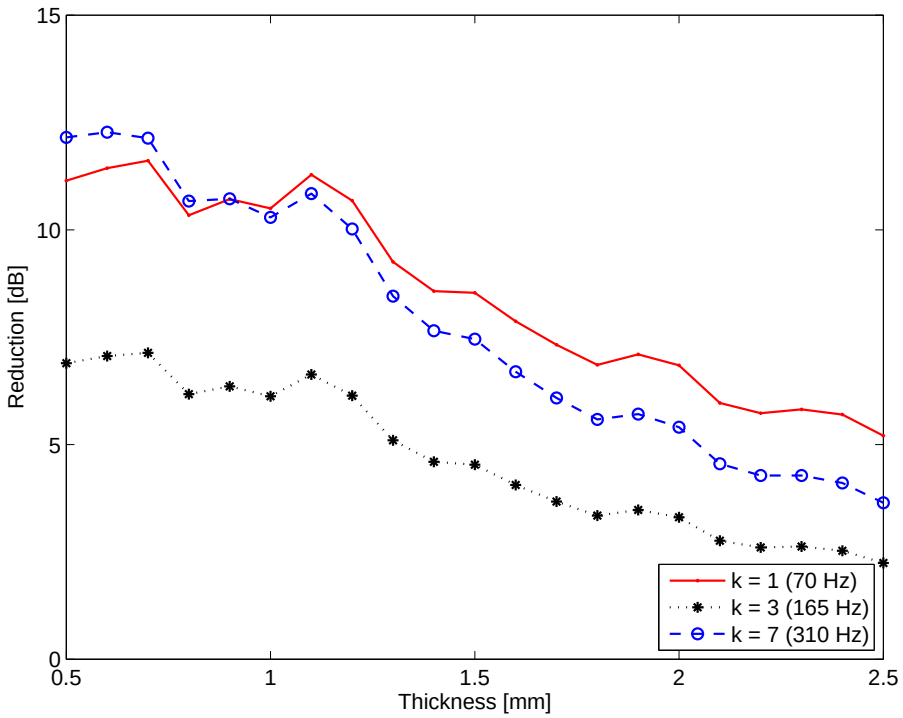

Figure 3.11: Maximum reduction index R_k ($k = 1,3,7$) computed by using simulated open loop FRFs as a function of thickness for constant width.

3.2.3 Width and thickness with constant volume

This section investigates the effect of the dimensions of the square piezoceramic patch on the stability and control performance. In the simulation study, the width of the square actuator varies between 25 mm and 50 mm, while the thickness is given between 2.9 mm to 0.26 mm in such a way as to keep the same volume. The part of simulation analysis has been validated with three sets of the measured FRFs taken on the panel with the piezoceramic patch actuators listed in Table 3.3.

Table 3.3: Geometric parameter of the square piezoceramic actuator considered in the parametric study regarding the actuator width and thickness

sample	$a_{pzt} \times a_{pzt} \times h_{pzt}$ [mm]	weight [g]
1	15.0 × 15.0 × 2.90	5.1
2	20.0 × 20.0 × 1.63	5.1
3	25.0 × 25.0 × 1.05	5.1

Figure 3.12 shows the Bode plots of three simulated (top plot) and measured (bottom plot) open loop FRFs $G_c(j\omega)$ between the out-of-plane velocity of the panel at the error sensor position and the input voltage to the piezoceramic actuators. In this case the square actuators have different dimensions, but the volume is kept constant to about 650 mm^3: i) 15 mm × 15 mm × 2.9 mm (blue faint line), ii) 20 mm × 20 mm × 1.63 mm (black solid line), and iii) 25 mm × 25 mm × 1.05 mm (red dotted line). Figure 3.13 shows the maximum control gain H_{max} and the phase crossover frequency ω_0 with reference to the width of the square actuator.

These figures confirm the indications obtained by the previous two parametric studies regarding width and thickness. Figure 3.12 highlights that the flexural actuation generated by the piezoceramic actuator rises up to the first higher frequencies modulation peak, as the width of the actuator increases and the thickness decreases. The Bode plots in Fig. 3.12 show that the first higher frequency amplitude modulation peak occurs at 68 kHz, 28 kHz, and 16 kHz with the 15 mm, 20 mm, and 25 mm square actuator. The bending wavelength at these frequencies is respectively predicted as 11.8 mm, 18.4 mm, and 24.3 mm. As discussed in Section 3.2.3, a thicker actuator adds stronger local stiffening effects, such that the local wavelength of the panel with thicker actuator becomes comparable with the actuator width at higher frequency. The left hand plot in Fig. 3.13 indicates that the maximum feed-

back gain H_{max} decreases as the width of the actuator increases, and the right hand plot highlights that the phase crossover frequency ω_0 monotonically decreases as the width of the actuator rises.

In summary, as indicated from the previous two parametric studies, a thinner and larger actuator results in better control performance. Figure 3.14 shows the maximum reduction index R_k ($k = 1,3,7$) obtained for a set of piezoceramic patches when the width are varied between 25 mm and 50 mm and the thickness is also varied in order to keep the volume equal to 656.25 mm^3. This plot confirms that a thinner and larger actuator produces a greater control performance around resonances of the lower order modes of the panel.

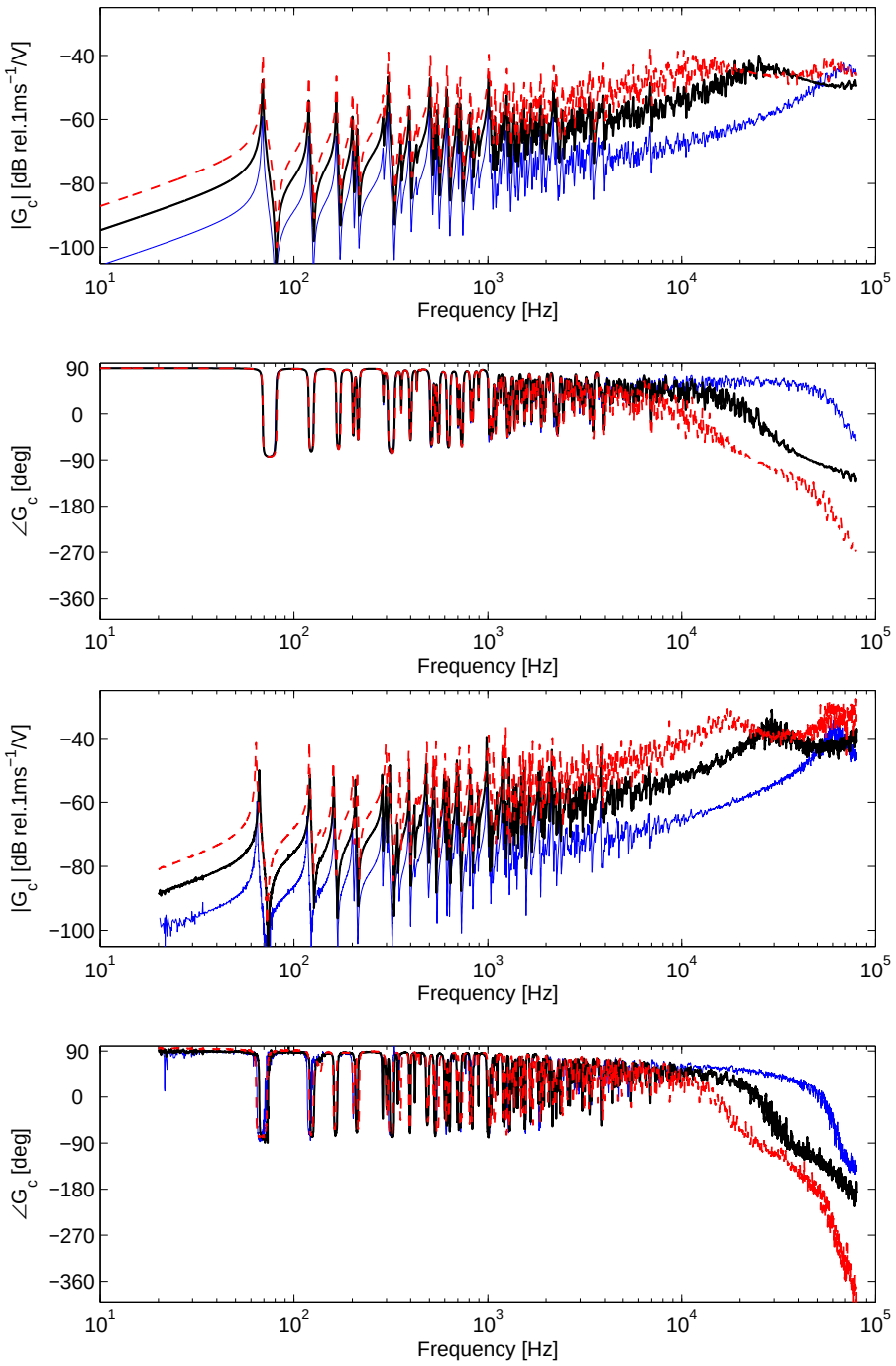

Figure 3.12: Bode plots of the simulated (top) and the measured (bottom) open loop FRFs on the panel with the square piezoceramic actuators with various widthes and thicknesses for constant volume; 15 mm × 15 mm × 2.9 mm (blue faint line), 20 mm × 20 mm × 1.63 mm (black solid line), and 25 mm × 25 mm × 1.05 mm (red dashed line)

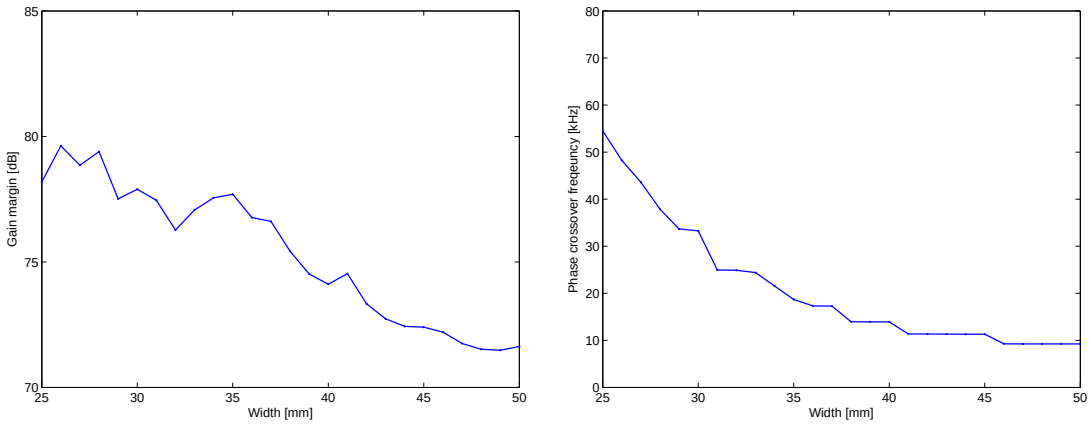

Figure 3.13: Maximum control gain H_{max} (left) and phase crossover frequency ω_0 (right) estimated by using predicted FRFs as a function of width and thickness for constant volume

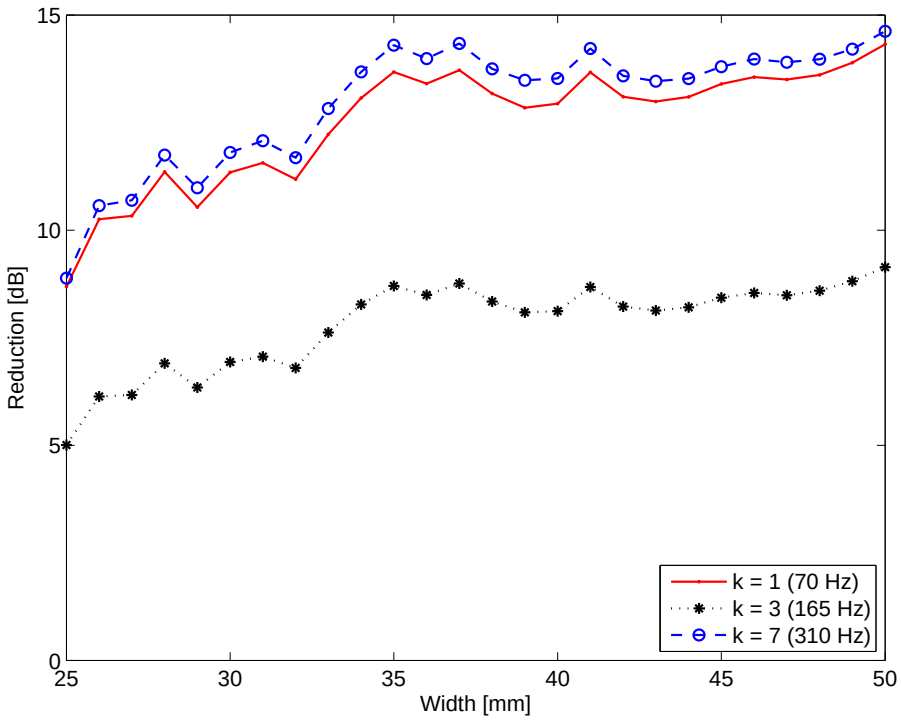

Figure 3.14: Maximum reduction index R_k (k = 1,3,7) (left), and maximum control gain H_{max} (right) estimated by using predicted FRFs as a function of width and thickness for constant volume

3.3 Conclusions

This chapter reports a parametric study on the control performance produced by a velocity feedback loop using a square piezoceramic actuator bonded on a rectangular panel. A simple formula has been derived using the open loop FRF in order to predict the maximum vibration reduction at well-separated resonances of the lower order modes of the panel. The parametric study has been conducted with reference to: a) width, b) thickness, and c) dimensions of the piezoceramic patch. In the third case, the dimensions have been varied in such a way as to keep the volume constant. The principal effects produced by the piezoceramic actuator on the open loop FRF can be summarized as follows: a) the mean amplitude rises as the width of the square actuator increases; b) the mean amplitude at low frequencies decreases as the actuator thickness increases and c) the phase lag increases as the width of the actuator increases. The relative influence of these effects produce contrasting effects, as shown in the parametric study presented in this chapter. As a conclusion, it has been found that increasing the width and reducing the thickness of the piezoceramic patch actuator improves the control performance over the control bandwidth in these simulation.

Chapter 4

Velocity Feedback Control using Triangular Piezoceramic Actuators

Chapters 2 and 3 have discussed the analytical formulation and the control performance of a single velocity feedback control loop using a square piezoceramic actuator and a velocity sensor bonded on a thin panel. In this chapter, a new configuration for the velocity feedback control unit is introduced, which consists of an isosceles triangular piezoceramic actuator with the velocity sensor at its tip. This new control unit is arranged with the triangular actuator along the edges of the panel in order to generates "boundary active damping", while a conventional control unit using a square patch actuator generates "surface active damping". This new arrangement acting along the boundary of the panel has a great potential advantage in that it is not invasive. Thus this configuration can be used in a wider class of application including windows for transportation vehicles, for example.

This chapter consists of four sections: In section 1, the stability and control performance of the new control unit is compared with that of the conventional control unit composed of a square strain actuator and a velocity sensor. Section 2 introduces a formula to estimate the actuation excitation terms produced by a triangular piezoceramic actuator on the panel. Section 3 presents mathematical models to predict the response of a thin plate equipped with a triangular piezoceramic actuator. The open loop FRF is analyzed in detail in terms of actuation components, and experimental results are presented to validate the proposed mobility model. A short

summary and conclusions are presented in section 4.

4.1 Triangular and square actuators; an experimental comparison

4.1.1 Experimental setup

Figure 4.1 shows the experimental rig used to test the new control unit. In order to maintain consistency with the study presented in Chapter 2 and 3, the same basic structure is considered, i.e. a thin rectangular aluminum panel clamped along its edges. The panel is equipped with a triangular piezoceramic patch actuator with a base length $b_{pzt} = 40$ mm, a height $t_{pzt} = 25$ mm, and a thickness $h_{pzt} = 0.75$ mm. The actuator is firmly bonded on the thin panel, with its base edge aligned along the perimeter of the panel. The base edge of the actuator is shifted 1 mm from the clamped border of the panel for electrical insulation purposes. The tip position of the triangular actuator is located at $(x_c, y_c) = (167.0 \text{ mm}, 26.0 \text{ mm})$ with reference to the lower left hand side corner of the panel. The triangular piezoceramic actuator has the same physical and piezoelectrical properties as the square piezoceramic actuator used in Chapter 2 and 3. The geometry and physical parameters of the triangular actuator are summarized in Table 4.1. More detailed piezoelectric properties of the piezoceramic patch is provided by the manufacturer, and are summarized in Appendix B.

Table 4.1: Geometric parameter and physical properties of the triangular piezoceramic actuator produced by ISTEC in Italy [63]

parameter	symbol	value
Base length [mm]	b_{pzt}	40.0
Height [mm]	t_{pzt}	25.0
Thickness [mm]	h_{pzt}	0.75
Tip angle [deg]	θ_{pzt}	77.3
Tip position [mm]	x_c, y_c	167.0, 26.0
Poisson's Ratio	ν_{pzt}	0.35
Density [kg/m^3]	ρ_{pzt}	7.82×10^3
Piezoelectric charge constant [m/V]	$d_{31} = d_{32}$	-183.5×10^{-3}

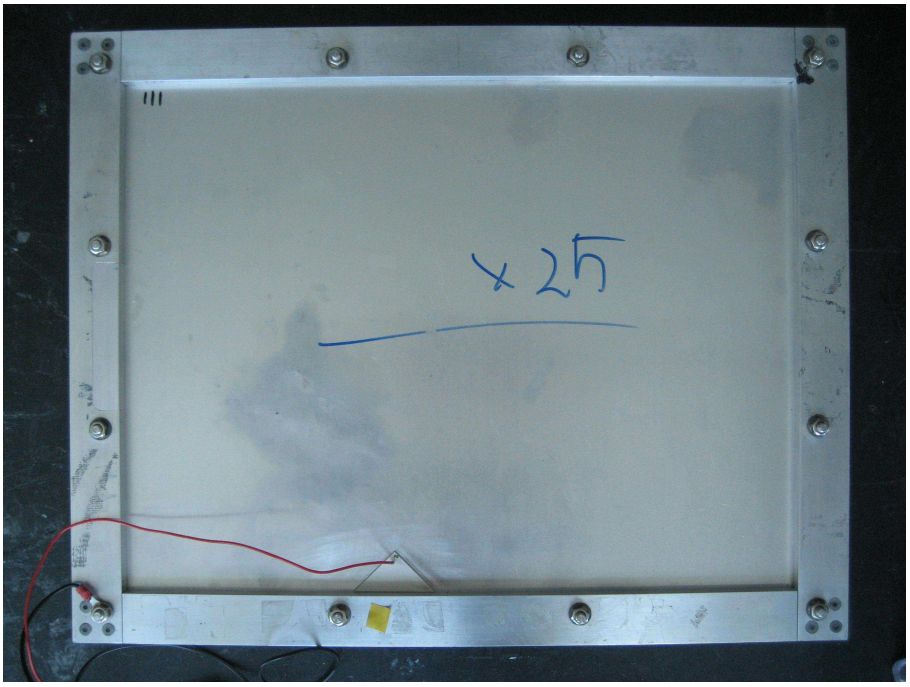

Figure 4.1: Clamped panel with a triangular piezoceramic patch actuator

4.1.2 Comparison

This section compares the control performance of the two velocity feedback control units using measured open loop FRF between the out-of-plane velocity of the panel and the driving voltage of the actuator; one control system is composed of a 20 mm $\times$ 20 mm $\times$ 1.0 mm square actuator with the velocity measured at its center located at $(x_c, y_c) = (136.6 \text{ mm}, 222.9 \text{ mm})$ with reference to the lower left hand side corner of the panel as shown in Fig. 2.1, and the other one is composed of a 40 mm $\times$ 25 mm $\times$ 0.75 mm triangular actuator with a velocity measured at its top tip, as shown in Fig. 4.1. The velocity of the panel is remotely measured by using a laser vibrometer.

The Bode and Nyquist plots for the measured open loop FRFs of the two control systems are shown in Fig. 4.2. The Bode plot indicates that, at low frequency up to around 500 Hz, the amplitude of the open loop FRF measured on the panel with a square actuator is slightly higher than that using a panel with a triangular actuator. The primary reason is the location of the error sensor in the two control systems: with the triangular actuator, the sensor is located close to the clamping edge of the panel. Thus, when the bending wavelength is longer than the distance between

the clamping edge and the velocity sensing position, the detected velocity signal is smaller, compared with the signal measured at the center of the square actuator, which is located in the middle of the panel. However, as frequency rises, and hence a quarter bending wavelength becomes comparable with the distance between the panel edge and the sensor, the amplitude of both FRFs become comparable.

At higher frequency, the amplitude of both FRFs is characterized by a wide frequency modulations. As discussed in Chapters 2 and 3, this frequency modulation is caused by the passive stiffness effects of the actuator. With the square actuator, the modulation effects are observed at frequencies where a multiple number of bending wavelength λ is equivalent to the distance between the edge of the actuator and the sensing position i.e. $\lambda = 10$ mm at 23.6 kHz for a 20 mm square actuator. When the triangular actuator is used, the first and second amplitude modulations are observed at frequency around 10 kHz and 45 kHz, respectively. These modulation effects are not as clearly marked as that of the square actuator. This is due to the fact that the lateral edges of the triangular actuator are not parallel, while the opposite edges of the square actuator are parallel. Thus, as shown in Fig. 4.3, the coincidence phenomenon between the "actuation distance" (i.e. the distance between the actuation points along the border of the actuator and the sensor position), and the bending wavelength (or multiples of the bending wavelength) varies over a wider range for triangular actuator than the parallel edges of the square actuator.

The phase plot of Fig. 4.2 indicates that the FRF measured on the panel with the square actuator is positive definite up to about 25 kHz, while the phase of the FRF with the triangular actuator is positive definite only up to about 2 kHz. In both cases, the phase constantly increases beyond these frequencies, and thus a bigger phase lag is generated with the triangular actuator at high frequency. This lower transition frequency for the triangular actuator was not predicted in the earlier theoretical study [43], and prompts a reexamination of the model used for the excitation generated by such a triangular device.

The Nyquist plots in Fig. 4.2 show that the locus of the FRF with triangular actuator enters the left hand quadrants in a clockwise rotation at around 2 kHz, and the locus crosses the real negative axis at around 3.1 kHz. As the phase lag increases with frequency, the locus of the open loop FRF goes back to the right hand

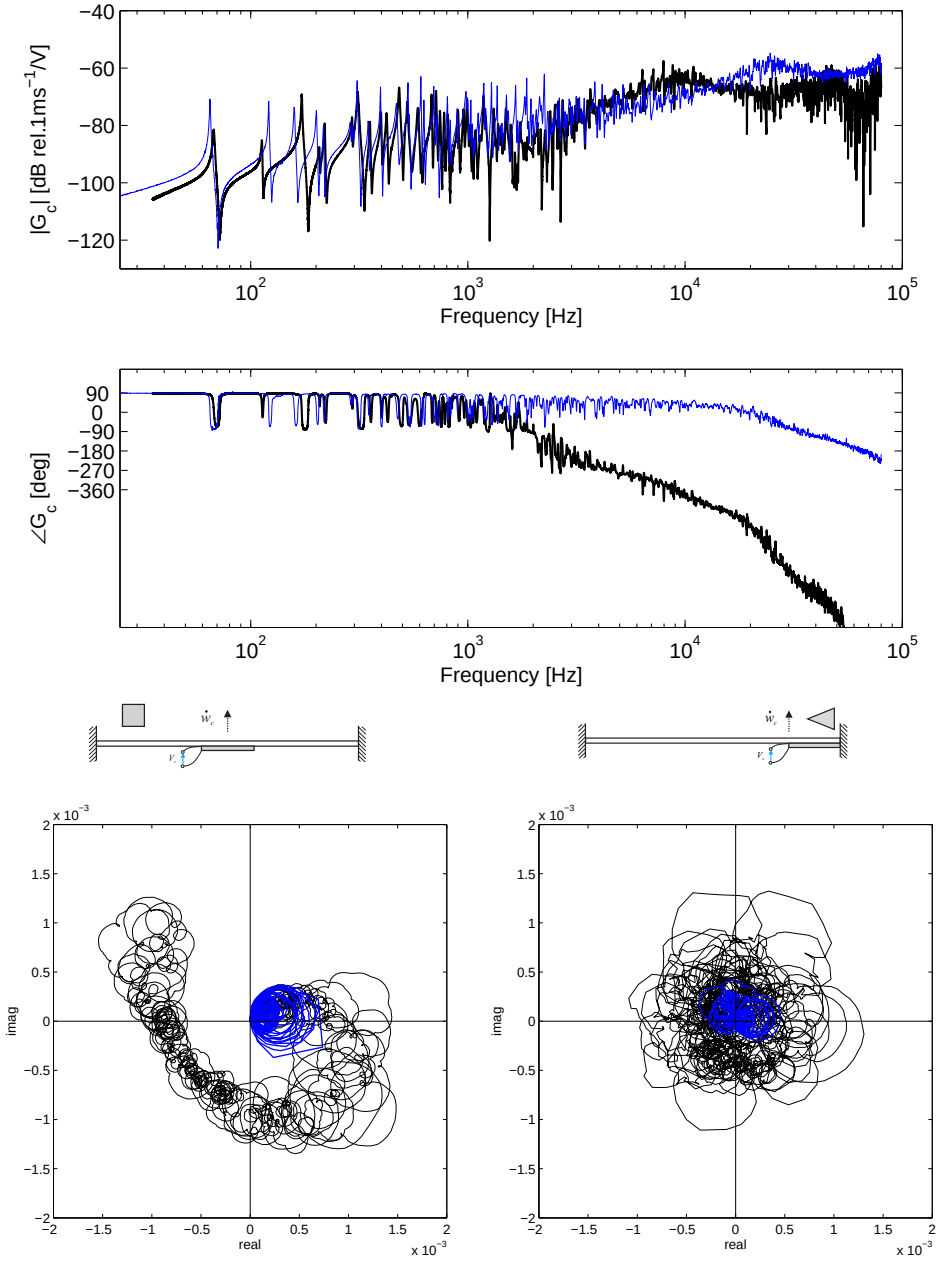

Figure 4.2: Top: Bode plot of the measured open loop FRF on the panel with the square actuator (blue-faint line) and with the triangular actuator (black-solid line). Bottom: Nyquist plots of the measured open loop FRF on the panel with the square actuator (left) and with the triangular actuator (right) between 25 Hz - 5 kHz (blue solid), 5 - 80 kHz (black faint).

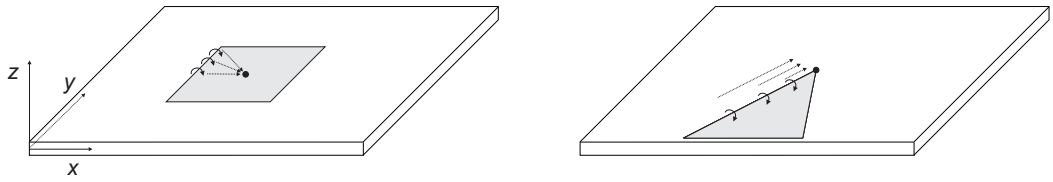

Figure 4.3: Actuation distances to the error sensor for the square and triangular actuators

side quadrants and eventually crosses the real negative axis again at around 20 kHz. Therefore, the control system formed by a triangular actuator with a velocity sensor at its tip vertex is only conditionally stable, as is to the control system with a square actuator, but with a lower transition frequency.

According to Chapter 3, when a conditionally stable control unit is used, the upper limit of the control performance at the k^{th} resonant frequency can be simply estimated with the following formula:

$$R_k = 20 \log_{10} |1 + \delta_k| \,, \tag{4.1}$$

where δ_k is given by the product of the amplitude of the FRF at the k^{th} resonant frequency and the maximum control gain, $\delta_k = |G(j\omega_k)|H_{max}$. The Bode plot indicates that the amplitude of open loop FRF with a square actuator $G(j\omega_k)$ is bigger than that with a triangular actuator at low frequency. The maximum control gain H_{max} is given by the reciprocal of the horizontal distance between the origin and the locus of $G(j\omega_0)$ at the frequency, where the locus crosses the real negative axis:

$$H_{max} = \frac{1}{|G_c(j\omega_0)|}. \tag{4.2}$$

Comparing the two Nyquist plots in Fig. 4.2, it can be seen that higher gain can be implemented with triangular actuator, because $|G_c(j\omega_0)|$, where ω_0 is the phase crossover frequency, is smaller than that with a square actuator. The combination of these two effects can be assessed by using the maximum reduction index R_k. Table 4.2 summarizes the R_k for the 1st, 3rd, and 7th resonances of the panel, which are observed at approximately 70 Hz, 165 Hz and 310 Hz respectively. This table highlights that the velocity feedback control system using triangular actuator has comparable control performance with that using the square actuator.

Table 4.2: Control performance of a single velocity feedback control loop

kth peak	Reduction [dB]	
	square	triangular
k=1 (70 Hz)	2.0	0.7
k=3 (165 Hz)	1.4	2.6
k=7 (310 Hz)	3.8	2.9

4.2 Actuation of the triangular piezoceramic actuator

4.2.1 Conventional modeling

Compared with the past studies on rectangular piezoceramic actuators, only a small number of papers considering control systems using spatially shaped strain actuators have been issued [43, 44, 57, 65–67]. The most important study regarding the modeling of triangular actuators has been carried out by Sullivan *et al.* [44, 66]. These authors have introduced a formula to estimate the excitation terms generated by a triangularly shaped strain actuator. Their studies indicate that a triangular actuator generates bending moments along its three edges plus transverse point forces at its three vertexes, as shown in Fig. 4.4.

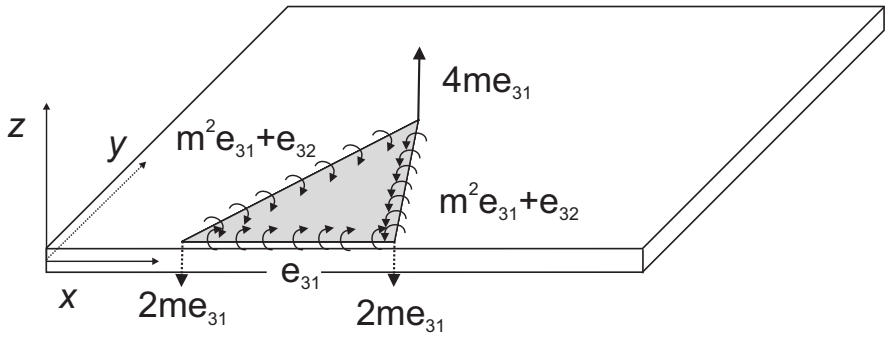

Figure 4.4: Schematic of the actuation model for the moment and force of the triangular actuator in Ref. [66]

In their paper, the strength of excitation terms generated by the piezoceramic patch

are given as:

$$f_t = -2me_{31} \tag{4.3a}$$

$$f_l = -2me_{31} \tag{4.3b}$$

$$f_r = 4me_{31} \tag{4.3c}$$

$$m_b = e_{31} \tag{4.3d}$$

$$m_l = m^2 e_{31} + e_{32} \tag{4.3e}$$

$$m_r = m^2 e_{31} + e_{32}, \tag{4.3f}$$

where f_t, f_l, and f_r respectively denote the generated point forces at the top, base left, and base right vertexes of the triangular actuator per unit voltage, and per unit thickness of the structure. m_b, m_l, and m_r are respectively bending moments along the base, and left and right lateral edges of triangular actuator per unit voltage and per unit thickness of the structure. m represents the aspect ratio of the triangular shape, $m = t_{pzt}/2/b_{pzt}$. The piezoelectric stress-charge constants, e_{31} and e_{32}, are derived from the piezoelectric strain-charge constants d_{31}, d_{32}, and d_{36}, assuming thin plate theory as reference [58]:

$$\begin{Bmatrix} e_{31} \\ e_{32} \\ e_{36} \end{Bmatrix} = \begin{bmatrix} \frac{E_{pzt}}{1-\nu_{pzt}^2} & \frac{\nu_{pzt}E_{pzt}}{1-\nu_{pzt}^2} & 0 \\ \frac{\nu_{pzt}E_{pzt}}{1-\nu_{pzt}^2} & \frac{E_{pzt}}{1-\nu_{pzt}^2} & 0 \\ 0 & 0 & \frac{E_{pzt}}{2(1+\nu_{pzt})} \end{bmatrix} \begin{Bmatrix} d_{31} \\ d_{32} \\ d_{36} \end{Bmatrix}, \tag{4.4}$$

where E_{pzt} and ν_{pzt} respectively denote the Young's modulus of elasticity and the Poisson's ratio of the piezoceramic actuator. The strain actuator used in this study is made out of a homogenous PZT - lead titanate zirconate - ceramic [63], which is a symmetric type of polarized polycrystalline ceramic material. This material is associated with the crystallographic class $6mm$ of the hexagonal crystal system. According to IEEE standard [70], this material shows $d_{31} = d_{32}$, and $d_{36} = 0$. Therefore, the piezoelectric stress-charge constant e_{31} is equal to e_{32}, and e_{36} is zero. Thus, according to Eq.(4.3), the force exerted at the top vertex has an opposite direction and is twice as big as the forces exerted at the base vertexes, and the bending moments produced along the lateral edges are $(m^2 + 1)$ times bigger than the bending moment along the base edge.

When the actuator has an equilateral triangular shape, this formulation leads to a paradoxical conclusion. When an equilateral triangular actuator is used, the magnitude of the exerted forces at all three vertexes should be identical, and hence zero, due to its geometric symmetry. However, this conclusion is contradicted by Eq. (4.3), which indicates that the derivation of these formulas might include potential errors.

To try to understand this paradoxical conclusion, we consider the simpler model for the triangular actuator, which is a superposed combination of the unidirectional piezoelectric strips (of infinitesimal width) in x- and y-directions, as shown in Fig. 4.5-(a1) and (a2). Assuming unidirectional strips, the piezoelectric strips aligned along y-axis shows $d_{32} = 0$, while strips aligned along x-axis show $d_{31} = 0$. Thus, as given in Eq. (2.3), the magnitude of the bending moments generated by the unidirectional piezoelectric strips per unit voltage are given by the following expressions:

$$m_{cx} = \frac{b_s d_{31} E_{pzt}}{1-\nu_{pzt}} \left(\frac{h_{pzt}+h_s}{2} \right) \tag{4.5a}$$

$$m_{cy} = \frac{b_s d_{32} E_{pzt}}{1-\nu_{pzt}} \left(\frac{h_{pzt}+h_s}{2} \right), \tag{4.5b}$$

where b_s denotes the width of the piezoelectric strip, thus the moments are independent of the length of the strip. Considering that the bending moments in x-direction can be modeled as a pair of out-of-plane forces pointing up and down to the panel, the bending moment model shown in Fig. 4.5-(a1) and (a2) are equivalent to the pair forces model shown in (b1) and (b2). The closely located forces shown by the dashed circles in Fig. 4.5-(b1) and (b2) cancel out, thus only the forces at the vertexes of the triangular actuator are left, as shown in Fig. 4.5-(c1) and (c2). It is noted that the forces at the top vertex of the triangular actuator points an opposite direction, and are twice as large as the forces exerted at bottom vertexes, as visually illustrated by the size of the circles. Thus, $f_{tx} + f_{lx} + f_{rx} = 0$ and $f_{ty} + f_{ly} + f_{ry} = 0$, which comply with force equilibrium. Moreover, the force generated by piezoelectric strips aligned along y-direction shows opposite dictions by that aligned along x-direction.

Combining the excitation terms produced by the strips in x- and y-directions, the

overall actuation forces at vertexes of the triangular actuator are given by:

$$f_t = f_{tx} + f_{ty} \tag{4.6a}$$

$$f_l = f_{lx} + f_{ly} \tag{4.6b}$$

$$f_r = f_{rx} + f_{ry}. \tag{4.6c}$$

If d_{31} is equal to d_{32}, then $f_{tx} = -f_{ty}$, $f_{lx} = -f_{ly}$, and $f_{rx} = -f_{ry}$, so that the terms in Eq. (4.6) cancel, and thus no forces are exerted. This indicates that, when the isosceles triangular actuator is made out of a symmetric type of polarized polycrystalline ceramic material, no point forces are generated at the vertexes of the triangular actuator. In contrast, if d_{31} is not equal to d_{32}, the triangular actuator does generate point forces at the vertexes as well as bending moments along its edges, because the terms in Eqs. (4.6) do not cancel. The overall force at the top vertex is in the opposite direction, and twice as large as that exerted at bottom vertexes. This result agrees with the conclusion given in Eq. (4.3) in Sullivan *et al.* [44].

In conclusion, Sullivan's theory thus works only with anisotropic piezoelectric material, e.g. PVDF, while it does not appear to be valid for PZT devices, which are always isotropic in the plane, i.e. $d_{31} = d_{32}$. It is not, however, clearly stated in Sullivan's paper that the proposed theory is only applicable for anisotropic material. In fact, both PVDF and PZT material are said to be considered in [44], which, according to the above discussion, is not appropriate. It should be noted, however, that even if the piezoceramic material is isotropic, any triangular actuator shape, which is not equilateral will still produces net forces at the corners, since the cancelation of the terms in Eqn. (4.6) will no longer be perfect.

4.2.2 Distributed modeling

In stead of Sullivan's theory, the distributed bending moment model is therefore used, which was introduced in Chapter 2 to predict the response of the panel with a square piezoceramic actuator, as illustrated in Fig. 4.6. In order to maintain a consistent formulation with that presented in the previous chapters, the triangular piezoceramic patch is segmented into a finite number of rectangular elements. As

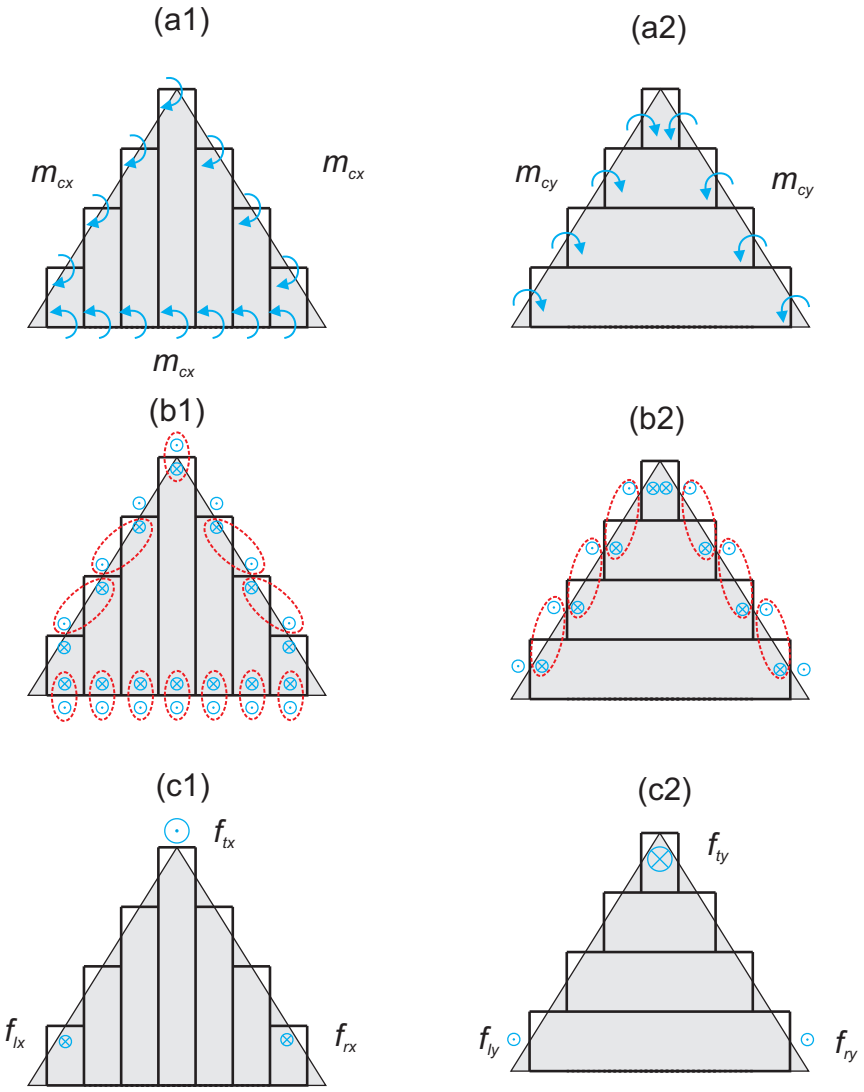

Figure 4.5: Schematic of actuation model for the rectangular piezoceramic patch actuator in x- (left) and y-direction(right). The upward force is shown by the circle with a dot at its center, and the downward force is shown by the circle with a cross.

shown in Fig. 4.6, the base edge of the actuator is subdivided into n_{tx} elements, while the actuator is subdivided into n_{ty} elements in y-direction. Thus, the dimensions of an element d_{ex} by d_{ey} are given as:

$$d_{ex} = \frac{b_{pzt}}{n_{tx}} \tag{4.7a}$$

$$d_{ey} = \frac{t_{pzt}}{n_{ty}}, \tag{4.7b}$$

where b_{pzt} and t_{pzt} respectively denote the base length and the height of the triangular actuator. The number of elements in x-direction, n_{tx}, is defined by, $n_{tx} = 2n_{ty}-1$, in order to easily create the mesh of the triangle object with a rectangular base elements. Therefore, the total number of the elements n_t is given by the square of n_{ty}, thus $n_t = n_{ty}^2$. The number of elements n_t has been chosen in such a way that the smaller value of d_{ex} and d_{ey} is shorter than a quarter of the flexural wavelength at the maximum frequency considered in this study, i.e. $\lambda_{\min} \approx 6$ mm at 80 kHz. Therefore, the 40 mm $\times$ 25 mm triangular piezoceramic patch has been subdivided into n_{tx} by $n_{ty} = 33$ by 17 elements, and the dimensions of the elements are given by $d_{ex} = 1.21$ mm and $d_{ey} = 1.47$ mm.

The bending moments produced by the triangular piezoceramic patch actuator are modeled by point moments located along four end-surfaces of the rectangular elements. Thus, the bending moments vector $\mathbf{m_c}$ is expressed by a $4n_t$-element column vector, as:

$$\mathbf{m_c} = m_c \begin{bmatrix} -\mathbf{d} & +\mathbf{d} & +\mathbf{d} & -\mathbf{d} \end{bmatrix}^T, \tag{4.8}$$

where $\mathbf{d}$ is a n_t-element vector with zero and one. m_c is the bending moment generated along the four edges of a rectangular element per unit voltage, given in Eq. (2.3).

Assuming an ideal velocity sensor and an ideal piezoceramic actuator, the complex transverse velocity of the panel at the sensor position $\dot{w}_c$ is given by the following mobility expression:

$$\dot{w}_c = \mathbf{Y_{ct}} \mathbf{m_c} V_c, \tag{4.9}$$

where $\mathbf{Y_{ct}}$ represents a $4n_t$-element row vector with the mobility functions between the velocity $\dot{w}_c$ at the velocity sensor and the actuation moments along the edges of

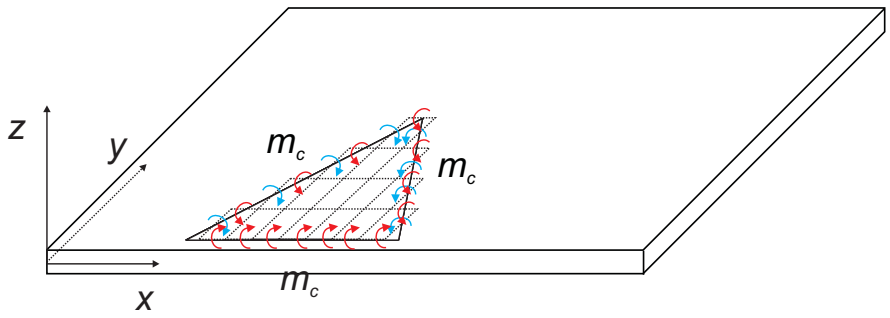

Figure 4.6: Schematic of the actuation model for the distributed moments of the triangular actuator.

the triangular actuator. A detailed expression for this mobility function is given in Appendix A.3. V_c is the driving voltage given to the actuator.

Figure 4.7 shows the Bode plots of the simulated open loop FRFs derived with Sullivan's model (top) and with proposed model given in Eq.(4.9) (bottom), and compared with the measured open loop FRF on the panel shown in Fig. 4.1. The top plot shows that, at low frequency below 1 kHz, the simulated and measured FRFs have similar amplitude spectra, but shifted by about 10 dB. In contrast, in the bottom plot, the measured FRF shows good agreements with the simulated FRF, which is derived using the proposed model with distributed bending moments. It indicates that the large differences in amplitude are caused by the point forces. As a force excites the panel more efficiently at low frequency, while the bending moment more efficiently excites the plate as the flexural wavelength approaches to the width of the actuator, i.e. at higher frequencies, the low frequency response of the panel is controlled by force excitation terms.

The phase plots indicates that the phase lag of the open loop FRFs is confined between $\pm$ 90 degree up to around 5 kHz derived with Sullivan's model, and up to 3 kHz with the proposed model with distributed bending moments, while the phase lag of the measured open loop FRF exceeds -90 degree at around 2 kHz. This is because Sullivan's model considers the force at the top vertex of the triangular actuator, which is collocated with the linear velocity sensor, and thus the sensor-actuator pair has better collocation and duality features than the one without the force.

At high frequency beyond around 3 kHz, the difference of two FRFs in both amplitude and phase gets smaller. In fact, the overall agreements between the measured and simulated response of the panel using both models are relatively poor, specially at mid-high frequency, because both mathematical models have been derived using the idealized sensor-actuator pair, and thus the passive effects produced by the actuator are ignored. As discussed in Chapter 2, it is important to consider the passive effects in order to accurately predict the response of a thin panel with a piezoceramic patch up to high frequencies.

Nevertheless, Fig. 4.7 confirms the conclusion obtained in Section 4.2.1, that the previous model suggested by Sullivan *et al.* has potential problems that less accurately model the measured response of the panel with the triangular actuator than the model with distributed bending moments.

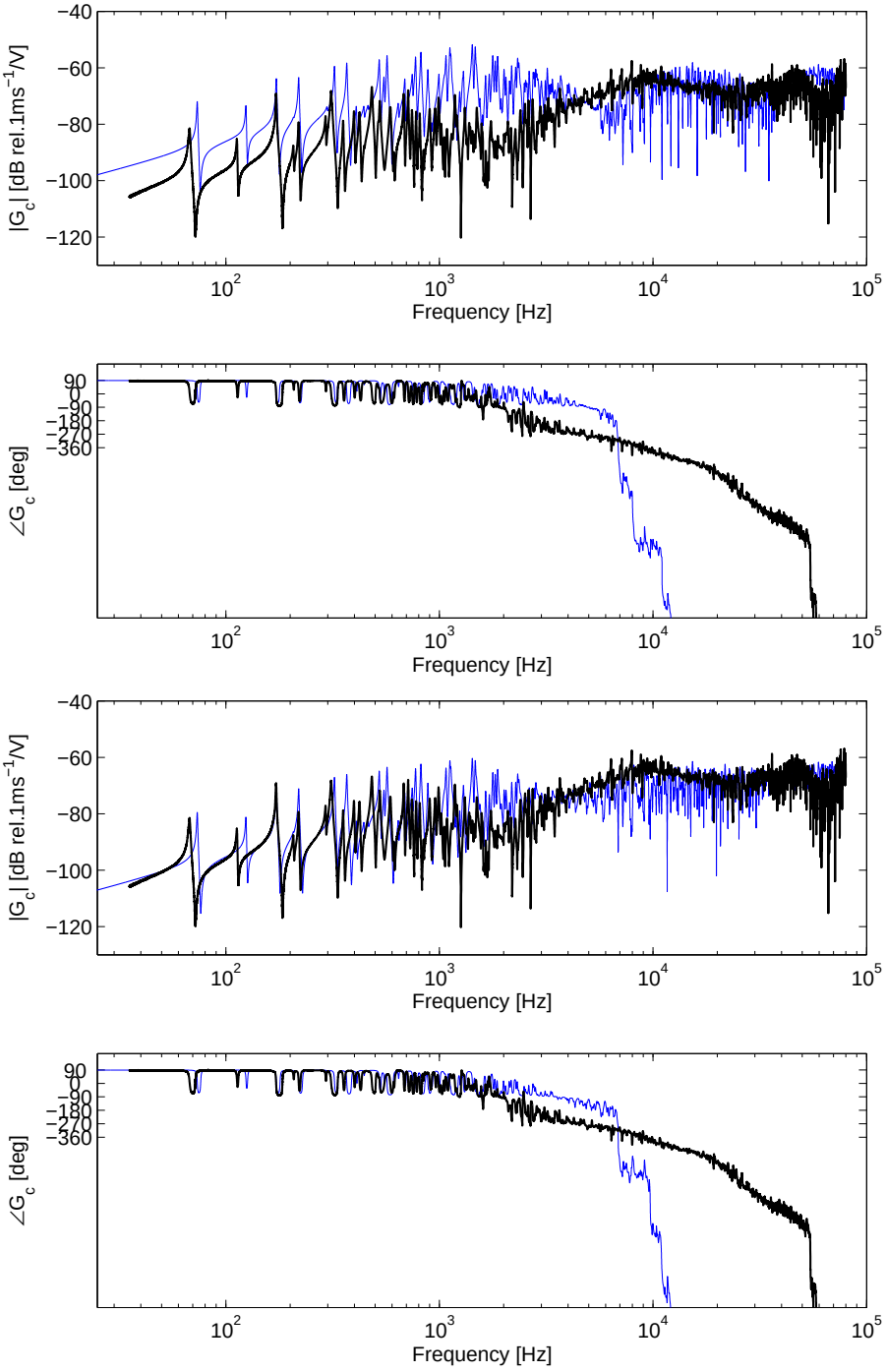

Figure 4.7: Top: Bode plot of the simulated open loop FRF derived with the Sullivan's actuation model (blue-faint line) and measured open loop FRF (black solid line); Bottom: Bode plot of the simulated open loop FRF derived with the proposed model distributed moments (blue-faint line) and measured open loop FRF (black solid line)

4.3 Modeling the local dynamics of a triangular actuator

This section presents developments of three model introduced for a triangular piezoceramic patch attached to a rectangular plate.

The first model takes into account the passive inertia and stiffness effects of the actuator. This model is equivalent to the fully coupled model for the panel with a square actuator introduced in Chapter 2.2.3. The second model includes the resilient mounting effects of the panel, and the third model considers both the passive effects of the actuator and the resilient mounting effects of the panel.

4.3.1 Modeling actuator mass and stiffness

As discussed in Chapter 2, it is important to consider the passive inertia and stiffness effects of the actuator in order to accurately predict the response of a thin panel with a piezoceramic patch up to high frequencies. In Chapter 2, the passive inertia and stiffness effects of the square actuator have been modeled by using arrays of lumped elements. The comparison with measured data has confirmed the validity of the lumped element model. Therefore, the passive effects of the triangular actuator are also modeled by using the distributed element method. In order to maintain a consistent modeling with the actuation moment produced by the triangular actuator shown in Fig. 4.6, the inertia and stiffness effects of the triangular actuator is modeled by subdividing the actuator into the n_t rectangular elements, as shown in Fig. 4.8. The transverse inertia effects of the elements are modeled by lumped masses locate at the center of each element. The stiffness effects of the elements are modeled by a pair of axial springs aligned parallel to the x- and y-axis of the panel. Thus, as for the square piezoceramic patch actuator, the cross axial stiffness effects between parallel strips have been neglected. Also, the self and mutual shear stiffness effects between parallel springs have been neglected. Finally, the cross stiffness effects due to coupled axial and shear stiffness effects between pairs of strips oriented one orthogonal to the other have been neglected.

According to Eq. (2.45), the open loop FRF for the fully coupled model of the panel

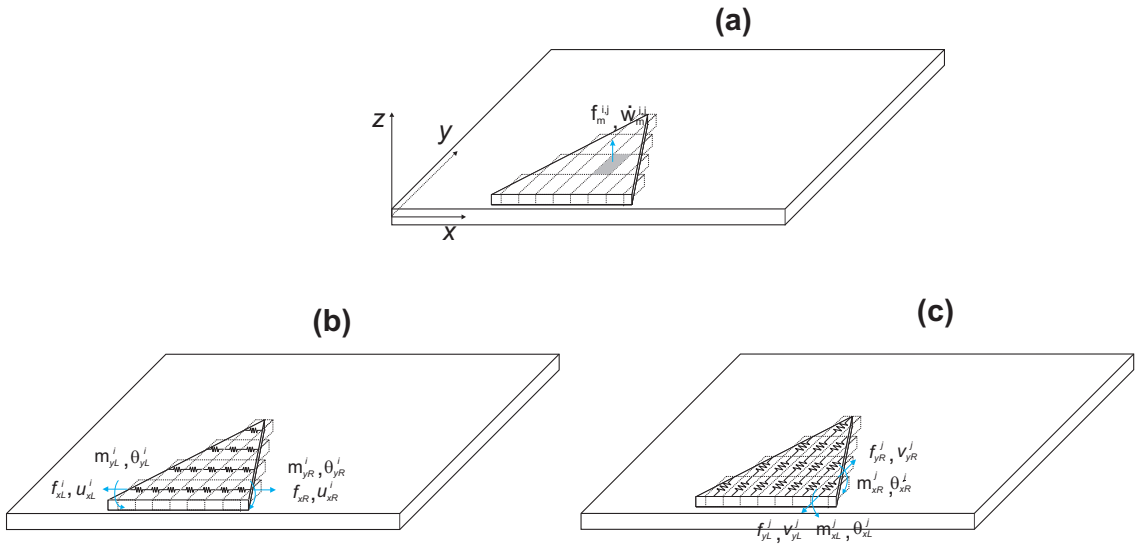

Figure 4.8: Schematic of the models for the triangular piezoceramic patch: inertial effect of the actuator mass (a), and the elastic effect of the actuator stiffness (b) and (c)

that includes inertia and stiffness effects of the triangular actuator is derived as:

$$G_c = \begin{bmatrix} \mathbf{Y_{ce}} & \mathbf{Y_{ct}} \end{bmatrix} \begin{bmatrix} \mathbf{I_d} + \mathbf{Z_e}\mathbf{Y_{ee}} & \mathbf{Z_e}\mathbf{Y_{et}} \\ \mathbf{Z_k}\mathbf{Y_{ke}} & \mathbf{I_s} + \mathbf{Z_k}\mathbf{Y_{kt}} \end{bmatrix}^{-1} \begin{Bmatrix} \mathbf{0} \\ \mathbf{m_c} \end{Bmatrix}. \tag{4.10}$$

The mobility functions Y_{ce}, $\mathbf{Y_{ee}}$, $\mathbf{Y_{et}}$, $\mathbf{Y_{ke}}$ and $\mathbf{Y_{kt}}$ have been introduced in Chapter 2, and the analytical formulas of these matrices are given in Appendix A.2. The identity matrices $\mathbf{I_d}$ and $\mathbf{I_s}$ have the dimensions of n_t by n_t, and $4n_t$ by $4n_t$, respectively.

The impedance matrices due to inertia and stiffness effects of the triangular actuator $\mathbf{Z_e}$ and $\mathbf{Z_k}$ are given below:

$$\mathbf{Z_e} = j\omega \frac{m_{pzt}}{n_t} \mathbf{I_d} \tag{4.11a}$$

$$\mathbf{Z_k} = \frac{1}{j\omega} \begin{bmatrix} c_{kx}\mathbf{I_d} & -c_{kx}\mathbf{I_d} & \mathbf{0} & \mathbf{0} \\ -c_{kx}\mathbf{I_d} & c_{kx}\mathbf{I_d} & \mathbf{0} & \mathbf{0} \\ \mathbf{0} & \mathbf{0} & c_{ky}\mathbf{I_d} & -c_{ky}\mathbf{I_d} \\ \mathbf{0} & \mathbf{0} & -c_{ky}\mathbf{I_d} & c_{ky}\mathbf{I_d} \end{bmatrix}, \tag{4.11b}$$

where m_{pzt} denotes the mass of the triangular actuator, $m_{pzt} = \rho_{pzt} b_{pzt} t_{pzt}/2$, and ρ_{pzt} denotes the mass density of the triangular actuator. The bending stiffness

coefficients of a segmented element c_{kx} and c_{ky} are given as:

$$c_{kx} = E_{pzt}\frac{2t_{pzt}}{b_{pzt}}h_{pzt}\left(\frac{h_{pzt}+h_s}{2}\right)^2 \tag{4.12a}$$

$$c_{ky} = E_{pzt}\frac{b_{pzt}}{t_{pzt}}h_{pzt}\left(\frac{h_{pzt}+h_s}{2}\right)^2, \tag{4.12b}$$

where h_s represents the thickness of the plate.

Figure 4.9 shows the Bode and Nyquist plots of the simulated open loop FRFs derived with the ideal model given in Eq.(4.9) and the model with the passive effects given in Eq.(4.10). The Bode plot in Fig. 4.9 highlights that at low frequency the amplitude of the FRF using the passive model is lower than that of the ideal model. The previous study regarding the square actuator discussed in chapter 2 has shown that the stiffness effect of the actuator reduces the amplitude of the FRF at low frequency. As the stiffness effects decrease with the frequency ω, the difference in amplitude between the two FRFs becomes smaller. At higher frequency beyond 3 kHz, the Bode plot of the FRF derived with the passive model is characterized by modulation effects in amplitude.

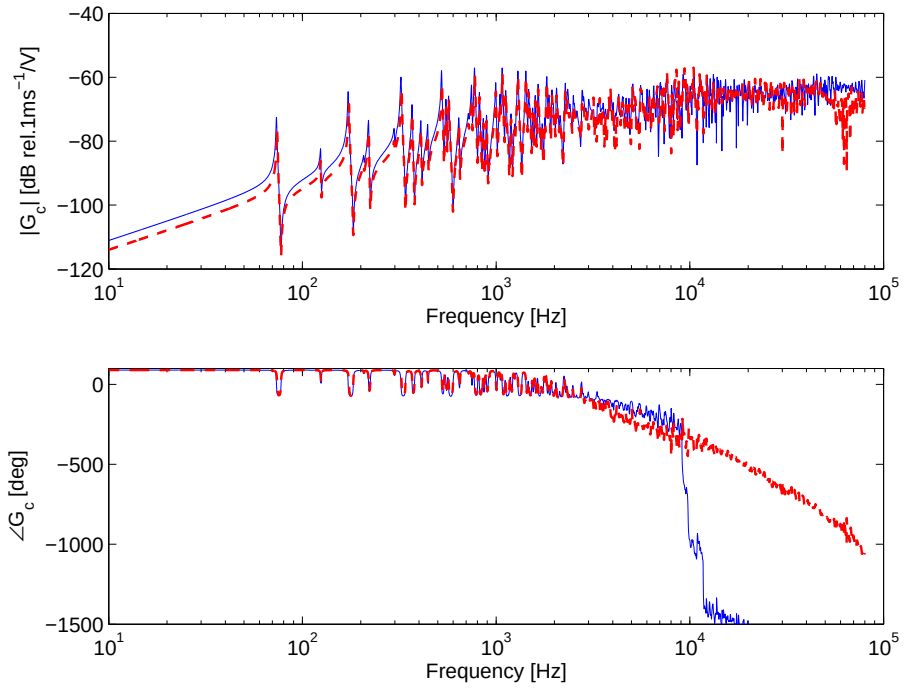

Figure 4.9: Bode plot of the open loop FRF derived with the ideal model with the distributed bending moments (blue-faint line) and the the models with the passive effects (red-dashed line).

4.3.2 Modeling boundary condition

As the triangular piezoceramic patch actuator is attached to the panel along its edge with 1 mm gap from the clamping frame, the response of the panel at the tip of the actuator, where the velocity sensor is attached, is strongly affected by the panel boundary condition. All the simulated results presented above are obtained by assuming clamped boundary conditions, in which the deflection along this edges is assumed to be zero, and the rotation with reference to the edge line is zero, as well. However, for the practical implementation of the test rig considered in this study, the boundary condition can neither be considered clamped nor simply supported. At lower frequencies where the wave length of the panel is much longer than the width of the clamping frame, both the deflection and the rotation of the panel along the edges are well canceled by the clamping flame. However, as frequency rise, and hence the wave length gets shorter, the motion of the panel along the edges is not fully counteracted by the frame, due to the rigidity of the frame and the manufacturing imperfection, such as non-perfect cross section shape and roughness of the surface. In this case, the boundary of the panel becomes closer to a simply supported condition, and eventually, free-free condition. Therefore, it is important to consider flexible boundary conditions, which allows transverse and/or rotational motion of the panel along its edges, instead of ideal clamped boundary condition. In this chapter, it is assumed that the linear motion of the panel is perfectly constrained by the boundary frame, while the rotation along the edge of the panel is resiliently restricted by rotational springs along the border.

In order to maintain a consistent formulation for the physical passive effects produced by the actuator, the boundary condition of the panel is modeled by using n_b distributed rotational springs along the x- and y-border, as shown in Fig. 4.10. The number of boundary springs n_b has been chosen in such a way that the distance between two adjacent springs is shorter than a quarter plate bending wavelength at the maximum frequency of interest. i.e. $\lambda_{\min} \approx 6$ mm at 80 kHz. Therefore, the resilient mounting condition has been modeled by using $n_b = 261$ rotational springs per each edge. In this case, the distance between two neighbor springs along x- and y-border becomes 1.59 mm and respectively 1.20 mm.

In this section, the passive inertia and stiffness effects of the triangular actuator

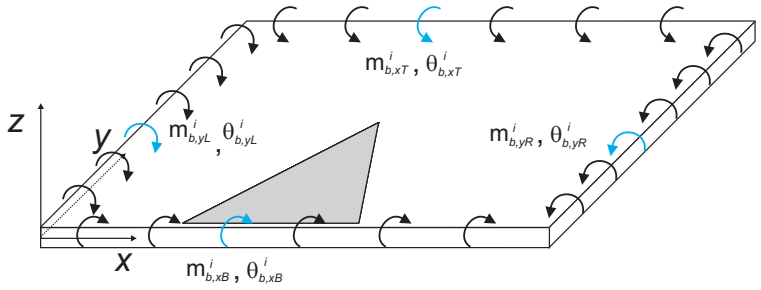

Figure 4.10: Schematic of the model for resiliently mounted panel

are not considered in order to highlight the passive effects produce by the flexible boundary conditions on the open loop FRF. The response of the panel can be given as the superposition of the responses due to the moment excitations of the piezoceramic actuator and the reactive moments produced by the rotational springs along the border of the resiliently mounted panel. Thus the complex transverse velocity at the sensor position $\dot{w}_c$ is given by the following mobility expression:

$$\dot{w}_c = \mathbf{Y_{ct}}\mathbf{m_c}V_c + \mathbf{Y_{cb}}\mathbf{m_b}, \tag{4.13}$$

where $\mathbf{Y_{ct}}$ denotes a $4n_t$-element row vector with mobility function betweens the velocity at the error sensor location $\dot{w}_c$ and the actuation moment produced by the triangular actuator on the panel with simply supported boundary conditions. $\mathbf{Y_{cb}}$ is a $4n_b$-element row vector with mobility functions between the transverse velocity $\dot{w}_c$ and the reactive moment along the edge of the panel. The detailed formulations for the mobility functions are given in Appendix A. The column vector $\mathbf{m_b}$ is composed of four n_b-elements column vectors:

$$\mathbf{m_b} = \begin{bmatrix} \mathbf{m_{x_0}} & \mathbf{m_{x_L}} & \mathbf{m_{y_0}} & \mathbf{m_{y_L}} \end{bmatrix}^T. \tag{4.14}$$

Each vector denotes the reactive moments generated by the rotational springs along

the $x = 0$, $x = L_x$, $y = 0$, and $y = L_y$ axis respectively:

$$\mathbf{m_{y_0}} = \begin{bmatrix} m^1_{by_0} & m^2_{by_0} & \cdots & m^{n_b}_{by_0} \end{bmatrix}^T \tag{4.15a}$$

$$\mathbf{m_{y_L}} = \begin{bmatrix} m^1_{by_L} & m^2_{by_L} & \cdots & m^{n_b}_{by_L} \end{bmatrix}^T \tag{4.15b}$$

$$\mathbf{m_{x_0}} = \begin{bmatrix} m^1_{bx_0} & m^2_{bx_0} & \cdots & m^{n_b}_{bx_0} \end{bmatrix}^T \tag{4.15c}$$

$$\mathbf{m_{x_L}} = \begin{bmatrix} m^1_{bx_L} & m^2_{bx_L} & \cdots & m^{n_b}_{bx_L} \end{bmatrix}^T. \tag{4.15d}$$

The reactive moment is given by the product of the impedance of the rotational springs z_b and the angular displacement along the edge of the panel $\theta_\mathbf{b}$, thus:

$$\mathbf{m_b} = -z_b \theta_\mathbf{b}. \tag{4.16}$$

Assuming a harmonic vibration, the angular displacement vector $\theta_\mathbf{b}$ can be expressed in terms of the angular velocities along the border of the panel with reference to either x- or y-axis:

$$\theta_\mathbf{b} = \frac{\dot{\theta}_\mathbf{b}}{j\omega}. \tag{4.17}$$

After substituting Eq.(4.17) into Eq.(4.16), the reactive moment vector $\mathbf{m_b}$ can be derived based on the angular velocities vector along the border of the panel:

$$\mathbf{m_b} = -\mathbf{Z_b}\dot{\theta}_\mathbf{b}, \tag{4.18}$$

where $\mathbf{Z_b}$ denotes the impedance matrix, given by the following formula:

$$\mathbf{Z_b} = \frac{z_b}{j\omega}\mathbf{I_b}, \tag{4.19}$$

where $\mathbf{I_b}$ is the $4n_b$ by $4n_b$ identity matrix.

The angular velocity vector $\dot{\theta}_b$ along the border of the panel can be written as the superposition of the responses of the panel generated by the actuation moments produced by the triangular actuator, and the reactive moment along the border of the resiliently mounted panel, as:

$$\dot{\theta}_\mathbf{b} = \mathbf{Y_{bt}}\mathbf{m_c}V_c + \mathbf{Y_{bb}}\mathbf{m_b}, \tag{4.20}$$

where $\mathbf{Y_{bt}}$ is a $4n_b$ by $4n_t$ matrix with the mobility function between the angular velocities along the edges of the panel and the actuation moment generated by the triangular actuator. $\mathbf{Y_{bb}}$ is a $4n_b$ by $4n_b$ matrix with the mobility functions between the angular velocities and the reactive moments along the panel border. Expressions for these mobility functions are given in Appendix A.

Substituting Eqs. (4.18) and (4.20) into Eq. (4.13), the velocity at the sensor position $\dot{w}_c$ can be expressed as a function of control moment,

$$\dot{w}_c = \left(\mathbf{Y_{ct}} + \mathbf{Y_{cb}}\left[\mathbf{I_b} + \mathbf{Z_b}\mathbf{Y_{bb}}\right]^{-1}\mathbf{Z_b}\mathbf{Y_{bt}}\right)\mathbf{m_c}V_c. \tag{4.21}$$

Using the equation above and Eq. (2.5), the open loop FRF derived with the flexible boundary model is given as:

$$G_c = \left(\mathbf{Y_{ct}} + \mathbf{Y_{cb}}\left[\mathbf{I_b} + \mathbf{Z_b}\mathbf{Y_{bb}}\right]^{-1}\mathbf{Z_b}\mathbf{Y_{bt}}\right)\mathbf{m_c}. \tag{4.22}$$

This equation allows to predict the response of a simply supported panel with rotational springs along its border, which resiliently restrict the rotation motion along the edges. When the impedance of the rotational springs along the edges of the panel z_b is equal to zero, this equation gives the response of the simply supported panel.

The Top plot in Fig. 4.11 compares the predicted open loop FRFs derived using the flexible boundary model with different boundary stiffness; $z_b = 50$ (blue faint line), 500 (red dotted line), and 10000 (black solid line) [N/m]. This plot highlights that, at low frequency as the boundary impedance z_b increases, the resonant frequencies of the panel are shifted up in frequency. As frequency rises, the spectra of the medium boundary stiffness model approaches that of the low boundary stiffness model, and above 5 kHz, both spectra are almost overlapped. At high frequency, the amplitude of the FRF derived with the high-impedance model is in general lower than the others.

The phase plot in Fig. 4.11 shows that the phase predicted by the low-impedance model starts from -90 degree. This indicates that, when the rotational motion of the panel along its border is softly constrained, the velocity of the panel at error sensor position is negative below the first resonant frequency. The phase is confined

between -90 and -270 degree up to about 3 kHz, and then a constant phase lag takes place. In contrast, with the high-impedance model the phase starts from +90 degree, and remains within ± 90 degree up to 5 kHz. As frequency rises, the difference in phase among the three FRFs becomes smaller.

The bottom plot in Fig. 4.11 shows the Bode plots of the predicted response of the panel with two ideal boundary conditions. The blue faint and black solid lines are respectively derived by assuming clamped and simply supported boundaries along all four edges of the panel. The blue faint line in the top and bottom plots in Fig. 4.11 indicates that, when the boundary stiffness is low, the spectra obtained by the flexible boundary model is similar to that of the simply supported model. The black solid line in Fig. 4.11 highlights that the open loop FRF derived using high boundary stiffness model agrees very well with that of the clamped model. These results indicate that when a moderate boundary stiffness is used, this mobility model can predict the response of a panel, whose boundary condition shifts from a clamped condition to a simply supported condition with reference to frequency.

In order to better understand the physics that determine the coupling between the panel and the triangular piezoceramic patch actuator, a frequency response function was decomposed into the excitation components of the triangular piezoceramic patch, as shown in Fig. 4.12.

The top, middle and bottom plots in Fig. 4.12 respectively show the Bode diagrams of the open loop FRFs derived using the resilient boundary model with different boundary stiffness, $z_b = 50$ [N/m], $z_b = 500$ [N/m], and $z_b = 10000$ [N/m]. Each plot includes three excitation components of the open loop FRF, such as the bending moment along left lateral edge(blue faint line), bending moment along right lateral edge (red dashed line), and bending moment along base edge (black solid line). As mentioned earlier, the base edges of the triangular actuator is aligned along the border of the panel with 1 mm distance from the edge of the panel, and thus the bending moment along base edge is exerted even for the high boundary stiffness model.

The blue faint and red dashed lines in Fig. 4.12 shows the mean amplitude of the FRF components due to the bending moments along lateral edges rises with

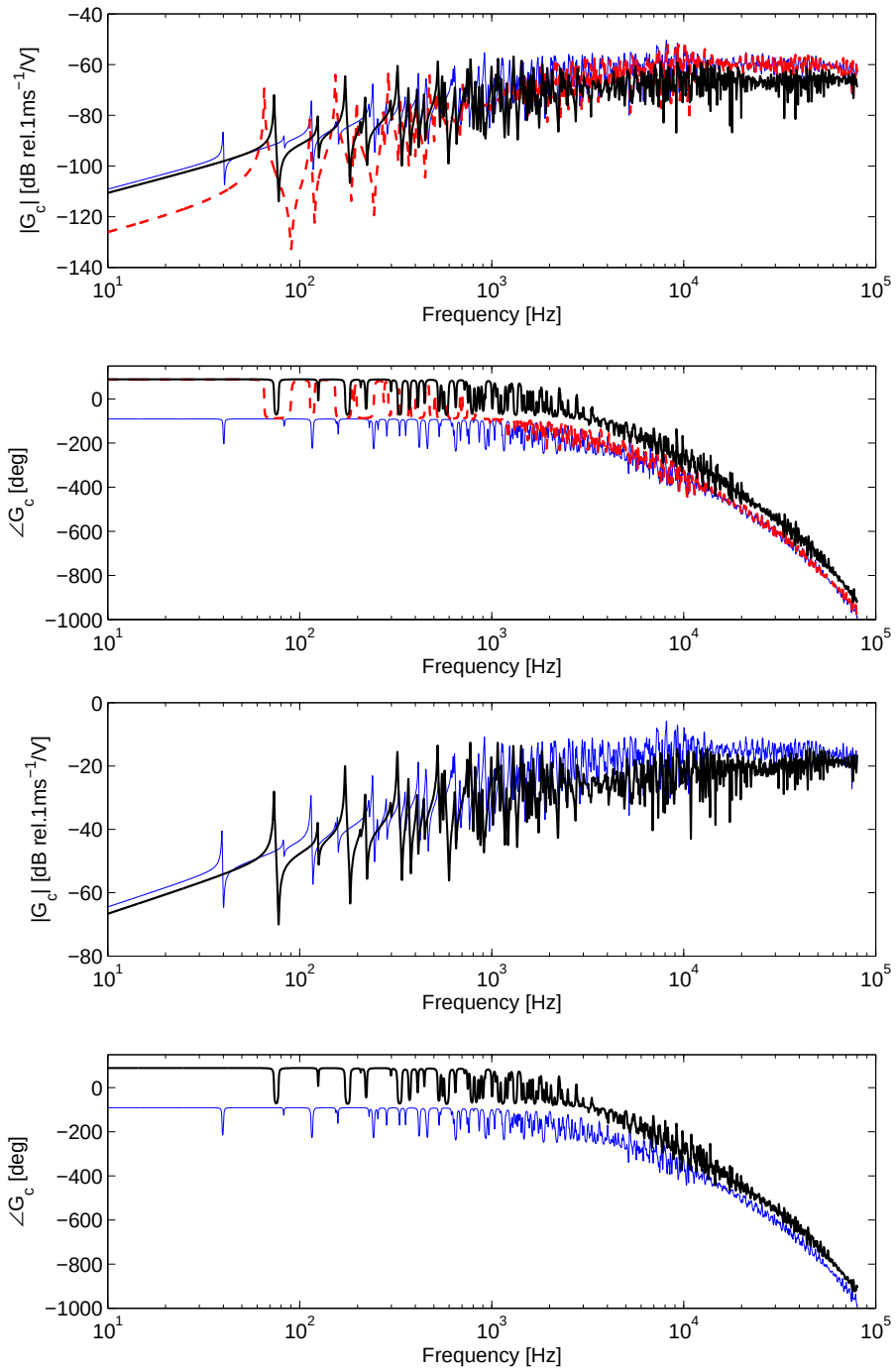

Figure 4.11: Top: Bode plot of the open loop FRF derived with the resilient boundary model with various boundary stiffness: $z_b = 50$ [N/m] (blue-faint line), $z_b = 500$ [N/m] (red-dashed line), $z_b = 10000$ [N/m] (black-solid line). Bottom: Bode plot of the open loop FRF derived with the simply supported model (blue-faint line) and the clamped model (black-solid line)

frequency up to 1 kHz, and then remains almost constant at around -80 dB. In contrast, the black solid line in Fig. 4.12 shows that the mean amplitude of the FRFs due to the moment along the base edge keeps rising with frequency in the whole frequency range. At around 5 kHz, the amplitude of all FRF components becomes low, because at these frequencies the response of the panel is controlled by modes with nodal lines close to the tip of the piezoceramic patch, where the sensor is located. This type of phenomenon is repeated at higher frequencies, where the response of the panel is yet again controlled by clusters of higher order modes with nodal lines close to the tip of the actuator.

The three plots in Fig. 4.12 indicate that the relative magnitude among the three actuation components changes with frequency. At low frequency the actuation moments along the lateral edges are comparable or higher than the moments along the base edge for any boundary stiffness models. At higher frequency, the dominant actuation components change from the lateral edge moments to the base edge moments. As the bending moments along the base edge produce an out-of-phase motion, when the actuation moments along the base edge become stronger than the others, the phase lag of the open loop FRF between the velocity sensor and the triangular actuator exceeds -90 degree.

It must be noted that, when the panel is perfectly clamped and the base edge of the actuator is accurately aligned along the perimeter of the panel, the line moment along the base edge is counteracted by the clamping frame, such that no line moment along the base edge is exerted on the structure. In practice, however, because of manufacturing imperfections, bonding inaccuracy and electrical insulation issues, it is rather difficult to perfectly align the base edge of the triangular actuator with the border of the panel. Therefore, in this thesis it is assumed that piezoceramic actuator is bonded on panel along the edge with 1 mm distance from the clamping frame.

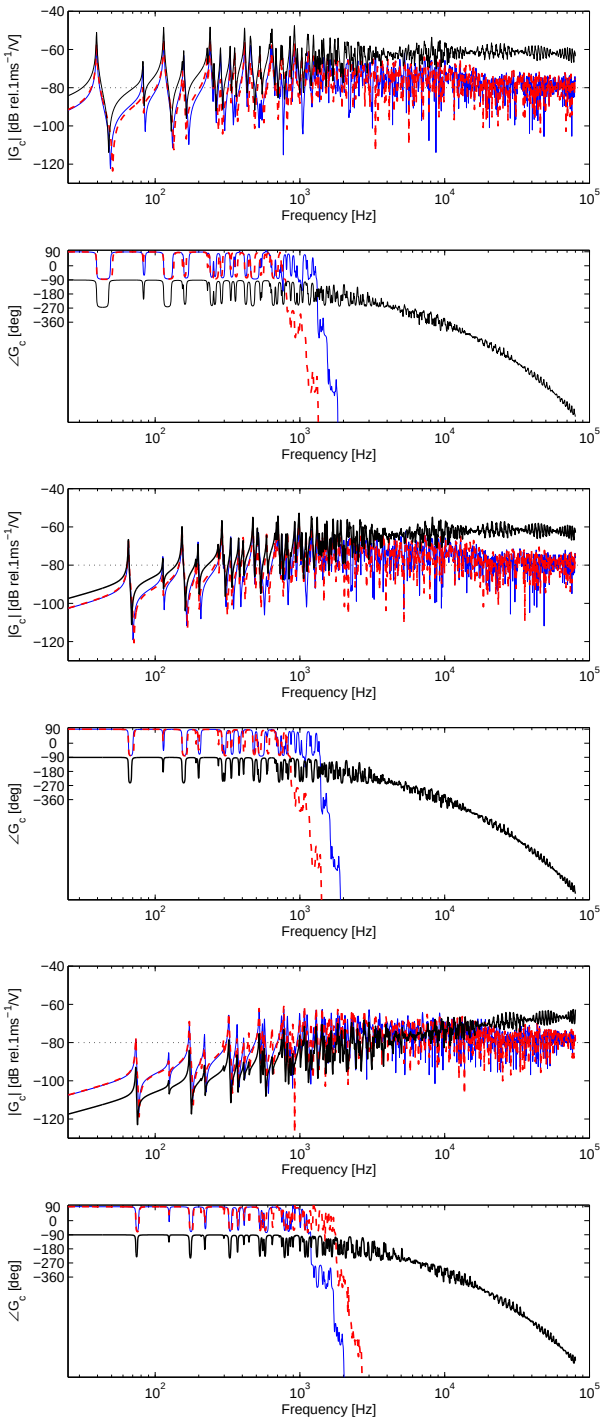

Figure 4.12: Bode plots of the three components of the open loop FRF derived with the resilient boundary model with various boundary stiffness: $z_b = 50$ [N/m] (top), $z_b = 500$ [N/m] (middle), $z_b = 10000$ [N/m] (bottom); bending moment along left lateral edge (blue faint line), bending moment along right lateral edge (red dashed line), and bending moment along base edge (black solid line).

4.3.3 Fully coupled model and experimental verification

In this section the measured open loop FRF is compared with the simulated open loop FRF derived with the fully coupled model, which takes into account both the passive mass and stiffness effects of the triangular actuator, and the resilient mounting effect of the panel. The formulation of the fully coupled model is derived by combining the two models discussed above. Thus, the fully coupled repones of the piezoceramic actuator bonded on a resiliently mounted panel can be expressed by the following mobility equation:

$$\dot{w}_c = \begin{bmatrix} \mathbf{Y_{ce}} & \mathbf{Y_{ct}} & \mathbf{Y_{cb}} \end{bmatrix} \begin{Bmatrix} \mathbf{f_e} \\ \mathbf{m_k} + \mathbf{m_c} V_c \\ \mathbf{m_b} \end{Bmatrix}. \tag{4.23}$$

According to Eq. (2.42) and Eq. (4.18), $\mathbf{f_e}$, $\mathbf{m_k}$ and $\mathbf{m_b}$ can be cast together in the following matrix expression:

$$\begin{Bmatrix} \mathbf{f_e} \\ \mathbf{m_k} + \mathbf{m_c} V_c \\ \mathbf{m_b} \end{Bmatrix} = - \begin{bmatrix} \mathbf{Z_e} & \mathbf{0_{ek}} & \mathbf{0_{eb}} \\ \mathbf{0_{ek}}^T & \mathbf{Z_k} & \mathbf{0_{kb}} \\ \mathbf{0_{eb}}^T & \mathbf{0_{kb}}^T & \mathbf{Z_b} \end{bmatrix} \begin{Bmatrix} \dot{\mathbf{w}}_\mathbf{e} \\ \dot{\theta}_\mathbf{b} \\ \dot{\theta}_\mathbf{r} \end{Bmatrix} + \begin{Bmatrix} \mathbf{0_e} \\ \mathbf{m_c} \\ \mathbf{0_b} \end{Bmatrix} V_c, \tag{4.24}$$

where $\mathbf{0_{ek}}$, $\mathbf{0_{eb}}$, and $\mathbf{0_{kb}}$ are matrices with zeros, with dimensions of n_t by $4n_t$, n_t by $4n_b$, and $4n_t$ by $4n_b$, respectively. $\mathbf{0_e}$ and $\mathbf{0_b}$ are respectively n_t-element and $4n_b$-element column vectors with zeros.

The transverse velocity vector $\dot{\mathbf{w}}_\mathbf{e}$, and the angular velocity vectors $\dot{\theta}_\mathbf{k}$ and $\dot{\theta}_\mathbf{b}$ are given as the superposition of the response of the panel generated by active moments of the actuator, passive effects of the actuator, and the resilient mounting effects:

$$\begin{Bmatrix} \dot{\mathbf{w}}_\mathbf{e} \\ \dot{\theta}_\mathbf{k} \\ \dot{\theta}_\mathbf{b} \end{Bmatrix} = \begin{bmatrix} \mathbf{Y_{ee}} & \mathbf{Y_{et}} & \mathbf{Y_{eb}} \\ \mathbf{Y_{ke}} & \mathbf{Y_{kt}} & \mathbf{Y_{kb}} \\ \mathbf{Y_{be}} & \mathbf{Y_{bt}} & \mathbf{Y_{bb}} \end{bmatrix} \begin{Bmatrix} \mathbf{f_e} \\ \mathbf{m_k} + \mathbf{m_c} V_c \\ \mathbf{m_b} \end{Bmatrix}, \tag{4.25}$$

where $\mathbf{Y_{eb}}$ denotes a n_t by $4n_b$ matrix with mobility functions between the velocities at the centers of the elements and the reactive moments along the border of the panel. $\mathbf{Y_{kb}}$ denotes a $4n_t$ by $4n_b$ matrix with mobility functions between the angular

velocities at the four edges of the rectangular lumped elements of the actuator and the reactive moments along the border of the panel. $\mathbf{Y_{be}}$ is a $4n_b$ by n_t matrix composed of mobility functions between the angular velocities along the border of the panel, and the forces produced by the inertia effect of the actuator on the center of the elements. $\mathbf{Y_{bt}}$ is a $4n_b$ by $4n_t$ matrix composed of mobility functions between the angular velocities along the border of the panel, and the reactive moment produced by the stiffness of the actuator along the four edges of the rectangular element. Detailed formulas for these mobility functions are found in Appendix A.

Substituting Eq. (4.24) and Eq. (4.25) into Eq. (4.23), the velocity at the sensor position is expressed as:

$$\dot{w}_c = \begin{bmatrix} \mathbf{Y_{ce}} & \mathbf{Y_{ck}} & \mathbf{Y_{cb}} \end{bmatrix} \begin{bmatrix} \mathbf{I_d} + \mathbf{Z_e}\mathbf{Y_{ee}} & \mathbf{Z_e}\mathbf{Y_{et}} & \mathbf{Z_e}\mathbf{Y_{eb}} \\ \mathbf{Z_k}\mathbf{Y_{ke}} & \mathbf{I_s} + \mathbf{Z_k}\mathbf{Y_{kt}} & \mathbf{Z_k}\mathbf{Y_{kb}} \\ \mathbf{Z_b}\mathbf{Y_{be}} & \mathbf{Z_b}\mathbf{Y_{bt}} & \mathbf{I_b} + \mathbf{Z_b}\mathbf{Y_{bb}} \end{bmatrix}^{-1} \times \begin{Bmatrix} \mathbf{0_e} \\ \mathbf{m_c} \\ \mathbf{0_b} \end{Bmatrix} V_c. \tag{4.26}$$

Using the equation above and Eq. (2.5), the open loop FRF of the fully coupled model, which includes both the passive effects of the actuator and the resilient mounting of the panel is derived as:

$$G_c = \begin{bmatrix} \mathbf{Y_{ce}} & \mathbf{Y_{ct}} & \mathbf{Y_{cb}} \end{bmatrix} \begin{bmatrix} \mathbf{I_d} + \mathbf{Z_e}\mathbf{Y_{ee}} & \mathbf{Z_e}\mathbf{Y_{et}} & \mathbf{Z_e}\mathbf{Y_{eb}} \\ \mathbf{Z_k}\mathbf{Y_{ke}} & \mathbf{I_s} + \mathbf{Z_k}\mathbf{Y_{kt}} & \mathbf{Z_k}\mathbf{Y_{kb}} \\ \mathbf{Z_b}\mathbf{Y_{be}} & \mathbf{Z_b}\mathbf{Y_{bt}} & \mathbf{I_b} + \mathbf{Z_b}\mathbf{Y_{bb}} \end{bmatrix}^{-1} \times \begin{Bmatrix} \mathbf{0_e} \\ \mathbf{m_c} \\ \mathbf{0_b} \end{Bmatrix}. \tag{4.27}$$

Figure 4.13 shows the Bode plot of the simulated open loop FRF predicted by using the fully coupled model with a boundary impedance $z_b = 1800$, and the measured open loop FRF using the test rig shown in Fig. 4.1.

Comparing the red dashed line with the black solid line in the Bode plots, it is noticed that the simulated open loop FRF well agrees with the measured FRF in terms of both amplitude and phase at frequency up to around 1 kHz. At around 1.1 kHz, the amplitude of the measured FRF goes down. In contrast, the amplitude of the predicated FRF tends to slightly rise with frequency up to 10 kHz. Thus, there is not perfect agreement between the two FRFs around 1.1 kHz. At higher frequency, the amplitude of the measured FRF is characterized by modulation peaks. These principal features of the measured FRF are reasonably well captured by the simulated open loop FRF, although the measured modulation effects are slightly stronger than the simulated one. The phase plot in Fig. 4.9 shows that the analytical model agrees relatively well with the measured phase up to 50 kHz. The phase lag of both FRFs exceeds -90 degree at around 1.1 kHz, and then the phase lag constantly increases.

In summary, Fig. 4.13 indicates that this fully coupled analytical model captures well the principle feature of the measured FRF. This model is used in Chapter 6 in order to investigate the effects of the physical dimensions of the triangular actuator on the stability and control performance.

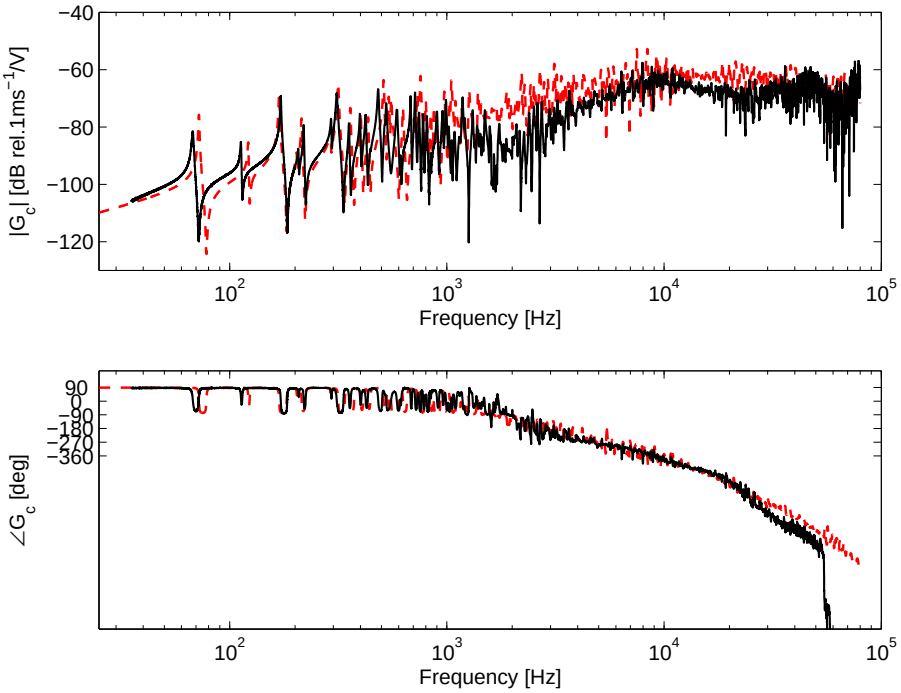

Figure 4.13: Bode plot of the simulated open loop FRF derived with the fully coupled model (red-dashed line) and measured open loop FRF (black-solid line).

4.4 Conclusions

This chapter presented the configuration of a new control unit, composed of a triangular piezoceramic actuator with a velocity sensor at its tip. This chapter has highlighted that the triangular actuator and velocity sensor pair has a comparable control performance with a square actuator and a velocity sensor at its center.

A fully coupled mathematical model has also been introduced for a resiliently mounted rectangular panel with a triangular piezoceramic patch actuator, which consider both the passive effects of the actuator patch and the flexible boundary condition of the panel. It is shown that the model predicts the measured results much better than the previous model of Sullivan *et al.*, which also leads to paradoxical results in the case of an equilateral triangular actuator.

The open loop FRF was decomposed into the excitation components generated by the three edges of the triangular actuator. At low frequency the response of the panel is determined by the bending moments along the lateral edges of the patch actuator. As frequency rises, the bending moments along the base edge more effectively excite the panel, and thus it controls the open loop FRF at higher frequencies. It must be noted that, when the panel is fully clamped, and the base edges of the triangular actuator is perfectly aligned along the border of the panel without the gap between the edge and the actuator, the bending moment generated by the base edge of the actuator is fully counteracted by the frame. In this study, the triangular actuator is bonded on the panel along the edge of the panel with 1 mm gap from the clamping frame.

The predicted response has been compared with the measured FRF to confirm the validity of both models. Both the measured and the simulated open loop FRFs are characterized by modulation peaks at high frequency, and the simulated response has in general a good agreement with the measured response.

The following chapter describes a decentralized velocity feedback control system implemented on a panel by using 16 such control units, in order to demonstrate the effectiveness of the triangular actuator and sensor pairs.

Chapter 5

Demonstration of the multi-input multi-output control system

Chapter 4 has compared the control performance of the single-input single-output (SISO) velocity feedback control systems, which are composed of triangular actuator with a velocity sensor at its tip, and a square actuator with a velocity sensor at its center. The measured open loop FRFs of both control loops have highlighted that the velocity feedback control system using triangular actuator has comparable control performance with that using the square actuator. It would be interesting to compared the control performance of the multi-input multi-output (MIMO) control systems using triangular and square actuators, as well as the SISO systems.

Recently Bianchi *et al.* [21] have presented a decentralized MIMO velocity feedback control system by using 4 by 4 array of square piezoceramic actuators and centrally located accelerometer sensors pairs. They have shown that significant levels of attenuation can be achieved in terms of both structural vibration of the panel and sound radiation by the panel. Therefore, this chapter presented a decentralized MIMO velocity feedback control system by using 16 triangular piezoceramic actuators and closely located accelerometer sensors pairs, in order to highlight the advantage of this new control configuration compared with the conventional control unit with square actuators. The control performance is discussed in terms of the structural vibration of the panel and its sound radiation in the frequency range 0 to 1 kHz in two stages: first, the passive control effect produced by the sensor-actuator

transducers, and second the active control effect of the 16 decentralized control loops. The passive control performance is assessed by comparing the responses of the panel without transducers and the panel with transducers but no feedback control. The active control effect is assessed by comparing the responses and sound radiation produced by the panel with transducers but no feedback control and the panel with transducers and decentralized velocity feedback control.

This chapter is organized in three sections. Section 1 describes the physical arrangements of the test rigs to implement the decentralized control system, as well as the design and the main features of the 16 channel analogue controller. In section 2, the stability properties of the control system are discussed using the generalized Nyquist criteria. Section 3 presents the experimental results regarding vibration reductions due to passive and active control effects. In section 4, the experimental results related to sound radiation from the panel are discussed.

5.1 Physical arrangements

The test structure is a rectangular aluminium panel clamped to a rigid frame, as discussed in the previous chapters. As shown in the left hand side picture in Fig. 5.1, this panel is now mounted on the open side of a Perspex box in order to measure the sound radiation by the panel. The box is composed of 30 mm thick Perspex plates, so that the sound transmission through the lateral walls of the box is much lower than that through the aluminium panel in the frequency range of interest [21]. The inner dimensions of the Perspex box are 414 mm $\times$ 314 mm $\times$ 400 mm. The panel is excited either by an acoustic field generated by a loudspeaker placed in the box (see Fig. 5.1), or by a point force generated by a shaker (LDS v201) acting on the aluminium panel. The shaker is fixed at $(x_p, y_p) = (167 \text{ mm}, 127 \text{ mm})$ with reference to the lower left hand side corner of the panel, as highlighted by the solid circle in Fig. 5.2.

5.1.1 Smart panel

As shown in right hand side picture in Fig. 5.1, 16 isosceles triangular piezoceramic patch actuators, having a size of 40 mm base length, 40 mm height and 1.0 mm

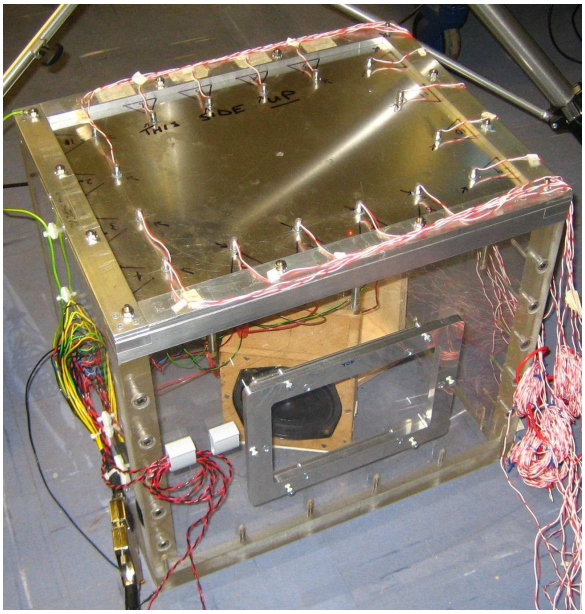
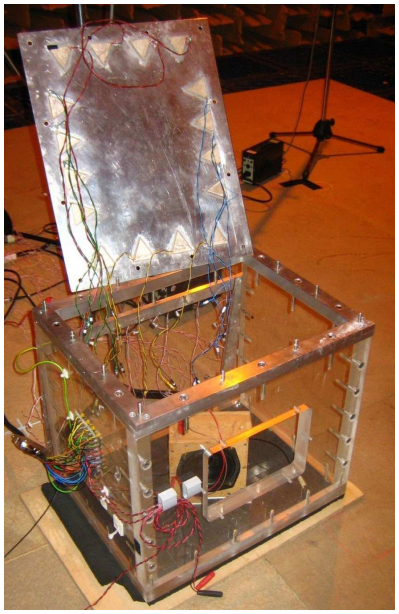

Figure 5.1: Smart panel mounted on a Perspex box

thickness, are bonded to the inner side of the panel using a thin layer of conductive glue. The geometric and the piezoelectric properties of the triangular piezoceramic actuators are given in Table 5.1. The layer of glue was maintained as thin as possible, i.e. approximately 0.05 mm. While the panel is used as ground reference (GND), a wire was soldered directly on the top vertex of the exposed side of each triangular patch to complete the electrical circuit necessary to drive the actuator.

Table 5.1: Geometric parameter and physical properties of the triangular piezoceramic actuator

parameter	symbol	value
Base length [mm]	b_{pzt}	40.0
Height [mm]	t_{pzt}	40.0
Thickness [mm]	h_{pzt}	1.0
Poisson's Ratio	ν_{pzt}	0.39
Density [kg/m^3]	ρ_{pzt}	7.7×10^3
Piezoelectric charge constant [m/V]	$d_{31} = d_{32}$	170×10^{-3}

As illustrated in Fig. 5.2, the 16 piezoceramic patches are evenly distributed along the perimeter of the panel, in such a way as the top vertex of the triangular actuator are placed along the virtual rectangular shape. Four actuators are evenly placed on each edge of the rectangular panel, and there is one actuator at each corner of the inner rectangular shape. The base edges of the actuator is aligned along the border

of the panel with 1 mm distance between the clamping frame and the base edge of the actuator. Therefore, the distances d_x between the centers of the base edges aligned along the $x = 0, l_x$ borders of the panel are given by:

$$d_x = (l_x - 2t_{pzt})/5 \tag{5.1}$$

where l_x is the length of the panel in x-axis, and t_{pzt} denotes the height of a triangular piezoceramic actuator, i.e. $t_{pzt} = 40$ mm. The distances d_y between the centers of the base edges aligned along the $y = 0, l_y$ borders of the panel are given by:

$$d_y = (l_y - 2t_{pzt})/3, \tag{5.2}$$

where l_y is the length of the panel in y-axis. The centers of the base edges of the outer patches aligned along the $x = 0, l_x$ borders of the panel are located at a distance $d_x + t_{pzt}$ from the $y = 0, l_y$ border, and the centers of the base edges of the outer patches aligned along the $y = 0, l_y$ borders of the panel are located at a distance t_{pzt} from the $x = 0, l_x$ border. Thus, as shown in the scheme of Fig. 5.2, top vertex of 16 actuators forms a virtual active boundary wedge with dimensions of $(l_x - 2t_{pzt}) \times (l_y - 2t_{pzt})$.

5.1.2 Sensor dynamics

At this stage, the accelerometer sensors are used instead of a laser vibrometer to close the velocity feedback control loops. As shown in the left hand side plot of Fig. 5.1, accelerometer sensors are bonded on the open side of the panel at the top vertices of each triangular actuator. The position of each accelerometer sensor is fixed at the top vertex of the corresponding triangular actuator bonded on the other side of the panel.

Accelerometers provide an output signal proportional to acceleration, vibration, and shock. Piezoelectric accelerometers are one of the most common sensing transducers, as piezoelectric materials have the ability to output an electrical signal proportional to the applied stress. In this study, high sensitivity tri-shear mode Inductively Coupled Plasma (ICP) accelerometer sensors (PCB Piezotronics, model 352C67) are used. A tri-shear accelerometer consists of seismic masses, base, piezoelectric

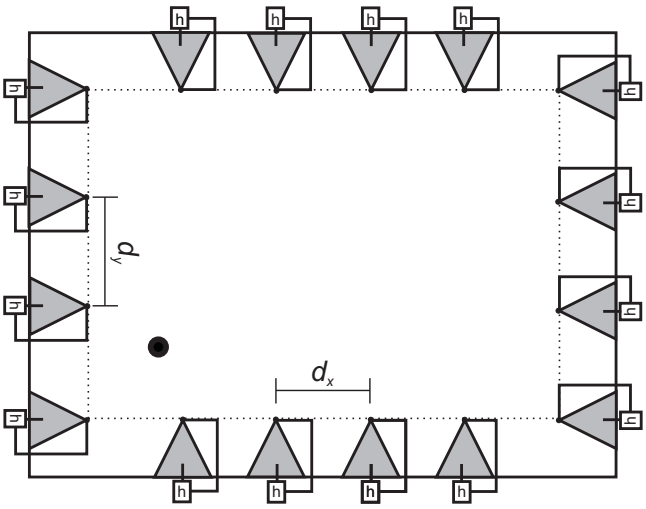

Figure 5.2: A rectangular panel with 16 decentralized velocity feedback control units using triangular piezoceramic patch actuators. The position of the primary force excitation is shown as a solid circle. A virtual active boundary wedge is depicted by dotted line.

material, preloaded ring, and a center post. As shown in Fig. 5.3, shear mode accelerometers sandwich the sensing material between a center post and the seismic mass. A compression ring or stud applies a preload force to create a rigid linear structure. Under acceleration, the mass applies a shear stress to the sensing material. The result is an electrical signal that is collected by the electrodes and transmitted by lightweight lead wires to the built in signal conditioning circuitry. The shear operation and small size gives a high frequency response while minimizing mass loading effects on the test structure. Thus, the upper frequency limit of the sensor used in this study is higher than 35 kHz, while the mass of the sensor is less than 6 g.

When a shear accelerometer is considered, the frequency response of the sensor is determined by the resonant frequency, which can be modeled as a simple single-degree-of-freedom system, as shown in Figure 5.4, where k_a and c_a respectively represent the stiffness and damping coefficients of the piezoelectric element, and w_s and w_c are the displacement of the seismic mass and the accelerometer base, which is firmly attached to the panel. According to Newtons second low, the equation of

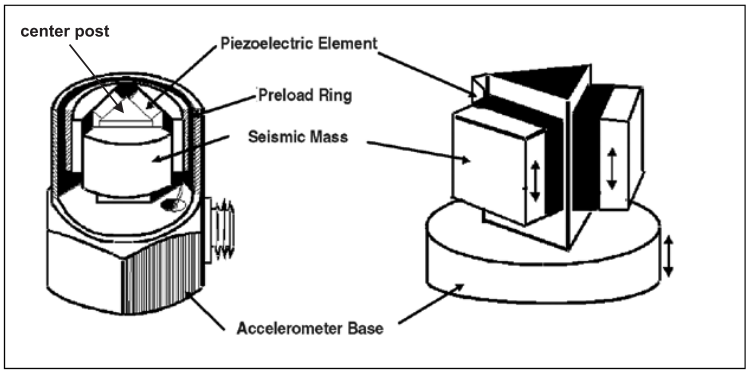

Figure 5.3: Internal structure of tri-shear piezoelectric sensing accelerometer 352C67

motion for this single degree of freedom system is given by the following expression:

$$m_a \ddot{w}_a = c_a(\dot{w}_c - \dot{w}_a) + k_a(w_c - w_s). \tag{5.3}$$

A voltage signal v_a generated by the sensor is given as the product the detection constant of the piezoelectric elastic element c_σ and the relative displacement between the seismic mass and the sensor base, thus:

$$v_a = c_\sigma(w_c - w_a). \tag{5.4}$$

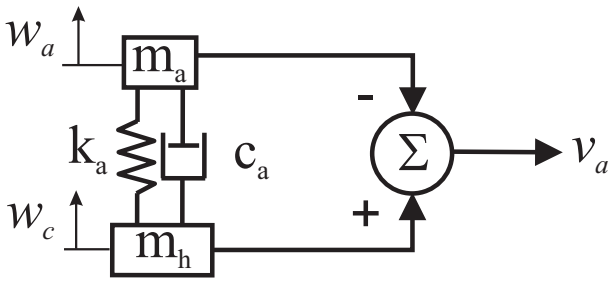

Figure 5.4: Schematic representation of the piezoelectric accelerometer transducer, which is modeled as a single degree-of-freedom system

Assuming harmonic excitation, the frequency response function $G_a(j\omega)$ between the sensor output voltage $v_a(j\omega)$ and the acceleration of the base mass $\ddot{w}_c(j\omega)$ is given by using to Eq.(5.4) and Eq.(5.3), as:

$$G_a(j\omega) = \frac{v_a}{\ddot{w}_c} = c_\sigma \frac{1}{\omega_a^2 - \omega^2 + 2j\zeta_a\omega\omega_a}, \tag{5.5}$$

where ω_a and ζ_a respectively denote the natural frequency and viscous damping factor of the piezoelectric elements in the sensor, given as:

$$\omega_a = \sqrt{\frac{k_a}{m_a}} \tag{5.6a}$$

$$\zeta_a = \frac{c_a}{2\sqrt{k_a m_a}}. \tag{5.6b}$$

Equation (5.5) indicates that below the resonance frequency of the accelerometer, the output voltage of the accelerometer sensor v_a is approximated as the opposite of the its base acceleration:

$$v_a \cong -\frac{c_\sigma}{\omega_a^2}\ddot{w}_c. \tag{5.7}$$

Therefore, as shown in Figure 5.5, at low frequency, the amplitude of $G_a(j\omega)$ is flat, and the phase angle remains 180 degree. Around 35 kHz, the Bode plot of the $G_a(j\omega)$ is characterized by a sharp peak with 180 degree phase shift, which is caused by the resonance of the accelerometer sensor. More details regarding the sensor dynamics can be found in reference [68].

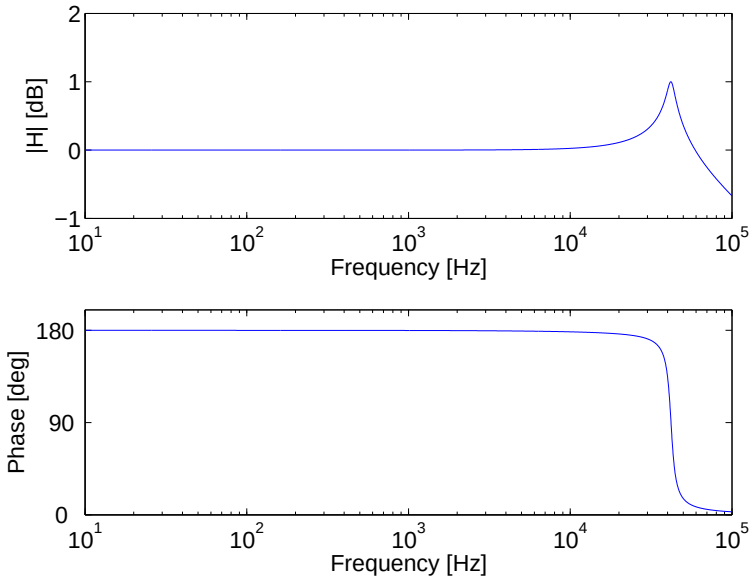

Figure 5.5: Frequency response function of the accelerometer

Figure 5.6 shows two open loop FRFs measured on the panel with 16 triangular actuators between one of closely located sensor-actuator pairs by using an accelerometer sensor (blue faint line) and by a laser vibrometer (black solid line). At low frequency below about 3 kHz, two open loop FRFs show very similar spectra. Above 3 kHz,

the open loop FRF measured by the accelerometer is characterized by a constant amplitude roll off and additional phase lag, which are introduced due to its mass loading effects of the accelerometer and its low signal strength beyond the resonant frequency. These effects of the sensor are more clearly visualized in two Nyquist plots in Fig. 5.6. The blue solid lines indicates that the size of the low frequencies circles in the right hand side quadrants are left unaltered, while the black dotted line shows that at higher frequency, where the locus occupies the left hand side quadrants, the size of the locus of the FRF measured by the accelerometer is squeezed towards the imaginary axis.

5.1.3 Decentralized multi-channel analogue controller

In order to implement the decentralized velocity feedback control, an analogue controller has been built for each control unit. The front view of the resulting 16-channel controlling device is shown in Fig. 5.7, and the corresponding internal analogue circuit for each channel is illustrated in Fig. 5.8. As shown in the circuit diagram, the analogue controller consists of 8 circuits: (1) a high pass filter, (2) an integrator, (3) a phase lag-compensator, (4) a non-inverting amplifier, (5) a voltage divider, (6) a voltage follower, (7) an inverter, and (8) a power amplifier.

To implement the active velocity feedback control loops, the error sensor output signals are connected to the input ports of the analogue controllers and the output signals are fed to the corresponding piezoceramic transducers. The low frequency noise of the input signal is first filtered by high pass filters with a cutoff frequency of 3.7 Hz. Then, the signals are integrated by integrators with an identical amplification gain, which provide the velocity signals. The integrated signals are then filtered by phase lag compensators, with a lower cutoff frequency of 550 Hz and an upper cut off frequency of 10.6 kHz, in order to improve the stability of the system, which is limited due to the non collocated property of the point sensor and strain actuator pairs. The resulting filtered signals at this point in the circuit can be measured via the BNC output port of each controller, marked as 'Velocity'. Then, the signals are applied to voltage dividers with independent gains for each channel, which can be tuned by the front dial on each controller unit, as shown in Fig. 5.7. Voltage followers are introduced after the resistor dividers as impedance adaptation stages

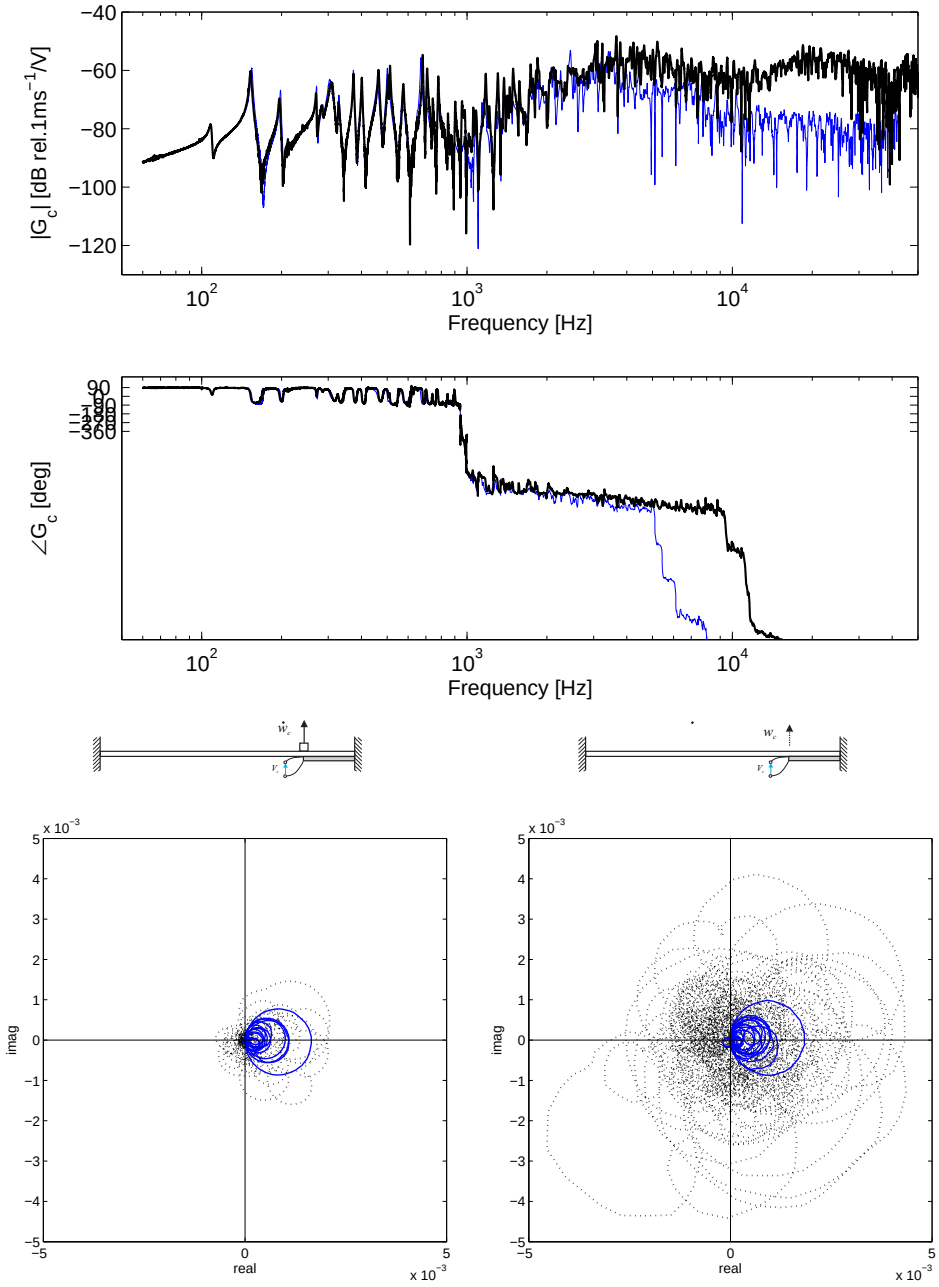

Figure 5.6: Top: Bode plot of the open loop FRF measured by the accelerometer sensor (blue faint line) and by the laser vibrometer (black solid line). Bottom: Nyquist plots of the open loop FRF measured by the accelerometer sensor (left) and by the laser vibrometer (right) between 50 Hz and 1 kHz (blue solid line), and between 1 and 80 kHz (black faint lline).

between the previous circuitry and the inverting amplifiers, respectively the power amplifiers. Depending on the position of the switch SW1, inverted or non inverted output signals may be generated as input for the power amplifiers. Inverted signals are necessary in order to implement negative feedback. The signals are finally amplified by power amplifiers with an identical amplification gain in order to drive the piezoceramic actuators. The output signals are accessible via the red port marked as 'Output'. More details regarding the controller can be found in reference [42].

Figure 5.7: Front view of the decentralized analogue feedback controller

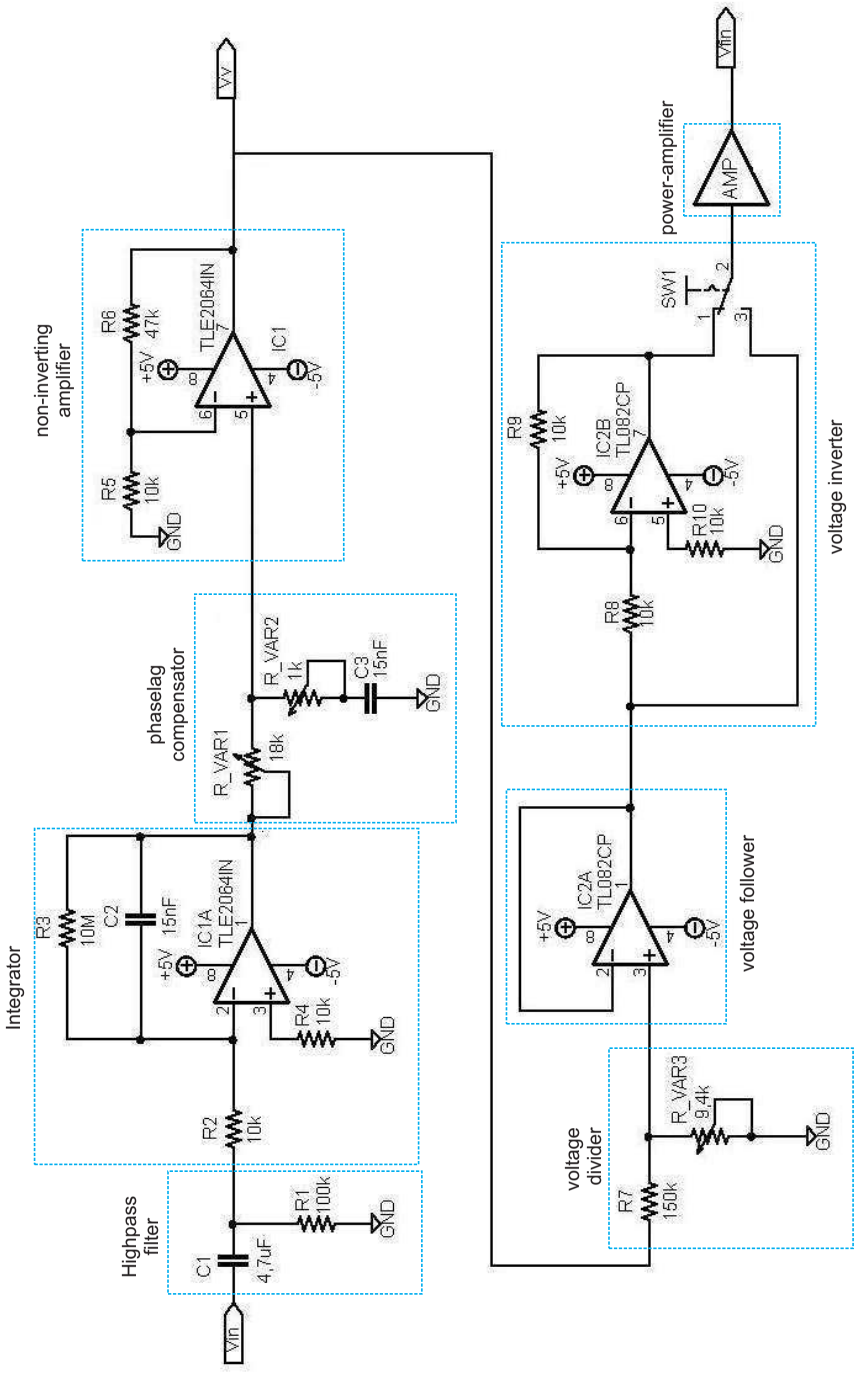

Figure 5.8: Circuit diagram of each 16 channel decentralized feedback control system

5.2 Stability

As shown in Fig. 5.9, the decentralized Multiple-Input-Multiple-Output (MIMO) control system can be formulated in terms of a classic disturbance rejection block diagram. Provided that the control system is stable, the vector of the spectra for the residual signals at the sensors output $\mathbf{y}(j\omega) = [y_1\, y_2 \ldots y_{16}]^T$ is given by:

$$\mathbf{y}(j\omega) = [\mathbf{I} + \mathbf{G}(j\omega)\mathbf{H}(j\omega)]^{-1}\, \mathbf{G_p}(j\omega) f_p(j\omega), \tag{5.8}$$

where $\mathbf{I}$ is the 16 by 16 identity matrix, and $\mathbf{G}(j\omega)$ is a fully populated matrix with the frequency response functions between the sensor signals $\mathbf{y}(j\omega)|_{fp=0}$ and the actuator control signals $\mathbf{u}(j\omega) = [u_1\, u_2 \ldots u_{16}]^T$, while no primary excitation is applied to the panel. $\mathbf{G_p}(j\omega)$ is a column vector of the frequency response functions between the sensor outputs $\mathbf{y}(j\omega)|_{H=0}$ and the primary disturbance input signal $f_p(j\omega)$, while no control excitation is applied to the panel. The disturbance input signal $f_p(j\omega)$ is either the driving voltage of the loudspeaker V_{in} or the applied force to the panel generated by the shaker F_{in}.

For decentralized control, the gain matrix, $\mathbf{H}(j\omega)$, is a diagonal matrix of fixed control gains for each control unit, multiplied by frequency response function of the analogue controller $H_T(j\omega)$. In this study the decentralized controller has the same constant gain h_0 over the frequency in each control loop. Thus, the feedback frequency response matrix $\mathbf{H}(j\omega)$ is given by:

$$\mathbf{H}(j\omega) = h_0 H_T(j\omega)\mathbf{I}. \tag{5.9}$$

The identical control gain h_0 is chosen to be the highest possible value for which the system remains stable.

It is well known that velocity feedback control using collocated and dual sensor-actuator pairs is unconditionally stable, even for multiple channels [17, 27]. In this case, the fixed feedback gains can, in principle, be increased without limit, so that the signals from the error sensors can be driven to zero. However, as discussed in the previous chapter, the triangular piezoceramic actuator and the velocity sensor pairs considered in this study strictly are neither dual nor collocated, such that the control

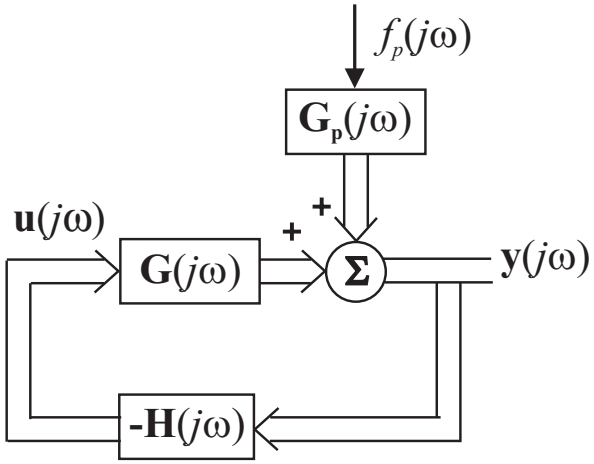

Figure 5.9: Disturbance rejection block diagram of the MIMO velocity feedback control system

system is only conditionally stable. Therefore the control performance is limited by the maximum stable control gain that can be implemented in the feedback loops.

The stability of MIMO decentralized control system can be assessed using the generalized Nyquist criteria [69]. Assuming that the open loop system is stable, this criteria states that the closed loop system depicted in Fig. 5.9 is stable if and only if the locus of the determinant of the measured return matrix, $\det[\mathbf{I}+\mathbf{G}(j\omega)\mathbf{H}(j\omega)]$, does not encircle the origin, nor passes though the origin, as the angular frequency ω varies between $-\infty$ and $+\infty$.

In order to assess the stability, the 16 by 16 elements of the open loop FRF matrix $\mathbf{G}(j\omega)\mathbf{H}(j\omega)$ has been experimentally obtained between 25 Hz and 42 kHz. This frequency range is sufficient to evaluate the stability, because the upper limit of the usable frequency range for a standard sensor is much lower than 42 kHz, and beyond the upper limit, the signal strength significantly decreases. Therefore, the higher frequency response of the system does not affect the stability property.

Figure 5.10 shows the Nyquist plots corresponding to the diagonal elements of the measured open loop FRF matrix $\mathbf{G}(j\omega)\mathbf{H}(j\omega)$, which would be important if any one of the feedback loops were closed individually. The locus between 25 Hz and 700 Hz is plotted by blue solid line, and the locus for frequencies above 700 Hz is plotted by black dotted line. The blue solid line in Nyquist plots is characterized by a series of circles, which are determined by the resonant response of the plate.

The circles start close to the origin, but are aligned along the positive real axis, due to the extra phase lag introduced by the phase-lag compensator in the analogue controller. The black dotted line highlights that the locus of the open loop FRF enters real negative quadrants at around 700 Hz due to not-collocation and non-dual properties, as discussed in the previous chapter. In general, the size of the low frequency resonant circles in the right hand side quadrants of the Nyquist plots is much bigger than that of the FRF at the cross over point on the real negative axis of the Nyquist plots. As discussed in Section 5.2, this is mainly due to the mass loading effects of the accelerometer sensor, and its upper limit of the usable frequency range. Although these plot can not be used to asses the stability of the 16 decentralized feedback loops, these plots clearly indicates that the non collocation and non duality properties of each sensor- actuator pair is likely to be characterized by instability problems at higher frequencies above 1 kHz.

Figure 5.11 shows the locus of $\det[\mathbf{I} + \mathbf{G}(j\omega)\mathbf{H}(j\omega)]$ between 25 Hz and 42 kHz. The locus between 25 Hz and 700 Hz is plotted by blue solid line, and the locus for frequencies above 700 Hz is plotted by black dotted line. The locus is characterized by a series of large circles at low frequency, which are determined by the resonant response of the plate. At low frequencies, the circles start close to the point $(1, 0j)$. As the frequency rises, the circles tend to drift away from $(1, 0j)$, and around 700 Hz the locus moves into the left-hand side of the vertical axis passing through the point $(1, 0j)$ due to propagation delays between the sensor and the actuator pairs. This plot indicates that the decentralized feedback control system under study is only conditionally stable, and thus generates positive feedback at high frequencies.

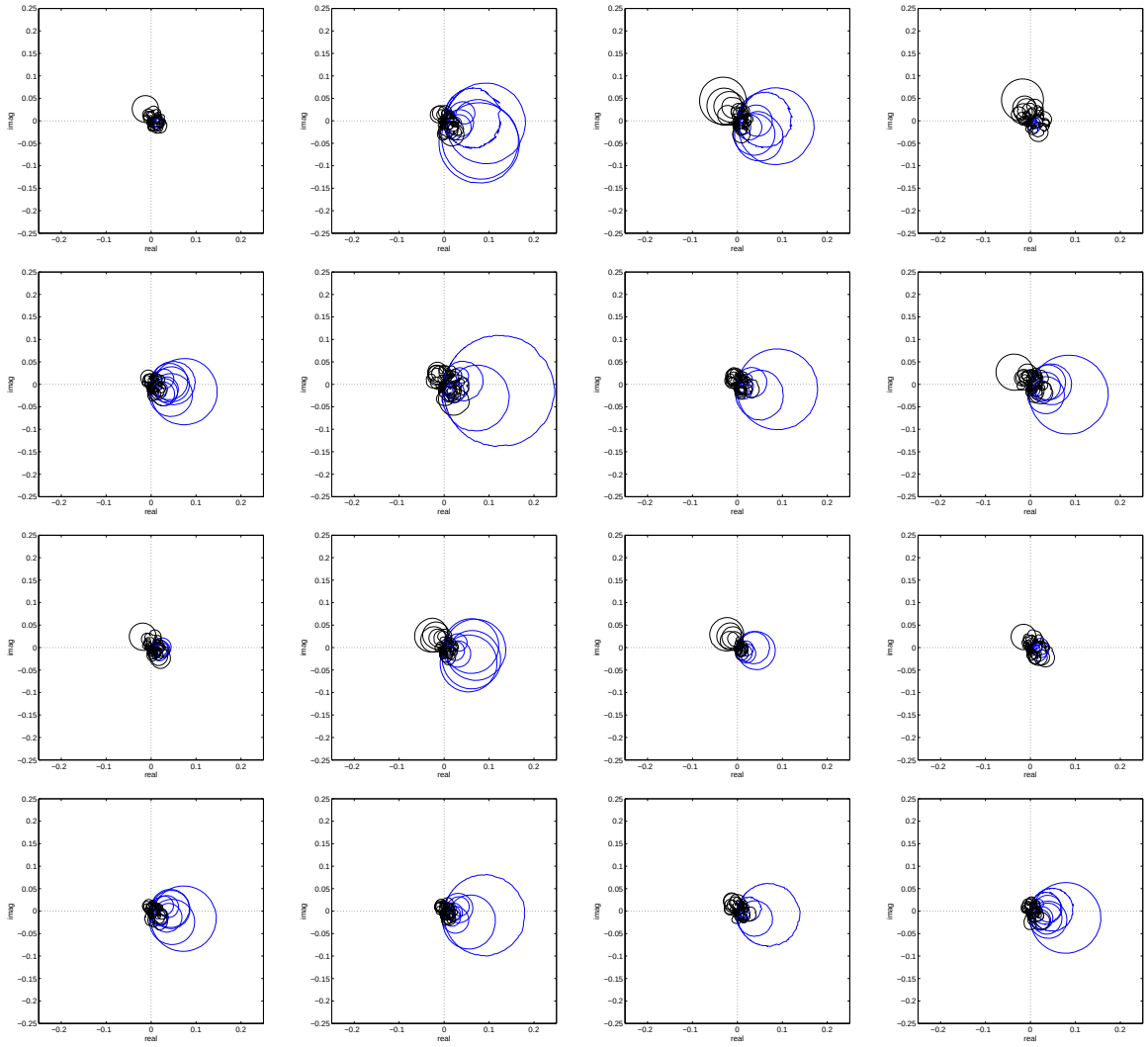

Figure 5.10: Nyquist plots of the diagonal elements of the open loop FRF matrix $\mathbf{G}(j\omega)\mathbf{H}(j\omega)$ measured on the panel with 16 triangular actuators of base length 40 mm and height 40 mm, between 25 Hz and 700 Hz (blue solid line), between 700 Hz and 42 kHz (black dotted line)

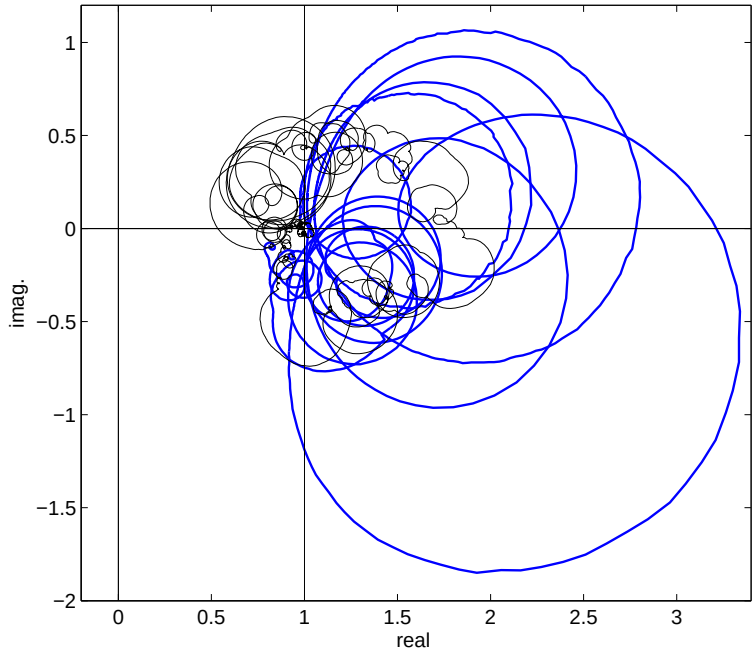

Figure 5.11: Locus of the determinant of the return matrix , $\det[\mathbf{I} + \mathbf{G}(j\omega)\mathbf{H}(j\omega)]$, measured on the panel with 16 triangular actuators of base length 40 mm and height 40 mm, between 25 Hz and 700 Hz (blue solid line), and between 700 Hz and 42 kHz (black dotted line)

5.3 Vibration control performance

The following two sections present the experimental results regarding the control performance of the new smart panel. In section 5.3, the control performance is discussed with reference to the vibration level of the panel in the frequency range 0 - 1 kHz. Section 5.4 presents the reduction in terms of the total radiated sound power in the same frequency range. For both cases, the control performance is discussed in two stages: the passive effect produced by the sensor-actuator transducers, and the active control effect of the 16 decentralized control loops. The passive control performance is assessed by comparing the responses and sound radiation produced by the panel without transducers (blue faint lines), and the panel with transducers but no feedback control (black solid lines). The active control effect is assessed by comparing the responses and sound radiation produced by the panel with transducers but no feedback control (black solid lines) and the panel with transducers and decentralized velocity feedback control (red dashed lines).

5.3.1 Passive control effects on structural vibration

The spectra of the vibration level has been derived by remotely measuring, with a scanning laser vibrometer, the out-of-plane velocity of the panel at the centers of a grid of 17 by 11 elements, hence a total of $N = 187$ points evenly distributed over the panel surface, as shown in Fig. 5.12. The averaged spectra K_E was derived by mean-square basis over the measurement surface, as:

$$K_E = \frac{1}{N} \sum_{i=1}^{N} |G_i|^2, \tag{5.10}$$

where G_i denotes the i^{th} frequency response function between the velocity of the panel at i^{th} measurement point and the primary excitation input.

Figure 5.13 shows the measured narrow band spatially averaged spectra of the out-of-plane vibration levels of the panel per unit structural primary excitation input F_{in} (top plot), and per unit acoustic primary excitation input V_{in} (bottom plot), respectively. The thick solid line represents the measured response of the plane plate without the actuators attached, while the faint line represents the response of the

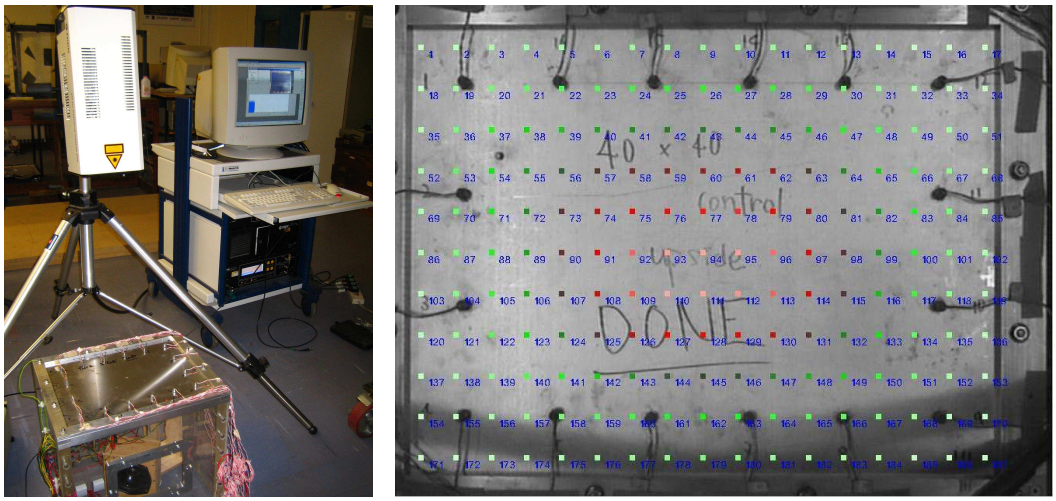

Figure 5.12: Picture of the laser-vibrometer (left), and the panel surface with the grid of the measurements points (187) scanned by the laser vibrometer (right)

panel equipped with 16 actuator and sensor pairs attached but no feedback control.

Comparing the two plots in Fig. 5.13, it can be observed that, when the panel is excited by a point force generated by a shaker, the response of the panel is characterized by a rather large number of resonant peaks. In contrast, when the panel is excited by acoustic field, the spectra show fewer sharp resonant peaks. When the panel is excited by acoustic field, the response of the panel is characterized mainly by the 1st, 3rd and 5th resonance frequencies, which correspond to the odd modes, (1,1), (3,1), and (1,3) of the panel, respectively. The peaks of the 2nd and 4th resonances, which are controlled by (2,1) and (1,2) vibration modes, are relatively low. This is due to the fact that the shaker excites nearly all structural modes of the panel, while the acoustic field generated by the loudspeaker efficiently excites only specific structural modes of the panel that are well coupled to the acoustic modes of the cavity underneath the panel [5].

The thick solid line and the faint line in Fig. 5.13 also highlight the fact that, when the 16 actuator and sensor pairs are bonded to the panel, the resonant peaks are shifted towards higher frequencies, and the amplitudes of the peaks are reduced by approximately 3 dB with acoustic excitation, and by a maximum of 10 dB with structural excitation. A significant increase in the natural frequencies is generated by the piezoceramic actuators, which generate a local stiffness effect on the panel especially at low frequencies, as discussed in chapter 2. The response at resonant

frequencies is reduced, because the bonding layer between the actuator and the panel adds some damping to the panel. The sensor-actuator control units also produce mass loading effects on the panel. As discussed in Section 5.1, however, these effects are most important at high frequencies above the frequency range considered in this study.

5.3.2 Active control effects on structural vibration

Figure 5.14 shows the 16 frequency response functions between the integrated signal of the accelerometer sensors and the structural primary excitation input F_{in}. The black solid line represents the measured response of the plate without control, while the red dotted line represents the response with decentralized velocity feedback control using the identical maximum control gain that guarantees stability. These plots indicate that the response of the panel at low frequency resonances is significantly reduced, by up to 20 dB at error sensor positions, because the velocity feedback control adds an active damping term on the plate. However, at higher frequencies beyond 700 Hz, the response of the panel is increased due to positive feedback effects, as suggested by the stability analysis presented in Section 5.2.

The two plots in Fig. 5.15 show the measured narrow band spatially averaged spectra of the out-of-plane vibration levels of the panel per unit structural primary excitation input F_{in} (top), and per unit acoustic primary excitation input V_{in} (bottom), respectively. The black solid line represents the responses and sound radiation produced by the panel with transducers but no feedback control, while the red dotted line is response of the panel with transducers and decentralized velocity feedback control.

This figure highlights that the active control system smoothes the resonant peaks between 100 Hz and 700 Hz by approximately 6 to 18 dB, except for the resonance peaks at around 390, 445 and 500 Hz. As listed in Table 5.2, these non-controlled peaks are dominated by the resonances of the cavity beneath the panel. The natural frequency of the rigid walled cavity underneath the panel is given by the following formula [71]:

$$\omega_{lmn} = \frac{c}{2}\sqrt{\left(\frac{n_x}{L_x}\right)^2 + \left(\frac{n_y}{L_y}\right)^2 + \left(\frac{n_y}{L_y}\right)^2}, \tag{5.11}$$

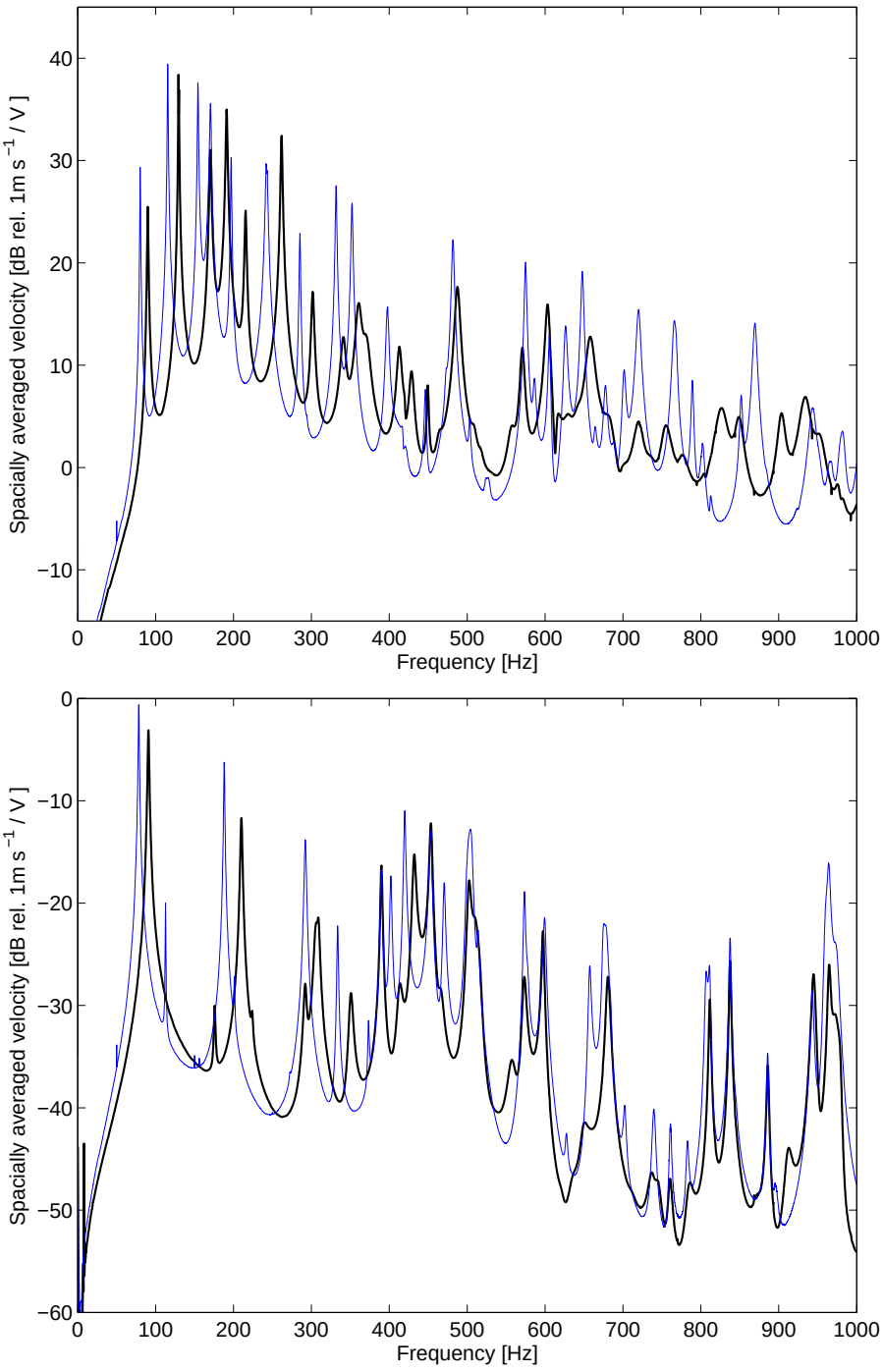

Figure 5.13: Narrow band spectra of the spatially averaged velocity of the panel, measured between 0 and 1 kHz, per unit force generated by the shaker (top) and per unit voltage driving the loudspeaker (bottom): without transducers (blue fain line), and with transducers but no feedback control (black solid line)

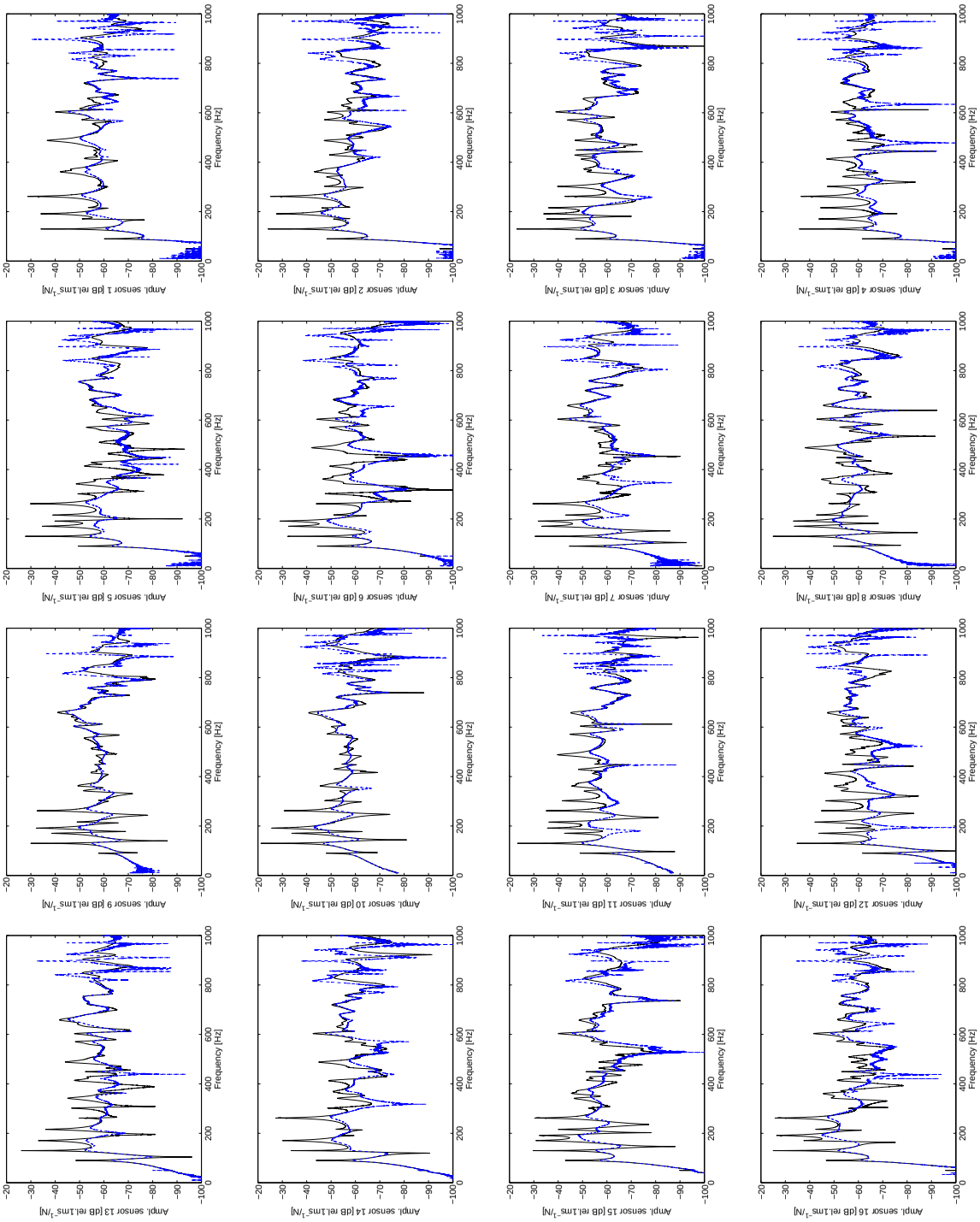

Figure 5.14: Narrow band velocity spectra of the panel at 16 control points measured by accelerometer error sensors between 0 and 1 kHz, per unit force generated by the shaker; without feedback control (black solid line), and with feedback control (blue dashed line)

where c denotes the speed of sound, and n_x, n_y, and n_z denote the mode number in $x-$, $y-$, and $z-$direction, respectively. L_x, L_y, and L_z denote the dimension of the internal cavity of the Perspex box in $x-$, $y-$, and $z-$direction, which are 414 mm, 314 mm, and 400 mm, respectively.

Using above equation, the first three natural frequency of the Perspex box are predicted as 414.3 Hz, 476.4 Hz, and 546.2 Hz, which correspond to the (1,0,0), (0,0,1), and (0,1,0) acoustic modes, respectively. The measured cavity resonant frequencies are slightly lower than the predicted ones, because the cavity inside the Perspex box does not have perfectly rigid walls, especially due to the smart panel on the top side. This cavity-plate coupling characteristic [72] is particularly strong with this test rig set-up. Therefore, it is expected that in applications, where the panel has no backing cavity, and is excited by an acoustic disturbance that comes from a free field or a very large enclosure with diffuse acoustic fields, the control performances would be more significant than those shown in Fig. 5.15. At frequencies higher than 700 Hz, the response of the panel slightly increases when control loops are closed, because of the positive feedback control effect mentioned in section 4.2.

Table 5.2: Measured resonant frequencies of the plane aluminium panel mounted on the Perspex box, and excited by an acoustic field

Frequency [Hz]	Domain
78.44	Structure (1,1)
112.8	Structure (2,1)
156.1	Structure (1,2)
188.1	Structure (3,1)
201.3	Structure (2,2)
249.8	Structure (3,2)
274.2	Structure (4,1)
292.2	Structure (1,3)
333.8	Structure (2,3)
373.3	Structure (4,2)
389.7	Acoustics (1,0,0)
402.0	Structure (3,3)
419.8	Structure (5,1)
453.0	Acoustics (0,0,1)
470.5	Structure (1,4)
504.4	Structure (5,2)
514.2	Acoustics (0,1,0)
573.4	Structure (6,1)

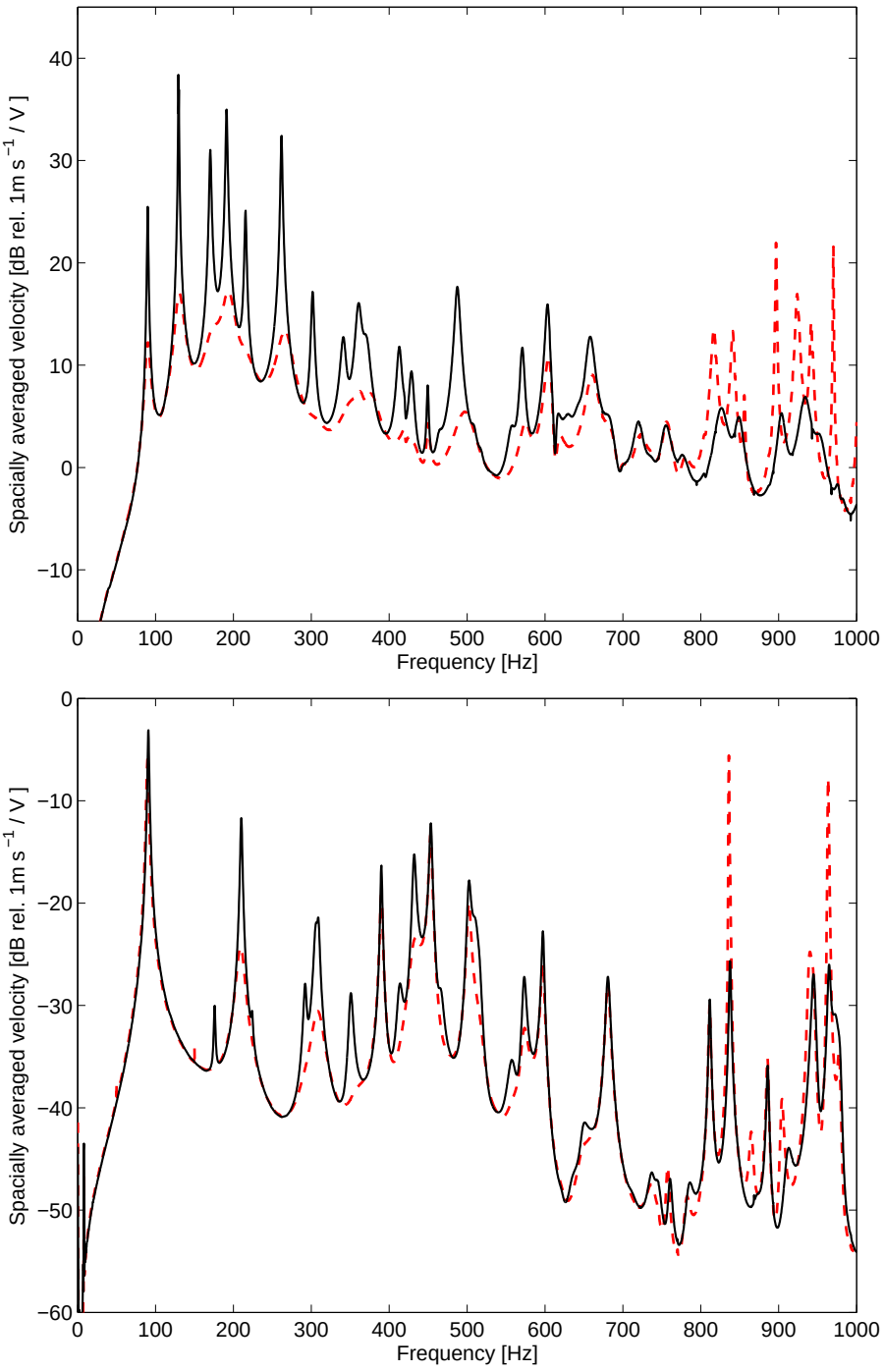

Figure 5.15: Narrow band spectra of the spatially averaged velocity of the panel, measured between 0 and 1 kHz, per unit force generated by the shaker (top) and per unit voltage driving the loudspeaker (bottom): without feedback control (black solid line), and with feedback control (red dashed line)

When active control is implemented, the spectrum of the vibration level has fewer peaks, as active damping can effectively reduce the response at resonances of the panel. This is confirmed by comparing the vibratory field of the panel at resonant frequency with and without control. Figure 5.16 shows the vibratory field of the smart panel excited by the acoustic field produced by the loudspeaker in the cavity at 258 Hz, which is the resonant frequency corresponding to the (3,1) natural mode of the panel. The pictures on the left hand side show the vibratory fields of the panel without control at phases $\phi = 0°$ (top), $\phi = 120°$ (middle) and $\phi = 240°$ (bottom). The right hand side pictures show the vibratory fields with decentralized MIMO velocity feedback control. The left hand side pictures indicate that the response of the plate at 258 Hz is dominated by the (3,1) natural mode of the panel. In contrast, the right hand side pictures highlight that when active damping is applied to the panel, the response is not characterized by the (3,1) natural mode shape. The (3,1) natural mode shape is still present, but with reduced amplitude, and thus the residual effects from the neighboring modes are observed especially in the middle picture in the right hand column of Fig. 5.16.

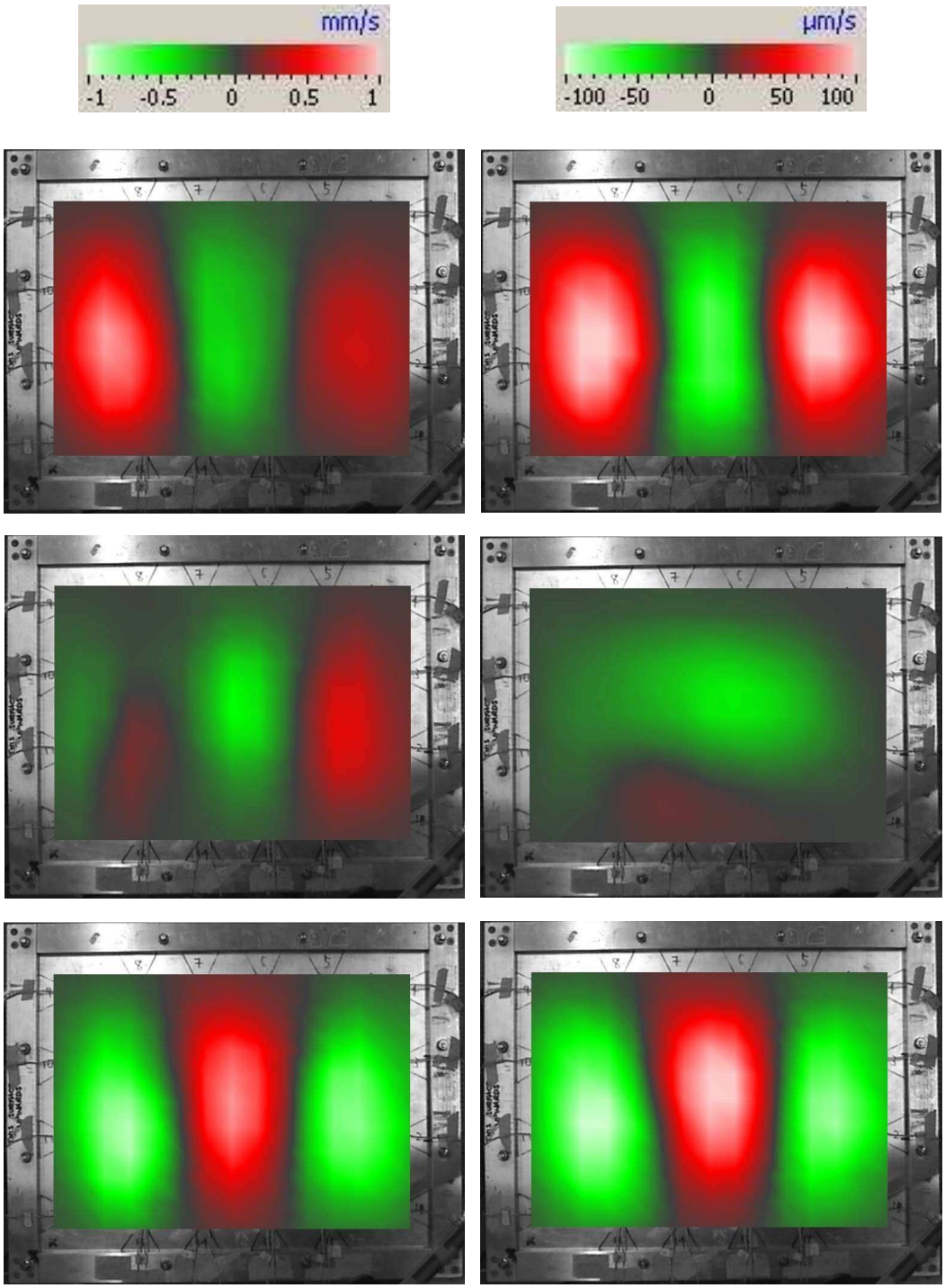

Figure 5.16: Vibratory fields of the panel excited by the loudspeaker at the 258 Hz resonance frequency, where the response is controlled by (3,1) natural mode of the smart panel; without the control (left column) and with control(right column) at phases $\phi = 0$ (top), $\phi = 120$ (middle) and $\phi = 240$ (bottom)

5.4 Sound radiation control performance

The sound radiation from the rectangular panel mounted on the rigid box were measured in a large anechoic chamber by using free-field microphones produced by Bruel & Kjaer (Type 4165). The chamber has a dimension of 9.15 m × 9.15 m × 7.32 m, and its walls, ceiling and floor are covered with 910 mm long wedge. Thus, the cut off frequency of the chamber is given by approximately 80 Hz.

The measurements are performed according to ISO 3744 [72], which specifies requirements for measurement surfaces and locations of microphones, procedures for measuring the sound pressure levels and methods to compute the sound power level from the surface averaged sound pressure level. This standard is strictly for hemi-anechoic environment measurement, and thus the floor of the anechoic chamber was covered with solid wooden baffle panels, as shown in the left hand side picture of Fig. 5.17. According to ISO 3744, acoustic measurements are obtained by using a parallelepiped array of nine microphones, as illustrated in the right hand side picture of Fig. 5.17. All geometric details of the microphone positions are given in Tables 5.3 and 5.4.

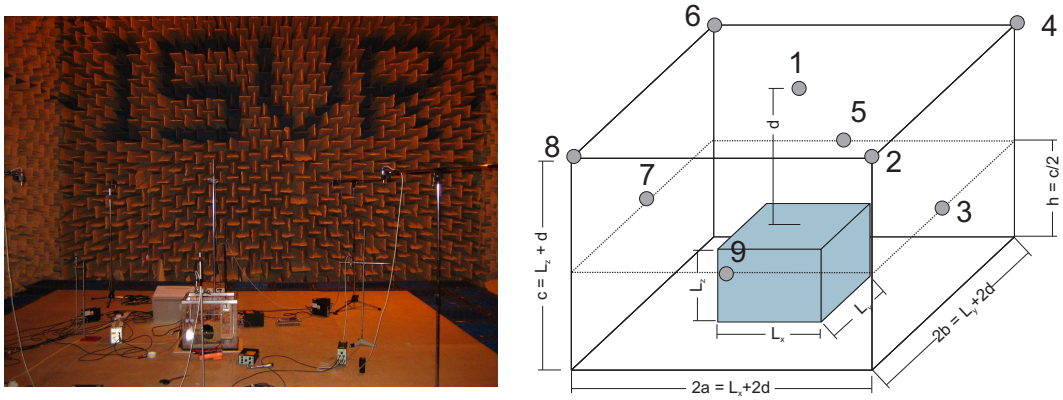

Figure 5.17: Picture of the chamber (left), and microphone positions in the anechoic chamber for a rectangular measurement surface according to ISO CD 3744 (right).

A sound pressure level L_p is derived using the measured pressure by a microphone p as:

$$L_p = 10 \log_{10} \frac{p^2}{p_{ref}^2} = 20 \log_{10} \frac{p}{p_{ref}}, \tag{5.12}$$

where p_{ref} is the reference value, i.e. $p_{ref} = 2 \times 10^{-5}$ [N/m^2] = 20 [μPa]. Thus, the average sound pressure level over the measurements surface, $\overline{L}_{pm}$, can be calculated

using sound pressure levels measured by nice microphones as:

$$\overline{L}_{pm} = 10 \log_{10} \left(\frac{1}{n_p} \sum_{i=1}^{n_p} 10^{\frac{L_{pi}}{10}} \right), \tag{5.13}$$

where n_p denotes the number of microphones, $n_p = 9$. Finally, the sound power level L_W emitted by the source is determined by using the following formula:

$$L_W = \overline{L}_{pm} + 10 \log_{10} S, \tag{5.14}$$

where S is the surface area of the measuring surface; i.e. $S = 8(ab+bc+ca) = 19.37$ [m^2]. It is recommended to include a correction factor Δ in Eq. (5.14) to take into account the absorption characteristics of the room and any nearby reflecting surfaces. However, in this study this correction factor is ignored.

Table 5.3: Coordinate of microphone measurement points of the parallelepipedic arrangement used in the anechoic chamber experiments

No.	x	y	z
1	0	0	c
2	a	-b	c
3	a	0	h
4	a	b	c
5	0	b	h
6	-a	b	c
7	-a	0	h
8	-a	-b	c
9	0	-b	h

Table 5.4: Values of the coordinate system of the parallelepipedic arrangement used in the anechoic chamber experiments

Parameter	Value [m]
L_x	0.475
L_x	0.375
L_x	0.428
a	1.238
b	1.188
c	1.428
d	1.0
h	0.714

5.4.1 Total radiated sound power - narrow band analysis

Figure 5.18 shows the measured narrow band total radiated sound power per unit structural primary excitation input F_{in} (top), and per unit acoustic primary excitation input V_{in} (bottom), respectively. The thick solid line represents the measured response of the plane plate without any control unit mounted, while the faint line represents the response of the panel equipped with 16 control units, but without active control. This figure shows as well that, when the 16 passive transducer pairs are attached to the panel, the resonances are shifted up in frequency, and the amplitudes of the spectra are reduced. Figure 5.18 also highlights that, the sound power responses are characterized by a smaller number of resonances compared with the spectra for the structural response presented in the previous section in Fig. 5.13. This is due to the fact that the even modes of the panel do not radiate sound efficiently [72].

Figure 5.19 shows the measured narrow band total radiated sound power per unit structural primary excitation input F_{in} (top), and per unit acoustic primary excitation input V_{in} (bottom), respectively. The thick solid line represents the responses and sound radiation produced by the panel with transducers but no feedback control, and the dotted line is the response of the panel with transducers and decentralized velocity feedback control. Figure 5.19 confirms the conclusion derived in the previous section regarding the structural reduction obtained by implementing decentralized feedback control; the sound pressure level transmitted via the panel at resonant frequencies can be significantly reduced up to around 700 Hz at all microphone locations. Higher than 700 Hz, the sound pressure level increase due to positive feedback effects.

Figure 5.19 indicates that the active control system reduces the resonant peaks between 100 Hz and 500 Hz by a maximum 15 dB, for both acoustic and structural excitations. At higher resonance frequencies, between 500 Hz and 700 Hz, although the control system suppresses the vibration of the structure, the sound power reduction is relatively poor. At frequencies higher than around 700 Hz, no active control effect is observed. In general, the obtained reduction in sound power is lower than that in structural vibration, since the radiation efficiency of the panel is not considered [5, 73].

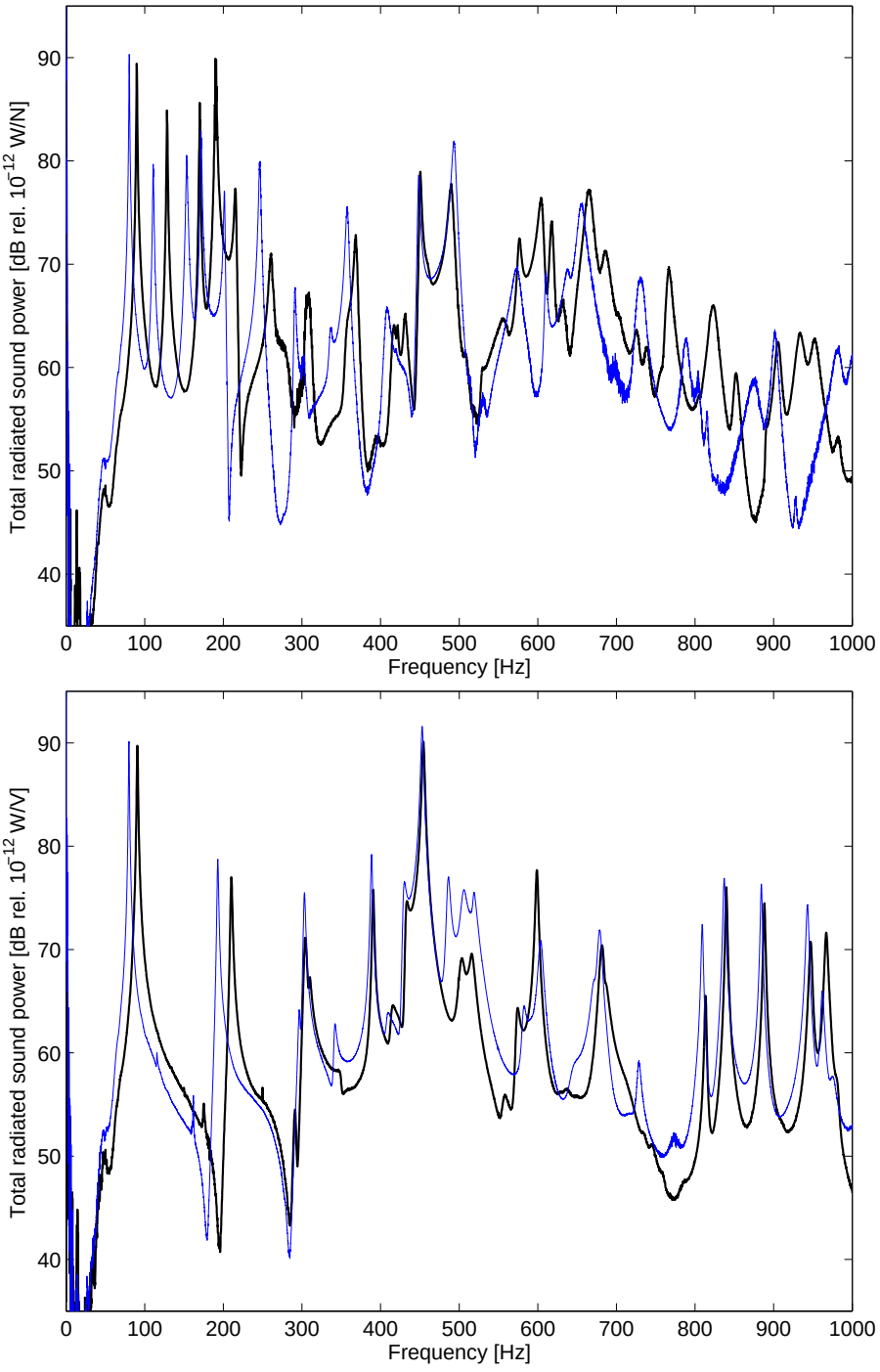

Figure 5.18: Narrow band spectra of the total radiated sound power, measured between 0 and 1 kHz, per unit force generated by the shaker (top) and per unit voltage driving the loudspeaker (bottom): without transducers (blue faint line), and with transducers but no feedback control (black solid line)

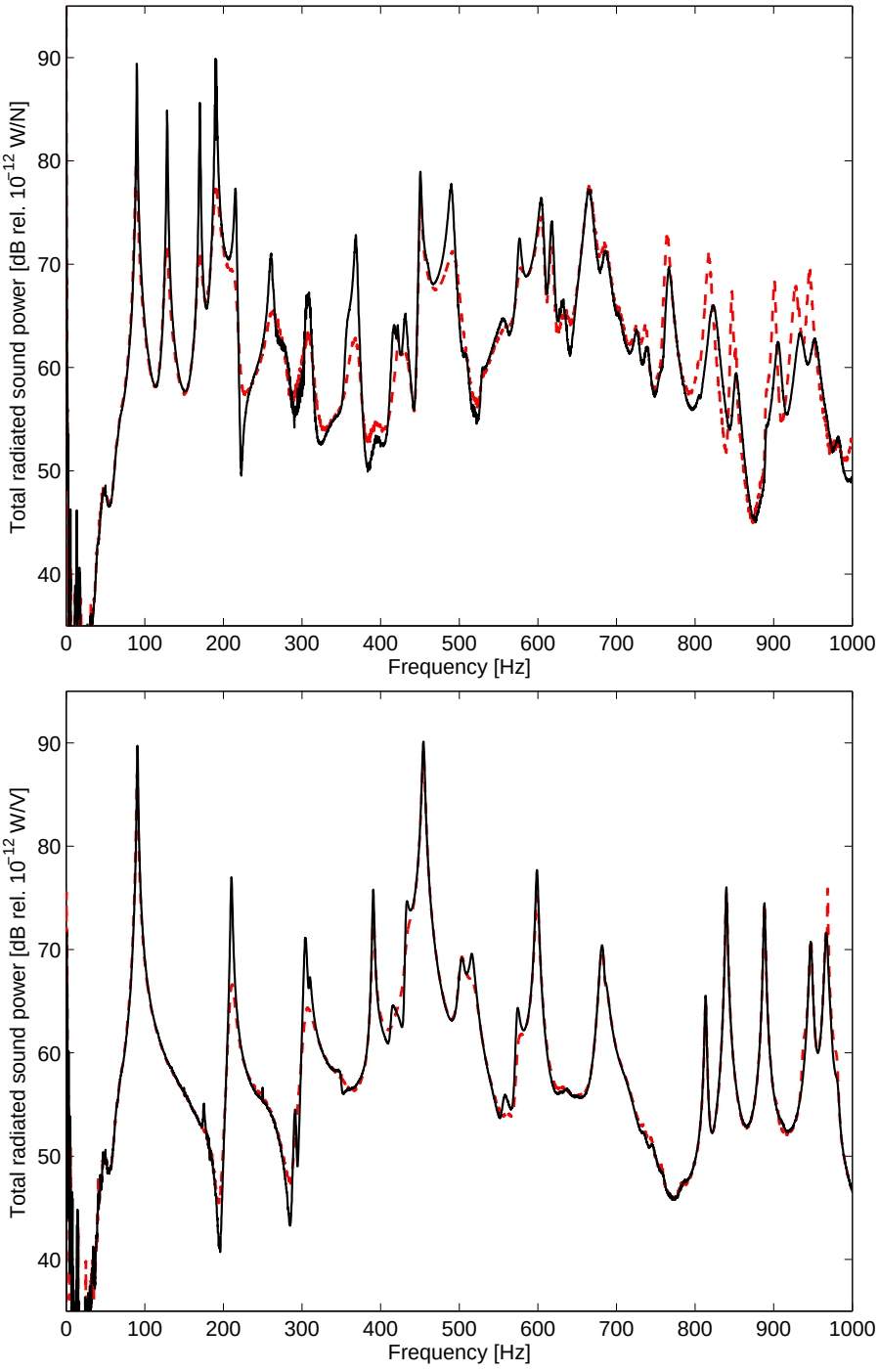

Figure 5.19: Narrow band spectra of the total radiated sound power, measured between 0 and 1 kHz per unit force generated by the shaker (top) and per unit voltage driving the loudspeaker (bottom): without feedback control (black solid line), and with feedback control (red dashed line)

5.4.2 Total radiated sound power - one-third octave band analysis

The previous subsection presented a narrow band frequency analysis, which is useful in understanding the control performance. When acoustic noise is measured, however, it is customary to analyze the continuous spectrum sound in constant percentage bandwidths, because the hearing system is responsive to frequency bands rather than individual frequencies. Therefore, in this section, one-third octave spectra [71] is used to evaluate the control performance in terms of the total radiated sound power per unit structural primary excitation input F_{in} (top), and per unit acoustic primary excitation input V_{in} (bottom), respectively. The primary excitation sources are driven by a pink noise signal between 0 to 1 kHz in order to give equal energy in all octave bands.

The top plots in Fig. 5.20 highlight that, when the 16 transducers are attached to the panel, the radiated sound power is significantly reduced, by 5 to 15 dB at the first three one-third octave bands for both acoustic and structural primary excitation. These reductions are generated by the shift of the resonant frequencies due to the increased stiffness of the panel. When active control is implemented, the radiated sound power is reduced by 1 to 7 dB for the fourth to the eleventh one-third octave band in both plots. No control effect is found in the first three one-third octave bands, where the response of the panel is not characterized by resonances, and thus cannot be controlled by implementing active damping. At higher frequencies, very little or no control effect is observed.

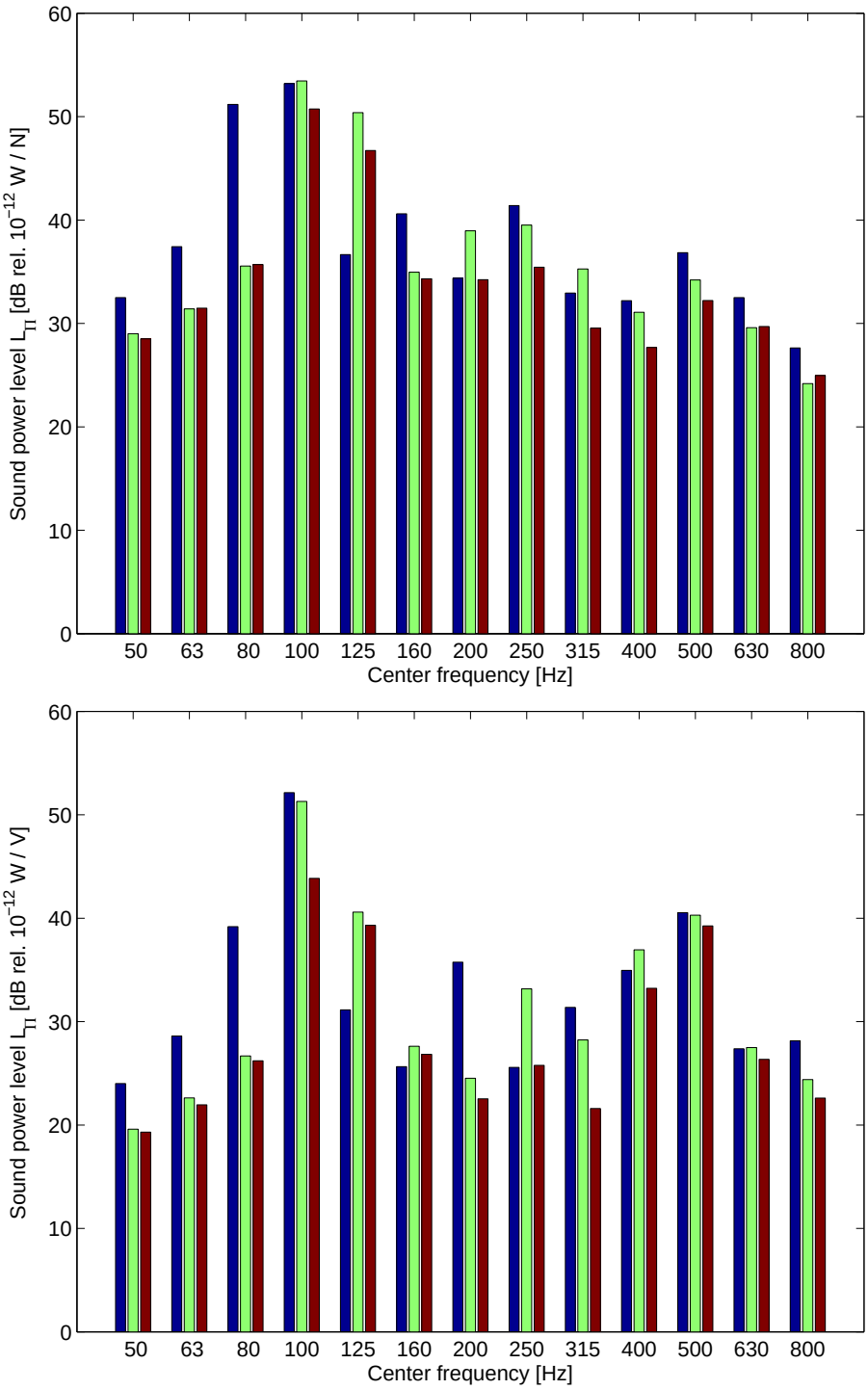

Figure 5.20: Total radiated sound power in one-third octave bands between 50 and 800 Hz center bands, per unit force generated by the shaker (top) and per unit voltage driving the loudspeaker (bottom): measured on the panel without transducers (first column), with transducers but no feedback control (middle column), and with transducers and feedback control (last column)

5.5 Conclusion

This chapter focuses on the experimental results regarding the control effectiveness of a smart panel using triangular piezoceramic actuator and accelerometer sensor pairs. 16 decentralized velocity feedback control loops have been implemented in order to generate active damping and to reduce both the response and the sound radiation via the panel at resonant frequencies.

The experimental results have highlighted that, when the control transducers are attached to the thin aluminium panel, its natural frequencies are shifted up due to the passive stiffening effect of the piezoceramic patch actuators, and the amplitudes of the resonant peaks are slightly reduced due to passive damping effects generated by the bonding layer and the dissipative effects induced by the short circuited piezoceramic actuators.

Significant levels of attenuation is achieved at the low resonant peaks in the frequency band between 100 and 700 Hz with reductions of up to 15 dB in both structural vibration and sound radiation, except for some resonance frequencies controlled by the resonances of the cavity under the panel. At frequencies higher than around 700 Hz, the vibration level and the radiated sound power slightly increases.

These results have been obtained from a prototype smart panel. It is believed that the control performance can be further enhanced by properly designing the size and shape of the triangular piezoceramic actuators in such a way as to improve the limit of the stable control gain and extend the frequency range. Therefore, the following chapter presents a theoretical and experimental study concerning the control performance of single or multiple velocity feedback loop(s) with various shapes and sizes of isosceles triangular actuators.

Chapter 6

Parametric Study of Triangular Piezoceramic Actuator

This chapter investigates the effect of the physical dimensions of triangular actuators on the stability and control performance of the velocity feedback control loop. The aim of this chapter is to provide general guidelines for the design of a feasible triangular actuator,which gives good stability properties allowing high feedback gains in order to obtain a good control performance and thus high active damping effects. The design parameters of the physical dimensions considered in this study are a) base length b) height, and c) combined base length and height of the triangular piezoceramic actuator. For the third parametric study, the height and base length vary in such a way that the aspect ratio of the triangular actuator is kept constant. The parametric study is carried out experimentally as well as theoretically in this chapter, rather than only by simulation, as in Chapter 3, since a large set of triangular actuators were available for the study.

The effects of the geometric parameters of the triangular actuator on the stability and control performance are investigated in two stages. First, a single-input single-output (SISO) control system is considered, and then the discussion moves to a decentralized multi-input multi-output (MIMO) control system. The control performance of the SISO system is assessed using the open loop FRF in terms of the maximum reduction index. The control performance of the decentralized multi-channel control system is experimentally measured in terms of structural vibration

reduction and sound radiation reduction.

6.1 Stability and control performance

The parametric analysis considers stability and control performance properties with reference to a) base length, b) height, and c) both base length and height of the triangular actuator. For the third parametric study, the dimensions are modified in such a way that the aspect ratio of the triangular actuator is kept constant. For all three parametric studies, the stability and control performance are assessed in two stages: first, a SISO velocity feedback control using a triangular actuator and a velocity sensor at its top vertex, and second, a decentralized MIMO velocity feedback control system, composed of 16 triangular piezoceramic actuators and 16 accelerometer sensors on the top vertex of the corresponding triangular actuator.

6.1.1 Single control unit

The parametric study begins with a SISO control system using a triangular piezoceramic actuator and an ideal velocity sensor. As introduced earlier in Chapter 3, the stability and control performance of a SISO system can be assessed by means of open loop FRF $G_c(j\omega)$ between the velocity of the panel at the error sensor position and the driving voltage of the triangular actuator. The fully coupled model presented and experimentally validated in Chapter 4 is used to predict the open loop FRF $G_c(j\omega)$. A simple formula was introduced in Eq.(3.6) to compute the maximum reduction index R_k, which denotes the upper limit of the obtainable vibration reduction at the kth resonant frequency ω_k of the panel. The formula of R_k is again addressed below:

$$R_k = 20 \log_{10} |1 + G_c(j\omega_k) H_{max}| \,, \tag{6.1}$$

where H_{max} is the maximum control gain, which is expressed as the reciprocal of the horizontal distance between the origin and the $G_c(j\omega)$ at the frequency, where the Bode phase is equal to -180 degree, which is referred to as the phase crossover frequency ω_0. As in Chapter 3, the maximum reduction index R_k is computed for the 1st, 3rd, and 7th resonances, which occur respectively at approximately 40 Hz, 160 Hz, and 330 Hz.

The part of theoretical study is validated by three sets of the measured FRFs for each parameter considered in the theoretical study, i.e. the change in base length, height, and both height and base length of the isosceles triangular piezoceramic patch. In total, six aluminum rectangular panels were constructed for the parametric study of the SISO control system. Each panel is equipped with a single piezoceramic actuator of different dimensions. The top vertex of the triangular actuator is located at (x_c, y_c) = (167.0 mm, t_{pzt}+1 mm) with reference to the lower left hand side corner of the panel, where t_{pzt} denotes the height of the triangular actuator. The y-coordinate of the top vertex of the actuator y_c is 1 mm bigger than the height of the triangular actuator, because the base edge of the actuator is shifted 1 mm from the clamped border of the panel for electrical insulation purposes.

It is important to emphasize that the stability analysis with a SISO control system does not provide the effective stability margin for a MIMO control system. However, the stability of a single control unit provides an important insight, whether or not the MIMO control system is to be only conditionally stable. Moreover, a general idea about the control performance of a multichannel control system is derived from the stability analysis of a single-input single-output control unit.

6.1.2 Multichannel decentralized control units

The discussion of MIMO system follows the theoretical and experimental results of the parametric study of the SISO control system.

The essential difference in a multichannel control system from single channel control system is that the stability of the entire system is usually not assessed by using individual frequency response functions, since the stability of each feedback control loop is affected by the other feedback loops. As discussed in section 5.2, the stability analysis for the multi-channel control system has been graphically illustrated by the plot of the determinant of the return matrix [69, 74], $\det[\mathbf{I} + \mathbf{G}(j\omega)\mathbf{H}(j\omega)]$.

The control performance of the decentralized multichannel control system is discussed in terms of structural vibration level of the panel and sound radiation from the panel in the frequency range 0 to 1 kHz, as in Chapter 5. The control effect is assessed by comparing the vibration level of a plane panel and sound radiation from

a plane panel with that from the panel with 16 control units and decentralized velocity feedback control. A detailed description regarding the physical arrangements to measure the spatially averaged mean velocity of the panel and to measure the sound radiation from the panel are respectively given in Section 5.3 and 5.4.

The multi-channel experimental measurements have been taken with three sets of smart panels for each parametric study in terms of height, base length, and both height and base length of the triangular actuator. In total, six smart panels were constructed in order to experimentally carry out the parametric study of the decentralized MIMO velocity feedback control. Each smart panel is equipped with 16 triangular piezoceramic actuators along the panel border and accelerometer sensors located at the top vertex of the triangular actuators. The design of the smart panel with 16 triangular actuators, which was introduced in Chapter 5, is illustrated again in Fig. 6.1.

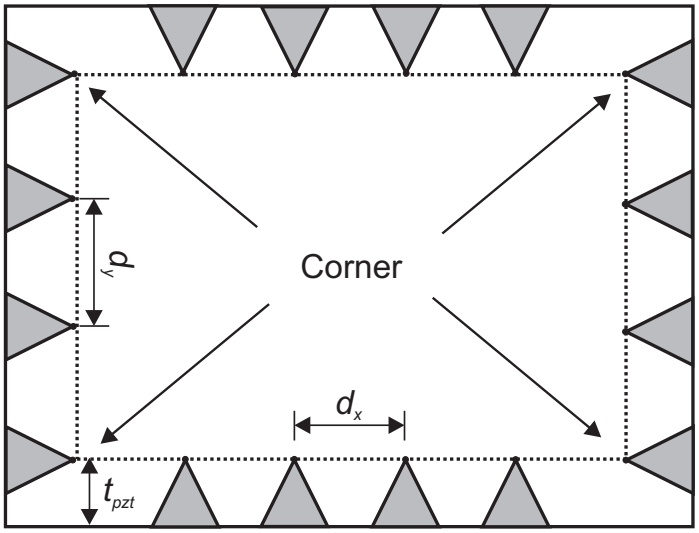

Figure 6.1: A rectangular panel with 16 evenly distributed triangular piezoceramic actuators. A virtual active boundary wedge is depicted by dotted line.

It must be underlined that the dimensions of the triangular piezoceramic actuator are limited in order to evenly allocate 16 control units on the panel, which is measured $l_x \times l_y = 414$ mm $\times$ 314 mm. The base length of the triangular actuator b_{pzt} must be shorter than the distance between two adjacent actuators along x- and y-axis, d_x and d_y. Furthermore, half the base length must be shorter than the height. Therefore,

the dimensions of the triangular actuator are limited to:

$$b_{pzt} \leq d_x = (l_x - 2t_{pzt})/5 \tag{6.2a}$$

$$b_{pzt} \leq d_y = (l_y - 2t_{pzt})/3 \tag{6.2b}$$

$$b_{pzt} \leq 2t_{pzt}. \tag{6.2c}$$

Combining the three formulas in Eq.(6.2), the base length of the triangular actuator b_{pzt} is bound to be shorter than $l_x/6 \simeq 69$ mm. Consequently the height of the actuator is bound to the following values:

$$\frac{b_{pzt}}{2} \leq t_{pzt} \leq \frac{l_x - 5b_{pzt}}{2}. \tag{6.3}$$

When the base length b_{pzt} is equal to 69 mm, the height is given to be 34.5 mm to comply with the constraint expressed in Eq.(6.3), and thus the dimensions of the actuator are completely fixed. In order to carry out the parametric study with reference to the height for constant base length, and vice versa, the dimensions of the triangular actuator must be shorter than the maximum limit. Thus, in this study the upper limit of the height and base length of the actuator is given as 50 mm. The thickness of the triangular piezoceramic patch actuator is constant, as the effect of the thickness on the stability and control performance of the velocity feedback control system has been discussed using a square actuator in Chapter 3.

6.2 Base length with constant height

This section investigates the effect of the base length of the isosceles triangular piezoceramic patch on the stability and control performance of both SISO and MIMO systems. In the theoretical parametric study on a SISO system, the base length of the triangular actuator b_{pzt} varies between 20 mm and 50 mm, while the height and the thickness are fixed to 25 mm and 0.75 mm, respectively. The part of this simulation analysis has been validated by three sets of the measured FRFs taken on the panel with the piezoceramic patch actuators listed in Table 6.1. In the experimental parametric study on a MIMO system, the vibration level and the sound radiation have been measured by using the smart panel equipped with 16 piezoceramic actu-

ators listed in Table 6.1.

Table 6.1: Geometric parameter of the triangular piezoceramic actuator considered in the parametric study regarding the actuator base length

sample	$b_{pzt} \times t_{pzt} \times h_{pzt}$ [mm^3]	aspect ratio	weight [g]
1	25.0 × 25.0 × 0.75	0.50	3.7
2	40.0 × 25.0 × 0.75	0.313	5.9
3	50.0 × 25.0 × 0.75	0.25	7.3

6.2.1 Single control unit

Figure 6.2 shows a comparison of the Bode plots of the simulated (top) and measured (bottom) open loop FRFs $G_c(j\omega)$ between the out-of-plane velocity of the panel at the error sensor position and the input voltage to the piezoceramic actuators with a constant height $t_{pzt} = 25$ mm and various base lengthes b_{pzt}; i) 25 mm (red faint line), ii) 40 mm (blue dotted line), and iii) 50 mm (black dashed line).

As plotted in Fig. 6.2, the predicted open loop FRFs show very good agreement with the measured ones in terms of both amplitude and phase at low frequency up to 1.5 kHz. At around 1.5 kHz, the peak amplitude of both predicted and measured FRFs become lower than the neighbor peaks, and the phase lag exceeds - 90 degree. This indicates that at around 1.5 kHz, the response of the panel is controlled by the modes, whose nodal lines are close to the tip of the triangular piezoceramic actuator. In fact, the wavelength of the panel at 1.5 kHz is predicted as approximately 48 mm. Thus, the half of the wavelength is comparable with the distance between the base edge of the actuator and the velocity sensor. Considering that the response of the panel at higher frequency is mainly controlled by the bending moment generated along the base edge rather than that along lateral edges, the further phase lag at around 1.5 kHz is caused by the time delay, which takes the bending wave generated at the base edge to travel to the tip of the triangular actuator at the velocity sensor location.

Above 1.5 kHz, the mean amplitude of both measured and predicted FRFs rises with both the frequency and the base length up to 10 kHz. Above 10 kHz, the spectra of the measured FRFs are characterized by modulation effects. The same

feature can be found in the simulated open loop FRFs, although the these amplitude modulation peaks are weaker than ones with measured FRFs. Above the first amplitude modulation, the mean amplitude of three FRFs are comparable.

The phase plots in Fig. 6.2 show that the phase lag of FRFs using three actuators with different dimensions show very similar spectra up to 10 kHz. Beyond 10 kHz, slightly bigger phase lag is generated by using the actuator with longer base length. Therefore, as shown in the right hand side plot in Fig. 6.3, the phase crossover frequency ω_0 slowly decreases as the base length rises. This indicates that the phase lag is not strongly related to the base length of the triangular actuator. Therefore, the effective frequency range, where the response of the panel can be reduced by a velocity feedback loop, remains unaltered with the change in the base length. The left hand side plot in Fig. 6.3 shows the maximum stable gain H_{max} that can be implemented to the SISO system before instability occurs. The plot highlights that, as the base length of the triangular actuator increases, the upper limit of the control gain monotonically decreases.

In summary, Fig. 6.4 shows the maximum reduction index R_k achieved by using a SISO velocity feedback control at kth (k = 1,3,7) resonant frequencies. This plot indicates that increasing the base length brings beneficial effects, as the maximum reduction index R_k slightly increases with base length.

6.2.2 16 channel decentralized control units

Figure 6.5 shows the locus of the det$[\mathbf{I} + \mathbf{G}(j\omega)\mathbf{H}(j\omega)]$ with unity gain measured between 25 Hz and 42 kHz using three smart panels equipped with 16 control units with different dimensions. The three plots shows that the size of the locus of the determinant increases with the base length. In all plot, the locus of the determinant is characterized by a series of circles. At low frequency, the circles start from the $(1,\ 0j)$, and the centers of the circles are aligned along the positive real axis. As frequency rises, although the circles still start from the origin, the centers of the circles drifts away from the positive real axis towards the imaginary negative quadrants, due to the extra phase lag generated by the phase lag compensator. At higher frequency, the locus enters the left hand side of the vertical line parallel to y-axis

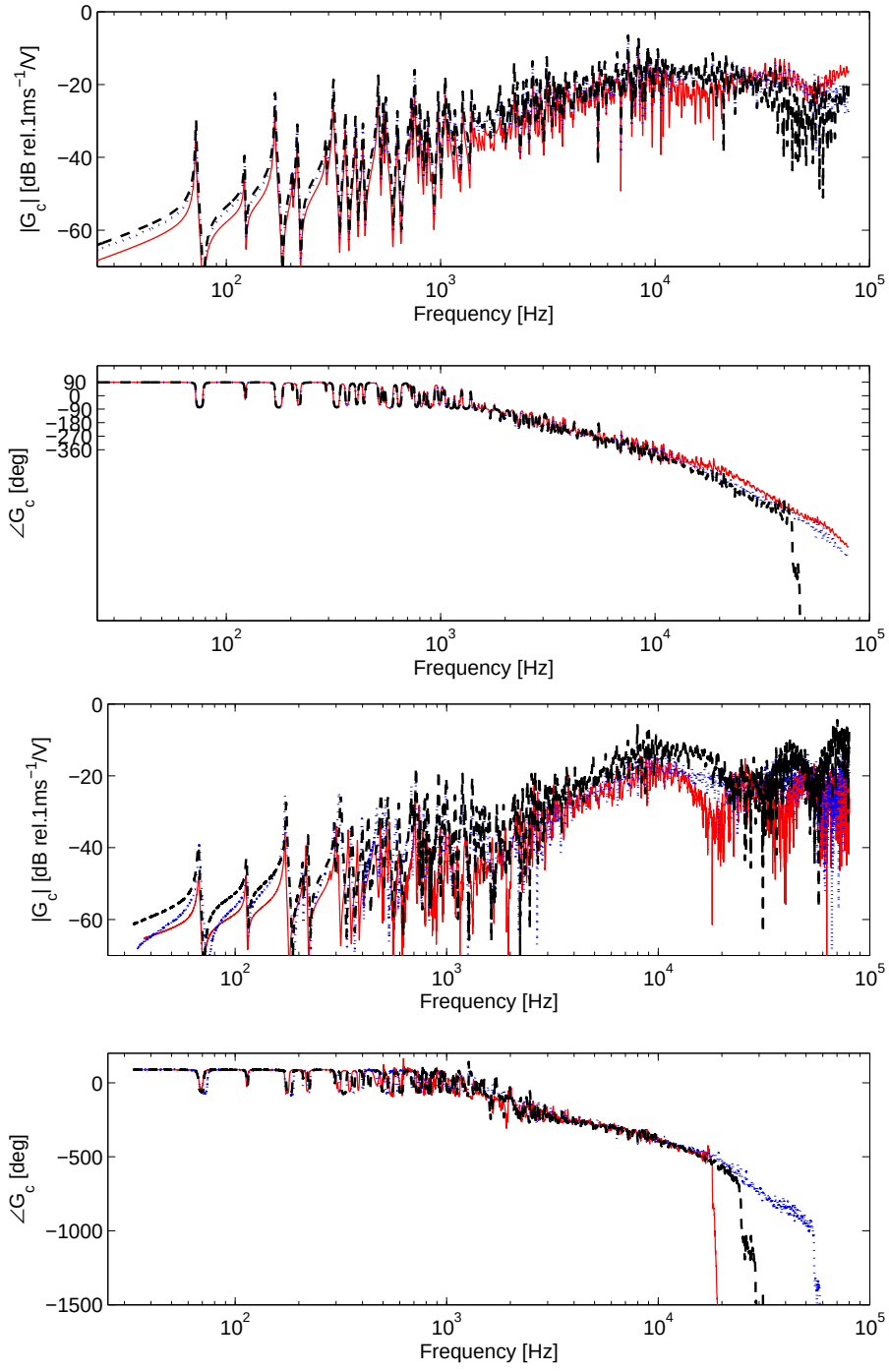

Figure 6.2: Bode plots of the simulated (top) and the measured (bottom) open loop FRFs on the panel with the triangle piezoceramic actuator with constant height 25 mm and various base length; 25 mm (red faint line), 40 mm (blue dotted line), and 50 mm (black dashed line).

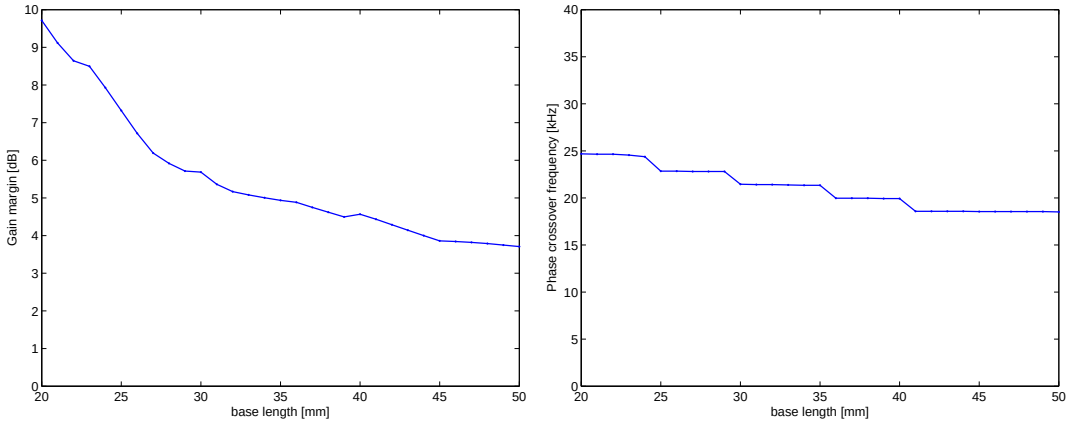

Figure 6.3: Maximum control gain H_{max} (left) and phase crossover frequency ω_0 (right), computed by using simulated open loop FRFs as a function of the base length b_{pzt} for constant height.

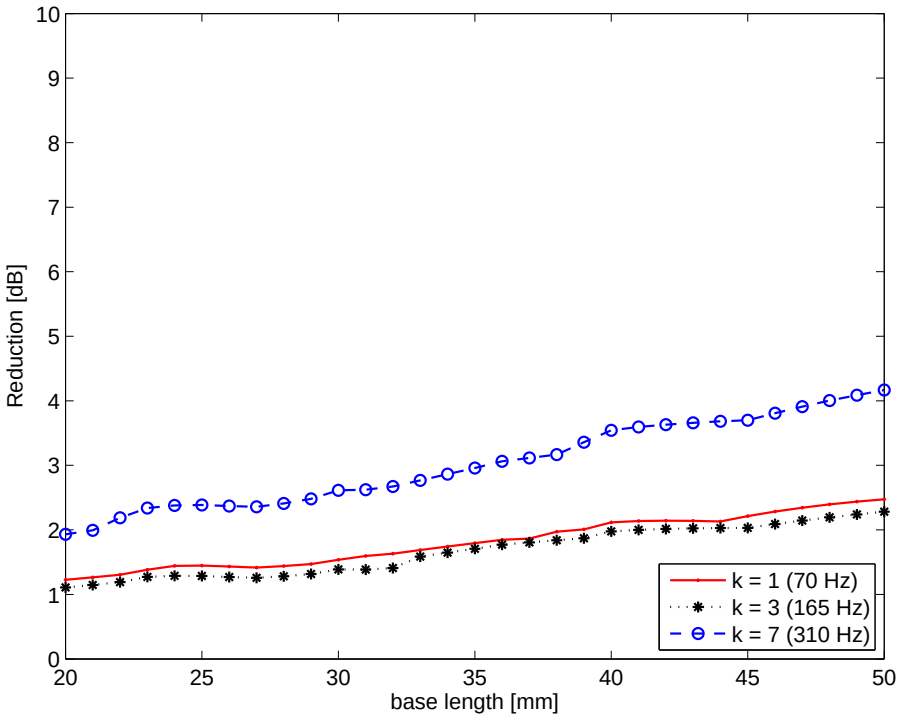

Figure 6.4: Maximum reduction index R_k (k = 1,3,7), computed by using simulated open loop FRFs as a function of base length for constant height

passing through the point $(1, 0j)$, and finally, at higher frequency beyond 1 kHz, the locus crosses the positive real axis again. According to the Nyquist criterion, this result indicates that these three decentralized velocity feedback loops are all only conditionally stable [69].

Table 6.2 summarized the identical control gains h_0, which is experimentally implemented for decentralized MIMO systems. As in Chapter 5, the control gain h_0 is chosen to be the highest possible value, for which the system remains stable. This table shows that as the base length of the triangular actuator increases, the highest possible gain h_0 decreases. This result confirms the parametric study using SISO systems presented in previous section. This table also highlights that, when the shaker is attached to the structure to generate the primary excitation, the maximum control gain is slightly higher than that used with the acoustic excitation generated by a loudspeaker. This is because the shaker adds further mass and damping terms on the structure. Thus, the amplitude of the open loop FRFs of the panel with the shaker becomes lower than that without the shaker at higher frequencies, where the phase lag exceeds -180 degree. As a result, the gain margin of the control system with the shaker is bigger than that without the shaker, and thus higher gain can be implemented.

Table 6.2: Control gain h_0, experimentally implemented for decentralized MIMO systems with primary force and acoustic filed disturbance

dimensions [mm]	Control gain h_0	
$b_{pzt} \times t_{pzt}$	force	acoustic field
25.0 × 25.0	5.3	4.6
40.0 × 25.0	2.5	2.4
50.0 × 25.0	1.7	1.6

Figure 6.6 show the narrow band spectra of the spatially averaged velocity of the panel measured between 0 and 1 kHz per unit force generated by the shaker (top), and per unit voltage driving the loudspeaker(bottom). Each plot includes four spectra measured by using a plane panel without control unit, and three panels with feedback control using 16 triangular actuators with various base lengthes. Table 6.3 summarizes the obtained vibration reduction at the first 9 resonant peaks, and the averaged reduction between at 1st and 9th resonant frequencies of the panel with a point force primary disturbance.

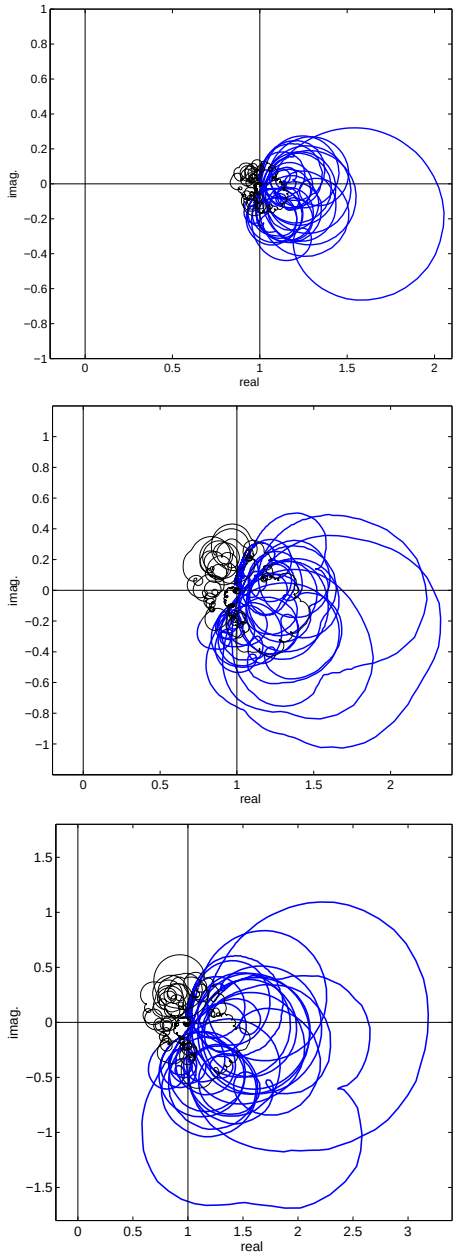

Figure 6.5: Locus of the det$[\mathbf{I}+\mathbf{G}(j\omega)\mathbf{H}(j\omega)]$ between 25 Hz - 1 kHz (blue solid line) and 1 - 42 kHz (black faint line) measured on the panel with 16 triangular actuators with dimensions of 25.0 mm $\times$ 25.0 mm (top), 40.0 mm $\times$ 25.0 mm (middle), 50.0 mm $\times$ 25.0 mm (bottom).

Four lines in Fig. 6.6 indicate that, as the base length of the actuator increases, the resonant peaks of the averaged velocity of the panel are shifted up in frequency. This is because the piezoceramic actuator adds the local stiffening effects on the panel. The difference in the peak frequency gets smaller as frequency rises, because the stiffness effect decreases with frequency.

The increase of the base length also results in the improvement of the narrow band control performance in the measured frequency range 0 to 1 kHz. This conclusion agrees with the indication obtained by the parametric study using SISO control systems. As summarized in Table 6.3, up to 5 dB improvement is obtained in the narrow band control performance by increasing the base length of the triangular actuator from 25 mm to 40 mm. However, it must be underlined that the measured vibration reductions are achieved by both passive and active effects of control units. As early discussed in Chapter 5, a part of the passive control effects is generated by viscous-elastic effect of the bonding layer between the actuator and the panel. Additionally, a weak shunt-damping effect is also generated by the internal electric resistance of the piezoceramic actuator, since they are attached to voltage amplifiers, and hence short circuited. Therefore, a bigger actuator can generate more passive damping effects because of larger area of actuator surface and bonding layer. It indicates that a part of higher control performance of bigger actuator is achieved by its stronger passive effects.

Figure 6.6 also shows that, when the panel is excited by an acoustic field generated by a loudspeaker, the resonant peaks at around 390 and 450 Hz are not attenuated by decentralized velocity feedback control. This is because these peaks are controlled by the resonances of the acoustic cavity under the panel. When the higher order resonances of the acoustic cavity control the response of the panel at around 800, 820, and 880 Hz, again no vibration attenuation is achieved.

Figure 6.7 shows the total radiated sound power by the panel, measured between 0 and 1 kHz per unit force generated by the shaker (top), and per unit voltage driving the loudspeaker(bottom). Each plot includes four spectra measured by using a plane panel without control unit, and three panels with feedback control using 16 actuators with various base lengthes.

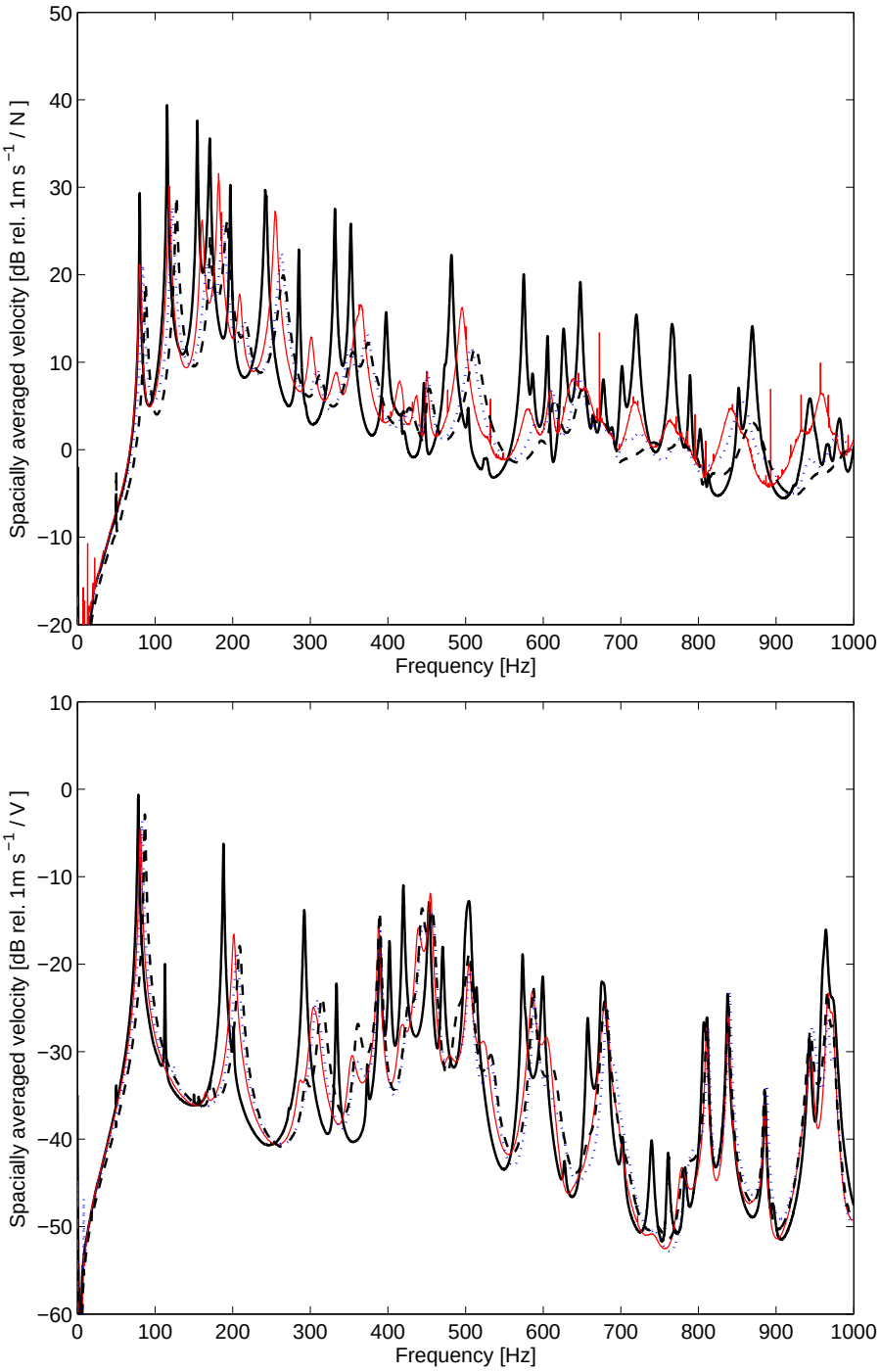

Figure 6.6: Narrow band spectra of the spatially averaged velocity of the panel measured between 0 and 1 kHz per unit force generated by the shaker (top), and per unit voltage driving the loudspeaker(bottom); measured by using (1) a plane panel without control unit (black solid line), and the panels with feedback control using the actuators with constant height and various base lengthes; (2) 25.0 mm × 25.0 mm (red faint line), (3) 40.0 mm × 25.0 mm (blue dotted line), and (4) 50.0 mm × 25.0 mm (black dashed line)

Table 6.3: Measured vibration reduction at resonant frequencies

frequency [Hz]	reduction [dB]		
	25 × 25	40 × 25	50 × 25
80.2	8.2	8.2	10.3
115.6	9.3	11.6	10.4
154.4	11.4	16.2	13.2
170.5	4.0	9.8	9.3
197.0	12.5	15.6	16.2
241.9	2.4	7.2	9.7
285.3	10.0	13.7	14.3
331.9	18.7	16.0	16.4
352.2	9.2	12.7	13.6
average	9.5	12.3	12.6

The top plot shows that the radiated sound power at 2nd and 4th peaks are amplified after velocity feedback control is implemented. It is not caused by the positive feedback at these frequencies, but rather caused by the low quality measurements of the reference spectra, which is obtained using a plane panel without control unit. As the response of a thin panel is principally controlled by damping at resonance frequencies [75], small variation of the structural damping can result in big changes of the peak amplitude. As mentioned early, the shaker and the clamping frame produce the additional damping effects on the panel. The amount of the added damping effects added to the panel depend on the torque used to tighten the screws to fix the frame and the head of the shaker, and also the attachment angle of the shaker to the panel. Therefore, when the panel or shaker is improperly arranged, they introduce additional high damping, which causes the low amplitude of the spectra at resonant frequencies.

Nevertheless, the narrow band control performance in terms of total radiated sound power is improved by increasing the base length of the triangular actuator in measured frequency range of 0 - 1 kHz. The obtained sound radiation reduction is in general lower than the obtained vibration reduction, because this control system does not consider the radiation efficiency of each mode [5].

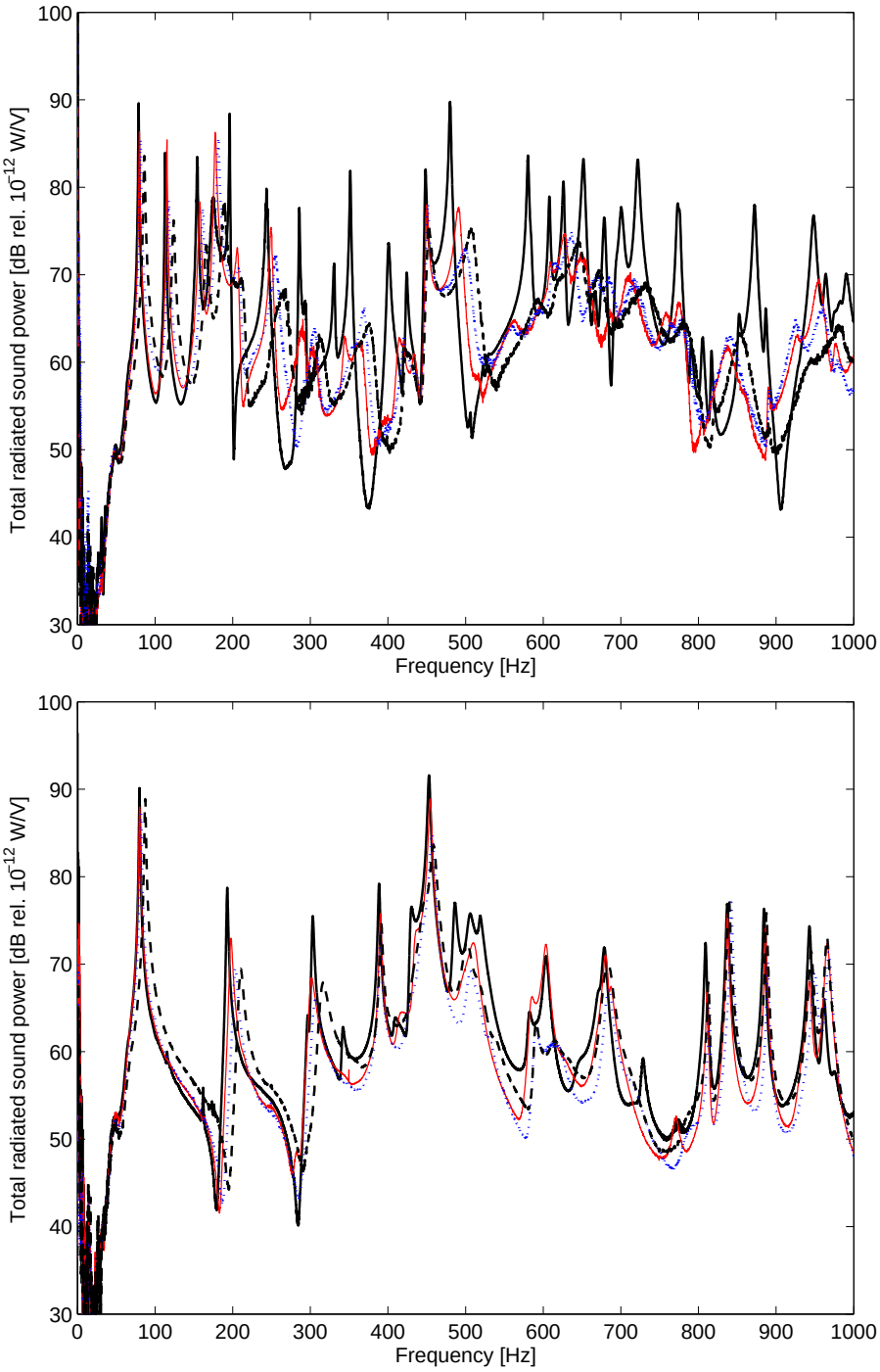

Figure 6.7: Narrow band spectra of the total radiated sound power, measured between 0 and 1 kHz per unit force generated by the shaker (top), and per unit voltage driving the loudspeaker(bottom); measured by using (1) a plane panel without control unit (black solid line), and the panels with feedback control using the actuators with constant height 25 mm and various base lengthes; (2) 25.0 mm × 25.0 mm (red faint line), (3) 40.0 mm × 25.0 mm (blue dotted line), and (4) 50.0 mm × 25.0 mm (black dashed line)

6.3 Height with constant base length

This section investigates the effect of the height of the isosceles triangular piezoceramic patch on the stability and control performance of both SISO and MIMO systems. In the theoretical parametric study on a SISO system, the height of the triangular actuator t_{pzt} varies between 20 mm and 50 mm, while the base length and the thickness are fixed to 40 mm and 0.75 mm, respectively. The part of this simulation analysis has been validated by three sets of the measured FRFs taken on the panel with the piezoceramic patch actuators listed in Table 6.4. In the experimental parametric study on a MIMO system, the vibration level and the sound radiation have been measured by using the smart panel equipped with 16 piezoceramic actuators listed in Table 6.4.

Table 6.4: Geometric parameter of the triangular piezoceramic actuator considered in the parametric study regarding the actuator height.

sample	$b_{pzt} \times t_{pzt} \times h_{pzt}$ [mm^3]	aspect ratio	weight [g]
1	40.0 × 25.0 × 0.75	0.313	5.9
2	40.0 × 31.5 × 0.75	0.394	7.4
3	40.0 × 40.0 × 0.75	0.5	9.4

6.3.1 Single control unit

Figure 6.8 shows a comparison of the Bode plots of the simulated (top) and measured (bottom) open loop FRFs $G_c(j\omega)$ between the out-of-plane velocity of the panel at the error sensor position and the input voltage to the piezoceramic actuators with a constant base length $b_{pzt} = 40$ mm and various heights t_{pzt}; i) 25 mm (red faint line), ii) 31.5 mm (blue dotted line), and iii) 40 mm (black dashed line).

Again, at low frequency the amplitude and phase of simulated and measured FRFs agree well. The amplitude of FRFs rises with both the height of the triangular actuator and the frequency. At around 800 Hz, the amplitude of both measured and simulated open loop FRFs using 40 mm height triangular actuator becomes low, and the phase lag exceeds - 90 degree beyond this frequency. The same phenomena occurs with other two FRFs using 31.5 mm and 25 mm height actuators respectively at 1.1 kHz and 1.5 kHz. According to classic thin plate theory, the bending length

of the panel at these frequencies are respectively predicted as 48 mm, 60 mm, and 75 mm, which are close to double length of the height of the triangular actuator. This indicates that at around these frequency, the sensor is located along the nodal line of the half wavelength of the mode, and thus the amplitude of the open loop FRF becomes low.

The phase plots show that, as the height of the actuator rises, the constant phase lag takes effect at lower frequency, and thus a bigger phase lag is generated at higher frequency. Therefore, as shown in the right hand plot in Fig. 6.9, the phase crossover frequency ω_0 decreases as the width of the actuator rises. Comparing two plots of the ω_0 in Figs. 6.3 and 6.9, it is shown that the phase crossover frequency ω_0 is mainly controlled by the height, rather than the base length of the actuator.

At higher frequency beyond 4 kHz, the amplitude of the measured FRFs are characterized by modulation effects. This characteristic of the measured FRFs is well replicated in the simulated open loop FRFs, although the peak frequency of the modulation is shifted up and down in frequency, and in general the predicted modulation effects are weaker than the measured ones. These plots also highlight that the mean amplitude of all FRFs becomes similar at higher frequency beyond the first modulation peak. Therefore, as graphically shown in the right hand side plot in Fig. 6.9, the control gain remains almost constant with small variation, while the height changes between 20 mm and 50 mm. This variation is caused because the crossing value of $G_c j\omega$over the real negative axis is strongly dependent on whether it occurs at either resonance or off-resonance.

To summarize these effects, Fig. 6.10 shows the maximum control index R_k achieved by using a SISO velocity feedback control at kth (k = 1,3,7) resonant frequencies. This plot highlights that the control performance is significantly improved by increasing the height of the triangular actuator. However, it is important to emphasize that the upper bound of the workable frequency range of active velocity feedback is more limited as height increases, because phase lag takes place at lower frequency. As discussed earlier, phase lag of the FRF using 40 mm height triangular actuator exceeds - 90 degree and reaches -180 degree below 1 kHz. Therefore, when 40 mm height actuator is used, the control system starts generating positive feedback effects below 1 kHz. As a conclusion, an increase of the height of the triangular actuator

causes two effects: (a) significant improvements of the low frequency control performance, and (2) reduction of the usable frequency range of the velocity feedback control.

6.3.2 16 channel decentralized control units

Figure 6.11 shows the locus of the det$[\mathbf{I} + \mathbf{G}(j\omega)\mathbf{H}(j\omega)]$ measured between 25 Hz and 42 kHz using three smart panels equipped with 16 control units with different dimensions summarized in Table 6.4. In Fig. 6.11, the loci start around $(1,\ 0j)$, and as frequency rises it enters the left hand side of the vertical line parallel to imaginary-axis passing through the point $(1,\ 0j)$. Finally, the locus drift further, and cross the positive real axis again. In top, middle, and bottom plot, the locus crosses over the real positive axis respectively above 1 kHz, around 1 kHz, and below 1 kHz. This indicates that as the height of the triangular actuator increases, the workable frequency range of feedback control system get smaller, and positive feedback effect takes place at lower frequency.

Table 6.5 summarized the control gains h_0, which is experimentally implemented for MIMO systems. In agreement with the indication obtained by Fig. 6.9, the maximum control gain remains almost constant with small variations in change of the height.

Table 6.5: Control gain h_0, experimentally implemented for decentralized MIMO systems with primary force and acoustic filed disturbance.

dimensions [mm]	Control gain h_0	
$b_{pzt} \times t_{pzt}$	force	acoustic field
40.0 × 25.0	2.5	2.4
40.0 × 31.5	1.5	1.5
40.0 × 40.0	2.1	2.2

The two plots in Fig. 6.12 show the narrow band spectra of the spatially averaged velocity of the panel measured between 0 and 1 kHz per unit force generated by the shaker (top), and per unit voltage driving the loudspeaker (bottom). Each plot includes four spectra measured by using a plane panel without control unit, and three panels with feedback control using 16 triangular actuators with various heights. 6.6 summarizes the obtained vibration reduction at the first 9 resonant

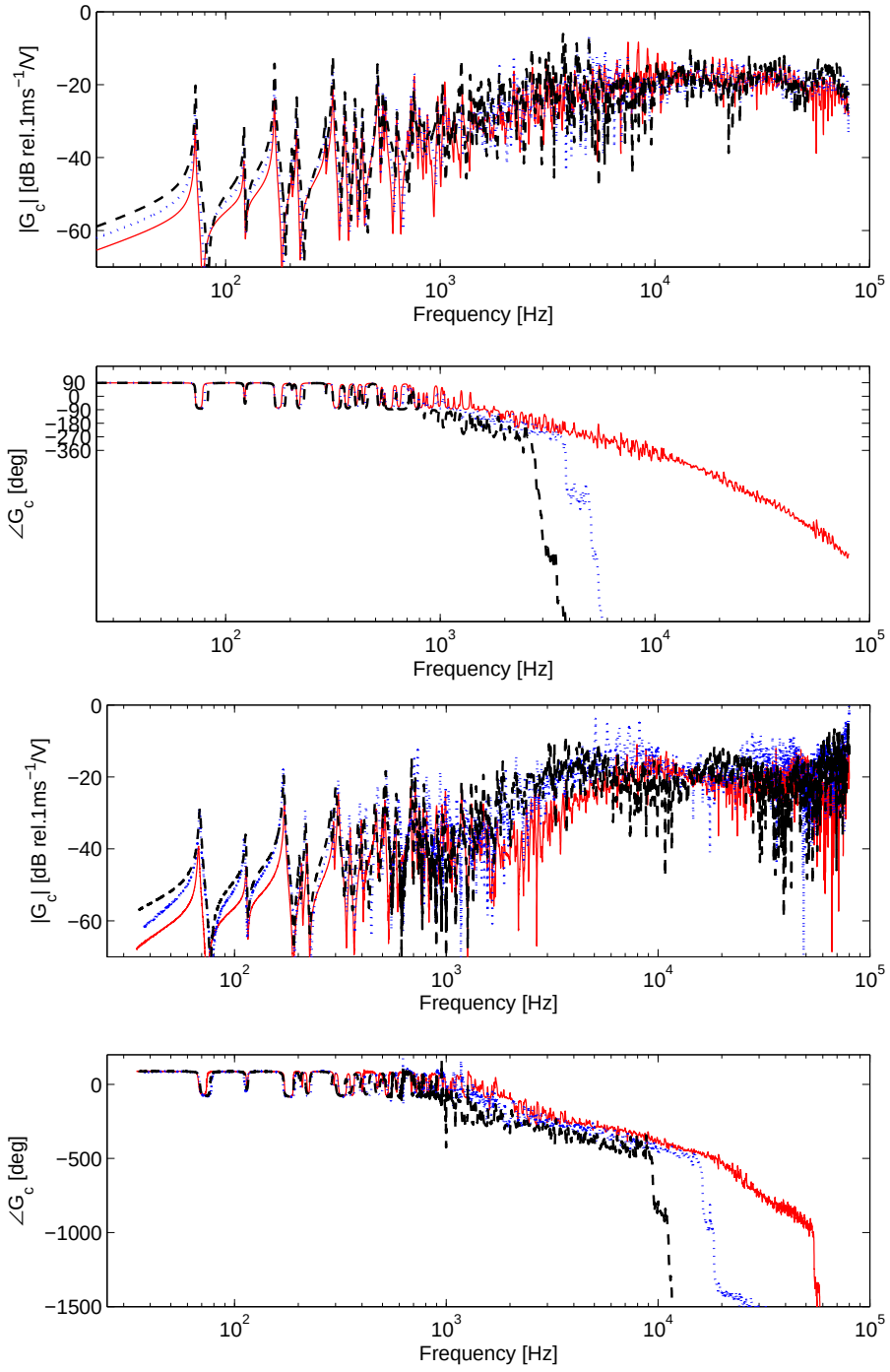

Figure 6.8: Bode plots of the simulated (top) and the measured (bottom) open loop FRFs on the panel with the triangle piezoceramic actuator with the constant base length 40 mm and various heights; 25 mm (red faint line), 31.5 mm (blue dotted line), and 40 mm (black dashed line)

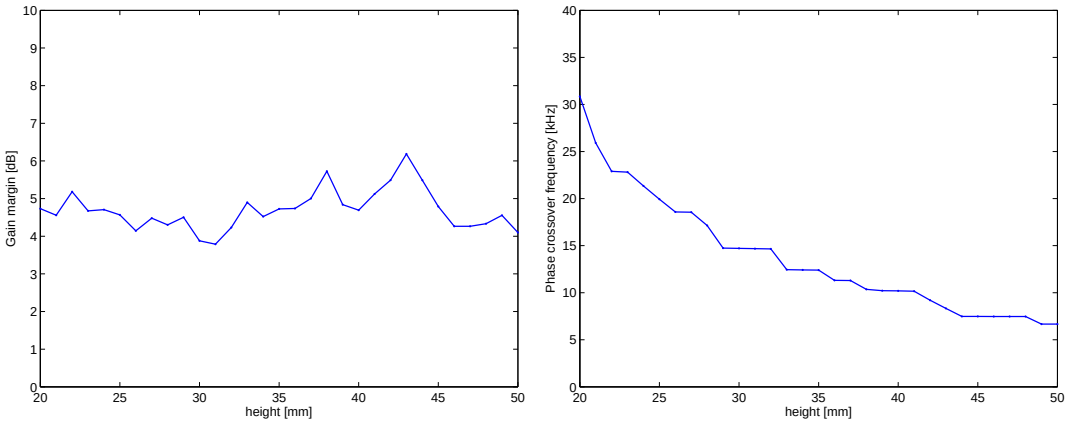

Figure 6.9: Maximum control gain H_{max} (left) and phase crossover frequency ω_0 (right), estimated by using predicted FRFs as a function of the height for constant base length

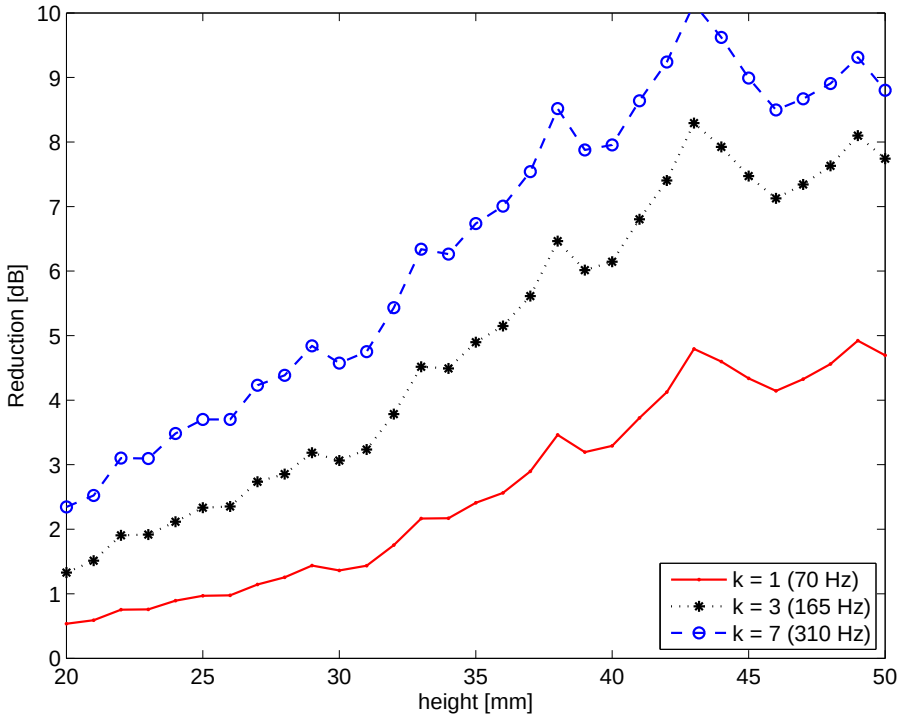

Figure 6.10: Maximum reduction index R_k ($k = 1,3,7$), estimated by using predicted FRFs as a function of the height for constant base length

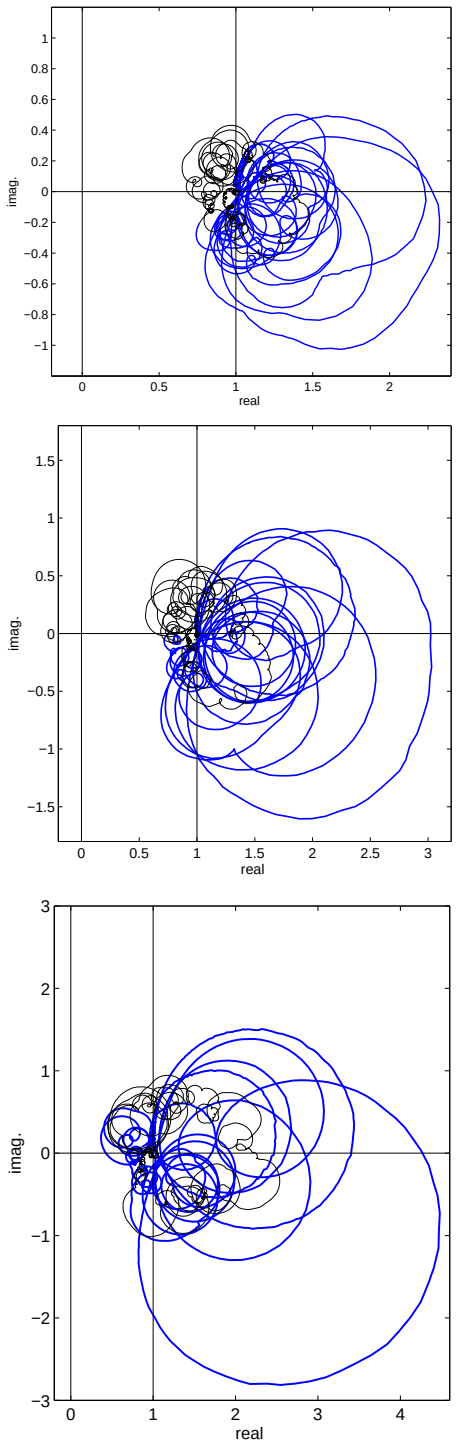

Figure 6.11: Locus of the $\det[\mathbf{I} + \mathbf{G}(j\omega)\mathbf{H}(j\omega)]$ between 25 Hz - 1 kHz (blue solid line) and 1 - 42 kHz (black faint line) measured on the panel with 16 triangular actuators with dimensions of 40.0 mm $\times$ 25.0 mm (top), 40.0 mm $\times$ 31.5 mm (middle), 40.0 mm $\times$ 40.0 mm (bottom).

peaks, and the averaged reduction between at 1st and 9th resonant frequencies of the panel with a point force primary disturbance.

Figure 6.12 shows that, at low frequency up to 550 Hz, the control performance is significantly improved by increasing the height of the triangular actuator. As listed in Table 6.6, the control performance is nearly doubled by increasing the height of the actuator from 25 mm to 40 mm for all listed resonant frequencies. However, Fig. 6.12 also indicates that the increase of height results in stronger positive feedback effect at higher frequency. When the decentralized control system is implemented by using 40 mm $\times$ 25 mm actuators, the vibration of the panel is attenuated in the entire measured frequency range, 0 to 1 kHz, because the positive feedback is produced outside of the operating frequency range. In constant, with 40 mm $\times$ 31.5 mm actuators the vibration level of the panel is attenuated up to around 900 Hz, and beyond this frequency, the vibration level slightly increase due to positive feedback. When the 40 mm $\times$ 40 mm triangular actuators are used, the reduction is obtained up to around 700 Hz only. Beyond this frequency, the response of the panel significantly increased, and thus the spectra of the averaged velocity level of the panel is characterized by sharp peaks, which are not present in the response measured with the plane panel.

Table 6.6: Measured vibration reduction at resonant frequencies.

frequency [Hz]	40 $\times$ 25	40 $\times$ 31.5	40 $\times$ 40
80.2	8.2	11.5	17.1
115.6	11.6	15.1	22.4
154.4	16.2	19.0	24.1
170.5	9.8	10.3	18.3
197.0	15.6	17.9	18.6
241.9	7.2	10.7	16.3
285.3	13.7	16.2	18.0
331.9	16.0	16.9	20.1
352.2	12.7	14.1	18.6
average	12.3	14.6	19.3

The two plots in Fig. 6.13 show the total radiated sound power via the panel, measured between 0 and 1 kHz per unit force generated by the shaker (top), and per unit voltage driving the loudspeaker(bottom). Each plot includes four spectra measured by using a plane panel without control unit, and three panels with feedback

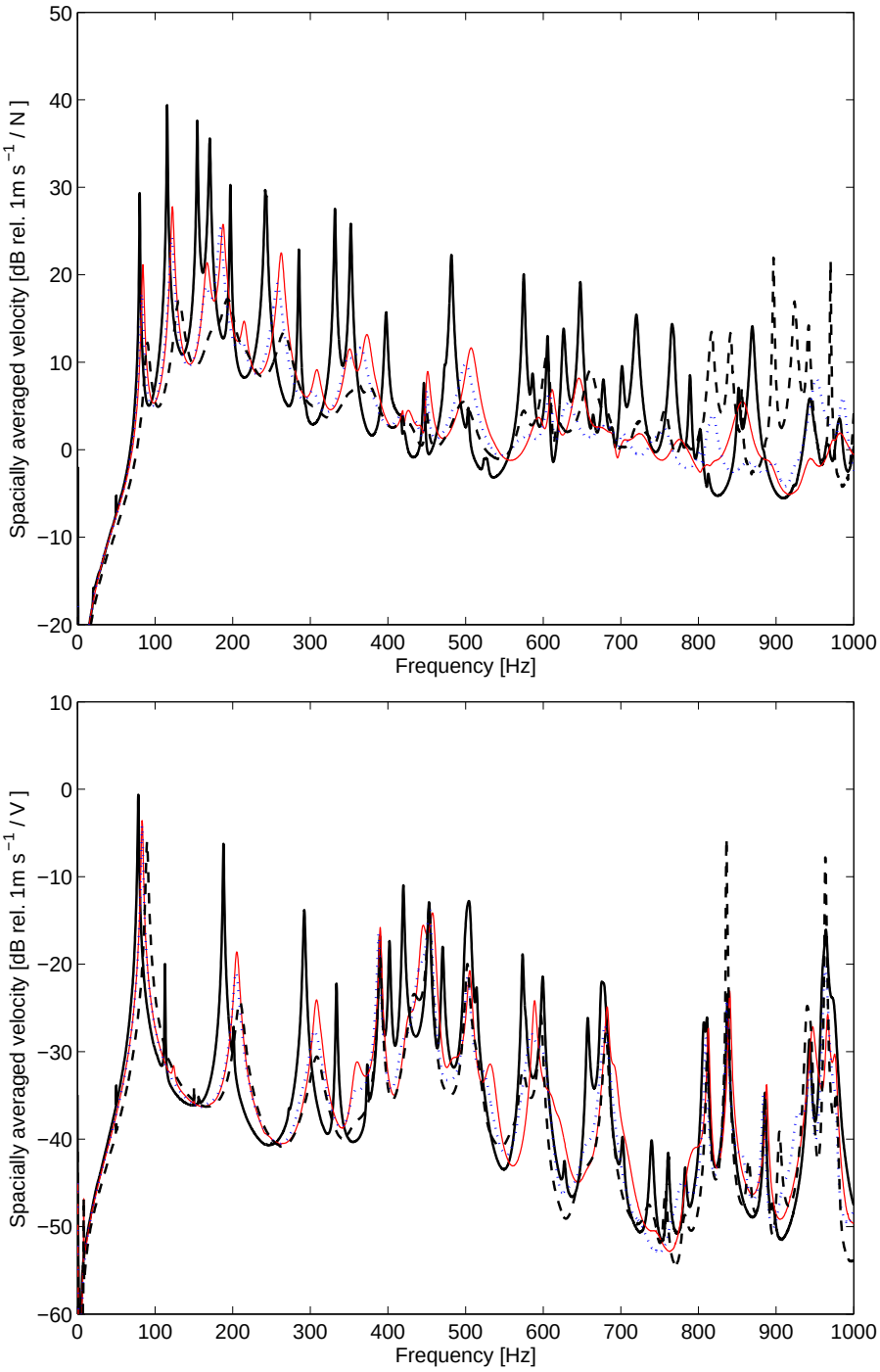

Figure 6.12: Narrow band spectra of the spatially averaged velocity of the panel measured between 0 and 1 kHz per unit force generated by the shaker (top), and per unit voltage driving the loudspeaker(bottom); measured by using (1) a plane panel without control unit (black solid line), and the panels with feedback control using the actuators with the constant base length and various heights; (2) 40.0 mm $\times$ 25.0 mm (red faint line), (3) 40.0 mm $\times$ 31.5 mm (blue dotted line), and (4) 40.0 mm $\times$ 40.0 mm (black dashed line)

control using the actuators with various heights.

The tendency of the obtained control performance in terms of sound radiation is slightly different from that of vibration levels. For example, comparing Figs. 6.12 with 6.13, stronger spillover effects are found by using 40 mm $\times$ 40 mm actuators for the structural vibration than that found for the sound radiation. The principle reason for this effect is that these two measurements were taken in different occasions, which caused small change in physical arrangements. Nevertheless, the overall tendency is the same, i.e. the control performance at low frequency is improved by the increase of the height of the actuator, but also results in limiting the working frequency range, where the control system can suppress the vibration of the structure. Furthermore, the positive feedback effect at higher frequencies is enhanced by increasing the height of the triangular actuator.

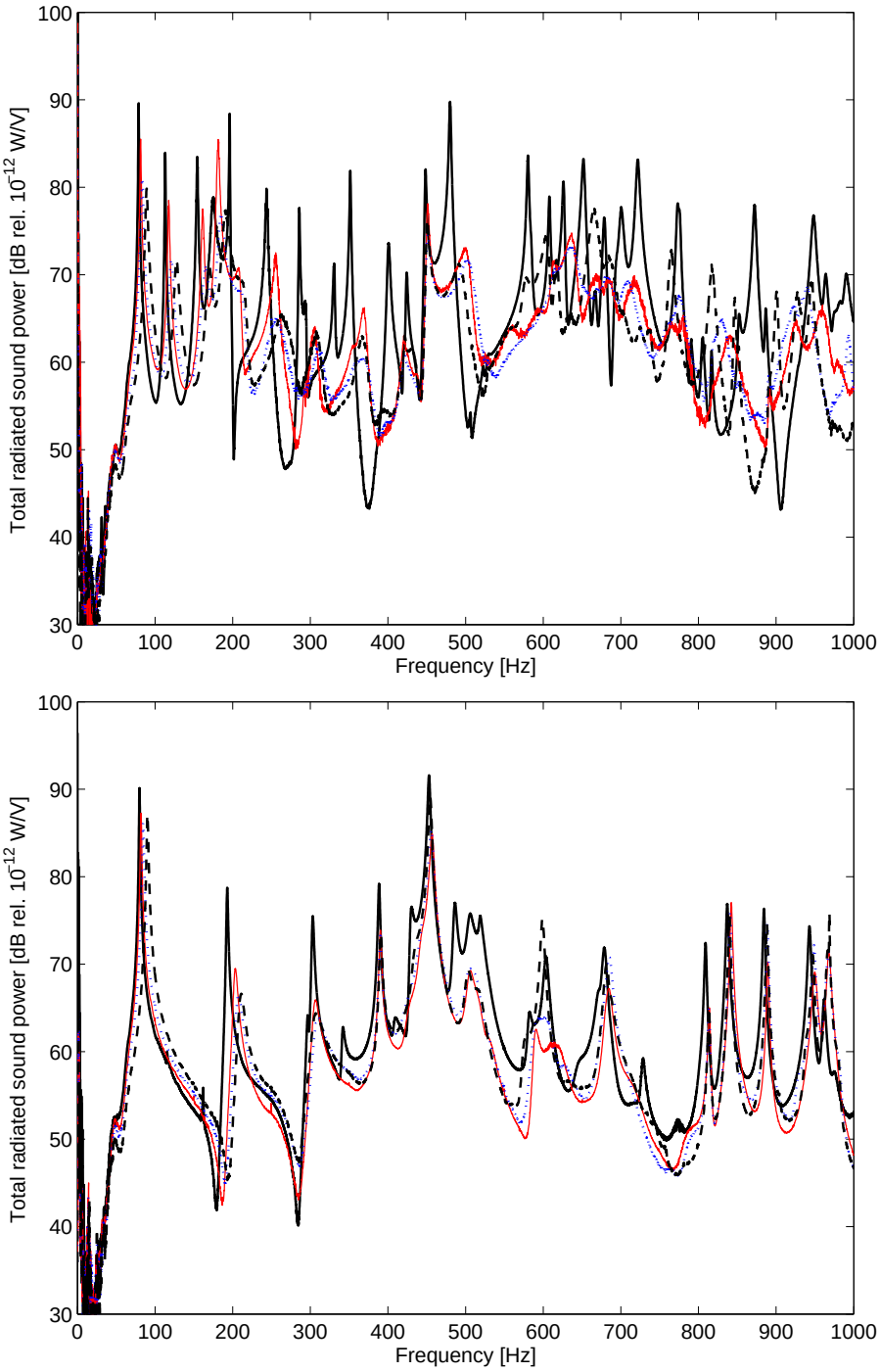

Figure 6.13: Narrow band spectra of the total radiated sound power, measured between 0 and 1 kHz per unit force generated by the shaker (top), and per unit voltage driving the loudspeaker(bottom)); measured by using (1) a plane panel without control unit (black solid line), and the panels with feedback control using the actuators with constant base length and various heights; (2) 40.0 mm × 25.0 mm (red faint line), (3) 40.0 mm × 31.5 mm (blue dotted line), and (4) 40.0 mm × 40.0 mm (black dashed line)

6.4 Base length and height with constant aspect ratio

This section investigates the combined effect of the base length and the height of the isosceles triangular piezoceramic patch on the stability and control performance of both SISO and MIMO systems. The base length and the height vary in such a way to maintain the constant aspect ration of the isosceles triangular shape. In the theoretical parametric study on a SISO system, the base length and the height of the triangular actuator vary between 20 mm and 50 mm, while the aspect ratio is fixed to 0.5. The part of this simulation analysis has been validated by three sets of the measured FRFs taken on the panel with the piezoceramic patch actuators listed in Table 6.7. In the experimental parametric study on a MIMO system, the vibration level and the sound radiation have been measured by using the smart panel equipped with 16 piezoceramic actuators listed in Table 6.7.

Table 6.7: Geometric parameter of the triangular piezoceramic actuator considered in the parametric study regarding the actuator dimensions.

sample	$b_{pzt} \times t_{pzt} \times h_{pzt}$ [mm^3]	aspect ratio	weight [g]
1	25.0 × 25.0 × 0.75	0.5	3.7
2	31.5 × 31.5 × 0.75	0.5	5.8
3	40.0 × 40.0 × 0.75	0.5	9.4

6.4.1 Single control unit

Figure 6.14 shows a comparison of the Bode plots of the simulated (top) and measured (bottom) open loop FRFs $G_c(j\omega)$ between the out-of-plane velocity of the panel and the input voltage to the piezoceramic actuators with a constant aspect ratio $AR = 0.5$ and various heights t_{pzt} and base lengthes b_{pzt} ; i) 25 mm × 25 mm (red faint line), ii) 31.5 mm × 31.5 mm (blue dotted line), and iii) 40 mm × 40 mm (black dashed line). Figure 6.15 shows the maximum control gain H_{max} (left) and the phase crossover frequency ω_0 (right) with reference to the height and hence the base length of the triangular actuator.

These figures confirm the indications obtained by the previous two parametric studies regarding the base length and the height of the triangular actuator. The amplitude plots in Fig. 6.14 highlights that the flexural actuation generated by the

piezoceramic actuator rises up to the first higher frequencies modulation peak, as the height and base length of the actuator increases. The phase plots of the measured open loop FRFs show that the phase lag exceeds - 90 degree at 1.5 kHz, 1.1 kHz, and 0.8 kHz with the 25 mm, 31.5 mm, and 40 mm height and base length triangular actuator, respectively. The left hand plot in Fig. 6.15 indicates that both maximum feedback gain H_{max} and the phase crossover frequency ω_0 decreases with small variations as the base length and the height of the actuator rises.

The maximum reduction index R_k plotted in Fig. 6.16 also agrees with the results derived from the previous two parametric studies regarding the base length and the height; i.e. the control performance is significantly improved by increasing the base length and/or height of the actuator. However, it must be underlined that the effective frequency range of the control system is further limited by using the actuator with longer height. Also, beyond the frequency range of control, the positive feedback occurs, which results in amplification of vibration level of the panel.

6.4.2 16 channel decentralized control units

Figure 6.17 shows the locus of the det$[\mathbf{I} + \mathbf{G}(j\omega)\mathbf{H}(j\omega)]$ measured between 25 Hz and 42 kHz using three smart panels equipped with 16 control units with different dimensions. Table 6.8 summarized the control gains h_0, which is experimentally implemented for MIMO systems. As expected from the pervious studies, both the effective frequency range and maximum control gain h_0 decrease as the size of the triangular actuator increases.

The two plots in Fig. 6.18 show the narrow band spectra of the spatially averaged velocity of the panel measured between 0 and 1 kHz per unit force generated by the shaker (top), and per unit voltage driving the loudspeaker(bottom). The two plots in Fig. 6.19 show the total radiated sound power by the panel, measured between 0 and 1 kHz per unit voltage driving the loudspeaker (top) or unit force generated by the shaker (bottom). Each plot includes four spectra measured with a plane panel without control unit and three panels with feedback control using the actuators with various base lengthes.

Figures 6.18 and 6.19 clearly indicate that low frequency control performance up

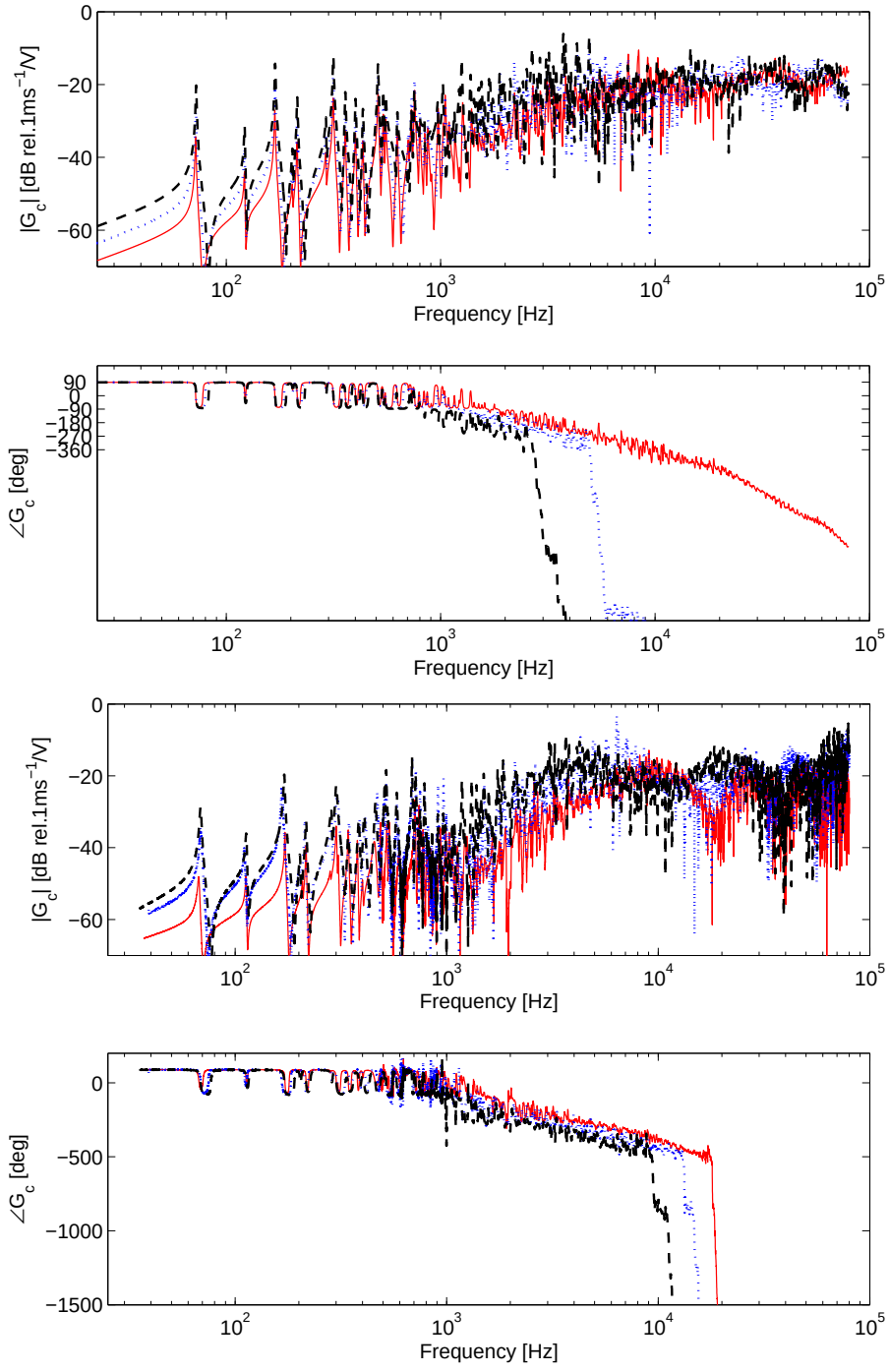

Figure 6.14: Bode plots of the simulated (top) and the measured (bottom) open loop FRFs on the panel with the triangle piezoceramic actuator with various base lengthes and heights; 25 mm × 25 mm (red faint line), 31.5 mm × 31.5 mm (blue dotted line), and 40 mm × 40 mm (black dashed line)

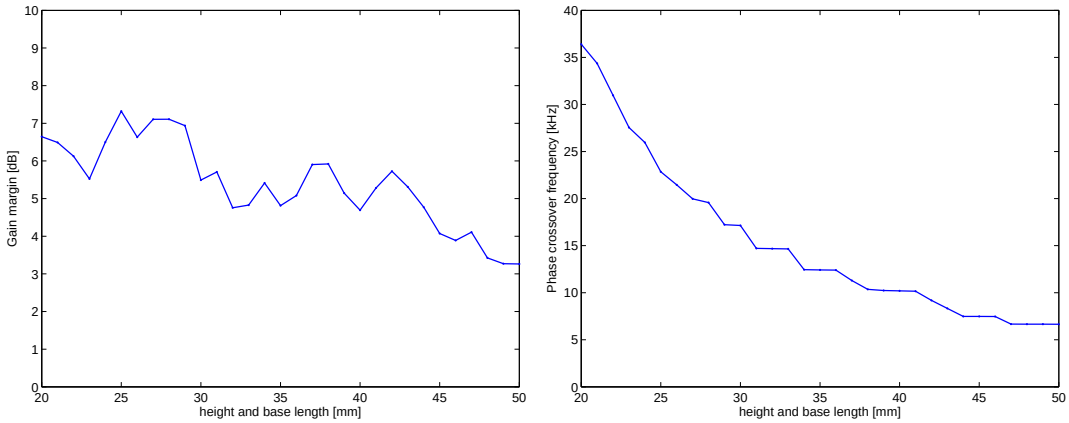

Figure 6.15: Maximum control gain H_{max} (left) and phase crossover frequency ω_0 (right), estimated by using predicted FRFs as a function of height and base length for constant aspect ratio

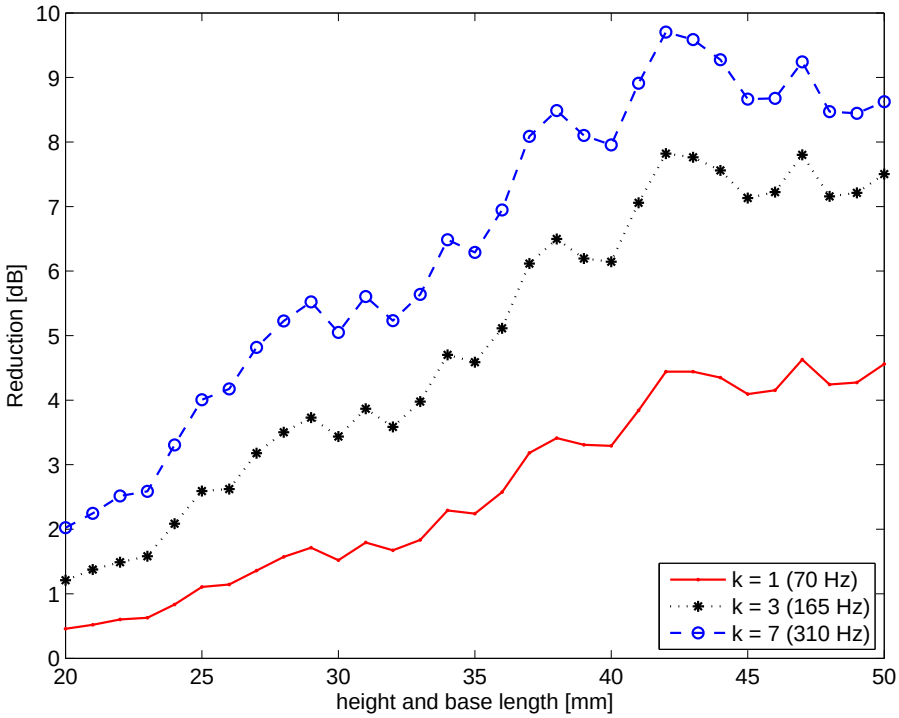

Figure 6.16: Maximum reduction index R_k ($k = 1,3,7$), estimated by using predicted FRFs as a function of height and base length for constant aspect ratio

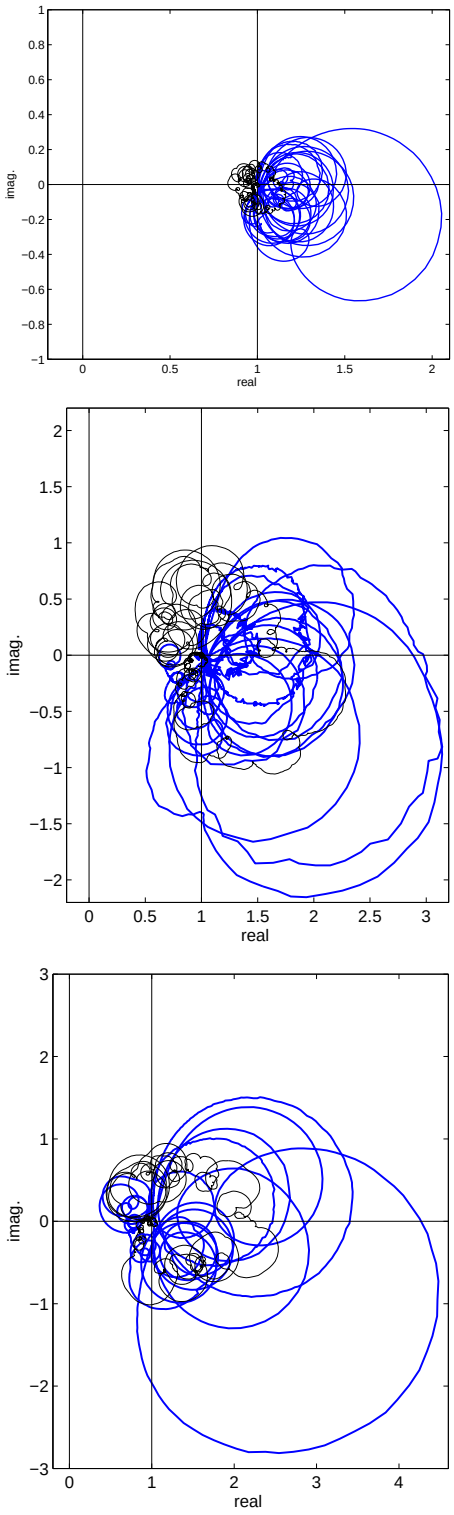

Figure 6.17: Locus of the det[$\mathbf{I}+\mathbf{G}(j\omega)\mathbf{H}(j\omega)$] between 25 Hz - 1 kHz (blue solid line) and 1 - 42 kHz (black faint line) measured on the panel with 16 triangular actuators with dimensions of 25.0 mm $\times$ 25.0 mm (top), 31.5 mm $\times$ 31.5 mm (middle), and 40.0 mm $\times$ 40.0 mm (bottom).

to around 500 Hz significantly increases by using bigger actuators. As listed in the Table 6.9, the control performance is more than doubled at the first 7 resonant frequencies by increasing the height and base length from 25 mm to 40 mm. However, at higher frequency beyond 700 Hz, the response of the panel is amplified by using decentralized velocity feedback control with 40 × 40 mm actuators, because of the positive feedback control effects.

In summary, as indicated by the previous two parametric studies regarding the base and height of the actuator, the effect of increasing the base length and height of the actuator on the control performance can be summarized in the following two points: (1) higher control performance at low frequency, and (2) smaller usable frequency range.

Table 6.8: Control gain h_0, experimentally implemented for decentralized MIMO systems with primary force and acoustic filed disturbance

dimensions [mm]	Control gain h_0	
$b_{pzt} \times t_{pzt}$	force	acoustic field
25.0 × 25.0	5.3	4.6
31.5 × 31.5	2.1	2.2
40.0 × 40.0	1.0	1.0

Table 6.9: Measured vibration reduction at resonant frequencies

frequency [Hz]	25 × 25	31.5 × 31.5	40 × 40
80.2	8.2	9.5	17.1
115.6	9.3	13.3	22.4
154.4	11.4	16.7	24.1
170.5	4.0	10.9	18.3
197.0	12.5	17.3	18.6
241.9	2.4	9.3	16.3
285.3	10.0	13.8	18.0
331.9	18.7	16.4	20.1
352.2	9.2	13.0	18.6
average	9.5	13.3	19.3

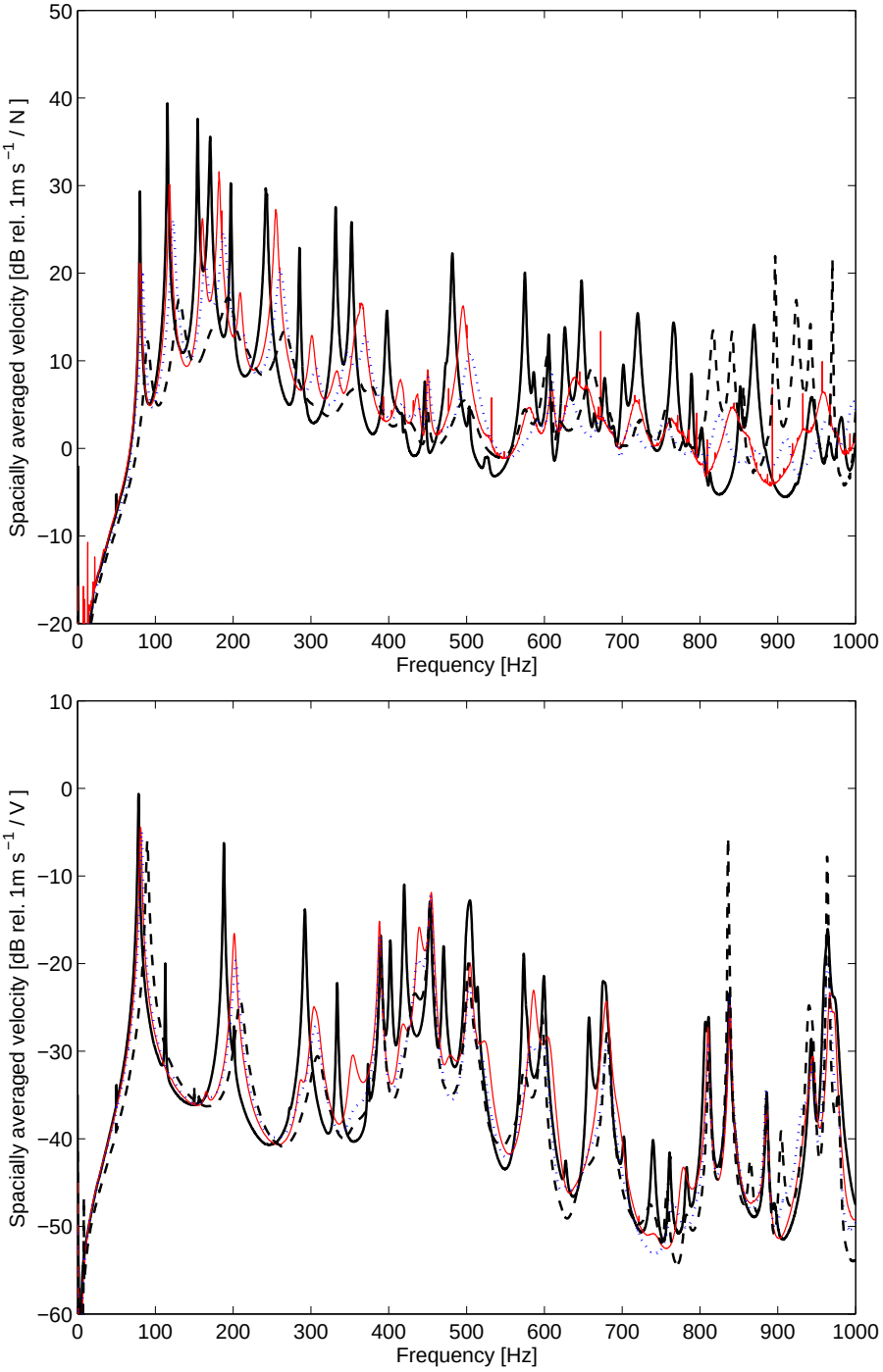

Figure 6.18: Narrow band spectra of the spatially averaged velocity of the panel measured between 0 and 1 kHz per unit force generated by the shaker (top), and per unit voltage driving the loudspeaker(bottom); measured by using (1) a plane panel without control unit (black solid line), and the panels with feedback control using the actuators with various base lengthes and heights; (2) 25 mm × 25 mm (red faint line), (3) 31.5 mm × 31.5 mm (blue dotted line), and (4) 40 mm × 40 mm (black dashed line)

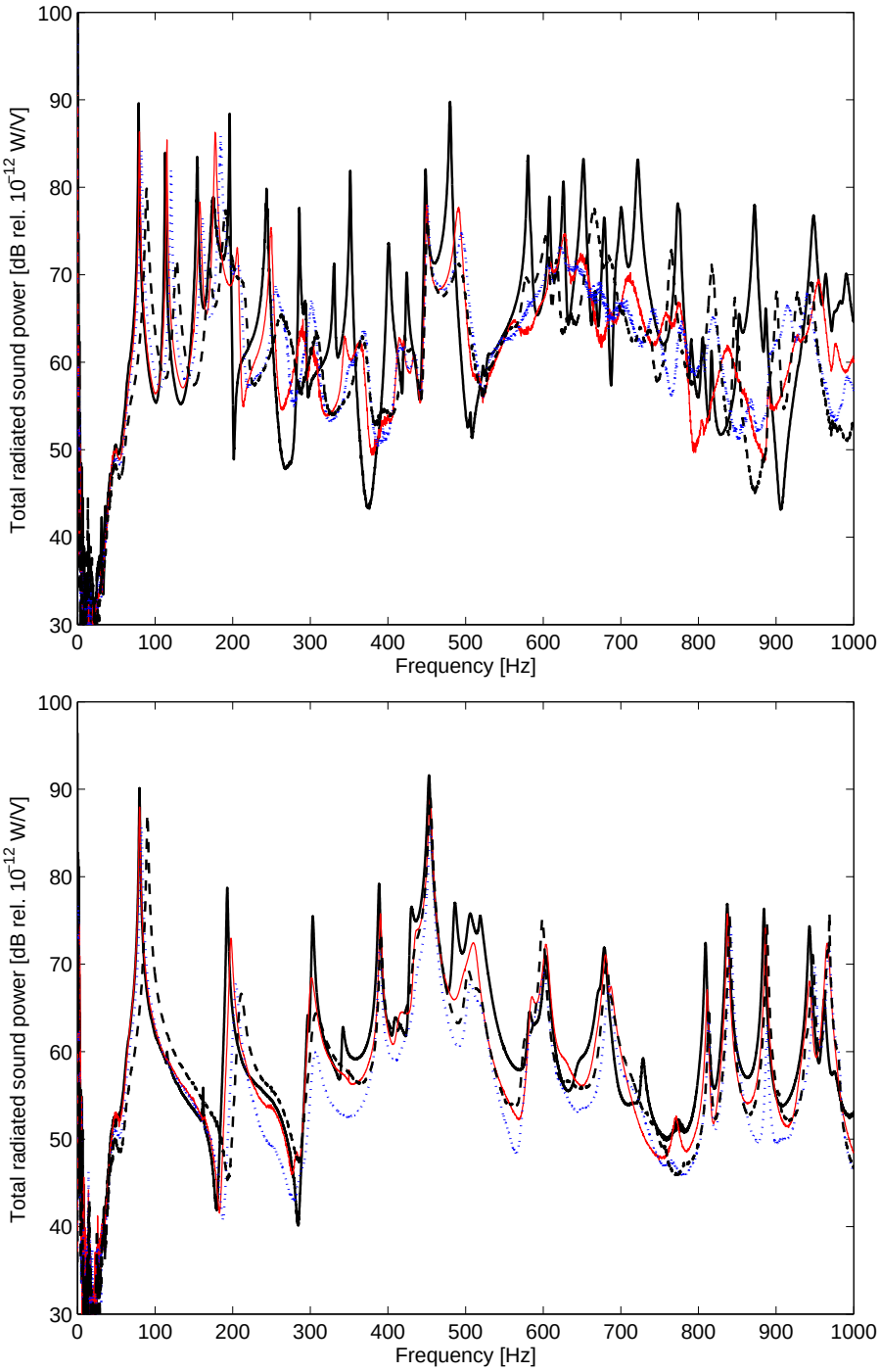

Figure 6.19: Narrow band spectra of the total radiated sound power, measured between 0 and 1 kHz per unit force generated by the shaker (top), and per unit voltage driving the loudspeaker(bottom); measured by using (1) a plane panel without control unit (black solid line), and the panels with feedback control using the actuators with various base lengthes and heights; (2) 25.0 mm × 25.0 mm (red faint line), (3) 31.5 mm × 31.5 mm (blue dotted line), and (4) 40.0 mm × 40.0 mm (black dashed line)

6.5 Conclusions

This chapter presented a parametric study of stability and control performance of the velocity feedback control using triangular piezoceramic actuator(s). The parametric study has been carried out in terms of (1) the base length, (2) the height, and (3) both height and base length of the triangular actuator. The stability and control performance are investigated in two stages; first, with a single-input and single-output control system, and second with the decentralized multi-input multi-output control system.

The parametric study on a SISO feedback control system can be summarized in the following conclusions: a) the low frequency actuation strength generated by the actuator rises with the base length and/or height increases, b) the maximum stable feedback gain decreases as the base length and/or height increase, c) the usable frequency range of the velocity feedback control is reduced as the height increase. As the first effect, the growth in actuation strength, is larger than the second effects, the decrease in the maximum control gain, the control performance is improved by increasing the height and/or base length of the triangular actuator over the bandwidth considered

The experimental parametric study with MIMO control systems confirmed the indication derived with SISO systems. Table 6.10 summarizes the measured vibration reductions averaged between at 1st and 9th resonant frequencies of the panel, which occur between 80 Hz and 350 Hz. This table clearly indicates that the control performance of the decentralized MIMO system using 16 triangular actuators is improved by increasing both base length and the height of the actuator. However, it must be emphasized that the increase of the height also results in limiting the usable frequency range of the control system. Beyond the usable frequency range, positive feedback is generated, and thus the control system amplifies both the vibration level and the sound radiation.

Table 6.10: Measured vibration reduction averaged between at 1st and 9th resonant frequencies.

	$t_{pzt} = 25.0$	$t_{pzt} = 31.5$	$t_{pzt} = 40.0$
$b_{pzt} = 25.0$	9.5	— (*1)	— (*1)
$b_{pzt} = 31.5$	— (*1)	13.3	— (*1)
$b_{pzt} = 40.0$	12.3	14.6	19.3
$b_{pzt} = 50.0$	12.6	— (*1)	— (*1)

(*1) The sample is not available.

Chapter 7

Conclusions and Recommendations for Further Study

7.1 Conclusions

The aim of this thesis has been: (1) to introduce a mobility model of rectangular and triangular piezoceramic actuators bonded on a panel, which allows an accurate prediction of the frequency response function up to high frequencies, (2) to provide general guidelines on the design of rectangular and triangular piezoceramic patches to implement velocity feedback control with velocity sensors, and (3) to experimentally demonstrate the implementation of decentralized MIMO control system using triangular piezoceramic actuators with accelerometer sensors.

In Chapter 2, a fully coupled model of a rectangular panel with a square piezoceramic patch actuator has been introduced, which considers passive inertial and elastic effects of the actuator patch. The validity of the fully coupled model has been compared with measurements taken on a panel with the piezoceramic patch actuator, which has confirmed that the fully coupled model captures the most important passive effects generated by the patch on the panel. The theoretical study highlighted that the inertia of the piezoceramic patch generates a constant amplitude roll off and phase lag of the open loop FRF at higher frequencies. Also, the bending

stiffness of the piezoceramic patch locally increases the stiffness of the smart panel, and thus lowers the amplitude of the open loop FRF at low frequencies. At higher frequencies, this stiffness effect is modulated by a coincidence phenomenon between the bending wavelength and the width of the square actuators, which causes wide band frequency peaks in the open loop FRF.

Chapter 3 presented a parametric study on the control performance achieved with a velocity feedback loop using a square piezoceramic actuator bonded on a rectangular panel. A simple formula has been derived using the open loop FRF in order to predict the maximum vibration reduction at the resonant peaks of lower order modes of the panel. The parametric study has been conducted with reference to: a) width, b) thickness, and c) dimensions of the piezoceramic patch. The principal effects produced by the piezoceramic actuator on the open loop FRF can be summarized as follows: a) the mean amplitude rises as the width of the square actuator increases; b) the mean amplitude at low frequencies decreases as the actuator thickness increases and c) the phase lag increases as the width of the actuator increases. It is concluded that increasing the width and reducing the thickness of the piezoceramic patch actuator improves the control performance over the bandwidth considered.

In Chapter 4, a new configuration for the velocity feedback control unit has been introduced, which is composed of a triangular piezoceramic actuator with a velocity sensor at its tip. A conventional modeling method was found to be less accurate and to lead to paradoxical results. A new fully coupled model of a rectangular panel with a triangular piezoceramic patch actuator has been developed in this thesis. The fully coupled model takes into account both the passive effects of the actuator patch and the resilient mounting effect of the panel. The proposed model has been compared with measurements taken on a panel with triangular piezoceramic actuators, and it was confirmed that in general the simulated response has was in good agreement with the measured response. The contribution to the open loop FRF have been considered of the indication excitation components generated by a triangular actuator. This has highlighted that the response of the panel was determined by the bending moments along the lateral edges of the patch actuator at low frequencies . As the frequency rises, the bending moments along the base edge excite the panel more effectively, and thus they dominate the FRF at higher frequencies.

Chapter 5 presented experimental results achieved with multi-channel decentralized velocity feedback control units having 16 triangular piezoceramic actuator and accelerometer sensor pairs. The control performance is discussed in terms of spatial structural vibration level of the panel and sound radiation in the frequency range 0 to 1 kHz. The closed loop experiments have highlighted that significant control effects are obtained in the frequency band between 100 and 700 Hz with reductions of up to 15 dB at the resonant peaks in both structural vibration and sound radiation. At frequencies higher than around 700 Hz, the vibration level and the radiated sound power slightly increased.

Chapter 6 described a parametric study of stability and control performance of the velocity feedback control using triangular piezoceramic actuators with velocity sensors. The parametric study has been carried out in terms of (1) the base length, (2) the height, and (3) both height and base length of the triangular actuator. The stability and control performance are investigated in two stages; first, with a single-input and single-output control system, and second with the decentralized multi-input multi-output control system. The findings of the parametric studies on SISO and MIMO control systems can be summarized in the following conclusions: (1) the control performance of the velocity feedback control using triangular actuator(s) with accelerometer sensor(s) is improved by increasing both base length and the height of the actuator, and (2) the usable frequency range of the control system is reduced by increasing the height of the actuator. Beyond the usable frequency range, positive feedback is generated, and thus the control system amplifies both the vibration level and the sound radiation.

7.2 Recommendations for further study

1. In this thesis, several mobility models were developed to predict the open loop FRF between the output signal of an ideal velocity sensor and the voltage signal drives a piezoceramic actuator. However, the decentralized MIMO feedback control system presented in Chapters 5 and 6 involved a practical velocity sensor, i.e. an accelerometer. A detailed investigation of effects of the accelerometer sensor dynamics on stability and control performance is a good direction for further work. Also, only a conventional inertial accelerometer has

been considered, but there may be advantages to using a MEMS accelerometer, whose response can be more carefully tailored for this application [76].

2. When a piezoceramic actuator is used with a point sensor, e.g. a velocity or accelerometer sensor, the stability of the feedback system is limited due to its non collocated and no dual properties. If a sensor-actuator pair is collocated and dual, transducers observe and excite the structure in a similar manner [27, 85], and thus better stability and higher control performance is expected. It would therefor be interesting to investigate the stability and control performance of velocity feedback control loops, composed of collocated piezoceramic sensor and actuator pair using the analytical models proposed in this thesis.

3. The theory presented in Chapter 4 suggests that triangular actuators would be more effective at producing forces at their vertexes if they are made from anisotropic piezoelectric material, such as PDVF. Their efficiency would thus be improved if such materials could be designed as stiff as PZT, and were thus able to exert significant forces on a panel.

4. In this thesis, the actuation of the piezoceramic patch is modeled by the bending moment along its border. In fact, when the piezoceramic patch is attached to a single side of the base structure, i.e. a thin panel in this thesis, the actuator generates in-plane forces for as well as the bending moments. Gardonio *et al.* [11] have shown that at high frequency the response of strain sensor-actuator pair is controlled by the in-plane longitudinal and shear vibration of the panel, rather than flexural motion. It may therefor be important to take into account the in-plane and shear vibration in order to get better agreements between predicted and measured response of the panel at high frequency, particularly if piezoceramic patch sensors as well as actuators are considered.

5. It is believed that the control performance could be further improved by designing better compensators in feedback loop. The performance of the decentralized MIMO feedback control system should be evaluated using different configurations of the controller.

6. In this thesis, the frequency response of the panel with a piezoceramic patch actuator is predicted with a mobility method. It would be interesting to

compare this method with a numerical method, e.g. finite element analysis, and the analytic results with inifinite plates.

7. The viscous elastic effects of bonding layers should be investigated in order to accurately evaluate the actuation strength of the piezoceramic patch bonded on the structure.

Appendix A

Plate Theory and Mobility Functions

A.1 General equations

The general formula for the mobility function Y_{ij} between a linear or angular velocity at positions (x_i, y_i), and a point force or moment excitation at positions (x_j, y_j) has been derived with a modal summation that takes into account the contribution of the first M and N natural modes in x- and y-direction [80]:

$$Y_{ij} = j\omega \sum_{m=1}^{M} \sum_{n=1}^{N} \frac{F_i F_j}{\Lambda[\omega_{mn}^2(1 + j\eta_s) - \omega^2]}, \tag{A.1}$$

where m and n respectively denote the modal index in x- and y-direction, and η_s denotes loss factor of the panel. Λ denotes the modal mass of the panel, which is given by:

$$\Lambda = \frac{4\rho_s h_s l_x l_y}{4}, \tag{A.2}$$

where l_x and l_y are the dimensions, and ρ_s and h_s the density and the thickness of the rectangular panel. ω_{mn} is the (m, n)th mode natural frequency of the plate, which can be calculated by suing the following formula [80]:

$$\omega_{mn} = \pi^2 \sqrt{\frac{D_s}{\rho_s h_s}} \sqrt{\frac{G_x^4(m)}{l_x^4} + \frac{G_y^4(n)}{l_y^4} + \frac{2H_x(m)H_y(n)}{l_x^2 l_y^2}}, \tag{A.3}$$

where $G_x(m)$, $H_x(m)$, $G_y(n)$, and $H_y(n)$ are function of the mode number m and n. Table A.1 gives these values for simply supported and clamped plates. D_s is the flexural of the plate, given below:

$$D_s = \frac{E_s}{1-\nu_s^2}\int_{-\frac{h_s}{2}}^{\frac{h_s}{2}} z^2 dz = \frac{E_s h_s^3}{12(1-\nu_s^2)}, \tag{A.4}$$

where E_s and ν_s denote the Young's modulus of elasticity, Poisson's ratio.

In Eq. (A.1), the general functions F_i and F_j represent the modal contributions respectively for the linear or angular velocities, and the point force or moment excitations. F_i and F_j have been derived from the natural modes ϕ and their derivatives in $x-$ and $y-$directions, ψ_x and ψ_y, respectively. The natural modes of a thin plate ϕ are given by the product of the beam natural modes functions ϕ_x and ϕ_y [80]:

$$\phi = \phi_x \phi_y. \tag{A.5}$$

For a simply supported plate, the beam function is given in the following formula:

$$\phi_x = \sin\left(\frac{m\pi x}{l_x}\right) \tag{A.6a}$$

$$\phi_y = \sin\left(\frac{n\pi y}{l_y}\right). \tag{A.6b}$$

For a clamped plate, the beam function is given below:

$$\phi_x = \cosh\left(\frac{\lambda_m x}{l_x}\right) - \cos\left(\frac{\lambda_m x}{l_x}\right) - \sigma_m\left\{\sinh\left(\frac{\lambda_m x}{l_x}\right) - \sin\left(\frac{\lambda_m x}{l_x}\right)\right\} \tag{A.7a}$$

$$\phi_y = \cosh\left(\frac{\lambda_n y}{l_y}\right) - \cos\left(\frac{\lambda_n y}{l_y}\right) - \sigma_n\left\{\sinh\left(\frac{\lambda_n y}{l_y}\right) - \sin\left(\frac{\lambda_n y}{l_y}\right)\right\}. \tag{A.7b}$$

σ_m and σ_n can be defined as follows:

$$\sigma_k = \frac{\cosh\lambda_k - \cos\lambda_k}{\sinh\lambda_k - \sin\lambda_k}, \tag{A.8}$$

where λ_k denotes the wavelength, and it can be obtained by numerically solving the

following equation:

$$\tan\frac{\lambda_i}{2}+\tanh\frac{\lambda_i}{2}=0 \quad , \quad i=\frac{k+1}{2}(k=1,3,...) \tag{A.9a}$$

$$\tan\frac{\lambda_j}{2}-\tanh\frac{\lambda_j}{2}=0 \quad , \quad j=\frac{k}{2}(k=2,4,...). \tag{A.9b}$$

Table A.1: Values of the constants for the natural frequencies of a rectangular plate with all four edges clamped (from reference [80])

Boundary conditions	m or n	G_x or G_y	H_x or H_y
Simply supported	1,2,3,...	m	m^2
Clamped	1	1.506	1.248
	2,3,4,...	$m+\frac{1}{2}$	$\left(m+\frac{1}{2}\right)^2\left[1-\frac{4}{(2m+1)\pi}\right]$

A.2 Square actuator

Chapter 2 has introduced the formula to predict the open loop FRF of the fully coupled model, which includes both inertia and stiffness effects of the square piezoceramic patch actuator. The fully coupled equation is again addressed below:

$$G_c=\begin{bmatrix}\mathbf{Y_{ce}} & \mathbf{Y_{cs}}\end{bmatrix}\begin{bmatrix}\mathbf{I_d}+\mathbf{Z_e}\mathbf{Y_{ee}} & \mathbf{Z_e}\mathbf{Y_{es}}\\ \mathbf{Z_k}\mathbf{Y_{ke}} & \mathbf{I_d}+\mathbf{Z_k}\mathbf{Y_{ks}}\end{bmatrix}^{-1}\begin{Bmatrix}\mathbf{0}\\ \mathbf{m_c}\end{Bmatrix}. \tag{A.10}$$

The above equation includes eight mobility vectors and matrices: i.e. $\mathbf{Y_{ce}}$, $\mathbf{Y_{cs}}$, $\mathbf{Y_{ee}}$, $\mathbf{Y_{es}}$, $\mathbf{Y_{ke}}$, and $\mathbf{Y_{ks}}$. This appendix provides the formulas to calculate these mobility functions.

- $\mathbf{Y_{ce}}$

  The i^{th} mobility function is defined between the velocity at the sensor $\dot{w}_c$ and the force at the center of the i^{th} element, f_m^i.

- $\mathbf{Y_{cs}}$

  This vector consists of four n_e^2-element row vectors as follows:

$$\mathbf{Y_{ck}}=\begin{bmatrix}\mathbf{Y_{w_c,m_{eL}}} & \mathbf{Y_{w_c,m_{eR}}} & \mathbf{Y_{w_c,m_{eB}}} & \mathbf{Y_{w_c,m_{eT}}}\end{bmatrix}. \tag{A.11}$$

In the above equation, the i^{th} item of $\mathbf{Y_{c,m_{eL}}}$ and $\mathbf{Y_{c,m_{eR}}}$ are defined between the velocity at the sensor $\dot{w}_c$, and the point moment along y-axis at the left and right edges of the i^{th} element, m^i_{eL} and m^i_{eR}. The i^{th} element of $\mathbf{Y_{w_c,m_{eB}}}$ and $\mathbf{Y_{w_c,m_{eT}}}$ are defined between the velocity at the sensor $\dot{w}_c$, and the point moment along x-axis at the bottom and top edges of the i^{th} element, m^i_{eB} and m^i_{eT}.

- $\mathbf{Y_{ee}}$

  The $(i,j)^{th}$ mobility function is defined between the velocity at the center of the i^{th} element $\dot{w}^i_e$, and the force at the center of the j^{th} element, f^j_e.

- $\mathbf{Y_{es}}$

  This matrix consists of four n_e^2 by n_e^2 matrices as follows:

$$\mathbf{Y_{ek}} = \begin{bmatrix} \mathbf{Y_{w_e,m_{eL}}} & \mathbf{Y_{w_e,m_{eR}}} & \mathbf{Y_{w_e,m_{eB}}} & \mathbf{Y_{w_e,m_{eT}}} \end{bmatrix}. \tag{A.12}$$

  In the above equation, the $(i,j)^{th}$ item of $\mathbf{Y_{w_e,m_{eL}}}$ and $\mathbf{Y_{w_e,m_{eR}}}$ is defined between the velocity at the center of the i^{th} element, $\dot{w}^i_e$, and the point moment along y-axis at the left and right edges of the j^{th} element, m^j_{eL} and m^j_{eR}. The $(i,j)^{th}$ element of $\mathbf{Y_{w_e,m_{eB}}}$ and $\mathbf{Y_{w_e,m_{eT}}}$ is defined between the velocity at the center of the i^{th} element $\dot{w}^i_e$, and the point moment along x-axis at the bottom and top edges of the j^{th} element, m^j_{eB} and m^j_{eT}.

- $\mathbf{Y_{ke}}$

  This matrix consists of four n_e^2 by n_e^2 matrices as follows:

$$\mathbf{Y_{ke}} = \begin{bmatrix} \mathbf{Y_{\theta_{eL},f_e}} & \mathbf{Y_{\theta_{eR},f_e}} & \mathbf{Y_{\theta_{eB},f_e}} & \mathbf{Y_{\theta_{eT},f_e}} \end{bmatrix}^T. \tag{A.13}$$

  In the above equation, the $(i,j)^{th}$ element of $\mathbf{Y_{\theta_{eL},f_e}}$ and $\mathbf{Y_{\theta_{eR},f_e}}$ is defined between the angular velocity along y-axis at the left and right edges of the i^{th} element, $\dot{\theta}^i_{eL}$ and $\dot{\theta}^i_{eR}$, and the force at the center of the j^{th} element, f^j_e. The $(i,j)^{th}$ element of $\mathbf{Y_{\theta_{eB},f_e}}$ and $\mathbf{Y_{\theta_{eT},f_e}}$ is defined between the angular velocity along x-axis at the bottom and top edges of the i^{th} element, $\dot{\theta}^i_{eB}$ and $\dot{\theta}^i_{eT}$, and the force at the center of the j^{th} element, f^j_e.

- $\mathbf{Y_{ks}}$

This matrix consists of 4 by 4 arrays of n_e^2 by n_e^2 matrix with mobility functions, as:

$$\mathbf{Y_{kk}} = \begin{bmatrix} \mathbf{Y}_{\theta_{eL},m_{eL}} & \mathbf{Y}_{\theta_{eL},m_{eR}} & \mathbf{Y}_{\theta_{eL},m_{eB}} & \mathbf{Y}_{\theta_{eL},m_{eT}} \\ \mathbf{Y}_{\theta_{eR},m_{eL}} & \mathbf{Y}_{\theta_{eR},m_{eR}} & \mathbf{Y}_{\theta_{eR},m_{eB}} & \mathbf{Y}_{\theta_{eR},m_{eT}} \\ \mathbf{Y}_{\theta_{eB},m_{eL}} & \mathbf{Y}_{\theta_{eB},m_{eR}} & \mathbf{Y}_{\theta_{eB},m_{eB}} & \mathbf{Y}_{\theta_{eB},m_{eT}} \\ \mathbf{Y}_{\theta_{eT},m_{eL}} & \mathbf{Y}_{\theta_{eT},m_{eR}} & \mathbf{Y}_{\theta_{eT},m_{eB}} & \mathbf{Y}_{\theta_{eT},m_{eT}} \end{bmatrix}. \tag{A.14}$$

The $(i,j)^{th}$ element of each matrix in the above equation is given between the angular velocity along the four borders of the i^{th} element, $\dot{\theta}^i_{eL}$, $\dot{\theta}^i_{eR}$, $\dot{\theta}^i_{eB}$ and $\dot{\theta}^i_{eT}$, and the moment along the four borders of the j^{th} element, m^j_{eL}, m^j_{eR}, m^j_{eB} and m^j_{eT}.

The modal contributions F_i and F_j for the above discussed six mobility functions in Eq. (A.10) are summarized in Table A.2.

Table A.2: Values of the modal contribution functions F_i and F_j for the mobility functions used in Eq. (A.10)

Mobility function	Item	F_i	F_j
$\mathbf{Y_{ce}}$	$\dot{w}_c/f^i_e$	$\phi(x_c,y_c)$	$\phi(x^i_e,y^i_e)$
$\mathbf{Y_{cs}}$	$\dot{w}_c/m^j_{eL}$	$\phi(x_c,y_c)$	$\psi_y(x^j_{eL},y^j_{eL})$
	$\dot{w}_c/m^j_{eR}$	$\phi(x_c,y_c)$	$\psi_y(x^j_{eR},y^j_{eR})$
	$\dot{w}_c/m^j_{eB}$	$\phi(x_c,y_c)$	$\psi_x(x^j_{eB},y^j_{eB})$
	$\dot{w}_c/m^j_{eT}$	$\phi(x_c,y_c)$	$\psi_x(x^j_{eT},y^j_{eT})$
$\mathbf{Y_{es}}$, $\mathbf{Y_{ke}}$	$\dot{w}^i_e/m^j_{eL} = \dot{\theta}^j_{eL}/f^i_e$	$\phi(x^i_e,y^i_e)$	$\psi_y(x^j_{eL},y^j_{eL})$
	$\dot{w}^i_e/m^j_{eR} = \dot{\theta}^j_{eR}/f^i_e$	$\phi(x^i_e,y^i_e)$	$\psi_y(x^j_{eR},y^j_{eR})$
	$\dot{w}^i_e/m^j_{eB} = \dot{\theta}^j_{eB}/f^i_e$	$\phi(x^i_e,y^i_e)$	$\psi_y(x^j_{eB},y^j_{eB})$
	$\dot{w}^i_e/m^j_{eT} = \dot{\theta}^j_{eT}/f^i_e$	$\phi(x^i_e,y^i_e)$	$\psi_y(x^j_{eT},y^j_{eT})$
$\mathbf{Y_{ee}}$	$\dot{w}^i_e/f^j_e$	$\phi(x^i_e,y^i_e)$	$\phi(x^j_e,y^j_e)$
$\mathbf{Y_{ks}}$	$\dot{\theta}^i_{eL}/m^j_{eL}$	$\psi_y(x^i_{eL},y^i_{eL})$	$\psi_y(x^j_{eL},y^j_{eL})$
	$\dot{\theta}^i_{eL}/m^j_{eR} = \dot{\theta}^j_{eR}/m^i_{eL}$	$\psi_y(x^i_{eL},y^i_{eL})$	$\psi_y(x^j_{eR},y^j_{eR})$
	$\dot{\theta}^i_{eL}/m^j_{eB} = \dot{\theta}^j_{eB}/m^i_{eL}$	$\psi_y(x^i_{eL},y^i_{eL})$	$\psi_x(x^j_{eB},y^j_{eB})$
	$\dot{\theta}^i_{eL}/m^j_{eT} = \dot{\theta}^j_{eT}/m^i_{eL}$	$\psi_y(x^i_{eL},y^i_{eL})$	$\psi_x(x^j_{eT},y^j_{eT})$
	$\dot{\theta}^i_{eR}/m^j_{eR}$	$\psi_y(x^i_{eR},y^i_{eR})$	$\psi_y(x^j_{eR},y^j_{eR})$
	$\dot{\theta}^i_{eR}/m^j_{eB} = \dot{\theta}^j_{eB}/m^i_{eR}$	$\psi_y(x^i_{eR},y^i_{eR})$	$\psi_x(x^j_{eB},y^j_{eB})$
	$\dot{\theta}^i_{eR}/m^j_{eT} = \dot{\theta}^j_{eT}/m^i_{eR}$	$\psi_y(x^i_{eR},y^i_{eR})$	$\psi_x(x^j_{eT},y^j_{eT})$
	$\dot{\theta}^i_{eB}/m^j_{eB}$	$\psi_x(x^i_{eB},y^i_{eB})$	$\psi_x(x^j_{eB},y^j_{eB})$
	$\dot{\theta}^i_{eB}/m^j_{eT} = \dot{\theta}^j_{eT}/m^i_{eB}$	$\psi_x(x^i_{eB},y^i_{eB})$	$\psi_x(x^j_{eT},y^j_{eT})$
	$\dot{\theta}^i_{eT}/m^j_{eT}$	$\psi_x(x^i_{eT},y^i_{eT})$	$\psi_x(x^j_{eT},y^j_{eT})$

A.3 Triangular actuator

Chapter 4 has introduced the formula to predict the open loop FRF of the fully coupled model, which includes both passive effects of the triangular piezoceramic patch actuator and resilient mounting effects of the rectangular panel. The fully coupled equation is again addressed below:

$$\dot{w}_c = \left\lfloor \mathbf{Y_{ce}} \quad \mathbf{Y_{ct}} \quad \mathbf{Y_{cb}} \right\rfloor \begin{bmatrix} \mathbf{I_d} + \mathbf{Z_e}\mathbf{Y_{ee}} & \mathbf{Z_e}\mathbf{Y_{et}} & \mathbf{Z_e}\mathbf{Y_{eb}} \\ \mathbf{Z_k}\mathbf{Y_{ke}} & \mathbf{I_s} + \mathbf{Z_k}\mathbf{Y_{kt}} & \mathbf{Z_k}\mathbf{Y_{kb}} \\ \mathbf{Z_b}\mathbf{Y_{be}} & \mathbf{Z_b}\mathbf{Y_{bt}} & \mathbf{I_b} + \mathbf{Z_b}\mathbf{Y_{bb}} \end{bmatrix}^{-1} \times \begin{Bmatrix} \mathbf{0_e} \\ \mathbf{m_c} \\ \mathbf{0_b} \end{Bmatrix} m_c V_c. \tag{A.15}$$

The above equation includes 12 mobility vectors and matrices: i.e. $\mathbf{Y_{ce}}$, $\mathbf{Y_{ct}}$, $\mathbf{Y_{cb}}$, $\mathbf{Y_{ee}}$, $\mathbf{Y_{et}}$, $\mathbf{Y_{eb}}$, $\mathbf{Y_{ke}}$, $\mathbf{Y_{kt}}$, $\mathbf{Y_{kb}}$, $\mathbf{Y_{be}}$, $\mathbf{Y_{bt}}$, and $\mathbf{Y_{bb}}$. The three mobility functions, $\mathbf{Y_{ce}}$, $\mathbf{Y_{ee}}$, are $\mathbf{Y_{ke}}$, are already discussed in the precious section. Moreover, the following three mobility functions $\mathbf{Y_{ct}}$, $\mathbf{Y_{et}}$, are $\mathbf{Y_{kt}}$ are respectively equal to $\mathbf{Y_{cs}}$, $\mathbf{Y_{es}}$, are $\mathbf{Y_{ks}}$, because the triangular actuator is modeled by arrays of rectangular elements. This section provides the formulas to calculate the other mobility functions used in Eq. (A.15).

- $\mathbf{Y_{cb}}$

  This mobility vector consists of four n_b-element row vectors as follows:

  $$\mathbf{Y_{cb}} = \left\lfloor \mathbf{Y_{w_c,m_{y0}}} \quad \mathbf{Y_{w_c,m_{yL}}} \quad \mathbf{Y_{w_c,m_{x0}}} \quad \mathbf{Y_{w_c,m_{xL}}} \right\rfloor. \tag{A.16}$$

  The i^{th} item of $\mathbf{Y_{w_c,m_{y0}}}$ and $\mathbf{Y_{w_c,m_{yL}}}$ are the mobility functions between the velocity at the sensor $\dot{w}_c$, and the ith point moment along the edge of the panel parallel to x-axis at $y = 0$ and $y = L_y$, as m^i_{y0} and m^i_{yL}, respectively. The i^{th} item of $\mathbf{Y_{c,Mx0}}$ and $\mathbf{Y_{c,MxL}}$ are the mobility functions between the velocity at the sensor $\dot{w}_c$, and the ith point moment along the edge of the panel parallel to y-axis at $x = 0$ and $x = L_x$, as m^i_{x0} and m^i_{xL}, respectively.

- $\mathbf{Y_{eb}}$

The mobility matrix $\mathbf{Y_{eb}}$ consists of four n_e^2 by n_b matrices as follows:

$$\mathbf{Y_{eb}} = \begin{bmatrix} \mathbf{Y_{we,m_{y0}}} & \mathbf{Y_{we,m_{yL}}} & \mathbf{Y_{we,m_{x0}}} & \mathbf{Y_{we,m_{xL}}} \end{bmatrix}. \tag{A.17}$$

The (i,j)th item of $\mathbf{Y_{we,m_{y0}}}$ and $\mathbf{Y_{we,m_{yL}}}$ are the mobility functions between the velocities at the center of the ith mass element of the actuator, and the jth point moment along the edge of the panel parallel to x-axis at $y = 0$ and $y = L_y$, as m_{y0}^i and m_{yL}^i, respectively.

- $\mathbf{Y_{kb}}$

  The matrix $\mathbf{Y_{kb}}$ consists of 4 by 4 arrays of n_e^2 by n_b matrix with mobility functions, as:

$$\mathbf{Y_{kb}} = \begin{bmatrix} \mathbf{Y_{\theta_{eL},m_{y0}}} & \mathbf{Y_{\theta_{eL},m_{yL}}} & \mathbf{Y_{\theta_{eL},m_{x0}}} & \mathbf{Y_{\theta_{eL},m_{xL}}} \\ \mathbf{Y_{\theta_{eR},m_{y0}}} & \mathbf{Y_{\theta_{eR},m_{yL}}} & \mathbf{Y_{\theta_{eR},m_{x0}}} & \mathbf{Y_{\theta_{eR},m_{xL}}} \\ \mathbf{Y_{\theta_{eB},m_{y0}}} & \mathbf{Y_{\theta_{eB},m_{yL}}} & \mathbf{Y_{\theta_{eB},m_{x0}}} & \mathbf{Y_{\theta_{eB},m_{xL}}} \\ \mathbf{Y_{\theta_{eT},m_{y0}}} & \mathbf{Y_{\theta_{eT},m_{yL}}} & \mathbf{Y_{\theta_{eT},m_{x0}}} & \mathbf{Y_{\theta_{eT},m_{xL}}} \end{bmatrix}. \tag{A.18}$$

- $\mathbf{Y_{be}}$

  The mobility matrix $\mathbf{Y_{be}}$ consists of four n_b by n_e^2 matrices as follows:

$$\mathbf{Y_{be}} = \begin{bmatrix} \mathbf{Y_{\theta_{y0},f_e}} & \mathbf{Y_{\theta_{yL},f_e}} & \mathbf{Y_{\theta_{x0},f_e}} & \mathbf{Y_{\theta_{xL},f_e}} \end{bmatrix}. \tag{A.19}$$

- $\mathbf{Y_{bt}}$

  The matrix $\mathbf{Y_{bk}}$ consists of 4 by 4 arrays of n_b by n_e^2 matrix with mobility functions, as:

$$\mathbf{Y_{bk}} = \begin{bmatrix} \mathbf{Y_{\theta_{y0},m_{eL}}} & \mathbf{Y_{\theta_{y0},m_{eR}}} & \mathbf{Y_{\theta_{y0},m_{eB}}} & \mathbf{Y_{\theta_{y0},m_{eT}}} \\ \mathbf{Y_{\theta_{yL},m_{eL}}} & \mathbf{Y_{\theta_{yL},m_{eR}}} & \mathbf{Y_{\theta_{yL},m_{eB}}} & \mathbf{Y_{\theta_{yL},m_{eT}}} \\ \mathbf{Y_{\theta_{x0},m_{eL}}} & \mathbf{Y_{\theta_{x0},m_{eR}}} & \mathbf{Y_{\theta_{x0},m_{eB}}} & \mathbf{Y_{\theta_{x0},m_{eT}}} \\ \mathbf{Y_{\theta_{xL},m_{eL}}} & \mathbf{Y_{\theta_{xL},m_{eR}}} & \mathbf{Y_{\theta_{xL},m_{eB}}} & \mathbf{Y_{\theta_{xL},m_{eT}}} \end{bmatrix}. \tag{A.20}$$

- $\mathbf{Y_{bb}}$

  The matrix $\mathbf{Y_{bb}}$ consists of 4 by 4 arrays of n_b by n_b matrix with mobility

functions, as:

$$\mathbf{Y_{bb}} = \begin{bmatrix} \mathbf{Y}_{\theta_{\mathbf{y0}},\mathbf{m_{y0}}} & \mathbf{Y}_{\theta_{\mathbf{y0}},\mathbf{m_{yL}}} & \mathbf{Y}_{\theta_{\mathbf{y0}},\mathbf{m_{x0}}} & \mathbf{Y}_{\theta_{\mathbf{y0}},\mathbf{m_{xL}}} \\ \mathbf{Y}_{\theta_{\mathbf{yL}},\mathbf{m_{y0}}} & \mathbf{Y}_{\theta_{\mathbf{yL}},\mathbf{m_{yL}}} & \mathbf{Y}_{\theta_{\mathbf{yL}},\mathbf{m_{x0}}} & \mathbf{Y}_{\theta_{\mathbf{yL}},\mathbf{m_{xL}}} \\ \mathbf{Y}_{\theta_{\mathbf{x0}},\mathbf{m_{y0}}} & \mathbf{Y}_{\theta_{\mathbf{x0}},\mathbf{m_{yL}}} & \mathbf{Y}_{\theta_{\mathbf{x0}},\mathbf{m_{x0}}} & \mathbf{Y}_{\theta_{\mathbf{x0}},\mathbf{m_{xL}}} \\ \mathbf{Y}_{\theta_{\mathbf{xL}},\mathbf{m_{y0}}} & \mathbf{Y}_{\theta_{\mathbf{xL}},\mathbf{m_{yL}}} & \mathbf{Y}_{\theta_{\mathbf{xL}},\mathbf{m_{x0}}} & \mathbf{Y}_{\theta_{\mathbf{xL}},\mathbf{m_{xL}}} \end{bmatrix}. \tag{A.21}$$

Table A.3: Values of the modal contribution functions F_i and F_j for the mobility functions used in Eq. (A.15)

Mobility function	Index	Item	F_i	F_j
$\mathbf{Y_{cb}}$	$\dot{w}_c/m^j_{eL}$	$\phi(x_c, y_c)$	$\psi_y(x_{eL}, y_{eL})$	
	$\dot{w}_c/m^j_{eR}$	$\phi(x_c, y_c)$	$\psi_y(x_{eR}, y_{eR})$	
	$\dot{w}_c/m^j_{eB}$	$\phi(x_c, y_c)$	$\psi_x(x_{eB}, y_{eB})$	
	$\dot{w}_c/m_{eT^j}$	$\phi(x_c, y_c)$	$\psi_x(x_{eT}, y_{eT})$	
$\mathbf{Y_{eb}}$, $\mathbf{Y_{be}}$	$\dot{w}^i_e/m^j_{y0} = \dot{\theta}^j_{y0}/f^i_e$	$\phi(x^i_e, y^i_e)$	$\psi_y(x^j_{eL}, y^j_{eL})$	
	$\dot{w}^i_e/m^j_{yL} = \dot{\theta}^j_{yL}/f^i_e$	$\phi(x^i_e, y^i_e)$	$\psi_y(x^j_{eR}, y^j_{eR})$	
	$\dot{w}^i_e/m^j_{x0} = \dot{\theta}^j_{x0}/f^i_e$	$\phi(x^i_e, y^i_e)$	$\psi_x(x^j_{eB}, y^j_{eB})$	
	$\dot{w}^i_e/m^j_{xL} = \dot{\theta}^j_{xL}/f^i_e$	$\phi(x^i_e, y^i_e)$	$\psi_x(x^j_{eT}, y^j_{eT})$	
$\mathbf{Y_{bb}}$	$\dot{\theta}^i_{eL}/m^j_{eL}$	$\psi_y(x^i_{eL}, y^i_{eL})$	$\psi_y(x^j_{eL}, y^j_{eL})$	
	$\dot{\theta}^i_{eL}/m^j_{eR} = \dot{\theta}^j_{eR}/m^i_{eL}$	$\psi_y(x^i_{eL}, y^i_{eL})$	$\psi_y(x^j_{eR}, y^j_{eR})$	
	$\dot{\theta}^i_{eL}/m^j_{eB} = \dot{\theta}^j_{eB}/m^i_{eL}$	$\psi_y(x^i_{eL}, y^i_{eL})$	$\psi_x(x^j_{eB}, y^j_{eB})$	
	$\dot{\theta}^i_{eL}/m^j_{eT} = \dot{\theta}^j_{eT}/m^i_{eL}$	$\psi_y(x^i_{eL}, y^i_{eL})$	$\psi_x(x^j_{eT}, y^j_{eT})$	
	$\dot{\theta}^i_{eR}/m^j_{eR}$	$\psi_y(x^i_{eR}, y^i_{eR})$	$\psi_y(x^j_{eR}, y^j_{eR})$	
	$\dot{\theta}^i_{eR}/m^j_{eB} = \dot{\theta}^j_{eB}/m^i_{eR}$	$\psi_y(x^i_{eR}, y^i_{eR})$	$\psi_x(x^j_{eB}, y^j_{eB})$	
	$\dot{\theta}^i_{eR}/m^j_{eT} = \dot{\theta}^j_{eT}/m^i_{eR}$	$\psi_y(x^i_{eR}, y^i_{eR})$	$\psi_x(x^j_{eT}, y^j_{eT})$	
	$\dot{\theta}^i_{eB}/m^j_{eB}$	$\psi_x(x^i_{eB}, y^i_{eB})$	$\psi_x(x^j_{eB}, y^j_{eB})$	
	$\dot{\theta}^i_{eB}/m^j_{eT} = \dot{\theta}^j_{eT}/m^i_{eB}$	$\psi_x(x^i_{eB}, y^i_{eB})$	$\psi_x(x^j_{eT}, y^j_{eT})$	
	$\dot{\theta}^i_{eT}/m^j_{eT}$	$\psi_x(x^i_{eT}, y^i_{eT})$	$\psi_x(x^j_{eT}, y^j_{eT})$	
$\mathbf{Y_{kb}}$	$\dot{\theta}^i_{y0}/m^j_{eL}$=$\dot{\theta}^j_{eL}/m^i_{y0}$	$\psi_y(x^i_{eL}, y^i_{eL})$	$\psi_y(x^j_{y0}, y^j_{y0})$	
	$\dot{\theta}^i_{y0}/m^j_{eR}$=$\dot{\theta}^j_{eL}/m^i_{yL}$	$\psi_y(x^i_{eL}, y^i_{eL})$	$\psi_y(x^j_{yL}, y^j_{yL})$	
	$\dot{\theta}^i_{y0}/m^j_{eB}$=$\dot{\theta}^j_{eL}/m^i_{x0}$	$\psi_y(x^i_{eL}, y^i_{eL})$	$\psi_x(x^j_{x0}, y^j_{x0})$	
	$\dot{\theta}^i_{y0}/m^j_{eT}$=$\dot{\theta}^j_{eL}/m^i_{xL}$	$\psi_y(x^i_{eL}, y^i_{eL})$	$\psi_x(x^j_{xL}, y^j_{xL})$	
	$\dot{\theta}^i_{yL}/m^j_{eL}$=$\dot{\theta}^j_{eR}/m^i_{y0}$	$\psi_y(x^i_{eR}, y^i_{eR})$	$\psi_y(x^j_{y0}, y^j_{y0})$	
	$\dot{\theta}^i_{yL}/m^j_{eR}$=$\dot{\theta}^j_{eR}/m^i_{yL}$	$\psi_y(x^i_{eR}, y^i_{eR})$	$\psi_y(x^j_{yL}, y^j_{yL})$	
	$\dot{\theta}^i_{yL}/m^j_{eB}$=$\dot{\theta}^j_{eR}/m^i_{x0}$	$\psi_y(x^i_{eR}, y^i_{eR})$	$\psi_x(x^j_{x0}, y^j_{x0})$	
	$\dot{\theta}^i_{yL}/m^j_{eT}$=$\dot{\theta}^j_{eR}/m^i_{xL}$	$\psi_y(x^i_{eR}, y^i_{eR})$	$\psi_x(x^j_{xL}, y^j_{xL})$	
	$\dot{\theta}^i_{x0}/m^j_{eL}$=$\dot{\theta}^j_{eB}/m^i_{y0}$	$\psi_x(x^i_{eB}, y^i_{eB})$	$\psi_y(x^j_{y0}, y^j_{y0})$	
	$\dot{\theta}^i_{x0}/m^j_{eR}$=$\dot{\theta}^j_{eB}/m^i_{yL}$	$\psi_x(x^i_{eB}, y^i_{eB})$	$\psi_y(x^j_{yL}, y^j_{yL})$	
	$\dot{\theta}^i_{x0}/m^j_{eB}$=$\dot{\theta}^j_{eB}/m^i_{x0}$	$\psi_x(x^i_{eB}, y^i_{eB})$	$\psi_x(x^j_{x0}, y^j_{x0})$	
	$\dot{\theta}^i_{x0}/m^j_{eT}$=$\dot{\theta}^j_{eB}/m^i_{xL}$	$\psi_x(x^i_{eB}, y^i_{eB})$	$\psi_x(x^j_{xL}, y^j_{xL})$	
	$\dot{\theta}^i_{xL}/m^j_{eL}$=$\dot{\theta}^j_{eT}/m^i_{y0}$	$\psi_x(x^i_{eT}, y^i_{eT})$	$\psi_y(x^j_{y0}, y^j_{y0})$	
	$\dot{\theta}^i_{xL}/m^j_{eR}$=$\dot{\theta}^j_{eT}/m^i_{yL}$	$\psi_x(x^i_{eT}, y^i_{eT})$	$\psi_y(x^j_{yL}, y^j_{yL})$	
	$\dot{\theta}^i_{xL}/m^j_{eB}$=$\dot{\theta}^j_{eT}/m^i_{x0}$	$\psi_x(x^i_{eT}, y^i_{eT})$	$\psi_x(x^j_{x0}, y^j_{x0})$	
	$\dot{\theta}^i_{xL}/m^j_{eT}$=$\dot{\theta}^j_{eT}/m^i_{xL}$	$\psi_x(x^i_{eT}, y^i_{eT})$	$\psi_x(x^j_{xL}, y^j_{xL})$	
$\mathbf{Y_{bt}}$	$\dot{\theta}^i_{y0}/m_t$	$\psi(x^i_{y0}, y^i_{y0})$	F_t	
	$\dot{\theta}^i_{yL}/m_t$	$\psi(x^i_{yL}, y^i_{yL})$	F_t	
	$\dot{\theta}^i_{x0}/m_t$	$\psi(x^i_{x0}, y^i_{x0})$	F_t	
	$\dot{\theta}^i_{xL}/m_t$	$\psi(x^i_{xL}, y^i_{xL})$	F_t	

Appendix B

PZT material

In this appendix the properties of the piezoceramic actuator are presented. Table B.1 shows the piezoelectric properties of the square and triangular actuators given by ISTEC, Italy [63].

Table B.1: Piezoelectric properties of the piezoceramic actuator, produced by ISTEC in Italy [63]

parameter	symbol	value
Sonic velocity [m/s]	V_{tr}	2767
Acoustic impedance [10^6 kg/m^{2}s]	Z	21.6
Mechanical quality factor	Q_m	84.6
	k_{33}	0.72
Electromechanical	k_{31}	-0.38
Coupling Factor	k_{15}	0.77
	k_p	0.67
Piezoelectric	d_{33}	355.0
charge constant	$d_{31} = d_{32}$	-183.5
10^{-3} m/V	d_{15}	724.4
Piezoelectric	g_{33}	25.9
voltage constant	g_{31}	-13.4
10^{-3} Vm/N	g_{15}	47.6
Relative dielectric	K_{33}^T	1551
constant	K_{11}^T	1718
	c_{11}^E	11.8
Elastic stiffness	c_{33}^E	11.7
(short circuit)	c_{44}^E	1.7
10^{10} N/m^2	c_{12}^E	7.3
	c_{13}^E	-7.6
Elastic compliance	s_{11}^E	16.7
(short circuit)	s_{33}^E	17.9
10^{-12} m^2/N	s_{44}^E	58.4
	s_{13}^E	-7.1

Appendix C

Experimental results

In this appendix, the detailed results of the experimental tests discussed in chapter 6 are presented. Figure C.2 to Fig. C.1 show the 4 by 4 arrays of Nyquist plots of the diagonal element of the measured open loop FRF matrix $\mathbf{G}(j\omega)$. The first and third rows of the array show the locus of the FRF between closely located sensor and actuator units along left and right edges of the panel parallel to y-axis, and the second and forth rows of the array show the locus of the FRF between closely located sensor and actuator units along bottom and top edges of the panel parallel to x-axis. The number of the sensor and actuator control units is illustrated in Fig. C.1. The locus between 25 Hz and 1000 Hz is plotted by faint line, and the locus for frequencies above 1000 Hz is plotted by black dotted line. Table C.1 shows the summary of the figures given in his appendix.

Table C.1: Summary of the figures

Figure No	Actuator [mm]
C.2	25.0 x 25.0
C.3	40.0 x 25.0
C.4	50.0 x 25.0
C.5	40.0 x 31.5
C.6	31.5 x 31.5
C.7	40.0 x 40.0

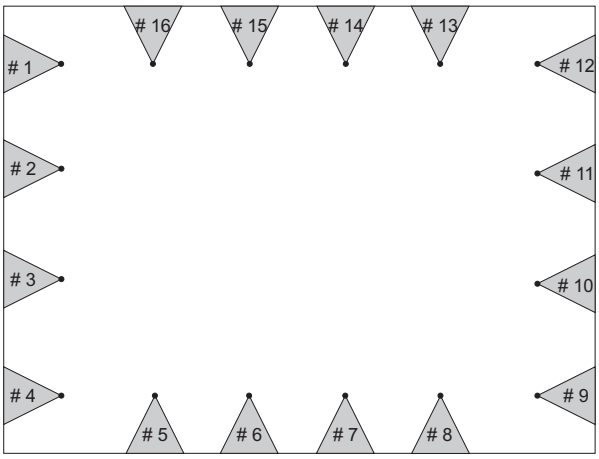

Figure C.1: A rectangular panel with 16 triangular piezoceramic actuators and its numbering.

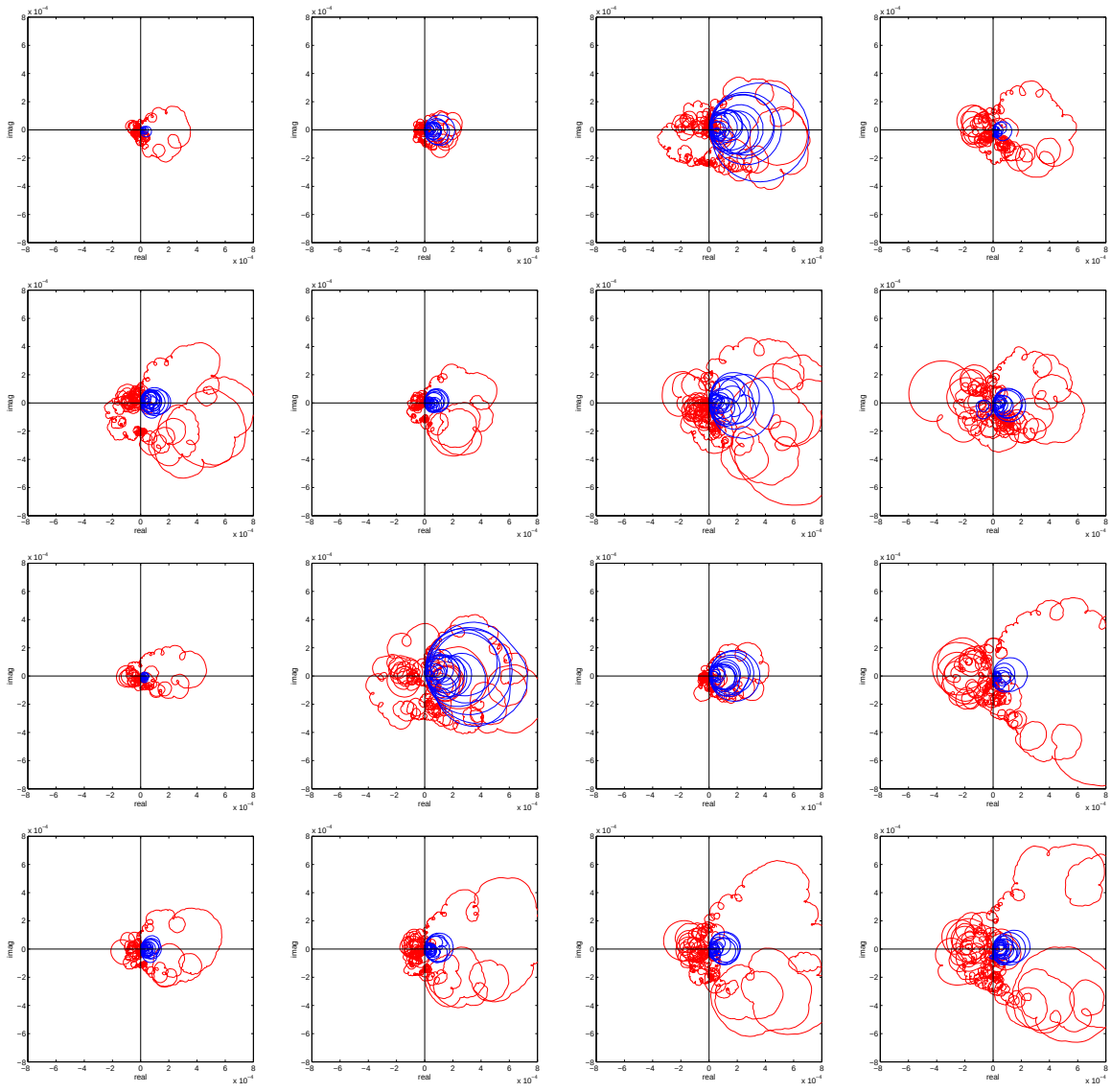

Figure C.2: Nyquist plots of the diagonal elements of the open loop FRF matrix $\mathbf{G}(j\omega)$ on the panel with 16 triangular piezoceramic actuators of base length 25 mm and height 25 mm between 25 Hz and 1 kHz (blue solid line), between 1 and 42 kHz (red dotted line)

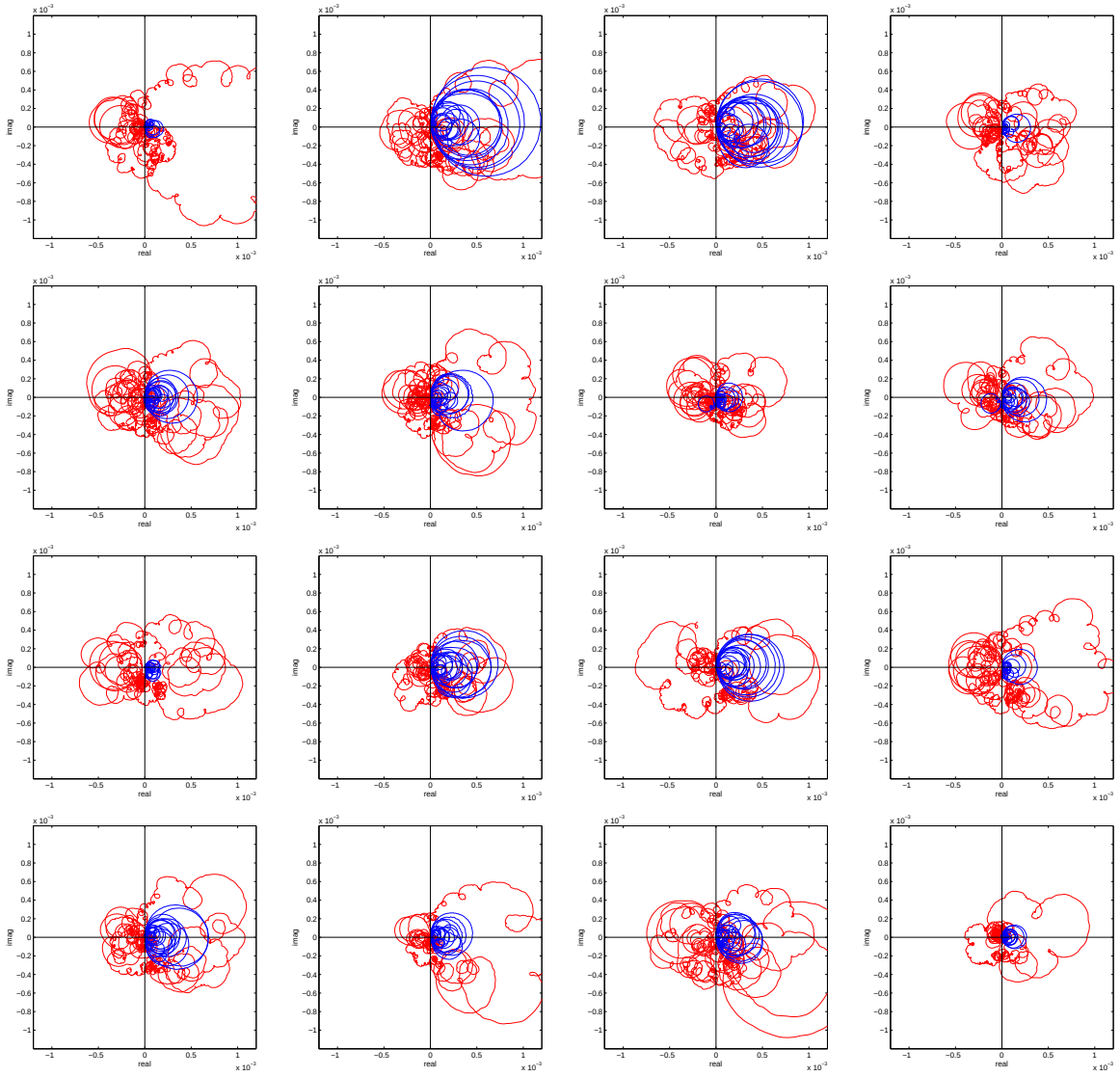

Figure C.3: Nyquist plots of the diagonal elements of the open loop FRF matrix $\mathbf{G}(j\omega)$ on the panel with 16 triangular piezoceramic actuators of base length 40 mm and height 25 mm between 25 Hz and 1 kHz (blue solid line), between 1 and 42 kHz (red dotted line)

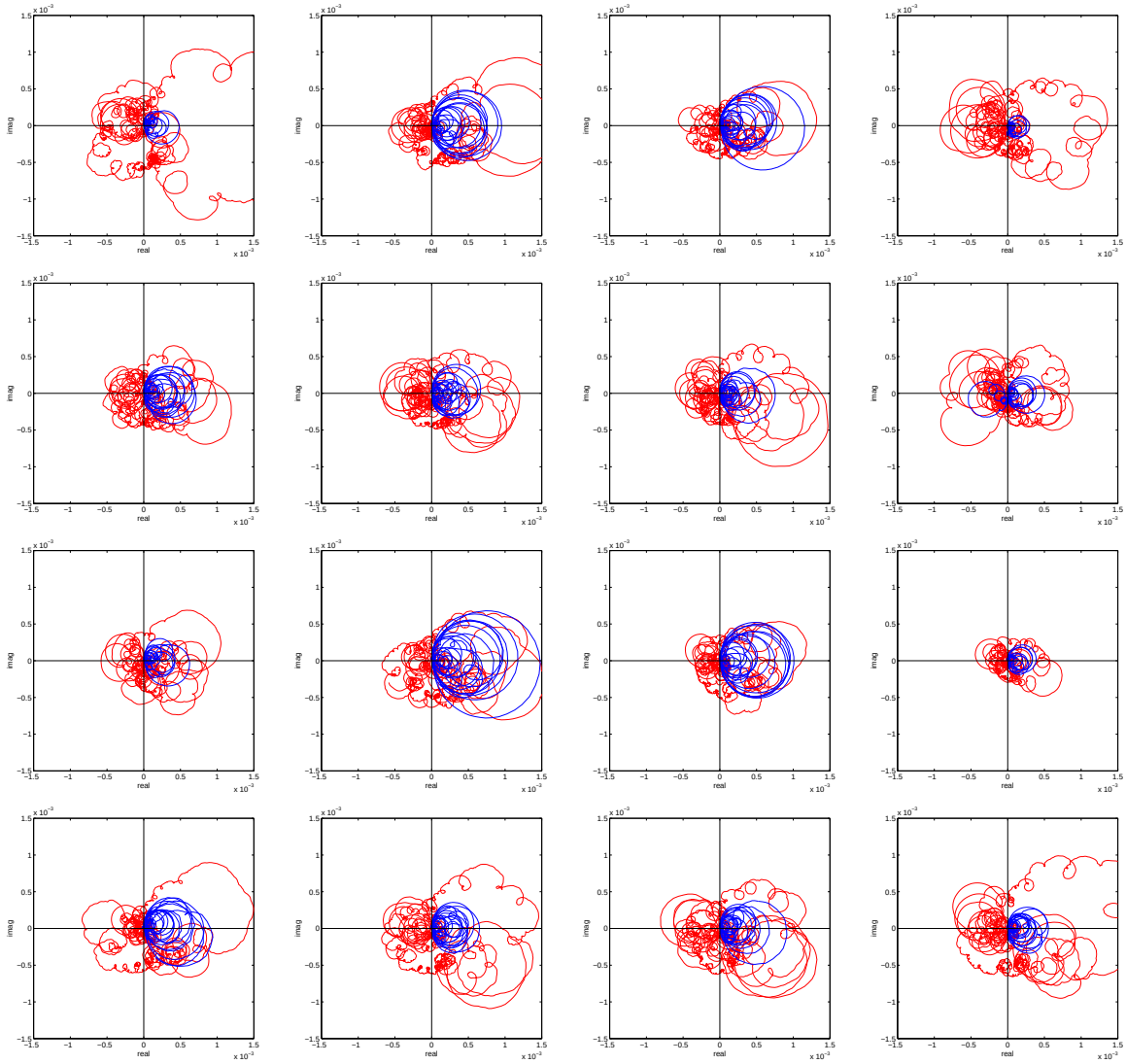

Figure C.4: Nyquist plots of the diagonal elements of the open loop FRF matrix $\mathbf{G}(j\omega)$ on the panel with 16 triangular piezoceramic actuators of base length 50 mm and height 25 mm between 25 Hz and 1 kHz (blue solid line), between 1 and 42 kHz (red dotted line)

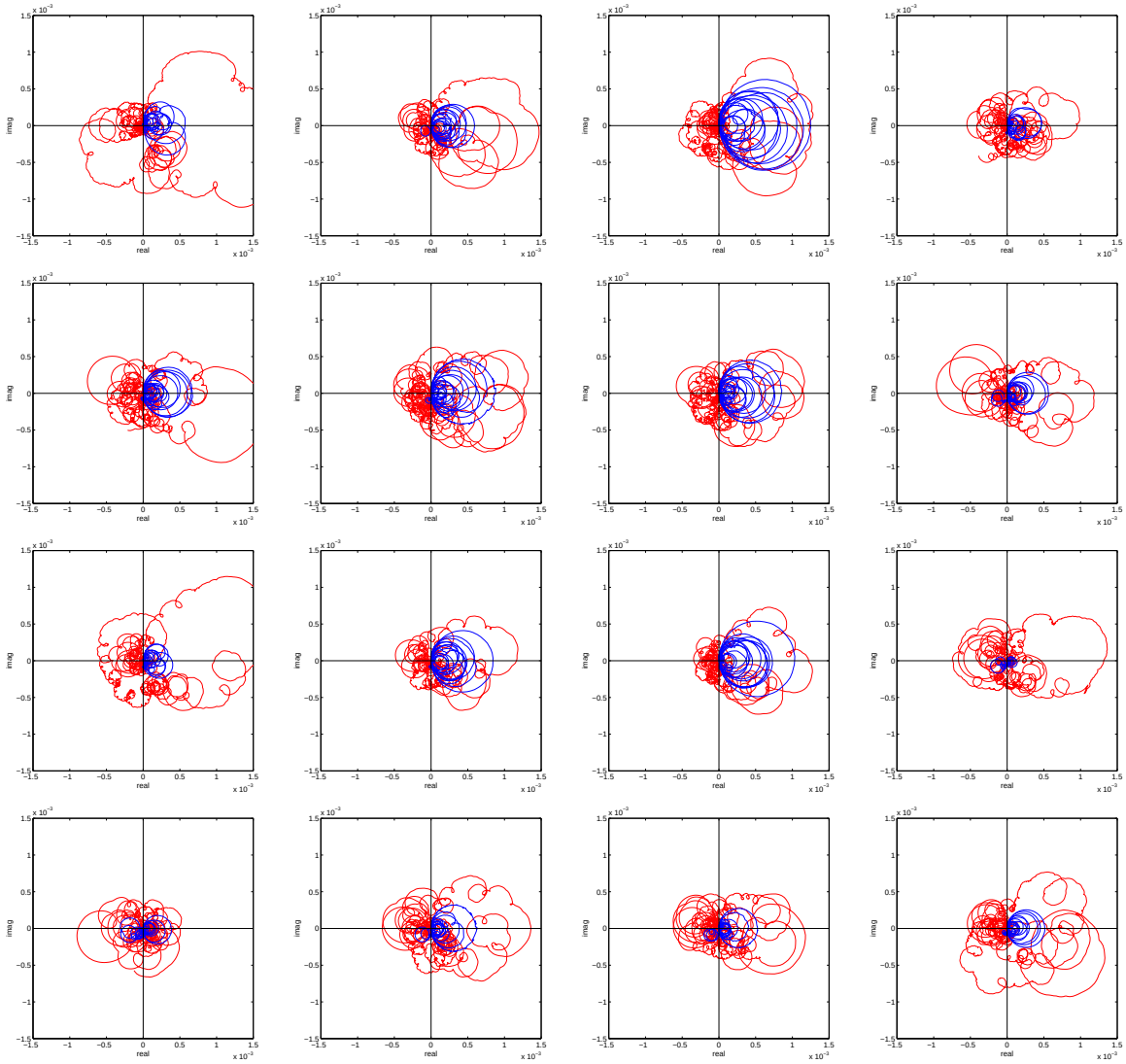

Figure C.5: Nyquist plots of the diagonal elements of the open loop FRF matrix $\mathbf{G}(j\omega)$ on the panel with 16 triangular piezoceramic actuators of base length 40 mm and height 31.5 mm between 25 Hz and 1 kHz (blue solid line), between 1 and 42 kHz (red dotted line)

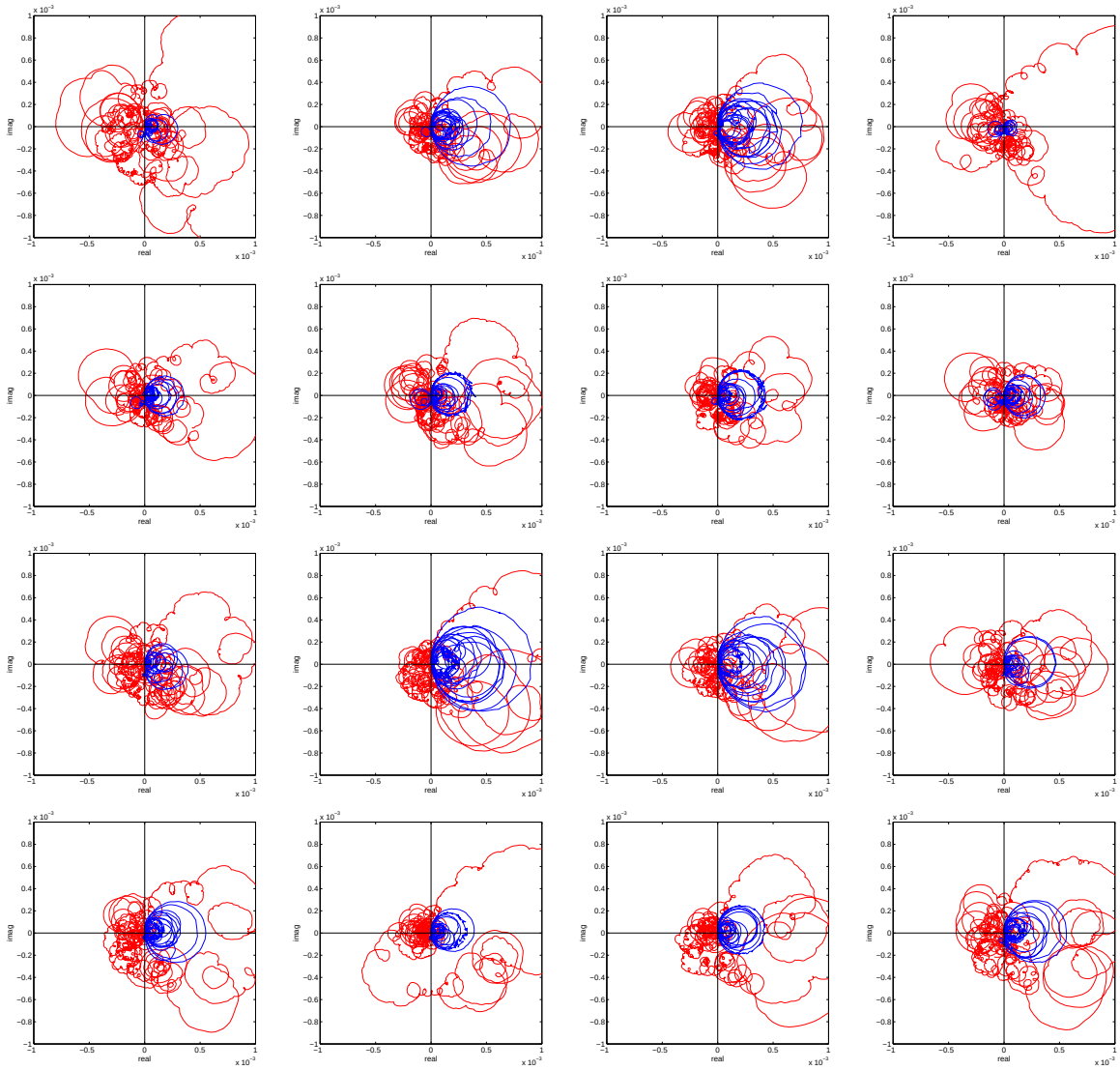

Figure C.6: Nyquist plots of the diagonal elements of the open loop FRF matrix $\mathbf{G}(j\omega)$ on the panel with 16 triangular piezoceramic actuators of base length 31.5 mm and height 31.5 mm between 25 Hz and 1 kHz (blue solid line), between 1 and 42 kHz (red dotted line)

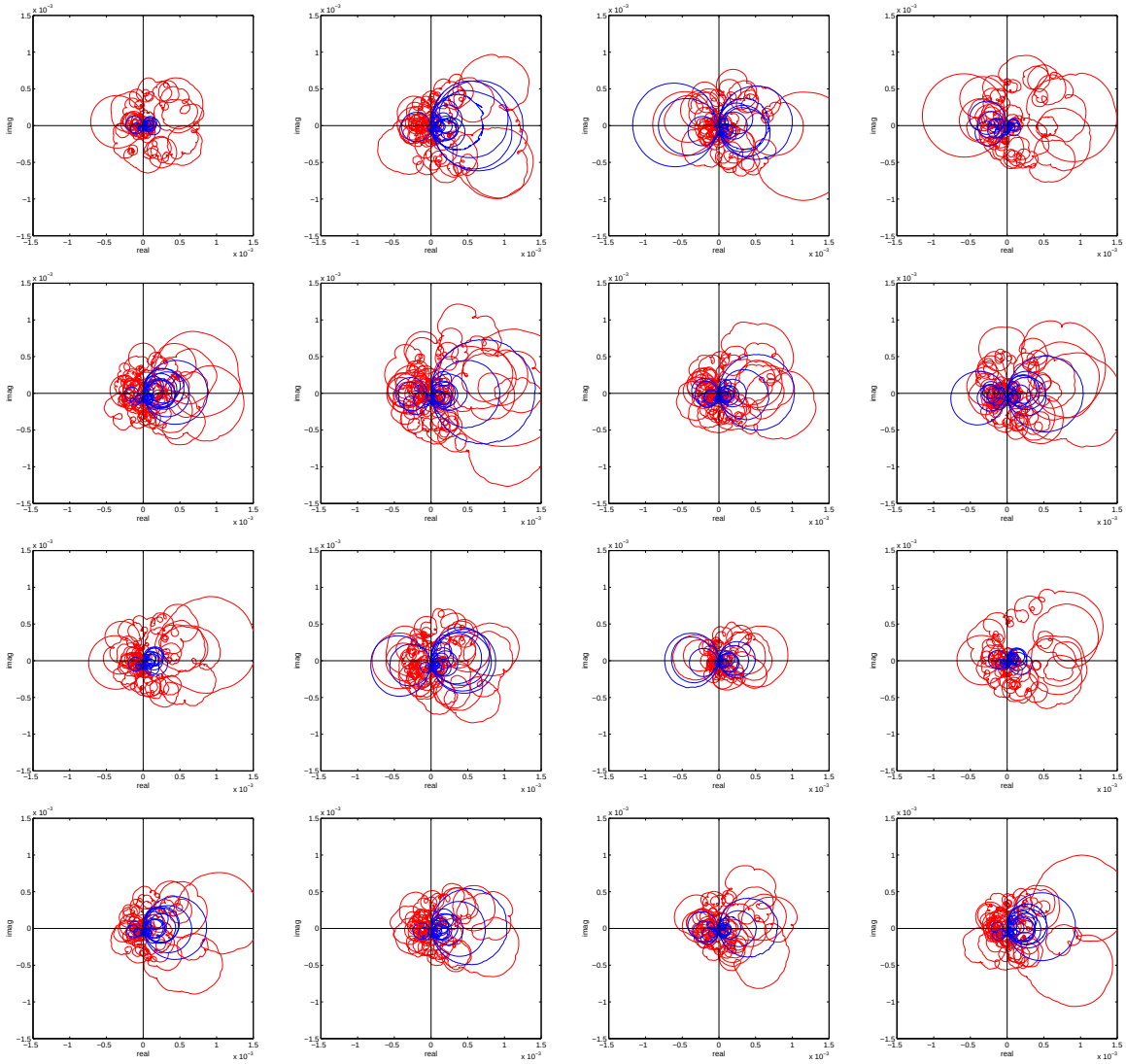

Figure C.7: Nyquist plots of the diagonal elements of the open loop FRF matrix $\mathbf{G}(j\omega)$ on the panel with 16 triangular piezoceramic actuators of base length 40 mm and height 40 mm between 25 Hz and 1 kHz (blue solid line), between 1 and 42 kHz (red dotted line)

Reference

[1] L. C. Cremer and M. Heckel, *Structure-Borne Sound*, Springer Verlag, 1988. 1.1

[2] F. J. Fahy and J. G. Walker, *Fundamentals of Noise and Vibration control*, Spon press, 1998. 1.1

[3] M. J. Brennan and N. S. Ferguson, *Vibration Control Advanced Applications in Acoustics, Noise and Vibration*, pp. 530-580, Spon press, 2004.

[4] D. J. Thompson and J. Dixon, Vehicle noise, in Frank J. Fahy and Johh G. Walker (eds.) *Advanced applications in acoustics, noise and vibration*, 236-291, London E and FN Spon, 2004 1.1

[5] F. Fahy and P. Gardonio, *Sound and Structural Vibration*, Academic Press, London 2007. 1.1, 1.2, 1.2.1, 1.2.2, 2.1.2, 2.1.2, 3.1, 5.3.1, 5.4.1, 6.2.2

[6] C. R. Fuller, S. J. Elliott, and P. A. Nelson, *Active Control of Vibration*, London Academic Press, 1997. 1.1, 1.2.1, 2.1.1

[7] C.R. Fuller, C.H. Hansen and S.D. Snyder, Active control of sound radiation from a vibrating rectangular panel by sound sources and vibration inputs: an experimental comparison, *Journal of Sound and Vibration*, 145 [2], 195-215, 1991.

[8] P. J. Carneal, and C. R. Fuller, An Analytical and Experimental Investigation of Active Structural Acoustic Control of Noise Transmission through Double Panel Systems *Journal of Sound and Vibration*, 272, 749-771, 2004.

[9] B. T. Wang, C. R. Fuller and E. K. Dimitriadis, Active control of noise transmission through rectangular plates using multiple piezoelectric or point force actuators, *Journal of the Acoustical Society of America*, 90, 2820-2830, 1991.

[10] E. K. Dimitriadis, C. R. Fuller, C. A. Roger, Piezoelectric actuators for distributed vibration excitation of thin plates , *Journal of Vibration and Acoustics Transactions of the ASME*, 113, 100-107 1991. 1.2.2, 2.1.1

[11] P. Gardonio, Y. S. Lee, S. J. Elliott and S. Debost, Analysis and measure of a matched volume velocity sensor and uniform force actuator for active structural acoustic control, *Journal of the Acoustical Society of America*, 110[6], 3025-3031, 2001. 1.2.1, 4

[12] P. Gardonio and S. J. Elliott, Smart Panels for Active Structural Acoustic Control, *Smart Materials and Structures*, 13, 1314-1336, 2004.

[13] R. L. Clark and C. R. Fuller, Optimal placement of piezoceramic actuators and polyvinylidene fluoride error sensors in active structural acoustic control approaches, *Journal of the Acoustical Society of America*, 92[3], 1521-1533, 1992.

[14] T. C. Scors and S. J. Elliott, Volume Velocity Estimation with Accelerometer Arrays for Active Structural Acoustic Control, *Journal of Sound and Vibration*, 258 [5], 867-883, 2002. 1.1

[15] R. L. Clark, W. R. Saunders and G. P. Gibbs, *Adaptive Structures: Dynamics and controls*, 2nd Edition, John Wiley and Sons, 2002. 1.1, 1.2, 1.2.2

[16] A. Preumont, *Vibration Control of Active Structures*, 2nd edition, Kluwer Academic Publishers, 2002. 1.1, 1.2, 1.2.2, 2.1.1, 3.1

[17] S. J. Elliott, P. Gardonio, T. C. Sors, and M. J. Brennan, Active vibroacoustic control with multiple local feedback loops, *Journal of the Acoustical Society of America*, 111[2], 908-915, 2002. 1.2, 5.2

[18] M. J. Brennan, S. J. Elliott, and X. Huang, demonstration of active vibration isolation using decentralized velocity feedback control, *Smart Materials and Structures*, 15, 19-22, 2006.

[19] P. Gardonio, E. Bianchi, and S. J. Elliott, Smart panel with multiple decentralized units for the control of sound transmission. Part I: theoretical predictions, *Journal of Sound and Vibration*, 274[1-2], 163-192, 2004. 1.2.1, 3.2

[20] P. Gardonio, E. Bianchi, and S. J. Elliott, Smart panel with multiple decentralized units for the control of sound transmission. Part II: design of the decentralized control units, *Journal of Sound and Vibration*, 274[1-2], 193-213, 2004. 1.2.1, 1.2.2

[21] E. Bianchi, P. Gardonio, and S. J. Elliott, Smart panel with multiple decentralized units for the control of sound transmission. Part III: Control System Implementation, *Journal of Sound and Vibration*, 274[1-2], 215-232, 2004. 1.2.1, 3.2, 5, 5.1

[22] N. Alujevi, P. Gardonio, and K. D.Frampton, Smart Double Panel with Decentralized Active Damping Units for the Control of Sound Transmission, *AIAA Journal*, 46[6], 1463- 1475, 2008. 1.2

[23] K. D. Frampton, Vibro-acoustic control with a distributed sensor network, *Journal of the Acoustical Society of America*, 119[4], 2170-2177, 2006. 1.2

[24] K. D. Frampton, Distributed group-based vibration control with a networked embedded system, *Smart Materials and Structures*, 14, 307-314, 2005. 1.2

[25] W. P. Engels, O. N. Baumann, S. J. Elliott, and R. Fraanje, Centralized and decentralized control of structural vibration and sound radiation, *Journal of the Acoustical Society of America*, 119, 1487-1495, 2006. 1.2

[26] O. N. Baumann, and S. J. Elliott,Global optimization of distributed output feedback controllers, *Journal of the Acoustical Society of America*, 122[3], 1587-1594, 2007. 1.2

[27] , M. J. Balas, Feedback Control of Flexible Systems Automatic Control, *IEEE*, 23[4], 673-679, 1978. 1.2, 5.2, 2

[28] J. Q. Sun, Some observations on physical duality and collocation of structural control sensors and actuators, *Journal of Sound and Vibration*, 194, 765-770, 1996. 1.2

[29] V. Jayachandran and J. Q. Sun, Unconditional stability domains of structural control systems using dual actuator-sensor pairs, *Journal of Sound and Vibration*, 208, 159-166, 1997. 1.2

[30] C. Paulitsh, P. Gardonio and S. J. Elliott, Active vibration control using an inertial actuator with internal damping, *Smart Materials and Structures*, 119, 2131-2140, 2006. 1.2

[31] C. G. Diaz and P. Gardonio, Feedback control laws for proof-mass electrodynamic actuators, *Smart Materials and Structures*, 16, 1766-1783, 2007.

[32] E. Bianchi, *Active structural acoustic control smart panel with small scale proof mass actuators*, PhD disseration, 2007. 1.2

[33] S. J. Elliott, M. Serrand, and P. Gardonio, Feedback Stability Limits for Active Isolation Systems with Reactive and Inertial Actuatorsc, *Journal ofvibration and acoustics-transactions of the ASME*, 123[2], 250-261 (2001). 1.2

[34] M. J. Brennan, K. A. Ananthaganeshan, and S. J. Elliott, Instabilities due to instrumentation phase-lead and phase-lag in the feedback control of a simple vibrating system, *Journal of Sound and Vibration*, 304[3-5], 466-478 (2007) 1.2

[35] B. Bingham, M. J. Atalla, and N. W. Hagood, Comparison of structural-acoustic designs on an active composite panel, *Journal of Sound and Vibration*, 244, 761-778, 2001. 1.2

[36] J.H. Han, I. Lee, Optimal placement of piezoelectric sensors and actuators for vibration control of a composite plate using genetic algorithms, *Smart Materials and Structures*, 8[2], 257-267, 1999. 1.2.1

[37] H. S. Tzou, and H. Q. Fu, A Study of Segmentation of Distributed Piezoelectric Sensors and Actuators, Part II: Parametric Study and Active Vibration Controls, *Journal of Sound and Vibration*, 172[2], 261-275 1994.

[38] S. Devasia, T. Meressi, B. Paden and E. Bayo, Piezoelectric Actuator Design for Vibration Suppression: Placement and Sizing, *Journal of guidance control and dynamics*, 16[5], 859-864, 1993.

[39] V.V. Varadan, J. Kim, and V.K. Varadan, Optimal placement of piezoelectric actuators for active noise control, *Journal of AIAA*, 35[3], 526-533, 1997.

[40] D. Halim, S.O.R. Moheimani, An optimization approach to optimal placement of collocated piezoelectric actuators and sensors on a thin plate, *Mechatronics*, 13 [1], 27-47, 2003. 1.2.1

[41] A. Preumont, Mechatronics: Dynamics of Electromechanical and Piezoelectric Systems, Springer,2006 1.2.1, 2.1.1

[42] E. Bianchi, *Smart panelwith an array of decentralized control systems for active structural acoustic control*, PhD disseration, 2003. 1.2.1, 5.1.3

[43] P. Gardonio and S. J. Elliott, Smart panels with velocity feedback control systems using triangularly shaped strain actuators, *Journal of the Acoustical Society of America*, 117, 2046-2064, 2005. 1.2.1, 4.1.2, 4.2.1

[44] J. M. Sullivan, J. E. Jr. Hubbard, and S. E. Burke, Modelling approach for two-dimensional distributed transducers of arbitrary spatial distribution, *Journal of the Acoustical Society of America*, 99, 2965-2974, 1996. 1.2.1, 1.2.2, 4.2.1, 4.2.1

[45] E. F. Crawley and J. Luis, Use of Piezoelectric Actuators as Elements of Intelligent Structures, *Journal of AIAA* , 25[10], 1373-1385, 1987. 1.2.2, 2.1.1

[46] E. F. Crawley and E. H. Anderson, Detailed models of piezoelectric actuation of beams, *Journal of Intelligent Material Systems and Structures*, 4, 100-107,1991. 1.2.2

[47] M. W. Lin, C. A. Rogers, Actuation response of a beam structure with induced strain actuators, *Adaptive Structures and Material Systems*,35, 166-173, 1995. 1.2.2

[48] S. J. Kim and J. D. Jones, Optimal Design of Piezoactuators for Active Noise and Vibration Control, *Journal of AIAA* , 29[10], 2047-2053, 1991. 1.2.2, 2.1.1

[49] G. P. Gibbs and C. R. Fuller, Excitation of thin beams using asymmetric piezoelectric actuators, *Journal of the Acoustical Society of America*, 92[6], 3221-3227, 1992. 1.2.2

[50] N. W. Hagood, W. H. Chung and A. Flotow, Modeling of piezoelectric actuator dynamics for active structural control, *Journal of Intelligent Material Systems and Structures*, 1[3] 327-354, 1990. 1.2.2

[51] F. Charette, C. Guigou, A. Berry, and G. Plantier, Asymmetric actuation and sensing of a beam using piezoelectric materials, *Journal of the Acoustical Society of America*, 96[4], 2272-2283, 1994. 1.2.2

[52] X. D. Wang and G. L. Huang, The coupled dynamic behavior of piezoelectric sensors bonded to elastic media, *Journal of Intelligent Material Systems and Structures*, 17, 883-894, 2006. 1.2.2

[53] J. Kim, V. V. Varadan, V.K. Varadan, Finite element modelling of structures including piezoelectric active devices, *International journal for numerical methods in engineering*, 40[5], 817-832, 1997. 1.2.2

[54] H. S. Tzou, and C.I. Tseng, Distributed piezoelectric sensor actuator design for dynamic measurement control of distributed parameter-systems - a piezoelectric finite-element approach, *Journal of Sound and Vibration*, 138[1], 17-34 1990.

[55] A. Benjeddou, Advances in piezoelectric Finite element modeling of adaptive structural elements: a survey, *Computers and Structures*, 76, 347-363, 2000. 1.2.2

[56] C. K. Lee and F. C. Moon, Laminated piezopolymer plates for torsion and bending sensors and actuators, *Journal of the Acoustical Society of America*, 85[6], 2432-2439, 1989. 1.2.2

[57] C. K. Lee and F. C. Moon, Modal Sensors/Actuators, *Journal of Applied Mechanics*, 57, 434-441, 1990. 1.2.2, 4.2.1

[58] C. K. Lee, Theory of laminated piezoelectric plates of the design of distributed sensors/actuators. Part I: Governing equations and reciprocal relationships, *Journal of the Acoustical Society of America*, 87, 1144-1158, 1990. 1.2.2, 4.2.1

[59] S. Koshigoe and J. W. Murdock, A unified analysis of both active and passive damping for a plate with piezoelectric transducers, *Journal of the Acoustical Society of America*, 93[1], 346-355, 1993. 1.2.2

[60] D. G. Cole, W. R. Saunders, and H. H. Robertshaw, Modal parameter estimation for piezostructures, *Journal of vibration and acoustics-transactions of the ASME*, 117[4], 431-438, 1995. 1.2.2

[61] M. J. Brennan, S. J. Elliott, and R. J. Pinnington, The dynamic coupling between piezoceramic actuators and a beam, *Journal of the Acoustical Society of America*, 102[4], 1931-1942, 1997. 1.2.2

[62] R. S. Langley and F. J. Fahy High-frequency structural vibration, in F. J. Fahy and J. Walker, *Energy and Variational Methods in Applied Mechanics*, 490-529, Willey, 1984. 2, 2.1.2

[63] C. Galassi, E. Roncali, C. Capiani, A. Costa, *Influence of processing parameters on the properties of PZT materials*, NATO Science Series 3 - High Technology, vol. 76, Eds. C. Galassi, M. Dinescu, K. Ukino, M. Sayer, Publ. Kluwer Academics, 75-86, 2000. (document), 2.1.1, 2.2, 3.2, 4.1, 4.2.1, B, B.1

[64] R. S. Langley and F. J. Fahy, *High-frequency structural vibration Advanced applications in acoustics, noise and vibration*, 490-529, E and FN Spon, 2004. 2.1.3

[65] , S. E. Burke, J. E. Hubbard, Jr., Active vibration control of a simply supported beam using a spatially distributed actuator, *IEEE*, 7[4], 25- 30, 1978. 4.2.1

[66] J. M. Sullivan, Jr J. E. Hubbard, and S.E.Burke, Distributed sensor/actuator design for plates: spatial shape and shading as design parameters, *Journal of Sound and Vibration*, 203[3], 473-493, 1997. (document), 4.2.1, 4.4

[67] S. Burke and J. Jr. Hubbard, Distributed Transducers for Structural Measurement and Control, *Advances in Control and Dynamic Systems, vol. 36*, Edited by C. T. Leondes, pp. 223-273 (1990). 4.2.1

[68] Y. Aoki, P. Gardonio, and S.J. Elliott, Strain Transducers for Active Control -Lumped Parameter Model-, *ISVR Technical Memorandum*, No. 956 (2006) 5.1.2

[69] S. Skogestad and I. Postlethwaite, *Multivariable Feedback Control; Analysis and Design*, 2nd Edition, Wiley, 2005. 5.2, 6.1.2, 6.2.2

[70] IEEE, *IEEE standard on piezoelectricity*, IEEE, 1988. 4.2.1

[71] D. A. Bies and C. H. Hansen, *Engineering Noise Control; theory and practice*, 3rd Edition, Spon press, 2003. 5.3.2, 5.4.2

[72] I. L. Ver, *Noise and Vibration Control Engineering: Principles and Applications*, John Wiley and Sons, 2005. 5.3.2, 5.4, 5.4.1

[73] S. J. Elliott and M. E. Johnson, Radiation modes and the active control of sound power, *Journal of the Acoustical Society of America*, 94, 2194-2204, 1993. 5.4.1

[74] S. J. Elliott, *Signal Processing for Active Control*, Academic Press, 2000. 6.1.2

[75] L. Meirovitch, *Dynamics and Control of Structures*, John Wiley and Sons, 1990. 6.2.2

[76] P. Gardonio, M. Gavagni, S. J. Elliott, Velocity sensor with an internal feedback control loop, *Smart Materials and Structures*, 14[6], 1517-1525 (2005) 1

[77] P. A. Nelson, and S. J. Elliott, *Active Control of Sound*, Academic Press, 1992.

[78] S. S. Rao, *Mechanical vibrations*, 3rd Edition, Addison-Wesley, 1995.

[79] J. N. Reddy, *Mechanics of Laminated Composite PlatesTheory and Analysis*, CRC 1996.

[80] P. Gardonio and M. J. Brennan, Mobility and impedance methods in structural dynamics Advanced applications in acoustics, noise and vibration, in F. Fahy and J. Walker (ed.), *Advanced Applications in Acoustics, Noise and Vibration*, 389-447, Taylor and Francis, 2004. (document), A.1, A.1, A.1, A.1

[81] J. N. Reddy, *Theory and analysis of elastic plates and shells, second edition*, CRC, 2006.

[82] P. Gardonio and S. J. Elliott, Modal response of a beam with a sensor-actuator pair for the implementation of velocity feedback control, *Journal of Sound and Vibration*, 284[1-2], 1-22, 2005.

[83] M. E. Johnson and S. J. Elliott, Acitve Control of Sound radiation using volume velocity cancellation, *Journal of the Acoustical Society of America*, 94, 2174-2186, 1995.

[84] Y-S. Lee, P. Gardonio, and S. J. Elliott, Volume velocity vibration control of a smart panel using a uniform force actuator and an accelerometer array, *Smart Materials and Structures*, 11, 863-873, 2002.

[85] S. E. Burke, J. E. Hubbard, and J. E. Meyer, Distributetrda nsducearnsd collocation *J. Mech. Syst. Signal Process*, 7[4], 349-361 (1993). 2